Ground-Based Autonomous Passive-Optical Staring Sensor for Orbital Object Detection and Position Measurement

A thesis accepted by the Faculty of Aerospace Engineering and Geodesy of the University of Stuttgart in fulfillment of the requirements for the degree of Doctor of Engineering Sciences (Dr.-Ing.)

by
Paul-Philipp Wagner
born in Wernigerode, Germany

Main referee:	Prof. Dr. rer. nat. Thomas Dekorsy
Co-referee:	Prof. Dr.-Ing. Nicolaas Sneeuw
Day of defense:	28. April 2022

Institute of Aerospace Thermodynamics (ITLR)
University of Stuttgart

2022

SELBSTÄNDIGKEITSERKLÄRUNG

Hiermit versichere ich, an Eides statt, dass ich die vorliegende Dissertation mit dem Titel „Ground-Based Autonomous Passive-Optical Staring Sensor for Orbital Object Detection and Position Measurement“ selbständig und ohne fremde Hilfe verfasst und keine anderen als die angegebenen Hilfsmittel benutzt habe. Die Stellen der Arbeit, die dem Wortlaut oder dem Sinne nach anderen Werken entnommen wurden, sind in jedem Fall unter Angabe der Quelle kenntlich gemacht.

Paul-Philipp Wagner, Stuttgart 10. Juni 2022

paul@wagner-wr.de
Solitudestr. 262
70499 Stuttgart
Germany

TABLE OF CONTENTS

GLOSSARY

LIST OF ABBREVIATIONS

Symbol	Explanation
AD	Aperture diameter
AFB	Air Force Base
AIUB	Astronomical Institute of the University of Bern
API	Application programming interface
APPARILLO	Autonomous Passive-Optical Staring of LEO Flying Objects
AR	Anti-reflective coating
BLOB	Binary Large Object
BRDF	Bidirectional reflectance distribution function
CCD	Charge coupled device
CCSDS	The Consultative Committee for Space Data Systems
CDM	Conjunction Data Messages
CMOS	Complementary metal-oxide-semiconductor
COSPAR	Committee on Space Research
COTS	Commercial off-the-shelf
CPF	Consolidated Laser Ranging Prediction Format (ILRS Data Format and Procedures Working Group)
CSpOC	Combined Space Operations Center (former JSpOC)
CSSI	Center for Space Standards & Innovation
CUDA	Compute Unified Device Architecture
DC	Direct current

DCR	Dark count rate
Dec	Declination (of the equatorial coordinate system)
DISCOS	Database and Information System Characterizing Objects in Space
DLR	German Aerospace Center (Deutsches Zentrum für Luft- und Raumfahrt e.V.)
DLR-TP	DLR Institute of Technical Physics
ECEF	Earth-centered, Earth-fixed (reference frame)
ECI	Earth Centered Inertial (reference frame)
EF	Electro-Focus (Canon EOS lens mount)
ESA	European Space Agency
FITS	Flexible Image Transport System
FLI	Finger Lake Instruments
FOV	Field of view
FPS	Frames per second
FWHM	Full-width-half-maximum
GEO	Geostationary orbit
GNSS	Global navigation satellite system
GP	General Perturbations
GPS	Global positioning system
GPU	Graphics processing unit
HEO	Highly elliptical orbits
HF	High frequency
IAA	International Academy of Astronautics
IADC	Inter-Agency Space Debris Coordination Committee
ID	Identification
ILRS	International Laser Ranging Service

IOD	Initial orbit determination
IS	Image stabilizer
ISO	International Organization for Standardisation
ISS	INTERNATIONAL SPACE STATION
IWF	Institute for Space Research (of the Austrian Academy of Sciences)
JSpOC	Joint Space Operations Center
Laser	Light amplification by stimulated emission of radiation
LEGEND	LEO-to-GEO Environment Debris Model
LEO	Low Earth Orbit
LIDAR	Light detection and ranging
LLR	Lunar laser ranging
LOS	Line-of-sight
MASTER	Meteoroid and Space Debris Terrestrial Environment Reference (by ESA)
MEO	Medium Earth orbit
MSL	Mean sea level
N	North
NASA	National Aeronautics and Space Administration
NEO	Near Earth objects
NORAD	North American Aerospace Defense Command
NP	Normal point
NTW	Normal / In-Track / Cross-Track system
OCS	Optical cross section
OGS	OPTICAL GROUND STATION
OOOS	Orbital Objects Observation Software (by DLR-TP)
PMD	Post mission disposal
PROOF	Program for Radar and Optical Forecasting (by ESA)

R/B	Rocket body
RA	Right ascension
RADAR	Radio detection and ranging
RCS	Radar cross section
RMS	Root-mean-square
RSO	Residential space object(s)
RSW	Radial /Along-Track / Cross-Track system
SATCAT	Satellite catalog
sCMOS	Scientific CMOS
SDR	Space debris laser ranging
SGP4/SDP4	Simplified General Perturbation 4 (orbit propagation model)
SLR	Satellite laser ranging
SNR	Signal to noise ratio
SP	Special Perturbations
SPAD	Single photon avalanche detector
SPD	Single photon detector
SSA	Space situational awareness
SSN	Space Surveillance Network (by USSTRATCOM)
SST	Space surveillance and tracking
SVD	Singular value decomposition
TCA	Time of closest approach
TDM	Tracking Data Message (file format, by CCSDS)
TEC	Thermo-electric cooler
TIRA	Tracking and imaging RADAR
TLE	Two-Line Elements

TTL	Transistor-transistor logic
TUM	Technical University of Munich
U	Rack unit (44.45 mm height)
UFO	Uhlandshöhe Forschungsobservatorium
UHF	Ultra-high frequency
UPS	Uninterruptible power supply
US	United States
USB	Universal serial bus
USM	Ultra-sonic motor
USSTRATCOM	United States Strategic Command
UTC	Universal Time Coordinated
VHF	Very high frequency
W	West
WGS84	World Geodetic System
ZIMSMART	ZIMMERWALD SMALL APERTURE ROBOTIC TELESCOPE

LIST OF SYMBOLS

Symbol	Unit	Explanation
$\vec{r}$	$\begin{bmatrix}\text{km}\\ \text{km}\\ \text{km}\end{bmatrix}$	Vector in cartesian coordinates
A	[m²]	Area
a	[m]	Semi-major axis (orbital element)
a'	[m]	Distance from the principle plane to the image plane
b	[km]	Baseline
c	[m/s]	Speed of light, $c = 2.998 \cdot 10^8$ m/s

D	[m]	Diameter
d	[m]	Diameter
e		Eccentricity (orbital element)
e^-		Elementary charge
E_P	[J]	Pulse energy
E_{RSO}	[ph/s/m²]	Photon flux
f	[Hz]	Frequency
f'	[m]	Focal length
$f\#$		F-number or focal ratio
FOV	[°] or [rad]	Field of view (full angle)
g	[1/sr]	Gain factor
G	[m³/kg/s²]	Gravitational constant, $G = 6.67408 \cdot 10^{-11}$ m³/kg/s²
h	[Js]	Planck constant, $h = 6.626 \cdot 10^{-34}$ Js
H	[W/m²]	Irradiance or Intensity or radiant flux density, Incidence or emitted power per area
h_{RSO}	[km]	Orbit height (above Earth surface)
I	[°]	Inclination with respect to the equatorial plane (orbital element)
$K(\chi)$	[km]	The prime vertical radius
L_b	[W/m²/sr]	Background illumination
L_{lvl}	[a.u.]	Light level
L_R	[W/m²/sr]	Radiance
m	[kg]	Mass
M_b	[mag/arcsec²]	Background brightness
M_{RSO}	[mag]	Visible magnitude
n		Number of measurements
N_b		Number of electrons by background radiation

N_{dark}		Number of electrons by dark noise
N_{Ph}		Number of photons
N_{read}		Number of electrons by read-out noise
N_{signal}		Number of signal electrons
p		Probability
$P(\varrho,\psi)$		Phase function
PSF	[W/m²]	Point spread function
q		Factor (used to model atmospheric transmission)
QE		Quantum efficiency
R	[km]	Range
r	[m]	Distance
R_E	[km]	Radius of the Earth, R_E = 6371 km
t_{exp}	[s]	Exposure time
t_P	[ns]	Pulse length
u_0	[s]	Time of pericenter passage (orbital element)
v	[m/s]	Velocity
V	[km]	Visibility
Wt	[a.u.]	Wetness; ≥ 1 eq. Rain
x	[m]	Position on image/aperture plane perpendicular to z
X	[m]	Cartesian coordinate
y	[m]	Position on image/aperture plane perpendicular to z
y_{px}	[µm]	Pixel size
z	[m]	Position on optical axis
Z	[m]	Cartesian coordinate
α	[°]	Altitude

α_{el}	[°]	Elevation (= altitude)
$\beta(\tilde{\nu})$		Absorption coefficient
γ	[°]	Right ascension
δ	[°]	Declination
$\measuredangle T_{Sky}$	[K]	Temperature difference between sky and ambient/ground
ζ	[rad]	Angle
ζ_{px}	[rad/px]	Angular resolution/Pixel scale (or pixel FOV)
η	[°]	Geographic latitude
θ	[rad]	Half-angle
Θ	[°]	Argument of pericenter (orbital element)
κ	[°]	Geodetic longitude
λ	[nm]	Wavelength
Λ	[°]	Geographic longitude
$\varrho_{diff,spec}$		Albedo/reflection coefficient (diffuse, specular)
σ	[m]	Width of Gaussian distribution
σ_N		Variance of noise
τ		Transmission
Υ		Vernal equinox
φ	[rad]	Angular displacement
Φ	[W]	Radiant power (Flux)
χ	[°]	Geodetic latitude
ψ	[°]	Phase angle
Ψ	[°]	Azimuth
Ω	[°]	Right ascension of the ascending node (orbital element)
ω_{RSO}	[rad/s]	Angular velocity

ABSTRACT

Active spacecraft operations heavily rely on a space surveillance network, which continuously scans, measures, and predicts space debris particle trajectories to avoid collision risks. Recent activities in large satellite constellations in Low Earth Orbit (LEO) will accumulate more than ten thousand satellites, doubling the number of active spacecraft. Due to the high density of debris, LEO is of highest interest for space surveillance. Beside RADAR sensors, space debris laser ranging can accurately measure the distance to resident space objects allowing highly precise orbit predictions. Due to their small field-of-view (FOV), laser ranging stations rely on an a-priori orbit information, which is usually obtained by a separate sensor network. A passive-optical sensor with a larger FOV represents a complementary tool to deliver the necessary initial orbit determination. Such a sensor is much more cost effective and easier to operate than RADAR sensors and therefore of high interest for a space situational awareness (SSA) network.

The development of a passive-optical sensor is described in this thesis, which operates autonomously to detect unknown orbital objects in LEO.

This thesis is structured in three parts. Initially a theoretical model is presented to estimate performance of a passive-optical sensor. It shows the influences of system properties and observing conditions on the detection threshold. Furthermore, deterministic simulations using ESA's PROOF software are performed, which provide a more detailed analysis of the detection rates and detection efficiencies during different observation conditions and system parameters.

In the main part, the system setup is explained including the software development, which plays a major role for the automation of the system. An image processing technique is implemented, which is able to reliably identify objects in LEO even when disturbances are present in the source images, such as high, transparent, or smaller clouds. Astrometric calibration is used to transform the coordinates of measured objects into equatorial coordinates and a standardized data export allows for sharing the data with existing tools or databases.

A weatherproofed housing protects the camera and lens. A weather station is used to trigger image acquisition. The passive-optical sensor is deployed for continuous observations and the data is automatically uploaded to a webserver. Data analysis shows the performance figures of

the system. Observation campaigns under three different line-of-sight (LOS) directions are performed and the detection rate, efficiency, threshold, and uncertainties are analyzed and compared to simulations. A line-of-sight to the North under 45° elevation is found to deliver the highest detection rates, while the observed Along-Track error is about ten times larger than the Cross-Track error.

Finally, the determined parameters of the passive-optical system are used to derive requirements to detect space debris as small as 10 cm in diameter.

KURZZUSAMMENFASSUNG

Der Betrieb aktiver Raumfahrzeuge hängt in hohem Maße von einem Weltraumüberwachungsnetzwerk ab, welches die Flugbahnen von Weltraummüllpartikeln kontinuierlich vermisst und vorhersagt, um Kollisionen zu vermeiden. Die jüngsten Aktivitäten große Satellitenkonstellationen in die erdnahe Umlaufbahn zu schicken, werden mehr als zehntausend Satelliten hinzufügen, wodurch die Zahl der aktiven Raumfahrzeuge verdoppelt wird. Aufgrund der hohen Trümmerdichte ist die niedrige Erdumlaufbahn von größtem Interesse für die Weltraumüberwachung. Neben RADAR-Sensoren kann die Laserbasierte Entfernungsmessung von Weltraummüll die Position hochgenau messen und ermöglicht damit präzise Bahnvorhersagen. Aufgrund ihres kleinen Sichtfelds sind Laser-Entfernungsmessstationen auf eine vorherige Bahninformation angewiesen, die von einem separaten Sensornetz gewonnen wird. Ein passiv-optischer Sensor mit einem größeren Sichtfeld stellt ein ergänzendes Instrument dar, um die erforderliche anfängliche Orbitbestimmung zu liefern. Ein solcher Sensor ist wesentlich kostengünstiger und einfacher zu bedienen als RADAR-Sensoren und daher von hohem Wert für ein Weltraumüberwachungs-Netzwerk.
Im Rahmen dieser Arbeit wird die Entwicklung eines passiv-optischer Sensors vorgestellt, der autonom betrieben wird, um unbekannte orbitale Objekte im niedrigen Erdorbit zu erkennen.

Es wird ein theoretisches Modell zur Abschätzung der detektierbaren Objektgrößen eines passiv-optischen Sensors vorgestellt. Es zeigt die Einflüsse von Systemeigenschaften und Beobachtungsbedingungen auf die Detektionsschwelle. Darüber hinaus werden deterministische Simulationen mit der ESA Software PROOF durchgeführt, die eine detailliertere Analyse der Detektionsraten und Detektionseffizienz unter verschiedenen Beobachtungsbedingungen und Systemparametern ermöglicht.
Im Hauptteil wird der Systemaufbau einschließlich der Softwareentwicklung erläutert, die eine wichtige Rolle bei der Automatisierung des Systems spielt. Es wird eine Bildverarbeitung implementiert, die in der Lage ist, alle Störungen wie unterschiedliche Wolken im Bild zu verarbeiten und Objekte im niedrigen Erdorbit zuverlässig zu identifizieren. Eine astrometrische Kalibrierung wird verwendet, um die Koordinaten der gemessenen Objekte in

äquatoriale Koordinaten umzuwandeln und ein standardisierter Datenexport ermöglicht den Austausch der Daten mit bestehenden Anwendungen oder Datenbanken.

Ein wetterfestes Gehäuse schützt die Kamera und das Objektiv, während eine Wetterstation genutzt wird, um die Bildaufnahme zu steuern. Der passiv-optische Sensor wird für kontinuierliche Beobachtungen eingesetzt und die gewonnen Daten automatisch auf einen Webserver hochgeladen. Die Analyse der Daten zeigt die Leistungsdaten des Systems. Es werden Beobachtungskampagnen unter drei verschiedenen Beobachtungsrichtungen durchgeführt und die Detektionsrate, -effizienz, -schwelle und die Messunsicherheiten analysiert und mit Simulationen verglichen. Es zeigt sich, dass eine Sichtlinie nach Norden unter 45° Elevation die höchsten Detektionsraten liefert, während der beobachtete Messfehler in Flugrichtung des Objektes etwa zehnmal größer ist als der Fehler quer zur Flugrichtung.

Schließlich werden die gewonnenen Parameter des passiv-optischen Systems verwendet, um die Anforderungen für die Erkennung von Objekten mit einem Durchmesser von nur 10 cm abzuleiten.

1. INTRODUCTION

Since the historic launch of the first artificial satellite SPUTNIK-1 in 1957, the number of manmade resident space objects (RSO) orbiting around Earth is constantly increasing. Nowadays almost 21 000 RSO are officially cataloged by the United States (US) Space Surveillance Network (SSN) with a dark figure of about 40% higher [1]. While about 6 000 RSO are active payloads, about 15 000 RSO are space debris [2]. Those numbers only represent the current detect- and trackable objects with sizes larger than 10 cm in the low Earth orbit (LEO) and 70 cm in the geostationary orbit (GEO) [3]. However, the total number of smaller debris is much larger [4]. Especially LEO is densely populated by space debris. One reason for employment of satellites in LEO is the relatively short distance from Earth's surface, which constitutes optimal conditions for Earth observation and telecommunication missions.

Collisions of RSO cause enormous fragmentation leading to a high number of smaller space debris objects. Thereby, an object with 1 cm in diameter causes a major threat to active satellites. Therefore, satellites need to be protected from impacts by small debris particles while collision avoidance maneuvers need to be performed to avoid collisions with larger space debris. In order to perform those maneuvers, it is necessary to continuously scan the Earth orbit to detect, measure, and predict space debris trajectories. The orbit prediction accuracy is crucial to avoid false-positive collision avoidance maneuvers to save valuable fuel for the active RSO. The perturbed nature of orbit dynamics requires to continuously track RSO for maintaining them in a catalog. Routinely, RADAR sensors scan LEO while GEO orbits are monitored based on measurements by optical telescopes. The resulting orbit prediction accuracy varies between 67 m and 517 m in LEO [5]. These large uncertainties result in a large safety margin and imply a high false-alert rate of collisions between an active satellite and space debris.

Another technology used to measure the position of an RSO is satellite laser ranging (SLR), which is commonly used in geodesy to measure changes in the Earth's gravitational field and to detect tectonic plate drifts [6]. SLR stations achieve distance measurement with an accuracy down to 1 cm to geodetic targets, yielding highly precise orbit predictions [7]. Orbit predictions published by the International Laser Ranging Service (ILRS) in the Consolidated Laser

Ranging Prediction Format (CPF) have residuals below 20 m [8]. To perform time of flight measurements on RSO, in general, SLR systems require the presence of a retro reflector on the RSO, which reflects the incoming light into the same direction backwards. In recent years more and more SLR stations are capable to perform laser ranging to space debris in LEO with an accuracy of about 1 m. This allows much better orbit predictions and lower false-alert rates, extending the lifetime of satellite missions [8]. Laser ranging stations are dependent on initial orbit information and good weather conditions in order to track the RSO and perform distance measurements, which is why RADAR sensors are still mandatory in space surveillance networks.

This thesis presents the development of an autonomous passive-optical staring sensor, which is called AUTONOMOUS PASSIVE-OPTICAL STARING OF LEO FLYING OBJECTS (APPARILLO), to employ modern ground-based optical sensors to be widely used in space surveillance networks. This ground-based passive-optical sensor shall detect LEO RSO and measure their angular position. The focus is on a smaller, more affordable sensor compared to RADAR which can partly replace RADAR sensors and still enable subsequent laser ranging of newly detected targets. Key elements of this thesis are described as follows: Section 1.1 gives more detailed information about the space debris environment and currently used space surveillance sensors are introduced in Chapter 2. The required theoretical background for passive-optical observations is explained in Chapter 3. In Chapter 4 the proposed combination of a passive- and active-optical sensor is presented, which can deliver highly accurate position measurements without any a priori RADAR sensor information. This work also includes simulations of theoretically expected system performance of a passive-optical sensor, as well as hard- and software of the APPARILLO system. Results from operational campaigns are presented and discussed in Chapter 5. Finally, Chapter 6 gives a summary of the presented results. The APPARILLO design is aimed to reduce sensor cost, and in combination with a space debris laser ranging sensor will improve orbit prediction accuracy in the future.

1.1. SPACE DEBRIS ENVIRONMENT

As consequence of satellite mission's end of lifetimes, as well as spaceflight related incidents and accidents, those manmade objects become non-functional. The Inter- Agency Space Debris Coordination Committee (IADC) defined space debris as "(…) all manmade objects including fragments and elements thereof, in Earth orbit or re-entering the atmosphere, that

are non-functional" [9]. Figure 1.1 shows the number of all objects officially cataloged by the US SSN, by object type. It shows that not only the number of active spacecraft is increasing, but also the number of non-functional objects. Additionally, it can be seen that the number of non-functional objects is larger than the number of active spacecraft. This discloses the threat of collisions of debris with active satellites. Two major fragmentation events are visible in the graph: First, the planned destruction of FENGYUN-1C by an anti-satellite weapon in 2007; secondly, the first accidental collision between an active satellite IRIDIUM 33 and defunct satellite COSMOS 2251 in 2009. These two events alone account for 30% of all cataloged residential space objects (RSO) [2].

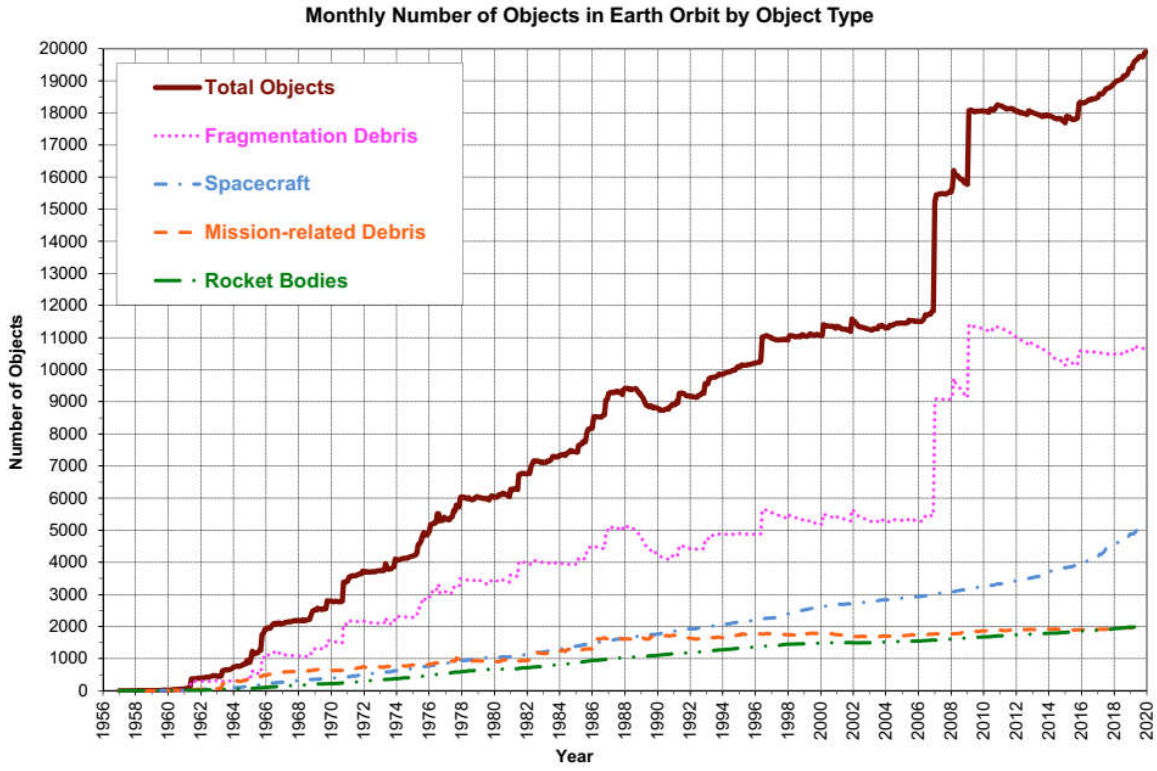

Figure 1.1: Monthly number of cataloged objects in Earth orbit by object type by US SSN since 1956. Two major fragmentation events occurred during an anti-satellite test in 2007 and an accidental collision between two satellites in 2009. 'Mission-related debris' includes all objects dispensed, separated, or released as part of the mission, while 'Fragmentation debris' includes satellite breakup debris and anomalous event debris. Source: [10].

Debris fragments and elements originate from a wide range of sources and are of different types. They can be sorted in mission related objects (like launch adapters or lens covers), leftovers from deployment of payloads (like upper stages from rockets) and inactive satellites. However, the majority of pieces belong to unintentional events [11]. These contain slag of rocket burns, degradation products from spacecraft like upper stages and satellites. But most of

all fragments result from collisions and explosions of rocket stages due to propellant, which often remain in orbit many years after launch. Figure 1.2 shows the relative amount between different types of the cataloged RSO population. Over half of the objects result from breakup events while payloads account for about 24% [2].

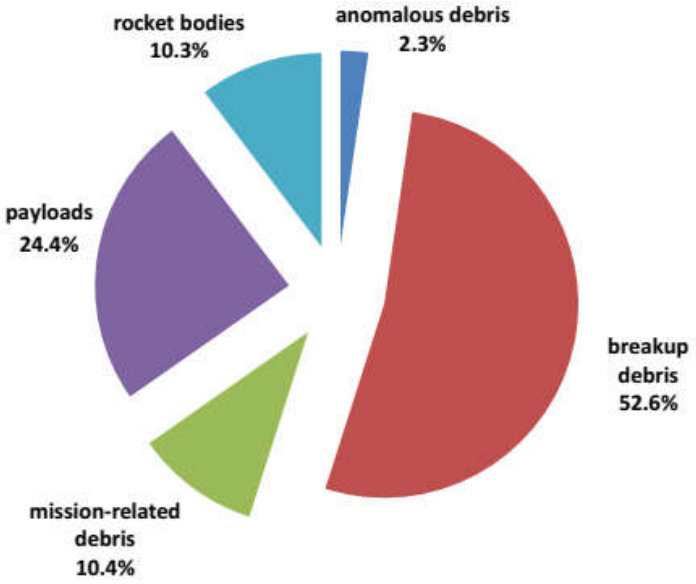

Figure 1.2: Relative segments of the cataloged in-orbit Earth RSO population (July 4th 2018). Breakup debris has the largest contribution, which is larger than all RSO released by common operation Source: [2].

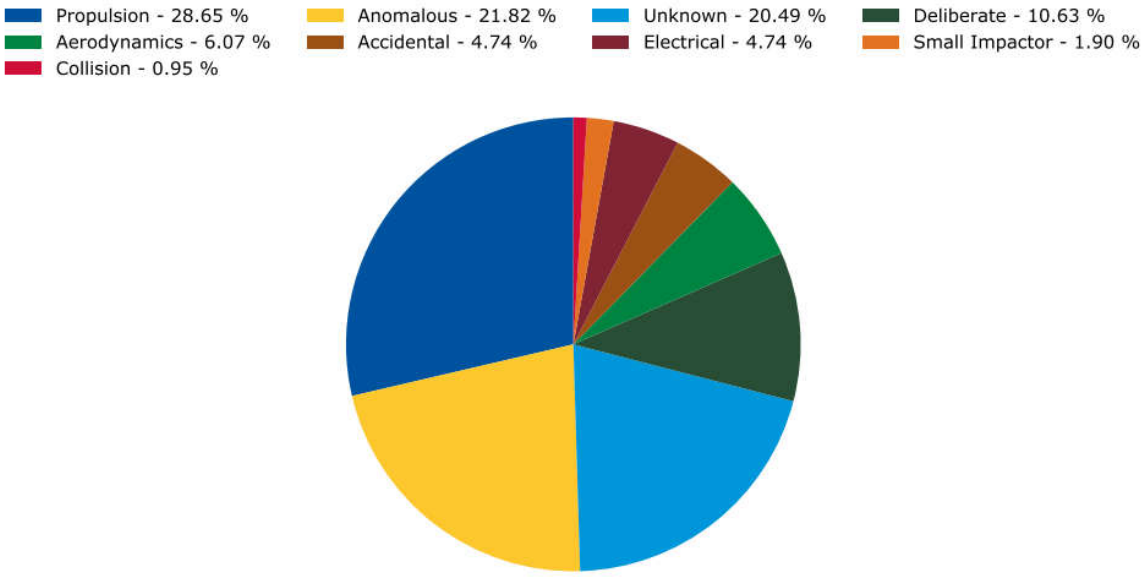

Figure 1.3: Event causes and their relative share for all past fragmentation events. The 'deliberate' category predominates due to the FENGYUN-1C anti-satellite test. The major cause of fragmentations is propulsion events. Source: [12].

Rocket bodies, mission-related debris[A], and anomalous debris[B] are objects caused by common orbital operation and combined amount to a total of 23% of cataloged objects. In contrast 52.6% of objects are caused by breakup debris. Events which cause breakup debris and their relative share are shown in Figure 1.3. Propulsion is the largest cause of fragmentation followed by anomalous and unknown events.

Especially the LEO is of high interest due to the close distance to the Earth surface but vanishing atmospheric drag. In 2018, 13 496 (60%) of 22 177 known objects were located in LEO [12]. In these densely populated regions the collision risk of space debris is increased strongly. Furthermore, many missions have a near polar orbit, which leads to a higher collision risk at polar regions. Another accumulation exists at the geostationary orbit (GEO) at an altitude of 35 786 km above the Earth's equator. Here, the orbital period is exactly one day. Hence, the apparent position of the satellite is fixed from the Earth surface. This makes it popular for communication or broadcast satellites and is the second most populated region after LEO. For detailed definitions of the orbital regimes see Appendix 9.6.

Figure 1.4 shows the spatial distribution of cataloged RSO in LEO for the last three decades. The increase from 2000 to 2010 was dominated by fragments generated from the previously mentioned anti-satellite test and accidental collision between two satellites, whereas the increase of RSO from 2010 to October 2020 was driven by the on-going build-up of the STARLINK large constellation and the proliferation of CubeSats below ~650 km altitude [13].

Note, that data shown in Figure 1.1 to Figure 1.4 only account for larger objects which can be detected and cataloged. Due to fragmentation, the total number of objects rises with smaller object sizes. According to ESA's Meteoroid and Space Debris Terrestrial Environment Reference (MASTER) model, the number of objects larger than 10 cm is 34 000, while 900 000 objects are between 1 cm to 10 cm in diameter and 128 million objects are between 1 mm to 1 cm [14]. However, only 28 160 objects are currently tracked and catalogued by the SSN [4], while orbit prediction data is publicly available for about 21 000 of those on CELESTRAK[C] [15].

[A] Mission-related debris results from the intentional release of objects during nominal on-orbit operations.

[B] Anomalous debris is produced in unplanned events that result a separation, usually at low velocities, of objects from the parent body.

[C] CELESTRAK's NORAD TLE catalog: www.celestrak.com/NORAD/elements/, Accessed December 5th 2020.

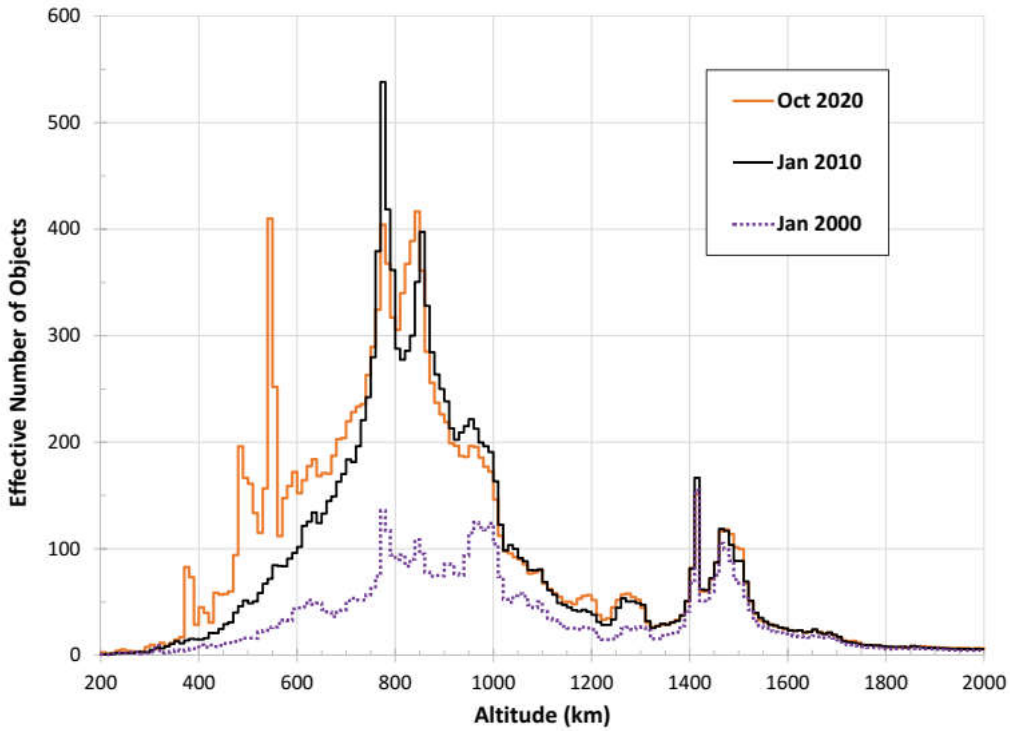

Figure 1.4: Effective numbers of objects (tracked by the SSN) per 10 km altitude bin depending on altitude above Earth's surface at three different epochs. Objects generated by the FENGYUN-1C anti-satellite test, and by the accidental collision between disfunct COSMOS 2251 and the operational IRIDIUM 33 satellite dominate the increase from 2000 to 2010, whereas, from 2010 to 2020 it is driven by the build-up of large constellations and the proliferation of CubeSats. Source: [13].

Due to high velocities of orbiting objects in LEO of 7.6 km/s in 400 km orbit height on a circular orbit, even small objects can cause a major damage to an active spacecraft. Additionally, human life is put into risk as astronauts are living and working at the INTERNATIONAL SPACE STATION (ISS) [16]. However, the current detection limit of object sizes in LEO is about 10 cm and larger [13]. This is why payloads need to be protected from impacts with smaller debris. Those impacts frequently occur and are reported by the media, see Figure 1.5 [17]. Impact with larger debris needs to be prevented by collision avoidance maneuvers by the active spacecraft. This requires the prediction of the debris object trajectory.

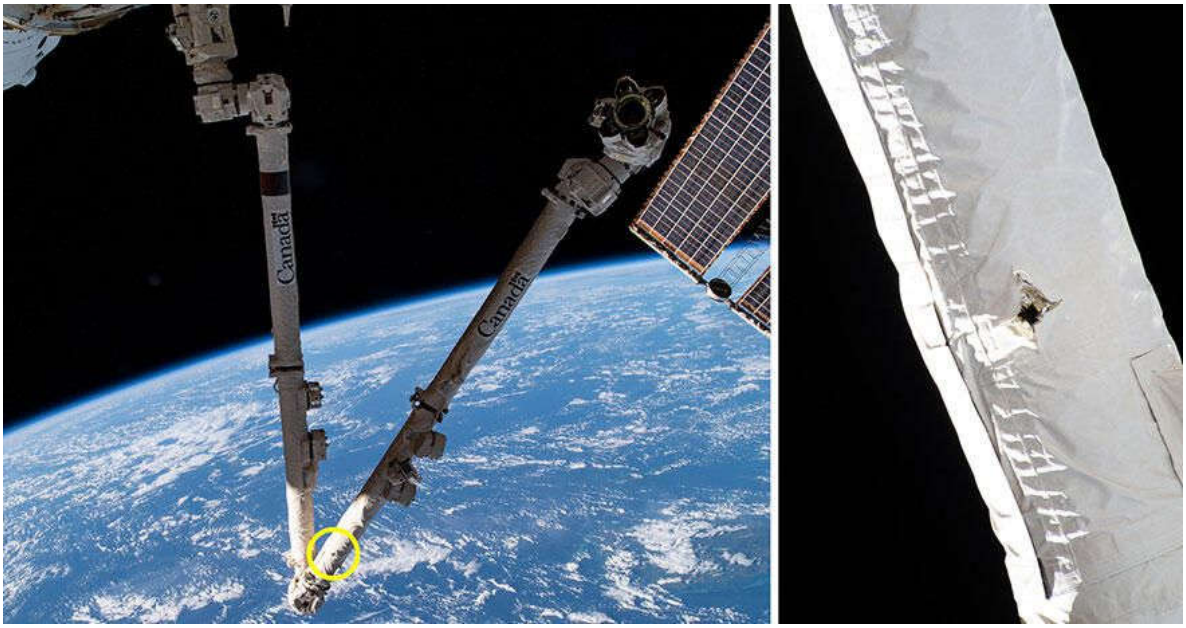

Figure 1.5: Example of frequent debris impacts on the Canadarm2 on the ISS in May 2021. Source: [17], © NASA/Canadian Space Agency.

Current predictions of debris objects in LEO are based on RADAR measurements and possess large uncertainties of up to 517 m for LEO RSO [5] (more details are explained in Chapter 2 later). This requires a large safety margin, resulting in a 10000:1 false alert rate [8]. Laser ranging measurements, on the other hand, have an order of magnitude better precision of the distance measurement (more details are given in Chapter 2.3), delivering much better orbit predictions [7]. Thus, more effective collision avoidance maneuvers between an active satellite and orbital debris can be performed with smaller false alert rates [8]. Figure 1.6 shows the number of annual alerts depending on the orbit accuracy. Orbit predictions in the Two-Line Elements (TLE) format are an order of magnitude less accurate than predictions in the Conjunction Data Messages (CDM) format. Predictions obtained by satellite laser ranging (SLR) on the other hand have an order of magnitude better accuracy, which results in fewer collision alerts.

Depending on the orbit height, residual atmosphere causes drag which implies that objects closer to Earth will slow down and reenter in the atmosphere after a certain time. Figure 1.7 shows the lifetime in years of an object with an area to mass ratio of 0.01 m^2/kg depending on perigee and apogee. At about 600 km orbit height an RSO will remain in orbit over a decade and in 800 km for over 100 years. This is why new debris accumulation needs to be prevented in the future to maintain current collision risks.

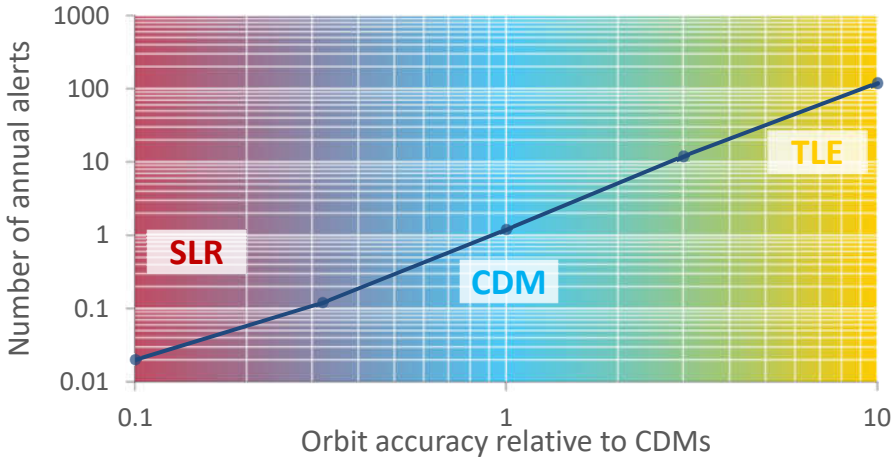

Figure 1.6: Number of annual alerts of a LEO RSO for a risk threshold corresponding to 90% risk reduction and a safety sphere with 4.5 m radius, as a function of orbit data quality relative to CDM. TLE predictions are an order of magnitude larger than CDM and two orders larger than predictions derived from SLR. Adopted from source: [8].

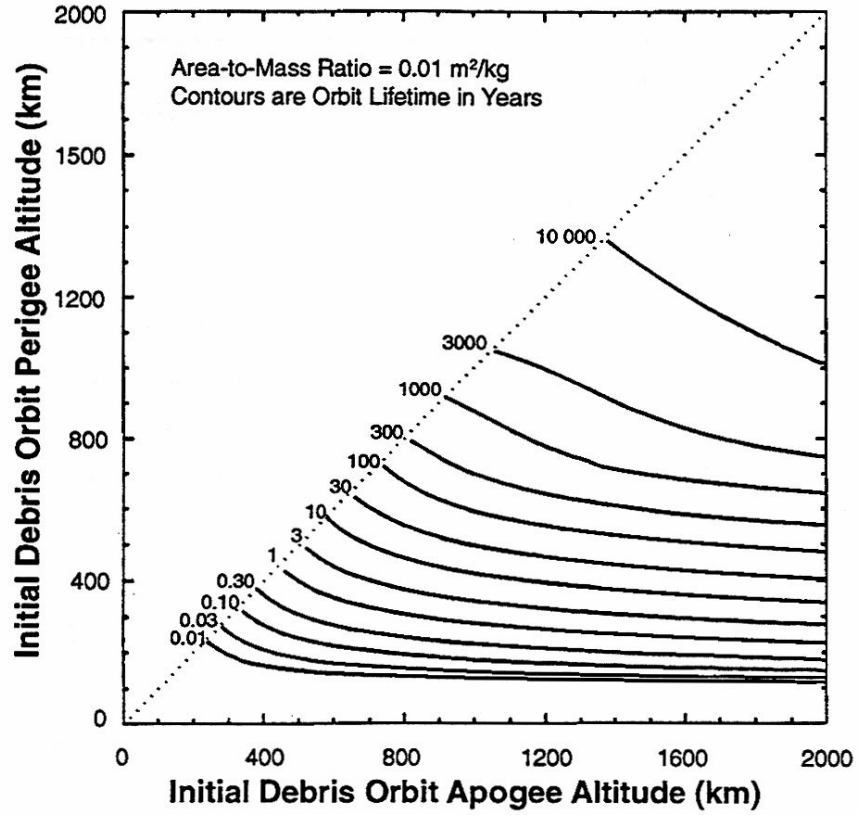

Figure 1.7: Orbit lifetimes for debris with an area-to-mass ratio of 0.01 m²/kg released in low altitude, low eccentricity orbits. Radiation pressure effects by solar activity are neglected in orbit lifetime calculations. Source: [18].

On orbit-collisions between two uncontrolled RSO or an explosion of an inactive spacecraft result into a large number of fragmented debris particles, enlarging the number of in orbit debris immensely. Kessler and Cour-Palais described in 1978 the risk of a self-sustaining cascading collision of space debris in LEO [19], which is known as Kessler syndrome. Nowadays, orbital debris population is precisely modeled and allows prediction of future debris populations. The major tools for these simulations are ESA's MASTER module, NASA's LEO-to-GEO Environment Debris Model (LEGEND) [20], and NASA's Orbital Debris Engineering Model (ORDEM) 3.0. As shown in Figure 1.3, the major contribution of today's space debris particles results from propulsion. This is why the removal of active satellites from highly populated orbits after its lifetime plays a major role to prevent the development towards a Kessler syndrome. This is called post-mission disposal (PMD) and is the most effective way to slow down the debris accumulation [10].

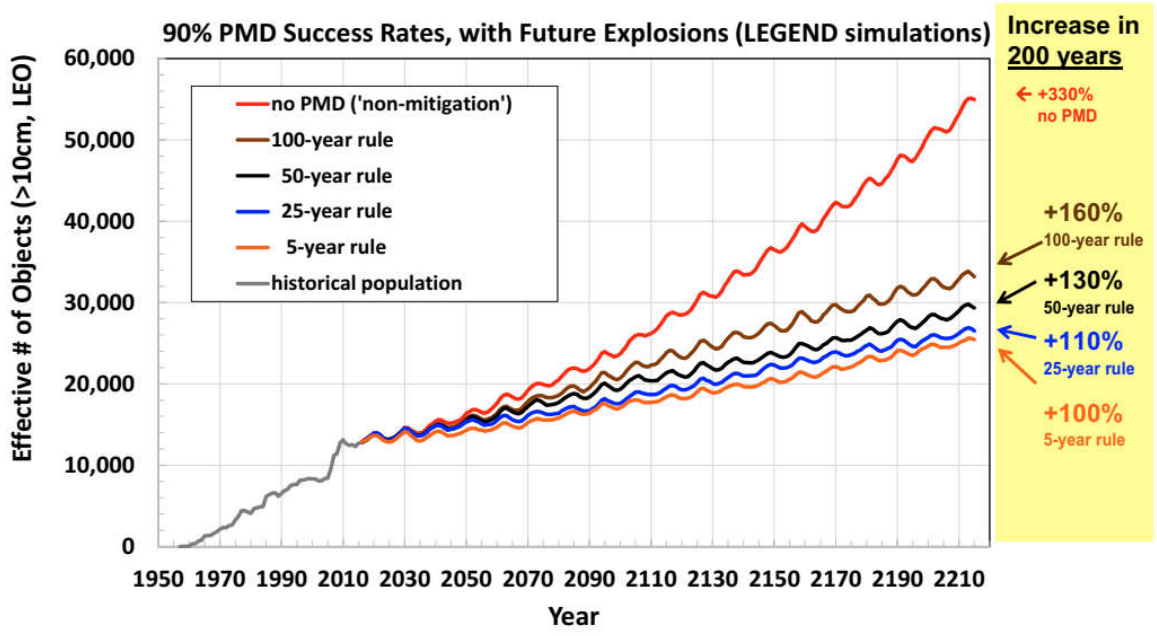

Figure 1.8: Effectiveness of the 25-year PMD rule compared to other PMD rules and 'non-mitigation' scenario. Projection results are based on averages of 100 Monte Carlo simulations each by the NASA LEGEND long-term debris environment model. A 90% success rate is assumed for PMD. Following PMD guidelines prevent future exponential buildup of RSO. Source: [10].

Figure 1.8 shows simulations by NASA's LEGEND tool of the evolution of the LEO RSO population for the next 200 years. It can be seen that the exponential growth can be prevented by following PMD guidelines, assuming a PMD success rate of 90%. This is why space debris mitigation guidelines ISO 24113 [21] define regions for GEO and LEO where a satellite is

supposed to be removed within 25 years after its lifetime. In GEO, satellites are transferred to a graveyard orbit after use, which lies above the GEO, while in LEO RSO are deorbited into Earth's atmosphere. As the name implies, those PMD guidelines are just guidelines and there is no institution to enforce the adherence to those guidelines. Most internationally accepted space debris mitigation measures can be traced back to the following objectives [12]:

- The limitation of space debris released during normal operations
- The minimization of the potential for on-orbit breakups
- Post mission disposal
- Prevention of on-orbit collisions.

More details of those mitigation measures and definition can be found in Appendix 9.8.

Despite preventing the accumulation of future debris, existing space debris can be removed actively. A lot of concepts have been put forward, while most of them require an active satellite to grab the debris object to deorbit it into Earth's atmosphere. This is generally a very expensive procedure, which is only meaningful to remove large debris object with the hazard of future fragmentation. Such missions are already planned by ESA, called ELSA-D, for 2021 and CLEARSPACE-1, for 2025 [22]. CLEARSPACE-1 will grab a VEGA secondary payload adapter to remove it from its orbit. The main goal of the CLEARSPACE missions is to grab and remove ENVISAT, which is the satellite with the largest threat of generating orbital break-up debris [23].
A concept to remove or modify orbits of small debris targets is by using ground-based laser. Utilizing photon pressure allows gently pushing small objects with the idea to prevent collisions between two passive debris objects [24]. Laser ablation on the other hand has a far higher impulse coupling efficiency, theoretically allowing to deorbit smaller targets from ground [25].
All active concepts require precise attitude and positional information about the debris target, hence development of operational ready surveillance technology with higher accuracy and attitude estimation are mandatory improve the feasibility of removal missions.

2. SPACE SITUATIONAL AWARENESS

Space situational awareness (SSA) is "the awareness and understanding of the orbital population, the awareness of the space environment, the awareness of threats to/by the orbital population, and addresses the related data policy, security and governance issues" [26], according to a definition used by ESA. To fulfill most SSA tasks, acquisition and monitoring of the orbital population is of central importance, which is referred to as *space surveillance* [27]. Space surveillance is defined as the "combined, routine tasks of operational detection, correlation with sources, characterization and orbit determination of space objects" [11]. It requires sensors which detect orbital objects, measure their position, and maintain latest orbit predictions in a database. This is obligatory to protect active satellites from collisions with space debris. The two main tasks of space surveillance are *surveying*; the detection of unknown objects, and *tracking*; the re-observation of already known objects using a-priori information.
To detect and measure orbital objects electromagnetic waves are used. The Earth atmosphere has certain transmission windows for electromagnetic radiation and two commonly used windows are in the optical and RADAR range (see Appendix 9.3 for definition of electromagnetic spectrum). The following Section 2.1 gives an overview of RADAR sensors which actively emit radio waves to the RSO and detect backscattered signals. Section 2.2 introduces the passive-optical sensor, which takes advantage from the fact that RSO in higher orbits are always illuminated by the Sun. Additionally, Section 2.3 introduces active-optical sensors which are used to perform accurate distance measurements utilizing laser ranging.

2.1. RADAR SENSORS - STATE OF THE ART LEO SURVEILLANCE

RADAR space surveillance sensors always emit an active signal, which is reflected by the RSO. Hence, the sensitivity of a RADAR decreases proportionally to the distance with the power of four [27] (see Appendix 9.3.2 for RADAR link equation). This limits the range of a RADAR sensor to lower orbits (LEO) only [11]. Surveillance RADAR sensors used to catalogue objects in LEO can detect RSO down to 10 cm [11]. The major benefit of RADAR sensors is their independence of weather as well as light conditions. For high frequencies (HF), up to ultra-high frequencies (UHF) (300 MHz – 3 GHz) the atmosphere stays transparent. Towards

higher frequencies the applicable atmospheric transmission window is limited to resonant effects of water vapor, but narrow windows allow to use frequencies up to the Ku-Band (40 GHz). Reflections and attenuations in the ionosphere limit the windows towards shorter frequencies.

Mainly, a RADAR sensor measures the time of flight Δt between the signal emission and reception. Additionally, the angular position of the received signal, the signal strength, and the Doppler-shift can be measured. The Doppler-shift f_d provides the range rate $\dot{r}$ of the measured object (Appendix 9.3.2). The signal strength gives the RADAR cross section (RCS), which results from the size and material composition of the RSO. Traditionally, RADAR sensors are dish shaped antennas, nowadays however more and more phased array RADAR sensors are in operation [27]. They allow various beam shapes and operational modes by adjusting the phase of each antenna, which is illustrated in Figure 2.1. Furthermore, transmitter and receiver can also be separated as bi- or multi-static systems.

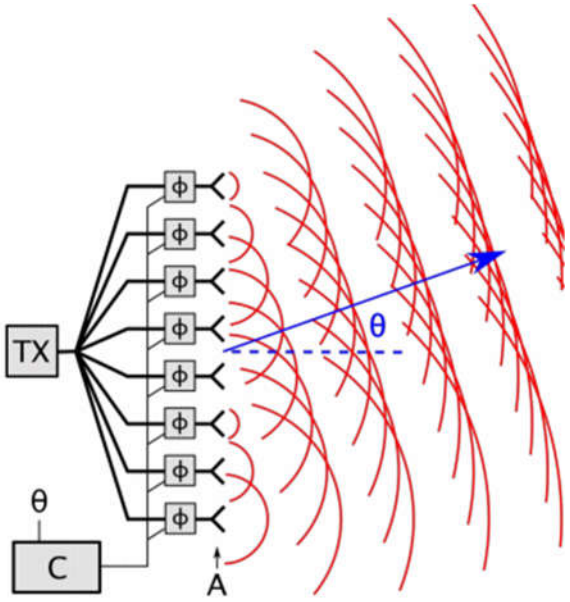

Figure 2.1: Phased array RADAR is an array of phase-controlled antennas, which emit a beam of radio waves that can be steered electronically into different directions, without physically turning the antenna. It consists of an array of multiple identical antenna elements (A), driven by a transmitter (TX). The feed current for each antenna passes through a phase shifter (Φ), which is controlled by a computer control system (C). The red lines illustrate the wave fronts of the individual emitted radio waves by each antenna. The waves superimpose in front of the antenna to a plane wave, which is traveling in a specific direction θ. By progressively delaying the phase of each antenna going up the line, the phase shifters cause the beam of radio waves to be emitted at an angle θ to the plane of the antennas. The beam direction can instantly be steered over a wide range in front of the phased array. Source: [28].

Due to the parabolic dish, reflector RADAR sensors have a small FOV. Thus, they are mainly used for tracking known objects. A state-of-the-art example sensor is operated by Fraunhofer Institute for High Frequency Physics and Radar Techniques (FHR) and is called TRACKING AND IMAGING RADAR (TIRA), see Figure 2.2. Its parabolic antenna has a diameter of 34 m with a peak transmitting power of 1 MW operating at 225 mm wavelength. Together with the Max-Planck-Institute for Radio Astronomy's Effelsberg RADAR telescope (bi-static configuration), which is a 100 m diameter receiving RADAR telescopes, objects down to 2 cm can be tracked [27].

Figure 2.2: TIRA antenna and dome operated by the Fraunhofer Institute FHR in Bonn, Germany. Source: [29].

The most important surveillance RADAR for the US SSN was the AIR FORCE SPACE SURVEILLANCE SYSTEM (AFSSS) a phased array RADAR, which consisted of 3 triplets of 1 emitter and 2 receivers with all sites distributed along 33° latitude in continental US [27]. It was a continuous-wave fully multi-static Very High Frequency (VHF) RADAR interferometer, and was decommissioned in 2013 due to its outdated design and high maintenance cost. For day-to-day maintenance for the year 2012, FIVE RIVERS SERVICES was contracted in 2011 with a volume of US$ 7 022 503 [30].

Currently, the most important RADAR is the AN/FPS-85 phased array RADAR at EGLIN Air Force Base (AFB) Site C-6, which is shown in Figure 2.3. Its transmitter has a diameter of 29 m and a peak power of 32 MW at 442 MHz with a maximum FOV of 105°. The receiver next to the transmitter has a diameter of 58 m. The site hosts its own power plant, fire station, and two water wells, which underlines the construction and maintenance scale of this system [31]. In return, the EGLIN RADAR contributes to 95% of all cataloged objects by the US SSN [11].

Figure 2.3: The AN/FPS-85 RADAR at EGLIN AFB Site C-6 in Florida, US. The RADAR is visible to the lower left. The smaller transmitter antenna (left) is 29 m large, while the receiver (right) is 58m large Source: [32].

These two examples show that RADAR sensors are large and complex. However, they deliver incredible performance figures. To cover all orbital regimes in LEO, a network of RADAR sensors is required and the largest RADAR network, the SSN, is presented in Section 2.4.

2.2. PASSIVE-OPTICAL SENSORS

Passive-optical sensors detect light from an external source which is reflected by the RSO. Therefore, the background radiation needs to be small to distinguish the RSO from the background noise. For ground-based sensors, this limits their operation to nighttime with clear sky conditions only. The Sun acts as the light source, hence RSO cannot be detected if they are in the Earth's shadow. An optical detector measures the apparent angular position and

brightness of the object. The brightness of an RSO depends on the distance, albedo, size, and phase angle between observer and Sun. Due to their passive working principle, the sensitivity decreases proportionally to the distance with the power of two. This makes passive-optical sensors more suitable in contrast to RADAR for space surveillance of objects beyond LEO. In GEO object are orbiting around the Earth in synch with the rotation of the Earth, which results in objects appearing at the same position in the sky. By measuring the angular position of an RSO over a longer time period using a telescope and utilizing astrometric calibration (see Chapter 3.4), an orbit can be determined to catalog this object. To cover the full GEO a network of telescopes at different latitudes is required (like SMARTNET [33]). Optical sensors contributing to the SSN can track and catalog objects down to 1 m in GEO [11], or 0.7 m according to Ref. [34].

In Figure 2.4 the most successful European sensor the OPTICAL GROUND STATION (OGS) at Tenerife is show, which is operated by ESA. It is a Cassegrain[D] type telescope with a 1 m aperture. The Ritchey-Chrétien[E] focus hosts a mosaic of 2 by 2 CCD sensors, which result in a FOV of 0.7°. The OGS covers 120° of the GEO ring, with a detection threshold of 15 cm object size in GEO [27].

Figure 2.4: The OGS is a 1 m space debris telescope at Tenerife, Spain, operated by ESA. Source: [29].

[D] A Cassegrain reflector is a combination of a primary concave and a secondary convex mirror.

[E] A Ritchey–Chrétien telescope is a specialized Cassegrain telescope with a hyperbolic primary and a hyperbolic secondary mirror.

Figure 2.5: The Astronomical Institute of the University of Bern (AIUB) operates the ZIMMERWALD SMALL APERTURE ROBOTIC TELESCOPE (ZIMSMART), which has 0.2 m aperture and is located at Zimmerwald, Switzerland. Source: [29].

More commonly smaller telescopes are used by surveillance networks, like the 30 cm aperture telescope of ZIMSMART2 [27] or 25 cm to 50 cm telescopes of SMARTNET [33]. A smaller 20 cm telescope ZIMSMART is shown in Figure 2.5.

Passive-optical sensors are much simpler, smaller, and easier to operate compared to RADAR. However, their downside is the limited observation window and dependencies on good weather conditions. Furthermore, optical sensors can only measure the angular position and not the range. Therefore, a large arc of the RSO's orbit needs to be measured to obtain a suitable orbit prediction.

This thesis presents the development of a passive-optical sensor for LEO RSO detection (see Chapter 4) and a detailed analytical model to estimate performance of passive-optical sensor is presented Chapter 3.

2.3. ACTIVE-OPTICAL SENSORS

Active-optical sensors on the other hand, use laser runtime measurements by emitting laser pulses to the RSO and receiving the reflected signal. The time difference Δt between emission and receiving results in a very accurate distance measurement. Laser beams have a much smaller divergence than RADAR sensors and therefore need more accurate a priori information about the RSO's trajectory. However, the precise distance measurements provide a much more accurate prediction over a longer time period [7]. A SLR station needs

transmitting optics including a laser source to transmit the laser pulses, and receiving optics including electronics to measure the runtime of the laser pulses. Laser ranging is currently used for satellite laser ranging (SLR) and becomes more established for space debris laser ranging (SDR) recently.

2.3.1. SATELLITE LASER RANGING

SLR is an established technology and was first performed in 1964 [35]. Nowadays, SLR is widely used in geodesy to measure Earth's gravity field, tectonic plate drifts, etc. [6] and in navigation to measure the position to satellites of the Global Navigation Satellite System (GNSS). To perform SLR, a satellite needs to be equipped with a retro reflector (corner cube reflector), which is an optical element which reflects incoming light back to the transmitter, independent from the angle of incidence. This improves the reflected signal dramatically. For geodetic measurements and navigation, precise position measurements are required which is why an existing global network of laser ranging stations perform SLR measurements routinely. This network is governed by the International Laser Ranging Service (ILRS). A sample ILRS ranging station operated by the GeoForschungsZentrum (GFZ) in Potsdam, Germany is shown in Figure 2.6.

Figure 2.6: The SLR station POTSDAM 3 (POT3) operated by GFZ is located in Potsdam, Germany. Source: [36].

SLR is generally limited to lower (LEO) up to medium Earth orbit (MEO), where the navigation satellites are located. It is also performed to the Moon, referred to as lunar laser

ranging (LLR), where APOLLO missions (APOLLO 11, 14, and 15) installed retro reflector arrays on its surface. However, this requires a very powerful laser and a large telescope.
The maximum range for SLR is limited by the laser pulse energy, laser beam divergence, retro reflector array area, and receiving aperture. The analytical laser link budget equation is described in Appendix 9.4.3. Laser ranging precision is limited to the laser pulse length, event timing electronics time jitter, and calibration of the station's location. By this means, very high accuracies up to a few millimeters can be achieved [35]. A common laser system of a SLR station, like POT3, has a pulse energy of 700 μJ at 532 nm wavelength with a repetition rate of 2 kHz [36]. The telescope utilizes a Coudé-path[F] in an azimuth-elevation mount to guide and transmit the laser pulses via a transmitter (15 cm beam diameter). The receiving aperture of POT3 is 0.44 m in diameter and a photon multiplier tube (PMT) is used for reflected laser photon detection [36].

The ILRS is a network of SLR stations and analysis centers that organizes the data acquisition and product generation. After a SLR station performed measurements, the orbit of the measured RSO is refined. Then the analysis center provides predictions of the orbit trajectory for follow-on observations by other ILRS stations. "This allows to maintain a higher level of accuracy for the orbits of this group of satellites, allowing a laser station to pick-up and track such a target without major additional efforts" [8]. Those prediction files are published in the Consolidated Laser Ranging Prediction Format (CPF) and can be accessed on the server of the Technical University of Munich (TUM) [37]. Utilizing these accurate predictions enable stations to perform ranging under daylight if the weather conditions are good. Hereby, background noise is temporal and spectrally filtered.

2.3.2. SPACE DEBRIS LASER RANGING

To perform laser distance measurements to space debris a much higher pulse energy is required as space debris targets are not equipped with a retro reflector. Consequently, laser light is scattered at the RSO instead of reflecting the light back to the transmitter. The general design of a space debris ranging sensor is identical to a SLR sensor, however the targets of interest (space debris) are not commonly tracked and measured by laser ranging sensors. Therefore, their orbit predictions have larger uncertainties as they are based on RADAR

[F] A telescope utilizing a Coudé-path has addition optics to guide the light along the two mechanical axis of the telescope mount.

measurements only. This requires passive-optical closed-loop tracking to facilitate continuous tracking with high accuracy and subsequent laser ranging. However, it requires the debris target to be illuminated by the Sun, which limits the operation to the nighttime only [29].

Figure 2.7 shows the laser ranging station that was used by Kirchner et. al. in 2012 to perform the first space debris laser ranging [38]. The benefits of debris laser ranging is that orbit predictions can be refined by one order of magnitude [7]. Furthermore, it was shown that the rotation and size of RSO can be measured [39]. Space debris laser ranging is generally limited to the LEO due to the weak back reflected signal.

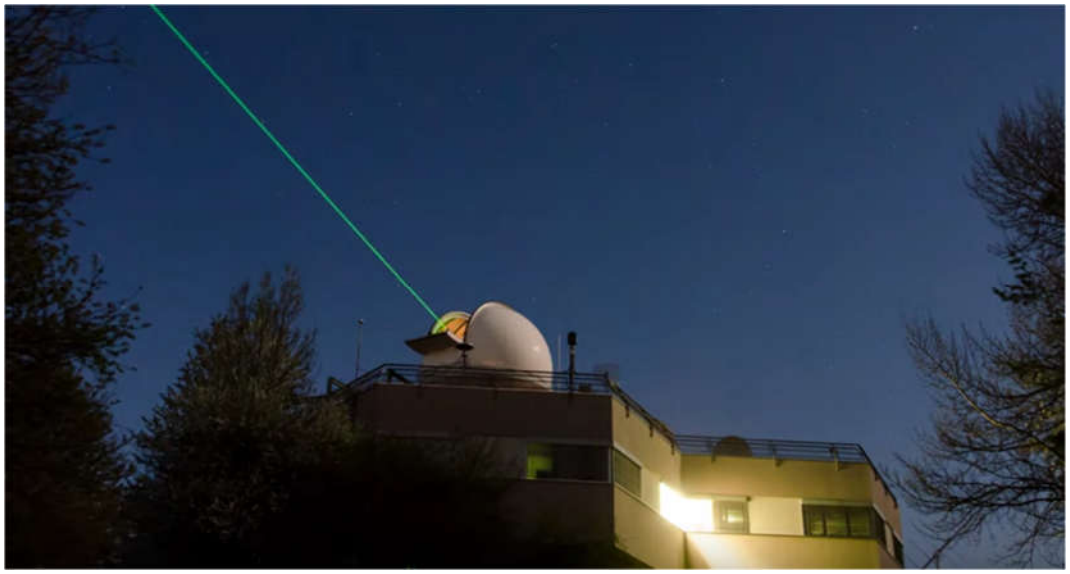

Figure 2.7: LUSTBÜHEL Observatory, located in Graz, Austria, was the first station to perform space debris laser ranging, and operated by the Institute for Space Research (IWF) of the Austrian Academy of Sciences (ÖAW). Source: [40].

Currently, it requires a separate RADAR sensor network to provide orbit predictions to track objects with a laser ranging station. Because of the high value and strong public interest in this topic, a cost-effective passive-optical sensor alternative to RADAR is introduced and demonstrated.

2.4. SPACE SURVEILLANCE NETWORK

Various space surveillance networks across the globe monitor the RSO population, see Ref. [27] for more details. However, for this thesis the US SSN is of major importance as it provides the most complete catalog of orbital objects publicly available. The US SSN is operated by the United States Strategic Command (USSTRATCOM) and consists of more

than 20 ground-based RADAR and optical sensors (the actual number remains unpublished) [27]. Figure 2.8 shows a map of the known sensor locations and types.

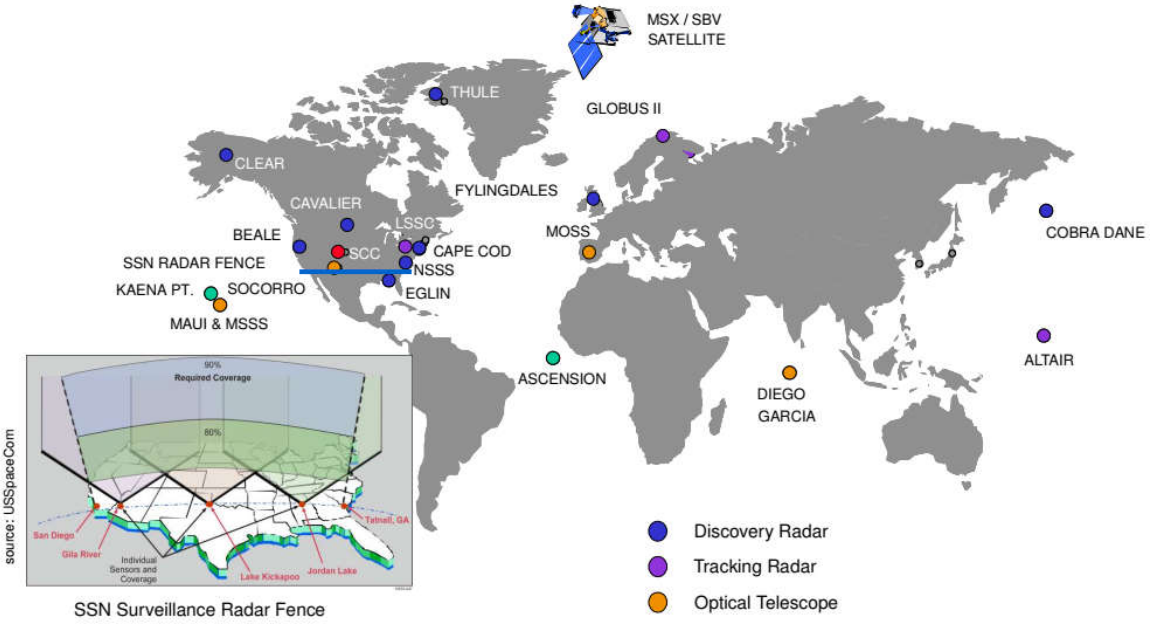

Figure 2.8: Map of known sensor locations with their type of the US SSN from 2011. Source: [41].

The network currently measures up to 100 000 observed RSO per day and the data is transferred to the Combined Space Operations Center (CSpOC) for processing. To set up and manage the catalogue, the SSN uses three different orbit estimation and propagation models: a model called General Perturbations (GP), a semi-analytical model, and a Special Perturbations model (SP) based on numerical integration [29]. Only less precise orbit predictions, produced with the GP model, is made available to the public on CELESTRAK [15] in the two-line-element (TLE) format. More details on the TLE format is given in Chapter 3.7.2. Each object detected by the SSN is managed in the North American Aerospace Defense Command (NORAD) TLE catalog and each object gets a dedicated NORAD identification (ID) number. The Center for Space Standards & Innovation (CSSI) offers the NORAD TLE catalog and a satellite catalog (SATCAT) [3], which lists all published NORAD objects with their ID including supplementary information of the RSO like RCS, origin, decay, apogee and perigee. However, the geometric shape and size of an object is not included. Approaches for converting the RCS to an optical cross section (OCS) are given in the Ref. [42], which however have to be treated with caution, since the OCS is influenced by the object's material and attitude.

2.5. CONSIDERATIONS FOR A PASSIVE-OPTICAL STARING SENSOR

Due to the small FOV of the tracking system and the small laser beam divergence, a laser ranging station needs a priori information of the objects trajectory to continuously track the object and perform range measurements. Thus, a priori orbit information of the RSO needs to be delivered by a separate sensor network. Currently, only RADAR systems in staring mode can fulfill this task of initial detection of unknown RSO in LEO. The downside of RADAR systems are their high hardware and operating cost. In contrast, a passive-optical system is smaller, simpler and easy to operate. This is why in this thesis a ground-based passive-optical sensor is developed to perform the initial object detection of LEO RSO. Such a sensor cannot replace RADAR, as they can operate day and night without weather restrictions. However, a simple, modular, autonomous, and weatherproofed system allows to operate a sensor network easily, extending existing SST network performance.

The passive-optical system measures apparent angular position of orbital objects with respect to the star background. It requires the sensor to have good observation conditions (weather and darkness) in order to image stars in the sky. At the same time the object to be observed needs to be illuminated by the Sun (more details are presented in Chapter 3). These conditions narrow the operational hours of this system compared to a RADAR system.

The focus on this thesis is on the development of a passive-optical staring sensor for LEO RSO detection, which results in a small and inexpensive sensor to be used in any SSA network. This system shall be ready for operational use and save the angular positions of each measured RSO in a standardized TDM (Tracking Data Message) format. This allows data exchange to external (already existing) databases or tracking stations. The future goal is to hand over the data and perform an initial orbit determination (IOD) such that a laser ranging station can perform continuous tracking and subsequent laser ranging. An operational sensor needs to meet following requirements for operational use:

- Autonomous operation
- Environmental protection
- Automatic data processing
- Standardized data export
- Evaluate sensor precession

Those requirements led to the design of the APPARILLO (AUTONOMOUS PASSIVE-OPTICAL STARING OF LEO FLYING OBJECTS) staring sensor. Following development steps have been performed within this thesis:

- Design of such a system including simulations, see Section 4.1 and 4.2 respectively
- Hard- and Software development, see Section 4.3 and 4.4 respectively
- System deployment and data analysis, see Section 5.1 and 5.2
- Projected performance and future steps, see Chapter 5.3

3. BACKGROUND

This Chapter describes the required theoretical background for passive-optical observations, and introduces coordinate systems and orbit dynamics.

In order to perform passive-optical observations, it is required that the RSO is illuminated by the Sun, while the observer is in the Earth's shadow. Otherwise the background light by the Sun and its scattered light in the atmosphere prevent imaging the RSO or stars. If the RSO is inside the Earth's shadow, it cannot be detected because it is too dark. Figure 3.1 illustrates the RSO observation: the observer *P* is located on the Earth's surface observing an RSO, which is illuminated by the Sun while orbiting in LEO. Secondly, the weather conditions need to be good to have a clear night sky. This limits the observation times to the night time when the weather allows clear view to the sky. Depending on the observer's location on the Earth and the line-of-sight (LOS), RSO will be in the Earth's shadow around midnight, which reduces the detectability for a few hours.

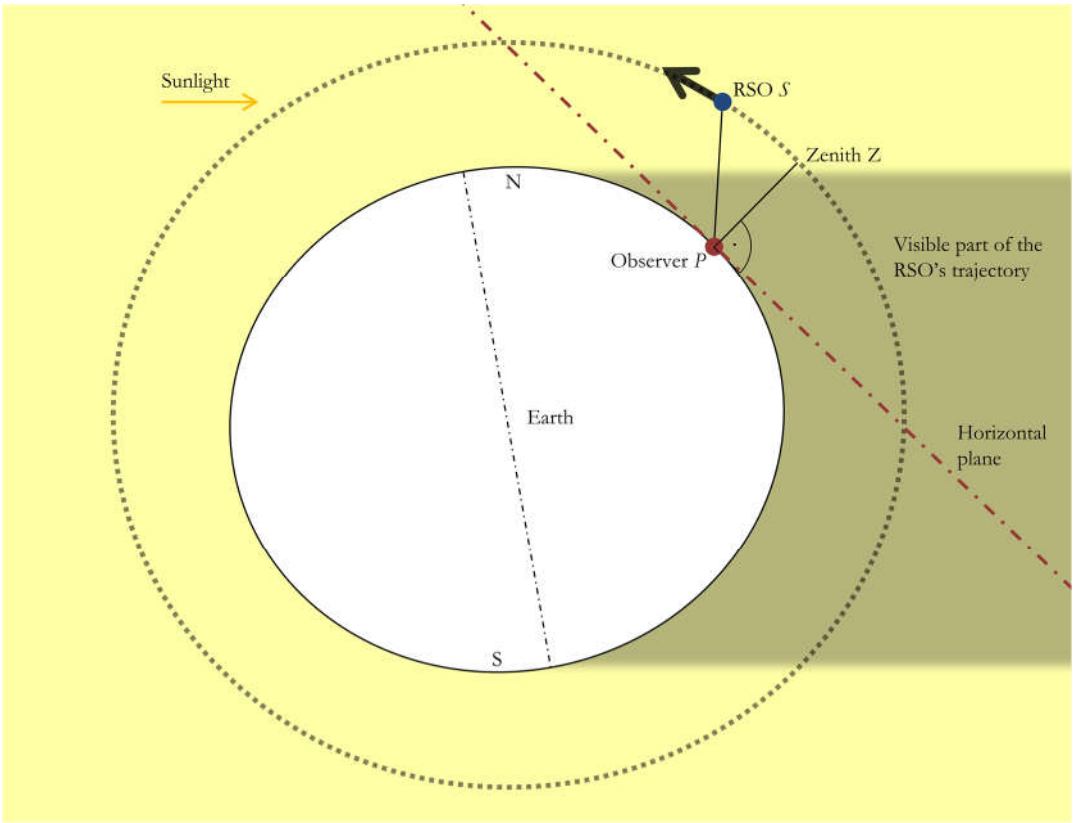

Figure 3.1: The RSO S (blue circle) orbits around the Earth (doted circle) and once it exits the Earth's shadow, it is illuminated by the Sun (yellow). The observer P (red circle) is located on the Earth's surface and observes the RSO. Figure is not in scale.

The proposed sensor uses optical imaging to measure RSO positions. With a camera system angles are measured relative to its optical axis and astrometric calibration is used to derive the angle relative to the stars (see Section 3.4). These coordinates are given in the equatorial coordinate system (see Section 3.5).

The first Section 3.1 describes general principles of paraxial optics and image formation. Secondly, the sensor technology is introduced in Section 3.2. The third Section 3.3 gives a detailed description on the theoretical calculation to estimate the system performance of a passive-optical staring system. Section 3.6 introduces simple orbit dynamics used within this work. Given the finite time the light travels from the RSO to the sensor and the high velocity of the RSO, the apparent position differs from the actual RSO position. This velocity aberration is explained in Section 3.7.

3.1. OPTICAL IMAGE FORMATION

Imaging systems can be used to measure the angle of an object with respect to the optical axis of the system. The focal length of the optical system is the distance from the position of the paraxial lens to the plane where all incoming collimated rays are focused on one point (in paraxial ray optics). In paraxial optics, as shown in Figure 3.2, image formation is given by the relation between focal length *f'*, distance of the focal plane to the principle plane *a'*, and the distance of the object to the principle plane *a* [43],

$$\frac{1}{f'} = \frac{1}{a'} - \frac{1}{a}. \tag{3.1}$$

In our scenario the object distance *a*, in relation to the focal length *f'*, can be seen as located at infinity ($a \rightarrow \infty$). Thus, the image plane is located in the focal plane *F'* of the optical system ($a' = f'$).

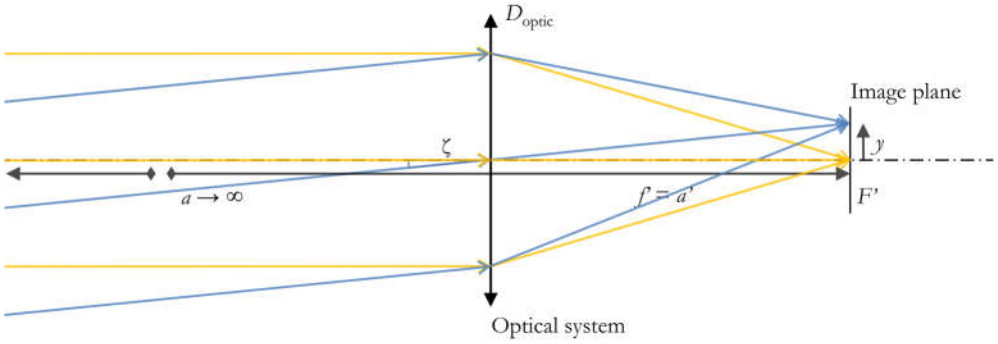

Figure 3.2: Paraxial imaging from an infinitely distant object ($a \rightarrow \infty$), where ζ is the angle of incidence, f' the focal length of the optical system, F' the focal plane, y the image height, and D_{optic} the diameter of the optical system.

When the image plane is equal to the focal plane of the optical system it results in the following relation between angle ζ and position *y* on the image plane.

$$\zeta = \arctan\left(\frac{y}{f'}\right) \cong \frac{y}{f'} \text{ [rad]}, \tag{3.2}$$

where, *y* is the position measured from the optical axis. For small angles (<10°) tan(*x*) can be approximated by *x*. In the same manner any spatial coordinate y can be converted to an angular coordinate and vice versa. For a given pixel size y_{px} and focal length of the system the angular resolution ζ_{px} of the system can be calculated. This is an important metric of the systems resolution. Furthermore, the *FOV* is a metric which corresponds to the observable orbital volume. The *FOV* can be calculated by the sensor size y_{sensor} and the focal length *f'*,

$$FOV = 2\arctan\left(\frac{y_{\text{sensor}}}{2f'}\right) \cong \frac{y_{\text{sensor}}}{f'} \text{ [rad]}. \tag{3.3}$$

The f-number *f#* is defined as the ratio between focal length *f'* and aperture diameter D_{optic} [43],

$$f\# = \frac{f'}{D_{\text{optic}}}. \tag{3.4}$$

It is a metric commonly used by photography lenses to describe the light gathering capabilities, as the pixel FOV affects how much light is collected from the solid angle. Note, this is why this metric does not correspond to the sensitivity of point sources. The f-number of a lens is commonly indicated by f/*f#* or 1:*f#*.

As explained previously, in the idealized paraxial optics light is focused on a single point. However, wave properties of the light cause diffraction. Furthermore, geometric aberrations of the optical system cause a distribution of focal points, which is described in the point spread function (PSF). The *PSF* is the irradiance distribution $\Phi_{\text{img}}(x, y)$ of an ideal point source on the image plane $A(x, y)$ of an optical system [43],

$$PSF(x, y) = \frac{\partial \Phi_{\text{img}}(x, y)}{\partial A(x, y)}. \tag{3.5}$$

For a diffraction limited radial symmetric optical system the *PSF* is given by the Airy function. The normalized distribution in dependence of the distance to the optical axis *r'* of the image plane is [43],

$$PSF(r') = \left(\frac{2\,J_1(\upsilon)}{\upsilon}\right)^2, \tag{3.6}$$

where J_1 is the first order Bessel function, with in the image plane normalized coordinate υ [43],

$$v = \frac{2\pi}{\lambda} x' \sin U' = \frac{2\pi}{\lambda} \frac{r_{\text{optic}} r'}{f'}, \tag{3.7}$$

where, r_{optic} is the radius of the system's circular aperture.

The spot size diameter d_{spot} of a point source on the image plane results from diffraction and geometrical PSF diameters, d_{airy} and d_{geo} respectively [43],

$$d_{\text{spot}} = \sqrt{{d_{\text{airy}}}^2 + {d_{\text{geo}}}^2}. \tag{3.8}$$

The *PSF* is not identical across the image plane, but for simplification of further analysis the *PSF* is approximated with a symmetric Gaussian distribution across the entire image plane,

$$PSF(x, y) = \frac{1}{\sigma^2 2\pi} \mathrm{e}^{-\left(\frac{x^2+y^2}{2\sigma^2}\right)}, \tag{3.9}$$

with a width σ in both directions. The relation between σ and full-width-half-maximum (*FWHM*) for a Gaussian function is,

$$\sigma = \frac{FWHM}{2\sqrt{2\ln 2}} \cong \frac{FWHM}{2.35482}. \tag{3.10}$$

3.2. OPTICAL DETECTOR TECHNOLOGY

The Sun emits a broad spectrum of electromagnetic waves, which is well described by black body radiation. The graph in Figure 3.3 compares the spectral irradiance of the sunlight on the Earth's surface with, and without atmospheric absorption to the ideal black body radiation.

For electronical detection of light, the photoelectric effect is commonly used, while the spectral response depends on the semiconductor materials. For the purpose of detecting light which is emitted by the Sun, Silicon (Si) based detectors are optimal. Their spectral response is located around the maximum of the solar radiation, see Figure 9.59 in Appendix 9.9.1. These detectors are commonly used for imaging applications and are widely available. More importantly, they are highly developed and show very low noise.

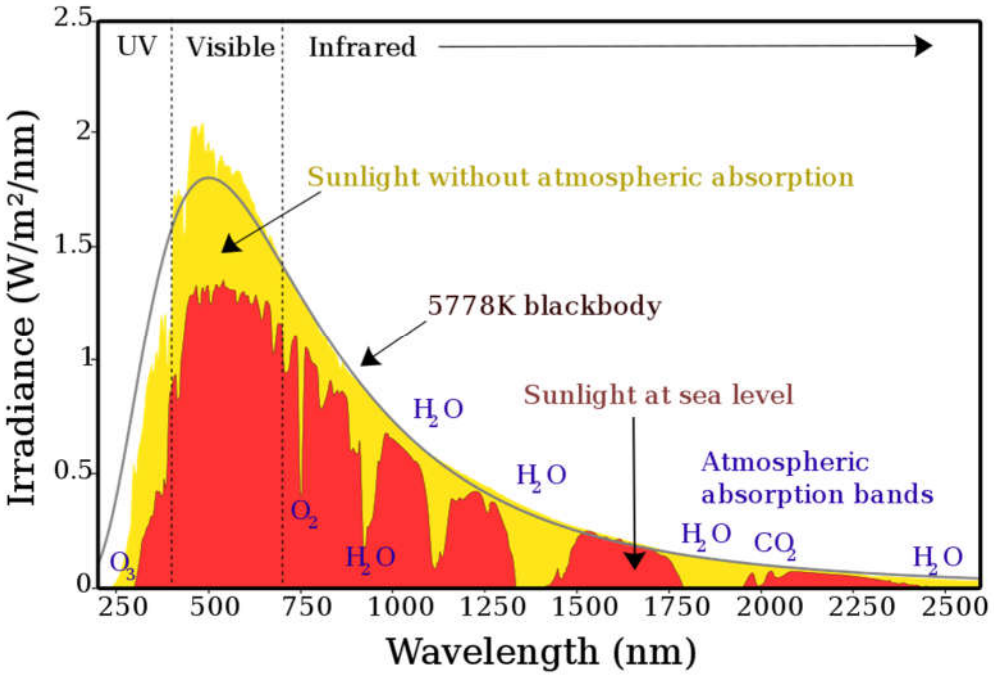

Figure 3.3: Spectral irradiance of the Sun as an ideal blackbody (black line), the actual sunlight without atmospheric absorption (yellow surface) and the sunlight at the sea level on the Earth (red surface). Due to the Sun's surface temperature, the main intensity is emitted at around 500 nm. Furthermore, effects in the Sun's and Earth's atmosphere cause absorption and scattering losses. Source: [44] © CC BY-SA 3.0.

A digital imaging detector is made of an array of single pixels. Each pixel is a photodiode which generates an electrical charge when it is irradiated by photons (photoelectric effect). The quantum efficiency QE is the ratio between detected electrons N_e and incident photons Φ_{Ph} [43],

$$QE(\lambda) = \frac{N_e}{\Phi_{\mathrm{Ph}}(\lambda)} \frac{h\,c}{e^-\,\lambda}. \tag{3.11}$$

The photo sensitive (active) area of the pixel is smaller than the width of the pixel y_{px}. This is why lenslet arrays are commonly used in front of the sensor to focus the incoming light onto the active area. Normally, the QE given in the sensor specifications already considers this effect.

Various noise sources limit the sensitivity of the photo detector. One source is the current of electrons in the absence of photons that are released randomly over time, referred to as dark noise (or dark current) N_{dark}. The dark noise is a thermal effect and can be reduced by cooling the sensor. Another is noise added during the read-out process, which is called read-out noise N_{read}. The read-out noise is added during the transfer of the electrical charges and typically becomes larger with faster read-out rates. Furthermore, for small signal powers the fundamental quantum noise is observed. This varies according to the Poisson statistics of the

discretely arriving photons. For a number N_{Ph} of photons, the peak-width σ_{back} of the distribution is given by [43],

$$\sigma_{\mathrm{back}} = \sqrt{N_{\mathrm{Ph}}}. \tag{3.12}$$

More information about imaging sensor's noise sources can be found in Chapter 8 of Ref. [43].

The signal to noise ratio (*SNR*) is the number of signal events (e.g. photons or electrons), N_{signal}, divided by the total variance of the different sources/distributions (e.g. noise) σ_N,

$$SNR = \frac{N_{\mathrm{S}}}{\sigma_{\mathrm{N}}} = \frac{\sum_{\mathrm{i}} N_{\mathrm{S(i)}}}{\sqrt{\sum_{\mathrm{i}} \sigma_{\mathrm{N(i)}}{}^2}}. \tag{3.13}$$

The average SNR increases by the amount of measurements *n* [43],

$$SNR = \sqrt{n}\, SNR_0. \tag{3.14}$$

Where, SNR_0 is the observed SNR in a single measurement, assuming that the SNR is constant within all measurements.

CCD (Charge coupled device) detectors carry the generated charges by shifting them row and column wise. In the end a single read-out circuit reads the charge and converts it to a digital signal for each pixel. The read-out mechanism allows combining the charges of neighboring pixels. This is called binning, where the number gives the count of pixels which are combined in both dimensions. Consequently, binning 2 results in the combination of 2 px by 2 px into a single pixel. CMOS (Complementary metal-oxide-semiconductor) on the other hand, have individual read-out circuits for each pixel. This provides much faster read-out speed independent on the resolution (with some limits). A more refined development of CMOS is the introduction of two separate circuits for low and high signals on each pixel, which is called scientific CMOS (sCMOS). This delivers low noise and a high dynamic range.

3.3. PASSIVE-OPTICAL LINK EQUATION

This section shows how the signal strength of an RSO can be calculated by a given optical staring sensor. To obtain a passive-optical link budget equation, Ref. [45] by Shell et al. is used and the SNR equation is converted to estimate the detectable object diameter d_{RSO} (detection threshold) for a given system. Figure 3.4 shows the geometrical relations between observer and RSO with the corresponding parameters.

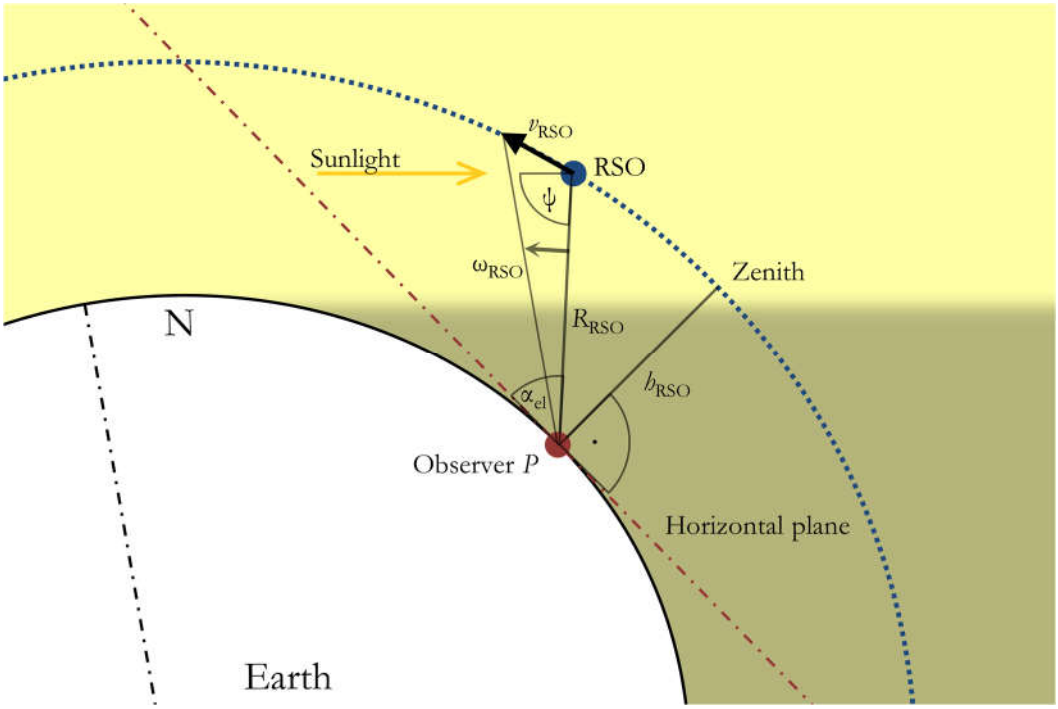

Figure 3.4: Geometric overview of the passive-optical observation of LEO RSO, based on Figure 3.1. The passive-optical sensor is located on the Earth's surface and its LOS elevation α_{el} is measured from the horizonal plane. The RSO orbits on a circular orbit with the velocity v_{RSO} and orbit height h_{RSO} above Earth's surface. The apparent angular velocity of the RSO seen from the observer is ω_{RSO}. The phase angle ψ is measured at the RSO between Sun and observer.

For a single pixel, which receives the signal, the *SNR* results from electrons of the signal N_{signal}, and the square root of the variances [43]. The background noise N_b is Poisson distributed, while the sensor noise is given as variance. Thus, the *SNR* is given as,

$$SNR = \frac{N_{\text{signal}}}{\sqrt{N_{\text{b}} + {N_{\text{read}}}^2}}, \tag{3.15}$$

where N_{read} is the read-out noise from the image sensor. The dark noise for short exposures (<1 s) in modern cooled Si-detectors is <0.1 e^- (see Section 4.3.2 Table 4.8) and therefore negligible.

To estimate the signal strength, the brightness M_{RSO} of the RSO needs to be calculated. For simplicity, the brightness for a spherical object, given in magnitude units, is given by [45],

$$M_{\text{RSO}} = -26.73 - 2.5\log\left(\frac{{d_{\text{RSO}}}^2}{{R_{\text{RSO}}}^2} \cdot P(\rho, \psi)\right) \text{[mag]}, \tag{3.16}$$

where d_{RSO} is the diameter of the RSO, R the distance from the observer to the RSO and $P(\rho, \psi)$ is the phase function of the RSO. The phase function depends on the reflectivity of the

object ϱ, and the angle ψ between observer and Sun. The phase function of a sphere with a specular reflectivity ϱ_{spec}, and diffuse reflectivity ϱ_{diff} is [45],

$$P(\rho,\psi) = \left(\frac{\rho_{\text{spec}}}{4} + \rho_{\text{diff}}\frac{2}{3\pi}(\sin(\psi) + (\pi-\psi)\cos(\psi))\right). \tag{3.17}$$

The photon flux E_{RSO} of the RSO calculated from the brightness M_{RSO} is given by [45],

$$E_{\text{RSO}} = 5.6 \cdot 10^{10} \cdot 10^{-0.4 \cdot M_{\text{RSO}}} \left[\frac{\text{ph}}{\text{s} \cdot \text{m}^2}\right]. \tag{3.18}$$

Combining previous Eq. (3.16) with (3.18), the photon flux can be calculated depending on d_{RSO}, R_{RSO}, and $P(\varrho, \psi)$:

$$E_{\text{RSO}} = 5.6 \cdot 10^{10} \cdot 10^{10.692} \cdot 10^{\log(P(\rho,\psi))} \cdot 10^{\log\left(\frac{{d_{\text{RSO}}}^2}{{R_{\text{RSO}}}^2}\right)} \left[\frac{\text{ph}}{\text{s} \cdot \text{m}^2}\right], \tag{3.19}$$

or

$$E_{\text{RSO}} = \frac{2.755 \cdot 10^{21} \cdot P(\rho,\psi) \cdot {d_{\text{RSO}}}^2}{{R_{\text{RSO}}}^2} \left[\frac{\text{ph}}{\text{s} \cdot \text{m}^2}\right]. \tag{3.20}$$

The major noise source is the background illumination L_{b}, which can be calculated by the background brightness M_{b}, given in magnitude per arcsec² unit, as follows [45],

$$\begin{aligned} L_{\text{b}} &= 5.6 \cdot 10^{10} \cdot 10^{-0.4 \cdot M_{\text{b}}} \cdot \left(\frac{180}{\pi}\right)^2 \cdot 3600^2 \\ &= \frac{2.3515 \cdot 10^{22} 10^{-0.4 \cdot M_{\text{b}}}}{\pi^2} \left[\frac{\text{ph}}{\text{s} \cdot \text{m}^2 \cdot \text{sr}}\right]. \end{aligned} \tag{3.21}$$

The electrons N_{b} generated by the background illumination L_{b} result from the exposure time t_{exp}, quantum efficiency QE, the pixel area ${y_{\text{px}}}^2$, the focal length f', the diameter d_{optic}, and transmission τ_{optic} of the optics [45],

$$N_{\text{b}} = \frac{QE\tau_{\text{optic}}{y_{\text{px}}}^2 t_{\text{exp}} \pi L_{\text{b}}}{1 + \frac{4f'^2}{{d_{\text{optic}}}^2}} = \frac{{d_{\text{optic}}}^2 QE\tau_{\text{optic}}{y_{\text{px}}}^2 t_{\text{exp}} \pi L_{\text{b}}}{{d_{\text{optic}}}^2 + 4f'^2}. \tag{3.22}$$

The nominal background brightness is 19.5 mag/arcsec² [46], a bright night sky has a brightness of 17.5 mag/arcsec² [47], and a dark night sky on a site with no light pollution is 21 mag/arcsec² [48]. In a city with light pollution the background brightness can range up to 15 mag/arsec² [49].

The signal electrons N_{signal} generated from the RSO's photon flux E_{RSO} are calculated similarly, while the pixel FOV υ_{px} is not relevant as the light from a single point (or angle) is focused onto the pixel,

$$e_{\text{signal}} = E_{\text{RSO}}\tau_{\text{atm}}\left(\frac{{d_{\text{optic}}}^2}{4}\pi\right)\tau_{\text{optic}}\tau_{\text{px}}\,QE\,t_{\text{signal}}. \tag{3.23}$$

Hereby, τ_{atm} is the nominal transmission of the atmosphere, τ_{px} is the couple efficiency of the light from the point source onto a single pixel, and t_{signal} is the time the RSO irradiates this pixel. During observations in staring mode the camera is pointed to a fixed direction and the RSO moves over the fixed image plane during the exposure. The time which the RSO illuminates a single pixel can be calculated by the apparent angular velocity of the RSO ω_{RSO} and the pixel FOV υ_{px}. The calculation of the apparent angular velocity depending on orbit height and elevation is explained in Section 3.6.1, see Eq. (3.47).

$$t_{\text{signal}} = \frac{\upsilon_{\text{px}}}{\omega_{\text{RSO}}} = \frac{y_{\text{px}}}{\omega_{\text{RSO}}f'} \tag{3.24}$$

This allows to calculate the *SNR* formula using equations from above ((3.22), (3.23) with (3.15)),

$$SNR = \frac{E_{\text{RSO}}\tau_{\text{atm}}{d_{\text{optic}}}^2\pi\tau_{\text{optic}}\tau_{\text{px}}\,QE\,y_{\text{px}}}{4\omega_{\text{RSO}}f'\sqrt{\frac{{d_{\text{optic}}}^2 QE\tau_{\text{optic}}{y_{\text{px}}}^2 t_{\text{exp}}\pi L_{\text{b}}}{{d_{\text{optic}}}^2 + 4{f'}^2} + N_{\text{read}}^2}}. \tag{3.25}$$

Using this equation exemplary calculations under different background brightnesses are shown in Figure 3.5. It can be seen that the SNR increases with a larger object size and that a larger background brightness decreases the SNR as expected.

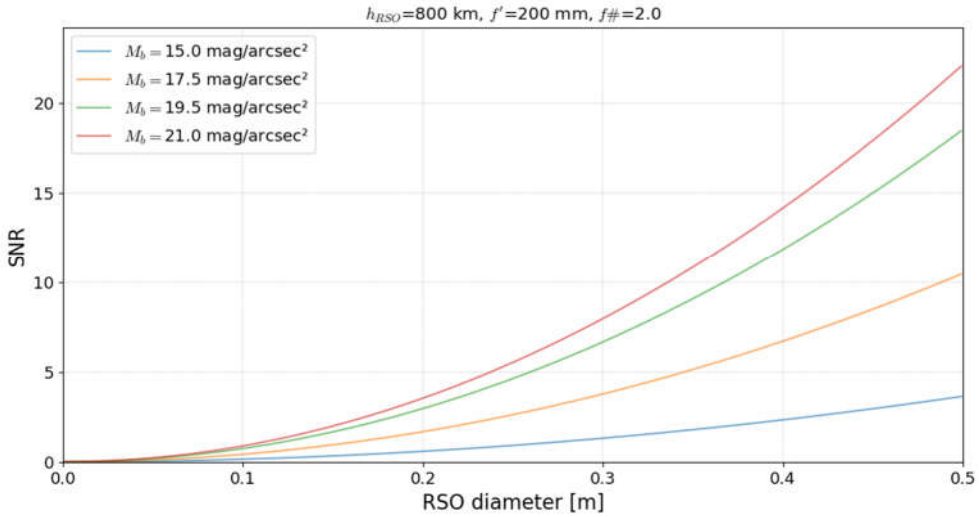

Figure 3.5: The SNR depending on the RSO diameter for four different background brightness M_b intensities. All simulation parameters are listed in Table 4.1.

The slant range (or distance) R_{RSO} between a station and an object in space with orbit height h_{RSO} is given as [50],

$$R_{\mathrm{RSO}} = -(R_{\mathrm{E}} + h_{\mathrm{station}}) \cos\left(\frac{\pi}{2} - \alpha_{\mathrm{el}}\right) + \sqrt{\left[(R_{\mathrm{E}} + h_{\mathrm{station}}) \cos\left(\frac{\pi}{2} - \alpha_{\mathrm{el}}\right)\right]^2 + 2R_{\mathrm{E}}(h_{\mathrm{RSO}} - h_{\mathrm{station}}) + h_{\mathrm{RSO}}^2 - h_{\mathrm{station}}^2}, \quad (3.26)$$

where R_E is the radius of the Earth, $h_{station}$ the station height and α_{el} the elevation of the object as observed from the station (in respect to the horizon). This equation can be approximated by,

$$R_{\mathrm{RSO}} = \frac{h_{\mathrm{RSO}}}{\sin(\alpha_{\mathrm{el}})}, \quad (3.27)$$

and is used to calculate R_{RSO}. Using this model, the *SNR* can be calculated depending on RSO orbit height. Figure 3.6 shows the calculated *SNR* depending on the RSO diameter and orbit height under both high and low background brightness.

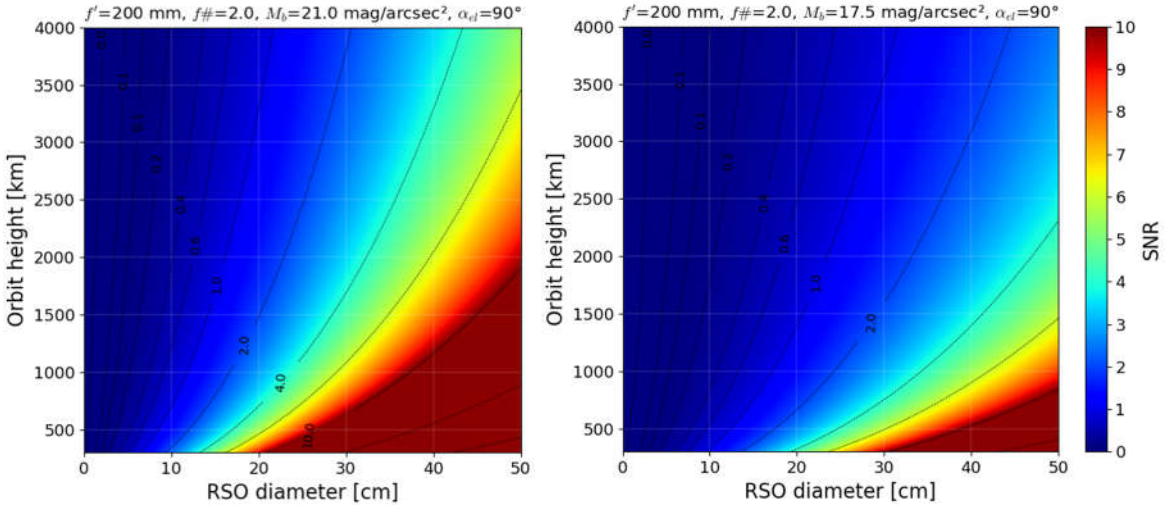

Figure 3.6: The SNR depending on the RSO orbit height and RSO diameter with 21 mag/arcsec² and 17.5 mag/arcsec² background brightness. Note, that the colors are chosen to show the detectability: red – very high, green – high, blue – low. All simulation parameters are listed in Table 4.1.

It can be seen that the SNR increases with lower orbit height and cubically with larger object diameter. The SNR is about a factor of two smaller at 17.5 mag/arcsec² compared to 21 mag/arcsec² background brightness.

The coupling efficiency τ_{px} is the amount of light from a single point source which irradiates the pixel area A_{px}. Hence, τ_{px} can be calculated as follows,

$$\tau_{\mathrm{px}} = \frac{\Phi(A_{\mathrm{px}} \cap PSF)}{\Phi(PSF)} = \int_{-\frac{x_{\mathrm{px}}}{2}}^{\frac{x_{\mathrm{px}}}{2}} \int_{-\frac{y_{\mathrm{px}}}{2}}^{\frac{y_{\mathrm{px}}}{2}} PSF(x,y)\, \mathrm{d}x\, \mathrm{d}y. \quad (3.28)$$

Where, x_{px} and y_{px} are the pixel size in x and y direction respectively. As explained in Eq. (3.9), the *PSF* is approximated by a symmetric 2D Gaussian function. Assuming that the PSF is centered on the pixel, the coupling efficiency results from the integral of the PSF over the pixel area,

$$\tau_{\mathrm{px}} = \int_{-\frac{x_{\mathrm{px}}}{2}}^{\frac{x_{\mathrm{px}}}{2}} \int_{-\frac{y_{\mathrm{px}}}{2}}^{\frac{y_{\mathrm{px}}}{2}} \frac{1}{\sigma^2 2\pi} e^{-\left(\frac{x^2+y^2}{2\sigma^2}\right)} \mathrm{d}x\, \mathrm{d}y. \tag{3.29}$$

To estimate the diameter of the RSO, Eq. (3.20) for E_{RSO} in Eq. (3.25) is solved for d_{RSO},

$$d_{\mathrm{RSO}} = \sqrt{\frac{SNR\ 4\ \omega_{\mathrm{RSO}}\ f'{R_{\mathrm{RSO}}}^2 \sqrt{\frac{{d_{\mathrm{optic}}}^2 QE \tau_{\mathrm{optic}} {y_{px}}^2 t_{\mathrm{exp}} \pi L_{\mathrm{b}}}{{d_{\mathrm{optic}}}^2 + 4f'^2} + N_{\mathrm{read}}^2}}{2.755 \cdot 10^{21}\ P(\rho,\psi)\ \tau_{\mathrm{atm}} {d_{\mathrm{optic}}}^2 \pi \tau_{\mathrm{optic}} \tau_{\mathrm{px}}\ QE\ y_{\mathrm{px}}}}. \tag{3.30}$$

Figure 3.7 shows the minimum detectable object size depending on the SNR detection threshold and aperture diameter using Eq. (3.30). Parameters of this calculation are explained in Chapter 4.2.1 later.

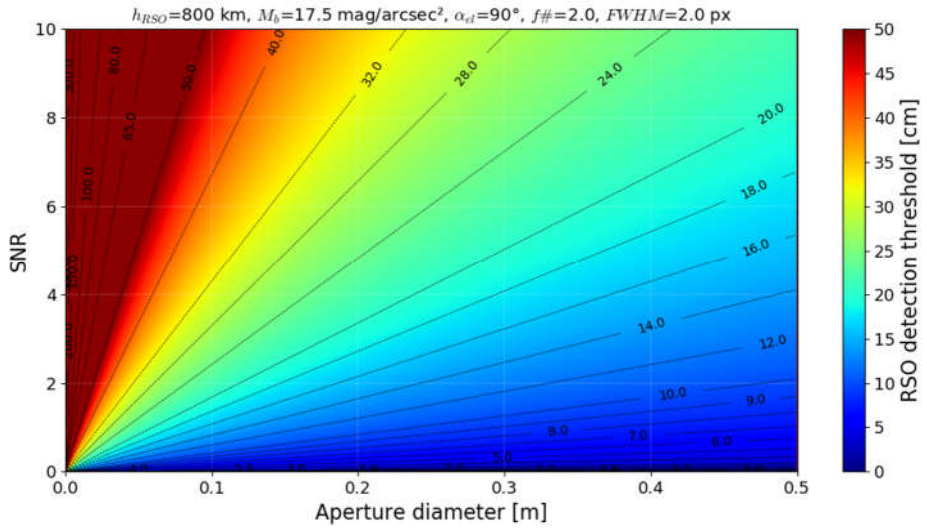

Figure 3.7: The RSO detection threshold depending on the SNR and aperture diameter. All simulation parameters are listed in Table 4.1.

The atmospheric transmission is an important quantity which determines the light intensity received by the sensor from an RSO. The transmission is the quotient of the intensity $\Phi(z)$ after a distance z in an absorptive medium to the intensity before entering the medium Φ_0 [43].

The absorption of light through a medium depending on the distance z with absorption coefficient $\beta(z)$ can be described by the Lambert-Beer law [43],

$$\tau_{\mathrm{atm}}(z) = \frac{\Phi(z)}{\Phi_0} = e^{-\int_0^z \beta(z)\mathrm{d}z}. \tag{3.31}$$

To describe the atmospheric transmission τ_{atm} the Kruse model is used, which is an empirical model to calculate the scattering losses β_0 in the atmosphere at sea level [51].

$$\beta_0(V,\lambda) = \frac{3.912}{V(z)}\left(\frac{\lambda}{550\ \mathrm{nm}}\right)^{-q} \tag{3.32}$$

Hereby is $V(z)$ the visibility and λ the wavelength in nm units, while q depends on the visibility to address different aerosol distributions [52],

$$q = \begin{cases} 1.6: & V > 50\ \mathrm{km} \\ 1.3: & 6\ \mathrm{km} < V < 50\ \mathrm{km}. \\ 0.585V^{1/3}: & V < 6\ \mathrm{km} \end{cases} \tag{3.33}$$

These scattering losses are valid at a specific altitude h, but due to pressure as well as aerosol concentration, β depends on the height, too. The total scattering coefficient β_{atm} decreases approximately exponentially with height h,

$$\beta_{\mathrm{h}}(\lambda, V, h) = \beta_0(\lambda, V)e^{-\frac{h}{h_{\mathrm{scale}}}}, \tag{3.34}$$

where $\beta_{\mathrm{h}}(\lambda, V, h)$ is the total scattering coefficient at height h and $\beta_0(\lambda, V)$ is the total scattering coefficient at sea level. h_{scale} is a scale height with a value of $h_{\mathrm{scale}} = 1.2$ km [53]. The transmission τ_{atm} through the atmosphere from the height h_{station} at which the sensor is located can be calculated by multiplying all the single transmissions of infinitesimal height increments dh,

$$\tau_{\mathrm{atm}}(\lambda, V) = \mathrm{e}^{-\int_{h_{\mathrm{station}}}^{\infty} \beta_{\mathrm{t}}(\lambda,V,h)\frac{\mathrm{d}h}{\cos\left(\frac{\pi}{2}-\alpha_{\mathrm{el}}\right)}}, \tag{3.35}$$

where α_{el} is the elevation angle at which the sensor is observing. The upper limit of the integral is set to infinity since the scattering coefficient gets negligibly small at increasing altitudes. In LEO, in which the targets of interest are located, this coefficient can be assumed to be 0.

With the height dependence of the scattering coefficient given in Eq. (3.34) the integral of Eq. (3.35) can be solved analytically leading to,

$$\tau_{\mathrm{atm}}(\lambda, V) = \mathrm{e}^{-\beta_{\mathrm{t}}(\lambda,V,0)\frac{h_{\mathrm{scale}}}{\cos\left(\frac{\pi}{2}-\alpha_{\mathrm{el}}\right)}\mathrm{e}^{-\frac{h_{\mathrm{station}}}{h_{\mathrm{scale}}}}}. \tag{3.36}$$

This equation shows that the atmospheric transmission depends on the elevation, visibility, wavelength, and station height. Observations are performed using Si-based detectors which are most sensitive at about $\lambda = 550$ nm, which is why this wavelength is used to calculate the transmission.

Figure 3.8 shows the minimum detectable object diameter depending on the visibility and elevation for a sub-optimal ($h_{station}$ = 500 m, M_b = 17.5 mag/arcsec²) and a good site ($h_{station}$ = 2000 m, M_b = 21 mag/arcsec²). It can be seen that the detection threshold is not affected by the observing elevation under good visibility conditions. A higher station height improves the atmospheric transmission, thus observations under smaller elevations affect the detection threshold only slightly. The detection threshold of a good site calculates to 18 cm compared to 28 cm for the sub-optimal site.

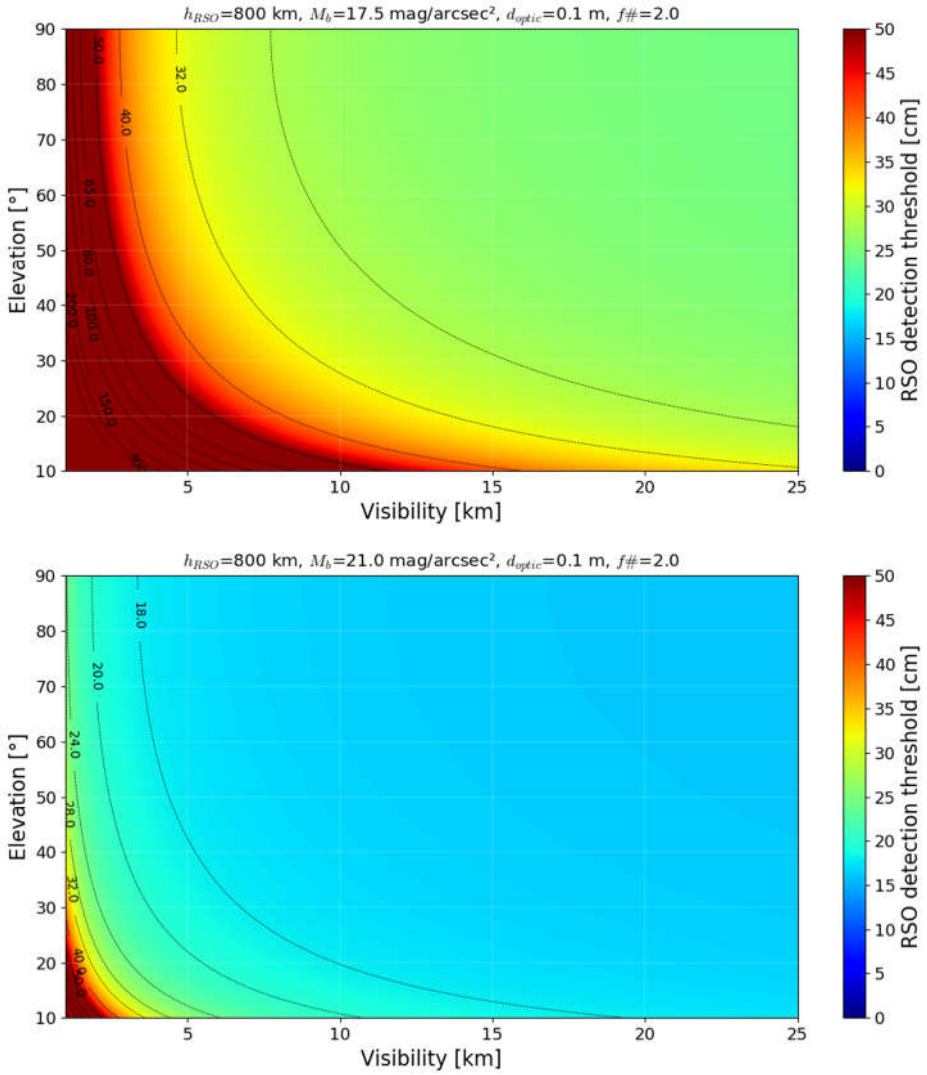

Figure 3.8: The RSO detection threshold depending on the visibility and LOS elevation under 17.5 mag/arcsec² background illumination and 0.5 km station height (top) and under optimal observation conditions with 21 mag/arcsec² and 2 km station height above Earth (bottom). All simulation parameters are listed in Table 4.1.

Equation (3.30) with (3.21) for M_b, (3.27) for R_{RSO}, (3.29) for τ_{px}, and (3.36) for τ_{atm} are used in Chapter 4.2.1 to estimate the system performance and compare different scenarios. Table 4.1

in Chapter 4.2.1 lists the complete simulation parameters used for the graphs in this Chapter (Figure 3.5 to Figure 3.8). Additional graphs using various conditions can be found in the Appendix 9.1.1.

When the noise by background illumination is dramatically higher than the read-out noise, N_{Read} can be set to zero. This simplifies Eq. (3.30) such that important parameters to detect smaller RSO are revealed,

$$d_{\mathrm{RSO}} \propto \sqrt{\frac{h_{\mathrm{RSO}}\, SNR\, \sqrt{t_{\mathrm{exp}} L_{\mathrm{b}}}}{P(\rho,\psi)\, \tau_{\mathrm{atm}}\, d_{\mathrm{optic}}\, \tau_{\mathrm{px}}\, \sqrt{QE\, \tau_{\mathrm{optic}}}}}. \tag{3.37}$$

To compare the link budget estimation with real objects, the given volume V_{RSO} is used to calculate the equivalent diameter d_{RSO} of a sphere,

$$V_{\mathrm{RSO}} = \frac{4}{3}\pi\left(\frac{d_{\mathrm{RSO}}}{2}\right)^3, \qquad d_{\mathrm{RSO}} = \sqrt[3]{\frac{6\, V_{\mathrm{RSO}}}{\pi}}. \tag{3.38}$$

Similarly, the equivalent circular diameter d_{RSO} of a given RSO cross-section A_{RSO} is given by,

$$A_{\mathrm{RSO}} = \pi\left(\frac{d_{\mathrm{RSO}}}{2}\right)^2, \qquad d_{\mathrm{RSO}} = \sqrt[2]{\frac{4\, A_{\mathrm{RSO}}}{\pi}}. \tag{3.39}$$

Furthermore, suitable system properties can be suggested as follows:

Location and observation time:

- A higher station height improves the atmospheric transmission, thus reducing the affected performance by water vapor in the atmosphere.
- Remote sensor location from places with light pollution for lower background illumination.
- A later observation after sunset or earlier before sunrise reduces the background illumination. However, depending on latitude and orbit height objects in LEO fall into the complete Earth shadow at different time.

Detector:

- The effect of dark noise is minor for cooled Si-based detectors.
- The read-out noise is minor compared to presence of background illumination.
- Quantum efficiency should be as high as possible.
- A larger pixel size results in a smaller detection threshold. However, this results in a smaller angular resolution.

- A larger detector size results in a larger FOV.

RSO:

- Properties cannot be controlled
- Objects with a small reflectivity are less likely to be discovered
- Objects in lower orbits are easier to detect
- In case of an rotating (tumbling) RSO, random specular reflections may result in a larger signal than expected.

Optics:

- Transmission over the whole detection spectrum should be as high as possible. Thus, anti-reflective coatings are recommended for refractive optics.
- For telescopes with reflective optics the central obscuration should be as small as possible.
- The aperture diameter should be as large as possible. If background illumination is dominant, a small *f#* results in larger noise, thus, decreasing effectiveness of a larger aperture.
- The focal length should be small to achieve a larger FOV. However, a larger focal length results in a smaller angular resolution.
- The width of the optical PSF should be smaller than the pixel size.

Image processing:

- Image processing techniques are recommended, which allow extraction of small SNR values from recorded RSO.

3.4. ASTROMETRIC CALIBRATION

Astrometric calibration takes measured star positions on the focal plane and maps them to cataloged stars. The process allows to transform positions measured on the focal plane to equatorial coordinates. Such a mapping model incorporates various characteristics of the observing system, which are:

- orientation of the focal plane
- plate scale
- radial non-linear deformations resulting from distortion of the optics

Usually, this mapping is realized by a least-squares adjustment process of measured stars to well distributed reference stars from the catalog [27]. This process is the core of the astrometric calibration and is also known as plate solving.

The astrometric calibration engine ASTROMETRY.NET [54], which is used in this work, groups four stars to form a quad [55]. First, the cataloged stars are pre-processed by forming a quad with the four brightest stars in a specific area of the sky. In Figure 3.9 it is illustrated how the relative positions between the two inner stars of that quad form a hash. These quads can be pre-processed and saved for different scales, which are used by the astrometric engine. Before performing the plate solving on the image, the brightest stars in the image are used to form the quads, while the brightness is only used to order the index of the stars, but not for the matching. Finally, the resulting hashes from the image can be compared with the indexed hashes from the cataloged stars. The result is verified by comparing the other measured quads until it passes the convincing threshold.

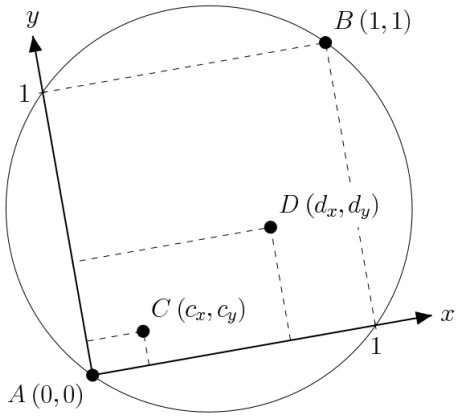

Figure 3.9: The astrometric engine used by ASTROMETRY.NET defines a quad hash code of four stars (A, B, C, and D). The hash code is defined by the position of C (c_x, c_y) and of D (d_x, d_y) in the coordinate system defined by A and B. Source: [55].

Usually, an astrometric engine allows to determine the stars from a source image, which is illustrated in Figure 3.10, or alternatively gives the option to directly input measured star positions. Once a mapping model is obtained, any coordinate on the recoded image can be transformed into equatorial coordinates.

Further details on the ASTROMETRY.NET engine can be found in Ref. [55]. Note, that this work initially used the software PINPOINT [56] as a preliminary astrometric engine, which was later replaced by ASTROMETRY.NET due to its more robust plate solving.

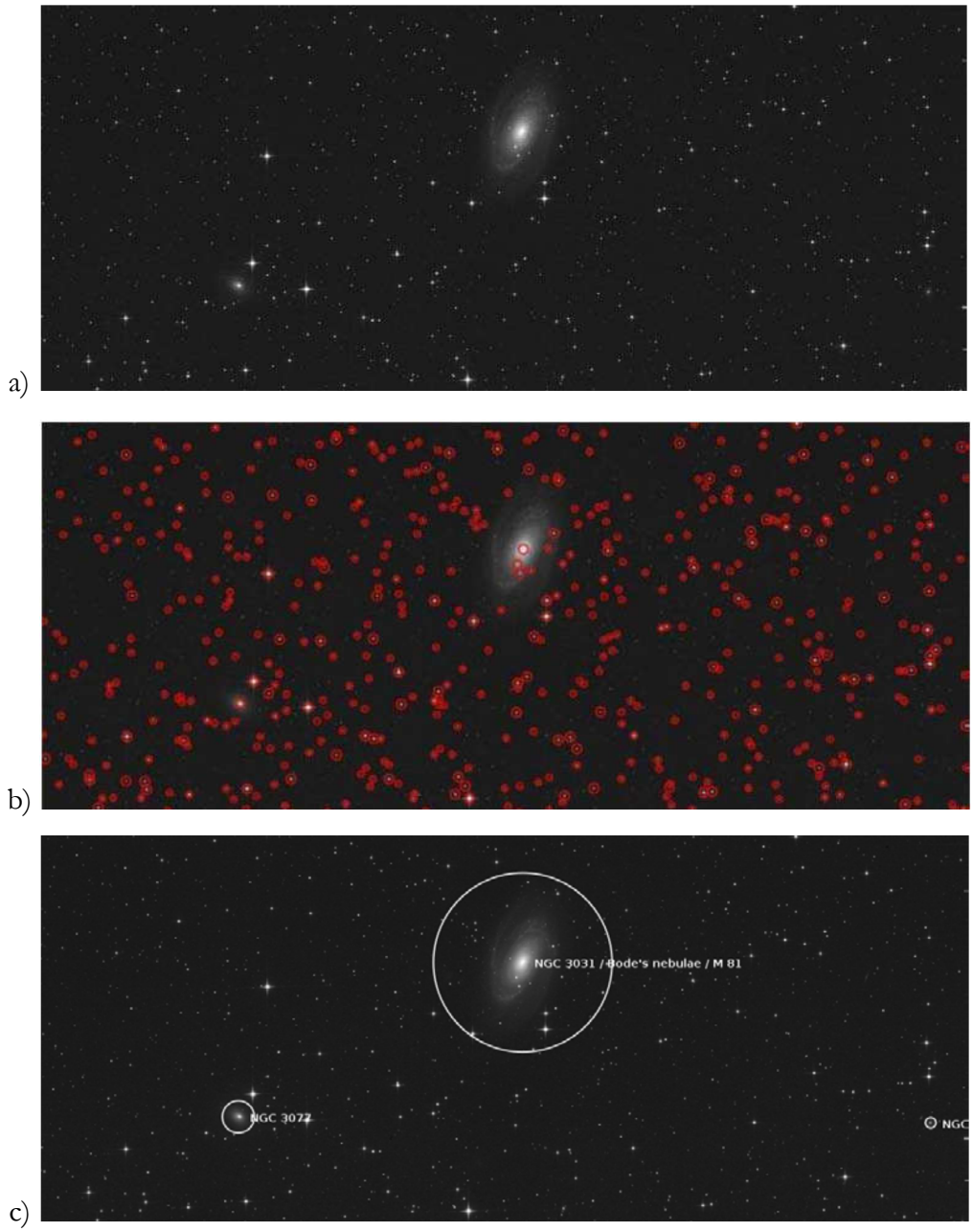

Figure 3.10: The astrometric calibration process takes the input image a) and extracts the sources (red circle) b). The plate solving maps the sources to catalogued sources (e.g. stars) c). Source: [55].

3.5. COORDINATE SYSTEMS

Definitions of coordinate systems used within this thesis are provided within this Chapter. The geodetic coordinate system defines the location on the Earth, which is used to describe the location of the observer (see Section 3.5.1). To define the observers LOS the topocentric reference frame is used, which is described in Section 3.5.3. Measured coordinates of the RSO are transformed from the focal plane into equatorial coordinates using astrometric calibration.

The equatorial coordinate system defines the celestial sphere which is concentric to Earth as illustrated in Figure 3.11 and is described in Section 3.5.2. A more detailed description on coordinate systems and reference frames can be found in Ref. [57].

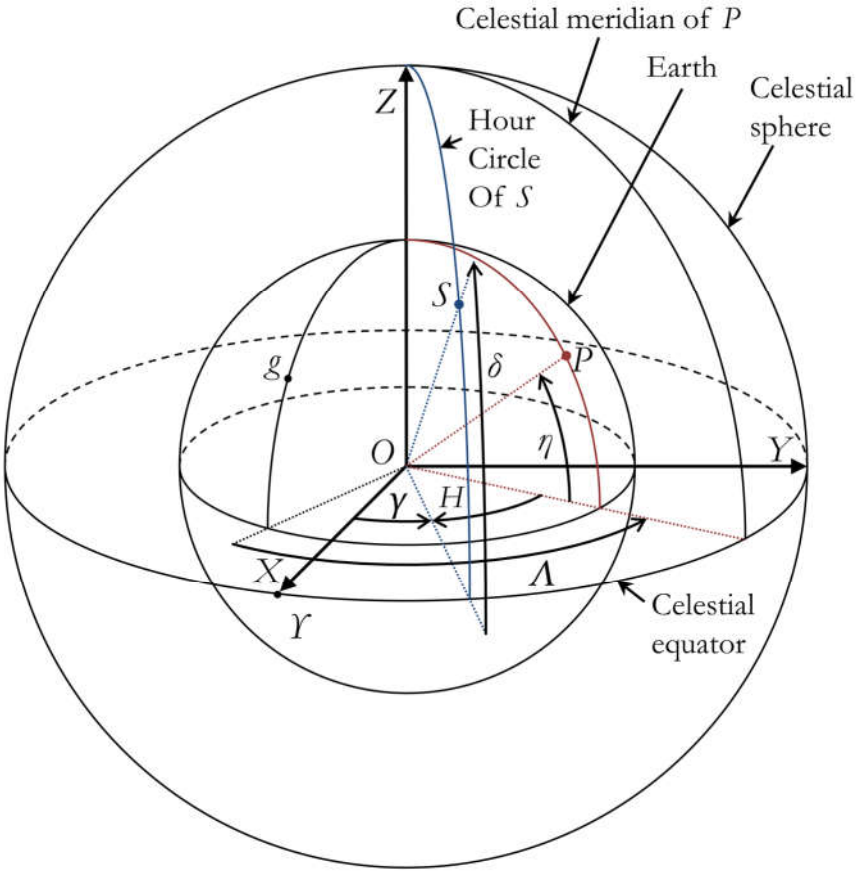

Figure 3.11: Concepts used to describe positions on Earth and on the celestial sphere. g denotes the Greenwhich meridian, N the North pole (rotational axis), P the position of the observer on the Earth surface, S the position of the RSO, Υ the vernal equinox, Λ the geographic longitude, η the geographic latitude, O the Earth center, γ the right ascension, and δ the declination. Adopted from: [57].

3.5.1. GEODETIC COORDINATES

The important parameters of the geodetic coordinate system in Figure 3.11 are as follows: The poles are the points where the rotation axis of the Earth crosses the idealistic Earth sphere, and the great circles passing through the poles are called meridians. The great circle perpendicular to the meridians, halfway between the poles is the equator. The upper part is called North pole (*N*)/northern hemisphere and the lower South pole/southern hemisphere. Geographic longitude *Λ* of a point *P* on Earth's surface is the position on the equator relative to a reference meridian. They are measured positive to the East or negative to the West from the Greenwich meridian *g*. Geographic latitude *η* is measured along the meridian relative to the

Earth's equator, ranging between 0° to 90° for the northern hemisphere and 0° to -90° for the southern hemisphere.

In reality geodetic coordinates are measured on the Earth's ellipsoid. To transform geodetic longitude κ and latitude χ with the height h_{station} above the ellipsoid into Earth Centered Inertial (ECI) reference frame the following equations are used [58].

$$\begin{aligned} X &= (K(\chi) + h_{\text{station}})\cos(\kappa)\cos(\chi), \\ Y &= (K(\chi) + h_{\text{station}})\cos(\kappa)\sin(\chi), \\ Z &= \left(\frac{{R_{\text{Pol}}}^2}{{R_{\text{E}}}^2}K(\chi) + h_{\text{station}}\right)\sin(\kappa), \end{aligned} \tag{3.40}$$

where R_{Pol} is the Earth's polar radius, R_{E} the Earth's equatorial radius, and $K(\chi)$ the prime vertical radius [58], which is given by,

$$K(\chi) = \frac{R_{\text{E}}}{\sqrt{1 - e^2\sin^2\chi}}. \tag{3.41}$$

Hereby, e is the eccentricity,

$$e^2 = 1 - \frac{{R_{\text{Pol}}}^2}{{R_{\text{E}}}^2}. \tag{3.42}$$

3.5.2. EQUATORIAL COORDINATE SYSTEM

The equatorial coordinate system is a celestial sphere with an infinite radius. In the geocentric approach the center is defined by the geo-center. In the topocentric perspective, however, the center is the observer's location at any point on Earth's surface. The celestial poles are defined where the Earth's rotation axis intersects with the celestial sphere. The Earth's north pole defines the Z-axis. The celestial equatorial plane is equal to the Earth's equatorial plane. The X-axis of the system is pointing from its origin to the vernal equinox direction, which is the direction where the Sun's center is located at the first day of spring. The system does not rotate with the Earth's rotation. Hence, the position of distant objects e.g. stars, etc. are projected onto fixed coordinates and measured by two angles, right ascension (RA) and declination (Dec). Right ascension γ encloses the vernal equinox Υ and the point S eastwards on the celestial equatorial plane. The declination δ encloses celestial equator and point S. A transformation of equatorial coordinates (γ, δ) to cartesian coordinates (X, Y, Z) in the ECI reference frame can be calculated as follows [57],

$$\begin{aligned} X &= R_{\text{RSO}}\cos(\delta)\cos(\gamma), \\ Y &= R_{\text{RSO}}\cos(\delta)\sin(\gamma), \\ Z &= R_{\text{RSO}}\sin(\delta). \end{aligned} \tag{3.43}$$

3.5.3. HORIZONTAL COORDINATE SYSTEM

The horizontal coordinate system is a topocentric reference frame, which is centered at the observer. It defines the angular direction relative to the horizon and geographic North pole. The azimuth Ψ is the angle on the horizontal plane between the North pole and the intersection of the meridian of point *S*. Where 0° is North, 90° East, 180° South, 270° West. The altitude α is the angle between the horizontal plane and the point *S*. Where 0° is on the horizontal plane and 90° zenith. Figure 3.12 denotes the definition of the azimuth Ψ and altitude α from the observer to a point *S* in the horizontal coordinate system.

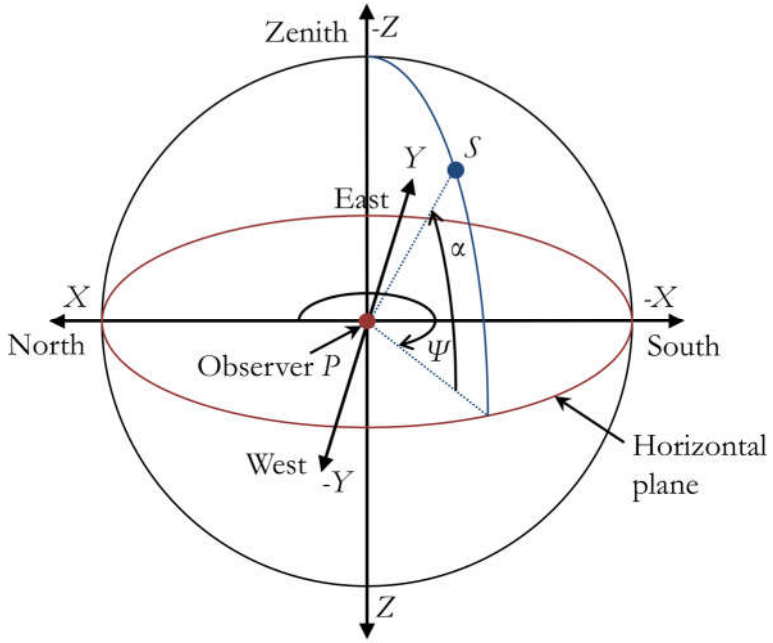

Figure 3.12: The horizontal coordinate system is centered at the observer and referenced to the horizontal plane. The azimuth Ψ is measured on the horizontal plane from the geographic North pole. And the altitude α is the angle from the horizontal plane to the point S. Adopted from: [57].

3.6. ORBIT DYNAMICS

Within this thesis a circular orbit is used to calculate both LEO RSO's velocity and the corresponding apparent angular velocity, see Section 3.6.1. In Section 3.6.2 the orbital elements are introduced briefly. As measurements are compared to TLE orbit predictions, its definition is described in Section 3.6.3.

3.6.1. NEWTON'S LAW OF GRAVITATION

Newton formulated in the gravitational law that two bodies attract each other directly proportional to their masses, and inversely to the square of their distance. The force F between two point masses m_1 and m_2, which are separated by the distance r can be formulated as [57],

$$F(r) = -G\frac{m_1 m_2}{r^2}, \tag{3.44}$$

where, G is the gravitational constant.

In the case of a satellite orbiting around Earth, m_1 is much smaller than m_2. The gravitational acceleration caused by the Earth (with the mass m_{Earth}) on an RSO at distance r from its center of mass can be expressed as [57],

$$a(r) = -G\frac{m_{\text{Earth}}}{r^2}. \tag{3.45}$$

Thus, the required velocity to orbit the Earth can be easily calculated. The first cosmic velocity describes the speed of an RSO necessary to maintain a circular orbit around Earth. The velocity v_{RSO} can be calculated as follows,

$$v_{\text{RSO}} \cong \sqrt{\frac{G \cdot m_{\text{Earth}}}{R_{\text{E}} + h_{\text{RSO}}}}, \tag{3.46}$$

where R_{E} is the Earth's radius and h_{RSO} the orbit height of the RSO above the Earth's surface. Note, this equation however is only valid for circular orbits. In LEO the eccentricity of RSO is almost 0, hence the velocity of LEO RSO can be calculated using Eq. (3.46).

The resulting apparent angular velocity ω_{RSO} of the RSO seen from the observer, is a projection of the velocity v_{Apparent} of the RSO ($\sin(\alpha_{\text{el}})v_{\text{RSO}}$), and depends on the RSO orbit height h_{RSO} (see Eq. (3.27)) and observing elevation α_{el},

$$\begin{aligned}\omega_{\text{RSO}} &= \arctan\left(\frac{v_{\text{Apparent}}}{R_{\text{RSO}}}\right) \cong \frac{v_{\text{Apparent}}}{R_{\text{RSO}}} \\ &= \frac{\sin^2(\alpha_{\text{el}})\, v_{\text{RSO}}}{h_{\text{RSO}}} = \frac{\sin^2(\alpha_{\text{el}})\sqrt{\frac{G \cdot m_{\text{Earth}}}{R_{\text{E}} + h_{\text{RSO}}}}}{h_{\text{RSO}}}.\end{aligned} \tag{3.47}$$

For RSO with velocities of 7.6 km/s at 400 km orbit height, the fact that $\tan(x)$ can be approximated by x, is used. Figure 3.13 shows the calculated apparent angular velocity for LEO RSO under three different observing elevations. A more descriptive form of representation of an orbiting object is introduced in the following Section 3.6.2.

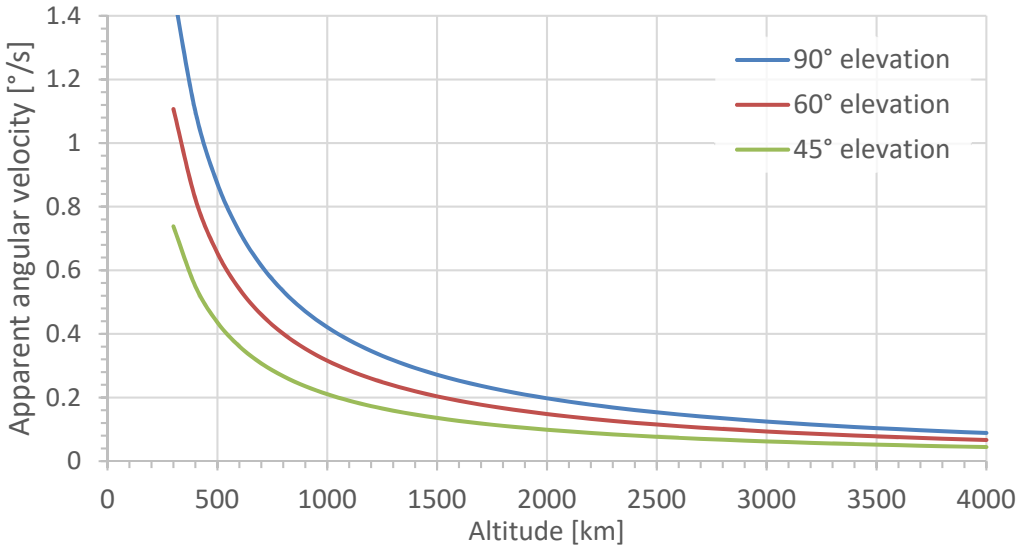

Figure 3.13: The apparent angular velocity depending on the orbit height of an RSO on a circular orbit, as seen from an observer on Earth's surface for three different elevations.

3.6.2. ORBITAL ELEMENTS

A satellite and its central body treated as a two-body problem yields a Keplerian orbit. A bound two-body orbit is unambiguously defined by position and velocity or by the 6 orbital elements;

- a . . . Semi-major axis
- e . . . Eccentricity
- I . . . Inclination with respect to the equatorial plane
- Ω . . . Right ascension of the ascending node
- Θ . . . Argument of pericenter
- u . . . Time since pericenter passage

Hereby a and e define the size and the shape of the orbit, Θ defines the orientation of the orbit in the orbital plane, and u defines the position of the RSO in the orbit at a certain time. The orientation of the orbital plane to the reference frame is defined by I and Ω, [27], [57]. Figure 3.14 illustrates these orbital elements and the range r of the RSO.

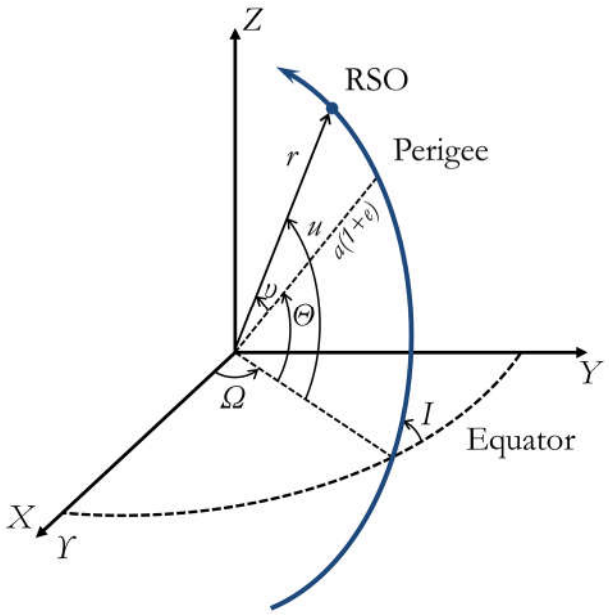

Figure 3.14: The classical orbital elements (a, e, I, Ω, ω, u) and range r of an elliptical RSO orbit (blue). Where υ is the true anomaly and Υ the vernal equinox. Adopted from: [27], [59].

In reality an RSO is subject to numerous external forces besides the gravitational attraction of its central body. These forces are generally referred to as perturbations, since they cause deviations from the ideal two-body case. These perturbations are:

- Atmospheric drag affects all RSO out to a distance of 2000 km orbit height. Note, that the atmospheric drag increases with lower altitudes and, therefore, can be considered as a natural sink for space debris.
- Gravitational force of the central body due to its non-spherical shape and inhomogeneous mass distribution.
- Radiation pressure also plays a role, as photons emitted by the Sun induce a force due to their momentum. The 27-day solar rotation cycle and 11-year Sun spots cycle affect the solar irradiation and modify the force as well.
- Third-body effects: Sun, Moon and other celestial bodies introduce additional forces on the RSO.

In order to perform precise orbit predictions all those perturbations need to be considered and modeled as accurately as possible. This requires additional and highly precise measurements to estimate the additional physical parameters.

Two satellite-based coordinate frames are commonly used [60]:

- The Radial/Along-Track/Cross-Track system (RSW) consists of a radial component $\overrightarrow{r_{\text{Radial}}}$, pointing from the Earth center of mass to the satellite $\vec{r_S}$, and a Cross-Track

component $\overrightarrow{r_{\text{Cross-Track}}}$, which is perpendicular to the orbital plane. Finally, the Along-Track component $\overrightarrow{r_{\text{Along-Track}}}$ is the cross product of the radial and Cross-Track component:

$$\overrightarrow{r_{\text{Along-Track}}} = \frac{\overrightarrow{r_{\text{Cross-Track}}} \times \overrightarrow{r_S}}{\|\overrightarrow{r_{\text{Cross-Track}}} \times \overrightarrow{r_S}\|},$$
$$\overrightarrow{r_{\text{Radial}}} = \frac{\overrightarrow{r_S}}{\|\overrightarrow{r_S}\|}, \qquad (3.48)$$
$$\overrightarrow{r_{\text{Cross-Track}}} = \frac{\overrightarrow{r_S} \times \overrightarrow{\dot{r}_S}}{\|\overrightarrow{r_S} \times \overrightarrow{\dot{r}_S}\|}.$$

- The Normal/In-Track/Cross-Track system (NTW) shares the same definition for the Cross-Track component. However, the In-Track component is defined to be parallel to the spacecraft's velocity vector, while the normal component is the cross product of the In-Track component and the Cross-Track component. Note, that both systems are equal in case of a circular orbit.

An illustration of both systems is shown in Figure 3.15.

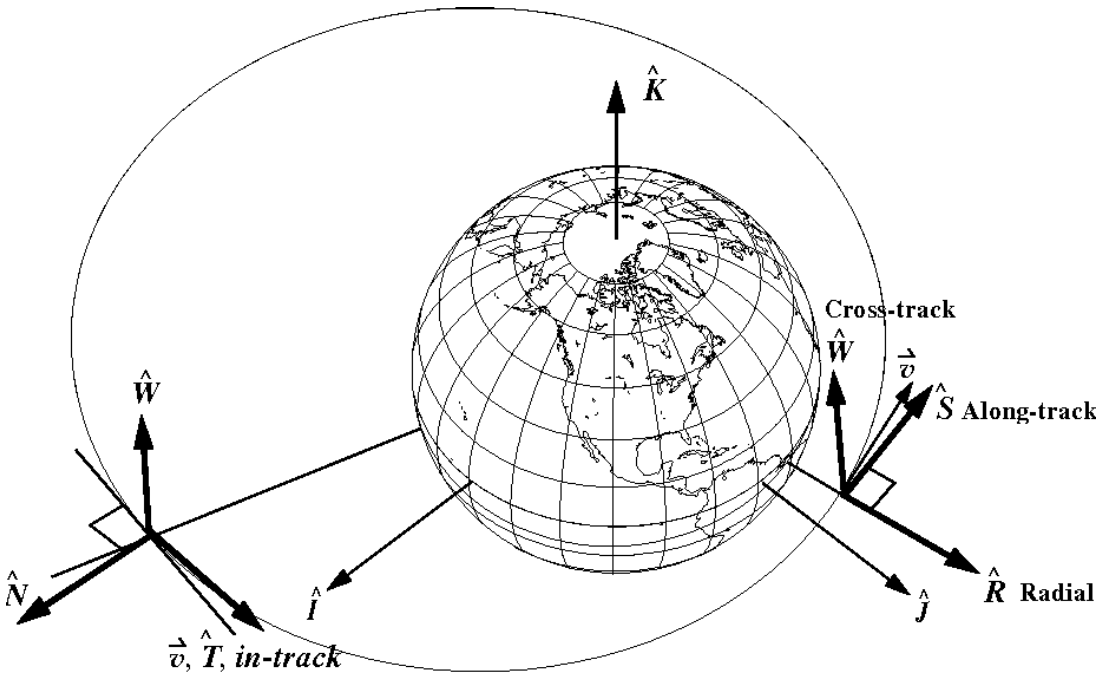

Figure 3.15: An illustration of the RSW and NTW satellite-based coordinate systems relative to the ECEF reference frame (K, I, J). The R-axis points from the Earth center to the RSO, the W-axis is normal to the orbital plane, and the S-axis is normal to the position vector $\vec{v}$. In the NTW system, the T-axis is always parallel to the velocity vector. The N-axis is normal to the velocity vector and the Cross-Track vector, which is not aligned with the radius vector, except for circular orbits, and at apogee and perigee in elliptical orbits (see Appendix 9.7 for definition). Source: [60].

3.6.3. NORAD TLE ORBIT FORMAT

TLE (two-line-element) was defined in the 70's by the NORAD. Historically, the format was defined and designed to work with punch cards. It contains a list of mean orbital elements for a given point in time for Earth orbiting objects. The first line consists of information about classification, launch and the object's ballistic properties. The second line contains information about the orbit. Figure 3.16 shows a TLE data set of the International Space Station (ISS) and Table 3.1 lists each element in the TLE format.

```
1 25544U 98067A 16133.73910976 .00008193 00000-0 12878-3 0 9996
2 25544 51.6441 234.8623 0002754 119.2388 339.6420 15.54576296999465
```

Figure 3.16: Example TLE set of the International Space Station (ISS), NORAD ID 25544.

To propagate TLE sets from USSTRATCOM [15] the analytical theory of the so-called Simplified General Perturbation 4 (SGP4/SDP4) model needs to be used [27]. However, the format's modeling of orbital perturbations provides limited precision. This tends to introduce a divergence between the actual position of the spacecraft and its prediction, which causes relatively large deviations over time. Furthermore, the format does not include any uncertainties of the described orbit. Ref. [27] concludes that for LEO RSO the prediction uncertainty ranges up to several hundred meters. In a publication from Flohrer et al. [5] a snapshot of the TLE catalog was analyzed and the average residuals are listed in Table 3.2. The published TLE orbital predictions have a deviation of up to 517 m for LEO RSO. These high residuals constitute naturally the accuracy of the analysis presented in this thesis, as it relies mainly on TLE information.

Line	Column	Description
1	1	Line number
	3-7	Satellite catalogue number
	8	Classification
	10-17	COSPAR object identifier (year-launch-piece)
	19-32	Element set epoch (UTC), two-digit year, DoY, fraction of day
	34-43	First derivative of the mean motion $\dot{n}$ [rev/day/2]
	45-52	Second derivative of the mean motion $\ddot{n}$ [rev/day^2/6]
	54-61	B^* drag term [Earth radii^{-1}]
	63	Element set type
	65-68	Element number
	69	Checksum
2	1	Line number
	3-7	Satellite catalog number
	9-16	Inclination I [°]
	18-25	Right ascension of ascending node Ω [°]
	27-33	Eccentricity e (leading decimal point assumed)
	35-42	Argument of perigee Θ [°]
	44-51	Mean anomaly M_0 [°]
	53-63	Mean motion n [rev/day]
	64-68	Revolution number at epoch
	69	Checksum

Table 3.1: Definition of each column of the TLE format. Source: [27].

LEO	$I < 30°$	$I > 30°$ $I < 60°$	$I > 60°$
Range error [m]	67	107	115
In-Track error [m]	118	308	517
Cross-Track error [m]	75	169	137

MEO	$I < 30°$	$I > 30°$ $I < 60°$	$I > 60°$
Range error [m]	191	71	91
Along-Track error [m]	256	228	428
Cross-Track error [m]	203	95	114

Table 3.2: Residuals of TLE based prediction uncertainties as a look-up table of averaged results from the analysis of the TLE catalog snapshot of January 1st 2008. Source: [5].

3.7. VELOCITY ABERRATION

The apparent position measured with the optical system differs from the actual position of the RSO. This is caused by both the finite travel time of the light that is scattered/reflected by the RSO and the speed of the RSO. To describe this effect, velocity aberration R_{VelAb} is introduced to describe the distance which the RSO travels while the signal of the object travels to the optical sensor with the speed of light c. To calculate the RSO velocity v_{RSO} a circular orbit is assumed (Eq. (3.46)) which depends on the distance to the Earth's center, $R_{\mathrm{E}}+h_{\mathrm{RSO}}$ [61].

$$R_{\mathrm{VelAb}} = \frac{R_{\mathrm{RSO}}\, v_{\mathrm{RSO}}}{c} = \frac{R_{\mathrm{RSO}}\sqrt{\frac{G \cdot m_{\mathrm{Earth}}}{R_{\mathrm{E}} + h_{\mathrm{RSO}}}}}{c}, \tag{3.49}$$

where R_{RSO} is the distance from the sensor to the RSO, G the Earth's gravity, m_{Earth} the Earth's mass, R_{E} the Earth's radius, and h_{RSO} the orbit height of the RSO.

The angular velocity aberration φ_{VelAb} is the projected velocity aberration, $\sin(\alpha_{\mathrm{el}})R_{\mathrm{VelAb}}$ by the range R_{RSO} and can be approximated to,

$$\varphi_{\mathrm{VelAb}} = \arctan\left(\frac{\sin(\alpha_{\mathrm{el}})\, R_{\mathrm{VelAb}}}{R_{\mathrm{RSO}}}\right) \cong \frac{\sin(\alpha_{\mathrm{el}})\sqrt{\frac{G \cdot m_{\mathrm{Earth}}}{R_{\mathrm{E}} + h_{\mathrm{RSO}}}}}{c}. \tag{3.50}$$

Figure 3.17 shows the time delay of the light from the RSO until the signal reaches the observer depending on the orbit height of the RSO and the corresponding angular velocity aberration under three different LOS elevations.

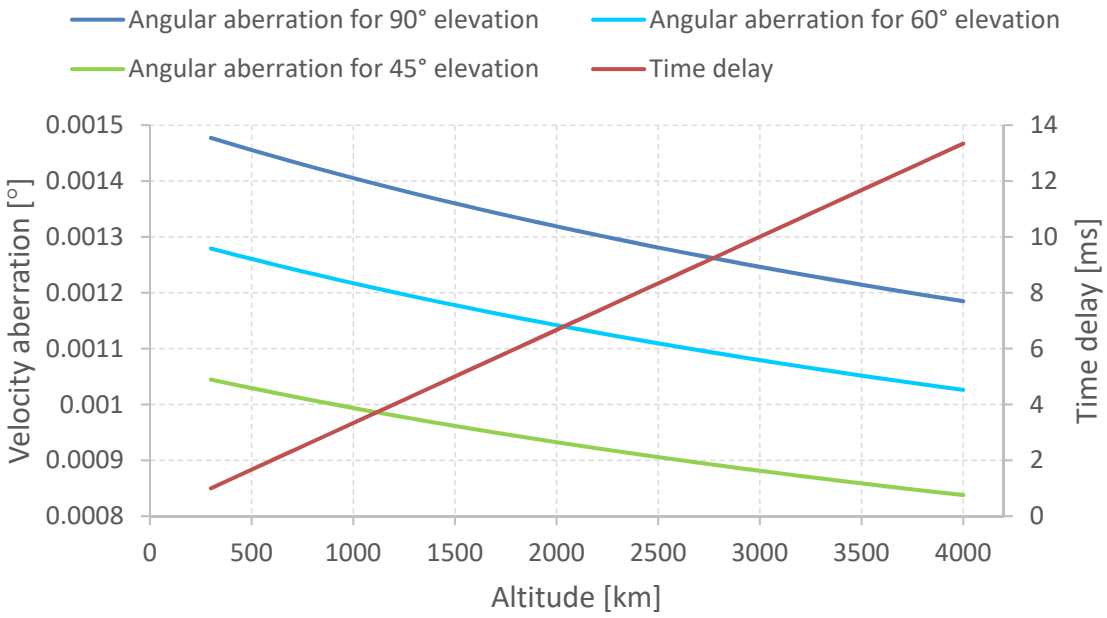

Figure 3.17: Time delay of the signal from the RSO to the observer and the corresponding angular aberration depending on the orbit height of the RSO. The angular aberration is shown for observer's LOS under 45°, 60° and zenith elevations. A circular orbit is assumed for calculations.

Additionally, the motion of the observer with respect to the geocentric center caused by the rotation of the Earth leads to the diurnal aberration. Its maximum is observed at the Earth equator with 0.32 arcsec [27] ($9.0 \cdot 10^{-5}$ °) and can be neglected within this work.

4. AUTONOMOUS PASSIVE-OPTICAL STARING OF LEO FLYING OBJECTS

This Chapter presents how a passive-optical sensor for LEO RSO detection is designed and deployed. Section 4.1 describes the concept, how a passive-optical staring sensor can contribute to an SSA network. Secondly, Section 4.2 shows simulations of the expected sensor performance to obtain preliminary design parameters. Finally, Section 4.3 and 4.4 describe the hard- and software setup of the APPARILLO (AUTONOMOUS PASSIVE-OPTICAL STARING OF LEO FLYING OBJECTS) staring sensor. Results of the automounts operation are presented and compared to simulations in Chapter 5.

4.1. ARCHITECTURAL IDEA

In Chapter 2 it is mentioned, that distance measurements by active optical sensors provide highly precise orbital predictions. However, they rely on existing preliminary orbit predictions in order to track RSO. Hence, any laser ranging sensor is dependent on current existing RADAR sensors. Currently, only the US SSN has a network of sensors to provide the most complete catalog of orbital predictions.

As an alternative, in this section is presented how a low-cost passive-optical sensor can be used to detect unknown objects and deliver a preliminary orbit prediction to hand it over to the active-optical sensor for performing highly accurate distance measurements. This would eventually allow cataloging of this newly discovered RSO. Figure 4.1 illustrates the concept of *stare and chase*: a passive-optical sensor detects new LEO RSO and the obtained angular measurements are used to calculate an initial orbit[G], allowing subsequent tracking and laser ranging to the RSO. The staring starts by continuous observation of the sky by one or more passive-optical sensors. The recorded images need to be processed to identify LEO RSO in

[G] An initial orbit is a rough estimate of the RSO's orbit. It is determined based on less accurate measurements and due to its large uncertainties, the initial orbit is only valid for a short time.

front of the star background. Astrometric calibration using the detected stars as a reference enables to transform the acquired streak's positions into equatorial coordinates. Using the angular measurements and location information of the observer, a preliminary initial orbit determination can be performed, which eventually can be handed over to the laser tracking sensor. Angular measurements of a short arc disallow to fully describe the orbital parameters, which is why the preliminary orbit is valid only locally and for a short time. Hence, the prediction uncertainties will be quite large which is why the laser tracking station needs to perform additional passive-optical closed-loop tracking. Therefore, already existing space debris ranging stations can be used within this proposed sensor network. Ideally, this happens within one pass of the object. Once the RSO can be continuously tracked, laser ranging can be performed which delivers a precise orbit determination and subsequent cataloging of this newly discovered RSO. This concept was already published in 2016 [62] and protected in Germany under a utility patent [63].

A first demonstration of a 'stare and chase' campaign including laser ranging was presented by Steindorfer et al. at the IWF at Graz, Austria in 2017 [64] and showed that a precise orbit determination is possible. However, a network of sensors is required to provide a global coverage of subsequent observations/measurements.

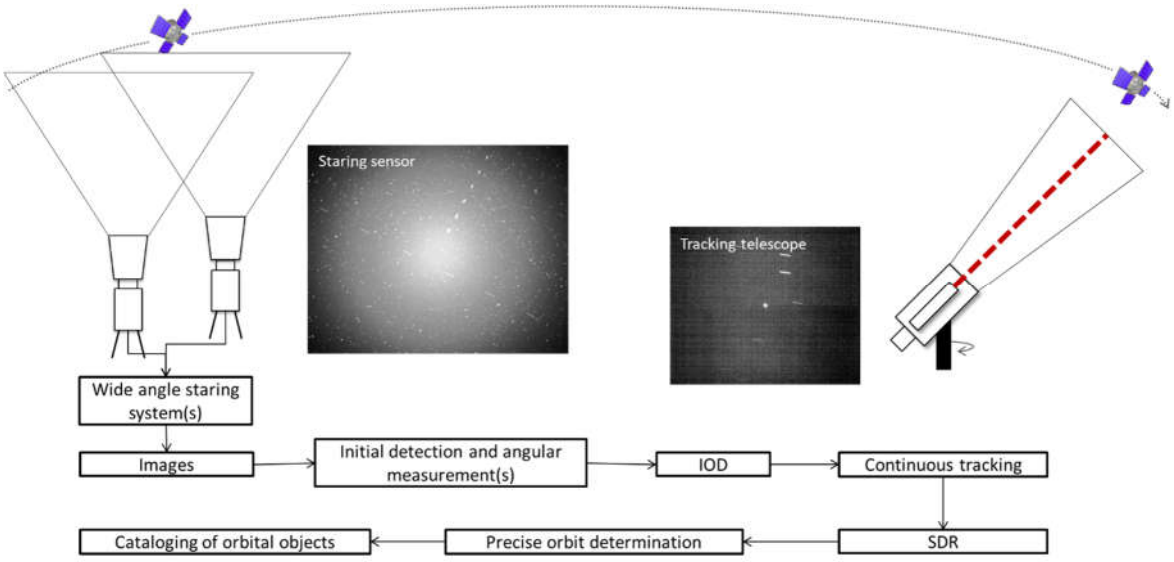

Figure 4.1: Schematic overview of the 'stare and chase' concept for detection and cataloging of unknown LEO RSO.

Within this Chapter, the passive-optical sensor is developed and presented with the goal to detect unknown objects, measure their angular position, export the measurements including necessary meta data, and transfer this to a database or tracking system. To enable an initial orbit determination (IOD) the angular measurements are exported as equatorial coordinates in the TDM (Tracking Data Message) format. To design such a system, simulations are performed in the next Section 4.2.

4.2. SIMULATIONS

Simulations of staring sensors help identify the final technical setup of the staring sensor and to estimate its performance. Two simulation tools are used to determine expected system performance of a passive-optical sensor. One is using the analytical equation presented in Chapter 3.3 (Eq. (3.30)). The second is the non-analytic simulation software PROOF (Program for Radar and Optical Forecasting) which simulates the orbital environment numerically [65]. This way observation campaigns can be simulated in a more profound way providing details that go further than just the detection threshold of the analytic equation.
The simulations help to choose the right camera and lens combination, as well as the optimal observation settings. Additionally, they can be used to give potential performance figures for future optimization (see Chapter 5.3).

4.2.1. PASSIVE-OPTICAL LINK BUDGET

To model expected system performance the theoretical calculation presented in Chapter 3.3 is used. Eq. (3.30) gives the system's sensitivity depending on a dozen of system properties and to estimate d_{RSO}, which gives the minimum detectable diameter of a spherical RSO. First, the set of standard parameters is presented in the next Section 4.2.1.1, followed by a set of parameter studies for various optical parameters of the system in Section 4.2.1.2. Finally, Section 4.2.1.3 shows how observation parameters affect the performance. Additional simulation results can be found in the Appendix 9.1.1.

4.2.1.1. Parameters

For these simulations, system parameters are chosen from the available hardware (see Chapter 4.2.2.5). The pixel size, read-out noise, and QE are given by the properties of the camera. For front illuminated silicon photodetectors, the QE averaged over a broad spectrum is 0.55 [45].

While aperture diameter, *f*#, and optical transmission are given by the optical properties of the lens. A broadband coated optical lens typically shows a transmission of about 0.85 [66]. The atmospheric transmission is calculated from the visibility, station height, and observing elevation for a wavelength of 550 nm, where the camera is most sensitive. A horizontal (α_{el}=0°) visibility of 10 km is a typical value for clear sky conditions at the system's location for central Europe. An exposure time of 1 s is used for observations in staring mode to ensure that LEO RSO are recorded as streaks and stars as points. For the *SNR* threshold a value of 3 is used, which is sufficient to prevent any false detections of a simple image processing method. The average reflectivity ρ_{RSO} of space debris is 0.175 [45]. For the simulations an orbit height of 800 km is chosen, as it is of special interest due to its dense debris population. Due to the 'unideal' location of the sensor in the city a background brightness of 17.5 mag/arcsec² is used to calculate the background noise [47]. For LOS elevation zenith is chosen, which promises the smallest detection threshold due to higher atmospheric transmission and smallest range. The phase angle for this constellation is chosen as 75° [67]. The FWHM of PSF is assumed to be 2 px, which results in a coupling coefficient of τ_{px} = 0.2. Table 4.1 lists all simulation parameters for their use in Eq. (3.30), including their typical values. If not stated otherwise, these values are used for graphs shown in this Chapter.

Parameter	Value	Description
QE (eff.)	0.55	Quantum efficiency
τ_{optic}	0.85	Transmission of the optical system
τ_{atm}	0.73	Transmission of the atmosphere
V [km]	10	Visibility
d_{optic} [m]	0.1	Diameter of the optical aperture
y_{px} [µm]	12	Pixel size
N_{read} [e$^-$]	15	Read-out noise electrons of the image sensor
f' [m]	0.2	Focal length of the optical system
$FWHM$ [px]	2	FWHM of the PSF
τ_{px}	0.20	Pixel coupling efficiency
M_b [mag/arcsec^2]	17.5	Background brightness
SNR	3	Signal to noise ratio
h_{RSO} [km]	800	Orbit height of the RSO
ϱ_{spec}, ϱ_{diff}	0.175	Specular and diffuse reflectivity of the RSO
ψ	75°	Phase angle between the RSO, the observer and the Sun
$f\#$	2	f-number of the optical system
t_{exp} [s]	1	Exposure time
α_{el} [°]	90	Vertical/elevation angle between horizon and observer's line of sight
$h_{station}$ [m]	500	Station height

Table 4.1: List of parameters and their values used for the calculation of the passive-optical link equation.

4.2.1.2. Optical parameters

Graphs in this Section show the detection threshold or minimum detectable RSO diameter of the system for various optical parameters. The two main properties of an optical system are the diameter of the aperture and the focal length. This can also be expressed in terms of f-number and aperture diameter, or f-number and focal length. The former is commonly used for telescopes, as this defines the system's sensitivity, and the latter is commonly used for imaging camera systems, as it defines FOV or angular resolution. For this work, mainly commercial off-the-shelf (COTS) cameras lenses are used, and Figure 4.2 shows the detection threshold depending on aperture diameter and f-number under three different background illuminations that represent a dark night sky with no light pollution with M_b = 21 mag/arcsec^2 [48], a bright

night sky with M_b = 17.5 mag/arcsec² [47], and a city with light pollution with M_b = 15 mag/arcsec² [49].

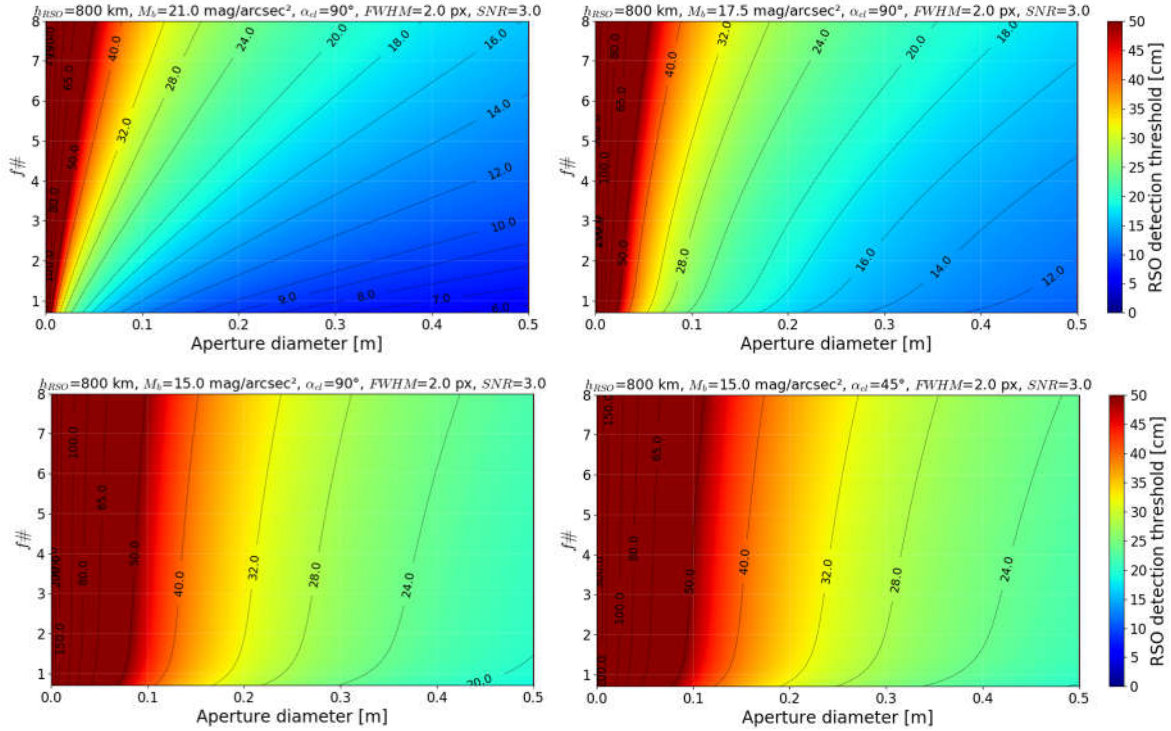

Figure 4.2: The detectable RSO size in 800 km orbit height with background illuminations of 21 mag/arcsec² (top left), 17.5 mag/arcsec² (top right), 15 mag/arcsec² (bottom left), and under 45° at 15 mag/arcsec² (bottom right) depending on optical system's diameters and f-number.

It can be seen that with larger aperture diameter the detection threshold drops. Due to the larger pixel-FOV at smaller f-numbers more background noise is collected by the system. This results in more linear detection threshold contours at lower background brightness. This implies, that a smaller f-number at the same aperture diameter is less beneficial due to high background illumination. For an optical system with 10 cm aperture and a f-number of 2, which is used in the experimental realization, the detection threshold under zenith is d_{RSO} = 18.5 cm with M_b = 21 mag/arcsec², d_{RSO} = 27 cm with M_b = 17.5 mag/arcsec², d_{RSO} = 46 cm with M_b = 15 mag/arcsec², and under 45° elevation it is d_{RSO} = 48.5 cm where M_b = 15 mag/arcsec². This shows that depending on the actual atmospheric transmittance and background brightness the system's sensitivity varies about 50%. To ensure the same detection threshold under 17.5 mag/arcsec² background brightness as under 21 mag/arcsec² background brightness, the aperture diameter needs to be two times larger at a f-number of 2.

Depending on the optical quality of the lens, incoming light of a single point source is spread across several pixels, thus less signal is collected by a single pixel (Eq. (3.29)). Figure 4.3 shows how the *SNR* is affected by *FWHM* of the PSF depending on the RSO diameter. It can be seen that the *SNR* increases by a factor of 5 between a *FWHM* of 2 px and 0.5 px or a factor of three between 1.5 px and 0.5 px. A *FWHM* of 0.5 px implies that effectively all the signal is collected by the pixel. The optical quality of three lenses are investigated under Section 4.3.3. in more detail.

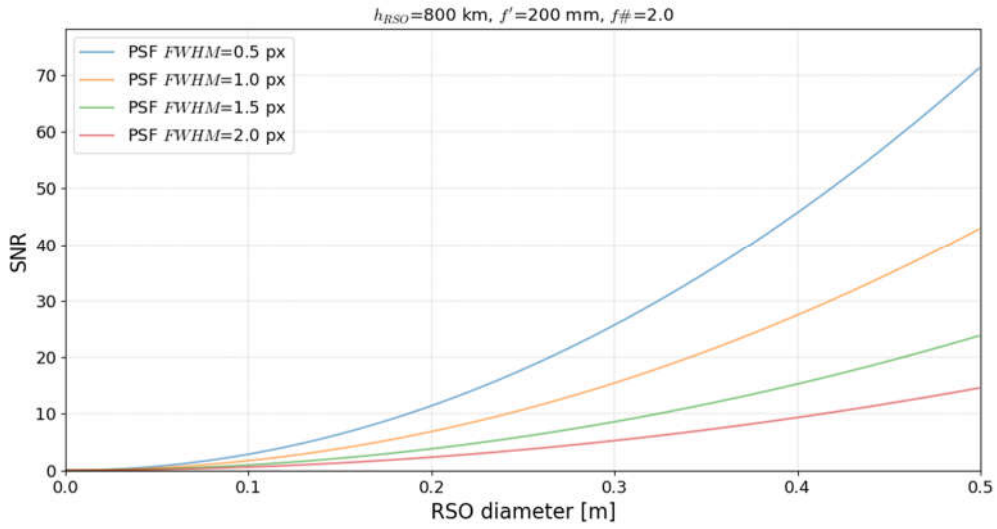

Figure 4.3: The SNR depending on RSO diameter with four different FWHMs of the PSF.

Depending on the chosen *SNR* threshold to extract an object in the digital image, the detection threshold of an RSO is improved dramatically, see Figure 4.4. Both parameters, *SNR* and aperture diameter equally contribute to the detection threshold. In Figure 4.4 it can be seen that this relation is linear, thus, a reduction of the *SNR* threshold of ten, is equivalent to an aperture diameter increase of ten. For example, in case of a 10 cm aperture diameter, the detectable size of an RSO is 12 cm for an *SNR*=0.5, 22 cm for an *SNR*=2, 38 cm for an *SNR*=6 and 49 cm for an *SNR*=10. However, the majority of parameters like *SNR* detection threshold, *FWHM* of the PSF, background brightness, transmission, or pixel size can only be optimized up to a certain point using COTS components, while the main performance gain is achieved by a large aperture diameter.

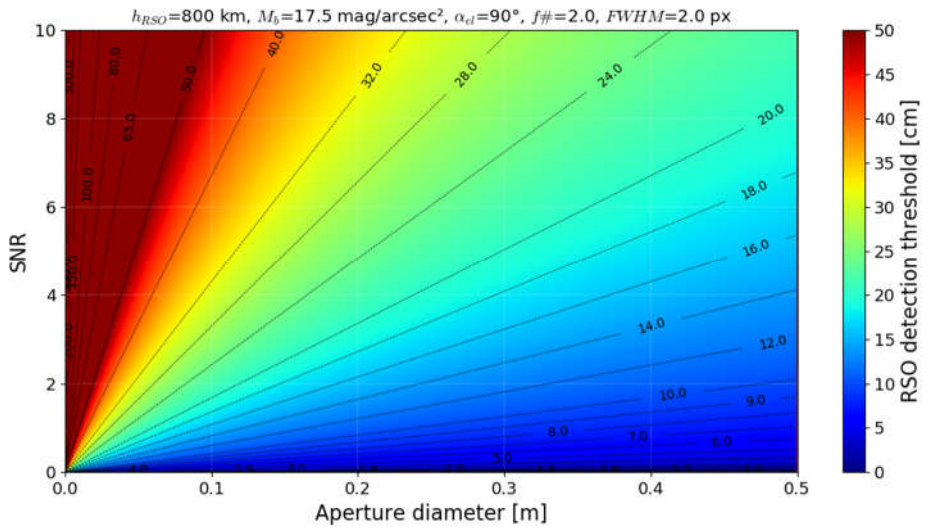

Figure 4.4: The minimum detectable RSO diameter depending on the SNR detection threshold and aperture diameter.

4.2.1.3. Observing parameters

Beside the optical parameters, Eq. (3.30) incorporates the observing elevation as well. The elevation α_{el} affects the range to the RSO (Eq. (3.27)), atmospheric transmission (Eq. (3.36)), and apparent angular velocity (Eq. (3.47)). The former two reduce the sensitivity at lower elevations, while the latter improves it. Figure 4.5 shows the RSO detection threshold as a function of the orbit height and elevation under optimal and sub-optimal conditions. It can be seen that the best performing observation condition is zenith under any circumstances. The RSO detection threshold becomes slightly larger for elevations below zenith increasing steeper towards smaller elevations, see Figure 4.5 (top). Hence, a smaller elevation is less beneficial under sub-optimal observation conditions, where the atmospheric transmission has a larger impact. For a sub-optimal site, in which the presented system is operated, the elevation should not be smaller than about 45°. The impact on the detection threshold is about 8.5% larger at 45° than on zenith (d_{RSO}=29.5 cm vs. d_{RSO}=32 cm at 1000 km orbit height). However, under optimal observation conditions the detection threshold is almost constant down to a LOS elevation of 30°. In this case, choosing a smaller LOS elevation of the sensor is highly recommended as a larger orbital volume can be observed at the same detection threshold, which results in more detected objects.

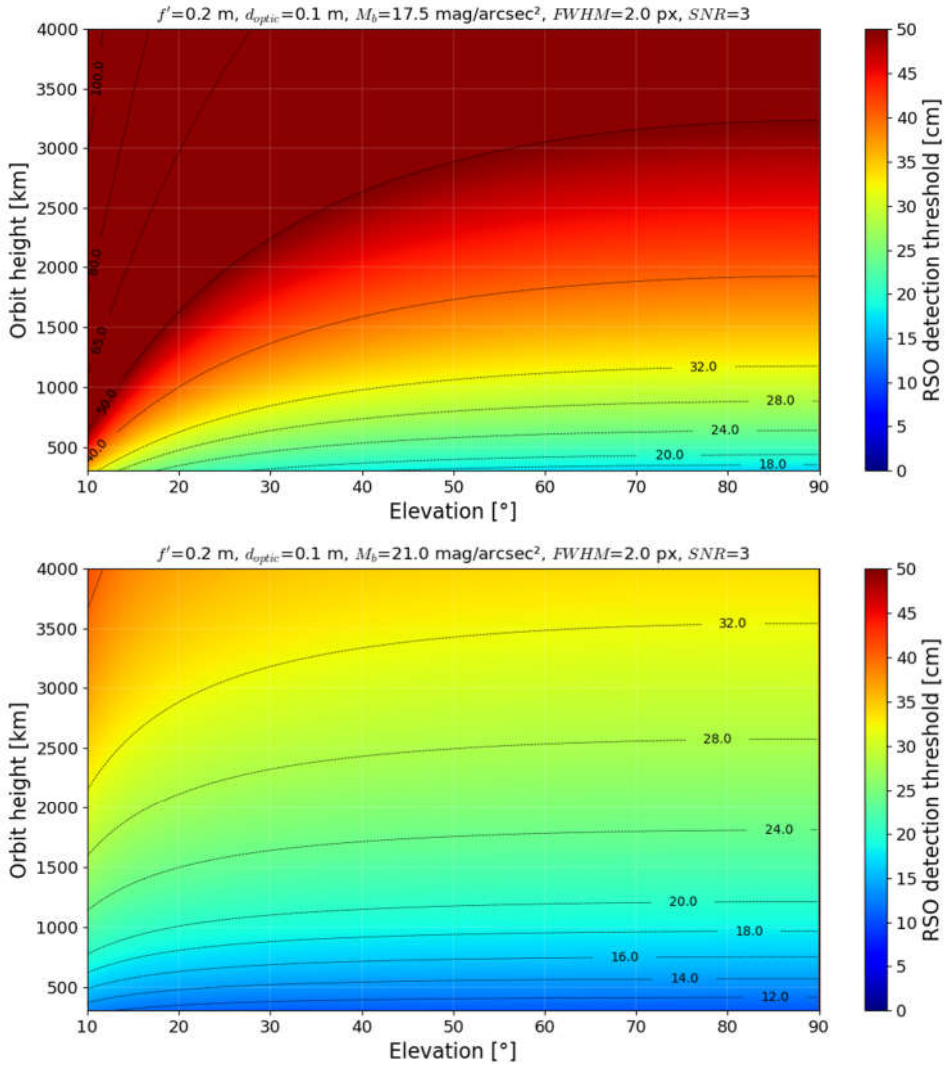

Figure 4.5: The detectable RSO diameter depending on the LOS elevation and RSO orbit height for a system with 10 cm aperture and an f# of 2. The top graph is simulated for sub-optimal conditions with a background brightness of 17.5 mag/arcsec² and a station height of 500 m. While the bottom graph shows the same simulation under optimal conditions with 21 mag/arcsec² background brightness and 2 km station height.

Naturally, a higher orbit results in smaller signal, thus the detection threshold becomes larger as shown in Figure 4.5. A larger variety how different parameters affect the system performance are shown in Appendix 9.1.1.

Note, that this simulation does not provide a rate of objects that can be detected. It is expected that a wider FOV covers a larger orbital volume and therefore detect more objects. Similar result is expected by observing at smaller elevation as this covers a larger orbital volume. For these scenarios PROOF simulations provide more information, which are presented in the following Section 4.2.2.

4.2.2. PROOF SIMULATIONS

To model geometric and radiometric conditions for an optical sensor ESA's software tool PROOF (Program for Radar and Optical Observation Forecasting) can be used. Originally, PROOF was developed to validate ESA's MASTER (Meteoroid and Space Debris Terrestrial Environment Reference) model but it proofed to be a versatile tool to simulate ground- as well as space-based optical and RADAR sensors [65]. PROOF and MASTER were developed at the Institute of Space Systems at the TU Braunschweig, Germany on behalf of ESA [68]. PROOF uses the European orbital population model MASTER and simulates an arbitrary population to verify the performance of a given optical or RADAR sensor [65]. PROOF simulates each object orbiting around Earth with statistical distributed object properties given by the MASTER model.

First, the simulation software calculates which RSO are crossing the sensor's FOV for a given observation. Then, a verified optical model, developed by AIUB (Astronomical Institute of the University of Bern) is used to determine which of these objects is detected by the given sensor. Due to the working principle it is only able to simulate a fixed system configuration during a specific observation period. This makes it less practical for determining optimal system parameters, as each configuration needs to be simulated individually over a large observation window to provide general performance figures. On the other hand, it provides more performance figures like the relation between detected and crossing RSO or detection rates over time depending on RSO diameter. A detailed description of PROOF and MASTER can be found in Ref. [68] and [65]. Next Section 4.2.2.1 describes how simulations are configured, followed by the simulation results in Sections 4.2.2.2 to 4.2.2.5.

4.2.2.1. Simulation setup

The presented simulations are performed using PROOF 2009. It has three modes; a deterministic, a statistical, and a hybrid. The deterministic mode uses actual predictions, like TLE, to simulate RSO orbits. The statistical mode uses the MASTER model to randomly simulate RSO according to their modeled distribution and size. Only this mode provides RSO geometries and allows to simulate objects smaller than 10 cm, which is why it is used for following simulations. The hybrid mode is a mixture between deterministic and statistical mode. For the simulations, observation time, and duration need to be specified as well as sensor details. The sensor can be either ground- or space-based, here ground-based optical is used to simulate the staring sensor. The optical model is based on visible wavelength only. The

utilized optical model takes the quantum efficiency of the camera, spectral atmospheric absorption and the *FWHM* of the PSF into account.

The simulation does not include any weather constraints, and similarly to the passive-optical link budget equation, optical aberrations are not considered. Further simplifications are a *FWHM* independent of the PSF from the image radius, and exclusion of vignetting. Thus, for the actual optical system a lower performance than in the simulations is expected.

Parameter	Value
Observation dates	2013.04.01 – 2013.04.10 2014.04.01 – 2014.04.10 2015.04.01 – 2015.04.10
Duration	11 h per day
Min. object size	0.1 m
Max. object size	100 m
Min. range	200 km
Max. range	4000 km
Geodetic latitude	48.78253°
Geodetic longitude	9.19641°
Geodetic altitude	355 m
Elevation	90°
Exposure time	1s
Gap time	4 s (FLI cameras) 2 s (ZYLA camera)
FWHM of the PSF	2 px
SNR Threshold parameter	3

Table 4.2: List of general simulation parameters to perform simulations of a passive-optical sensor with PROOF.

For better comparison all simulations are performed using the same settings, only varying those parameters which are compared. For the time period April is chosen as it is close to the vernal equinox at 21st of April, which ensures a constant detection rate over the entire night for zenith LOS (see Section 4.2.2.5). To reduce statistical fluctuations, simulations are averaged for

the first ten nights in April for three different years (see Table 4.2). The sensor is setup with a fixed LOS to zenith and the exposure time is set to 1 s, which is identical to the chosen value in the real system. For the simulations the orbit height regime from 200 km to 4000 km is simulated. The minimum object size is set to 0.1 m for small aperture systems and 0.01 m for large aperture systems. As location the DLR (German Aerospace Center) observatory UFO (UHLANDSHÖHE FORSCHUNGSOBSERVATORIUM) is chosen to allow comparison between simulations and measurements (more on the operational observation location is given in Section 4.3). The *SNR* detection threshold is assumed to be 3 and the *FWHM* of the PSF is set to 2 px for each simulated system. The gap time between frames is used as 4 s for the CCD cameras and 2 s for CMOS cameras. The general simulation parameters are listed in Table 4.2. The sensor specific settings are selected according to the sensor hardware, in this case the ANDOR ZYLA is selected as the standard camera. Table 4.3 lists the relevant parameters of the cameras used for simulation with PROOF in this Chapter. Note, that in the actual observations the FLI cameras were employed.

Camera	**ZYLA***	**FLI PL09000**	**FLI PL16803**	**CMOS**
Product name	ANDOR ZYLA 5.5	FLI PL09000	FLI PL16803	GS3-U3-41C6NIR
Sensor	sCMOS: Fairchild	CCD: On Semi KAF-09000	CCD: On Semi KAF-16803	CMOS: CMOSIS CMV4000
Sensor area [mm x mm] (width x height)	17.2 x 14	36.8 x 36.8	36.8 x 36.8	11.3 x 11.3
Pixels [px]	2650 x 2160	3056 x 3056	4096 x 4096	2048 x 2048
Pixel size [µm]	6.5	12	9	5.5
Dark noise [e^-/s]	0.14	0.02	0.005	125
Read noise [e^-]	2.6	15	14	13
Gap time	2	4	4	2

Table 4.3: List of camera properties which are used for PROOF simulations. (denotes the standard camera used for PROOF simulations) [69], [70], [71], [72].*

The simulations return properties of detected and crossing objects like RSO diameter, range, orbit information, and type of object. This data is used to evaluate the detectability depending on the range. Additionally, a histogram of the detected and crossing objects depending on the

RSO diameter is returned by the simulations. Using this data the detection rate is calculated of simulated observations.

First, a validation of the circular orbit assumption through PROOF is performed. Figure 4.6 shows the angular velocity for zenith LOS of simulated RSO and the theoretical curve under the circular orbit assumption from the previous Chapter 3.6.1, see Eq. (3.47). Except a few outliers, which have an eccentric orbit, simulated angular velocities of crossing RSO match the theoretical curve very well, verifying the validity of the circular orbit assumption used through all analysis in this thesis.

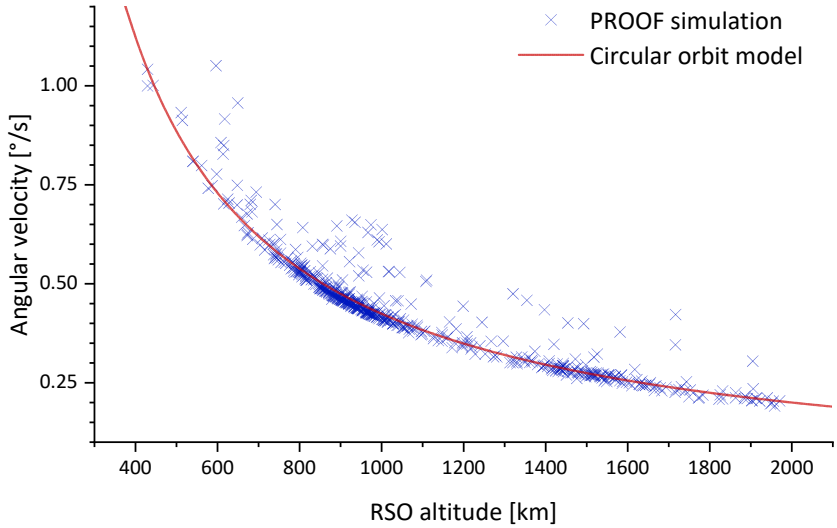

Figure 4.6: The angular velocity depending on RSO altitude of simulated objects by PROOF (blue cross) compared to the theoretical calculation of a circular orbit (red line), see Eq. (3.47). For the data simulated by PROOF RSO altitude denotes the altitude at time of closest approach (TCA).

4.2.2.2. Optical parameter

In this section, among the optical parameters, focal length and aperture diameter are varied. In the first simulation shown in Figure 4.7, the detection rate is studied depending on focal length with a fixed aperture diameter of 40 mm (blue) or a fixed focal ratio (red). The respective aperture diameter and FOV are listed in Table 4.4 while the ANDOR ZYLA is used as a camera.

***f'* [mm]**	25	50	75	100	125	150	175	200
d_{optic} [mm] @ *f#* = 1.25	20	40	60	80	100	120	140	N/A*
***FOV* [°]**	47.92	25.06	16.85	12.68	10.16	8.47	7.27	6.36

Table 4.4: Properties of the optical systems used for PROOF simulations presented in Figure 4.7 and Figure 4.8. (System configuration was not simulated)*

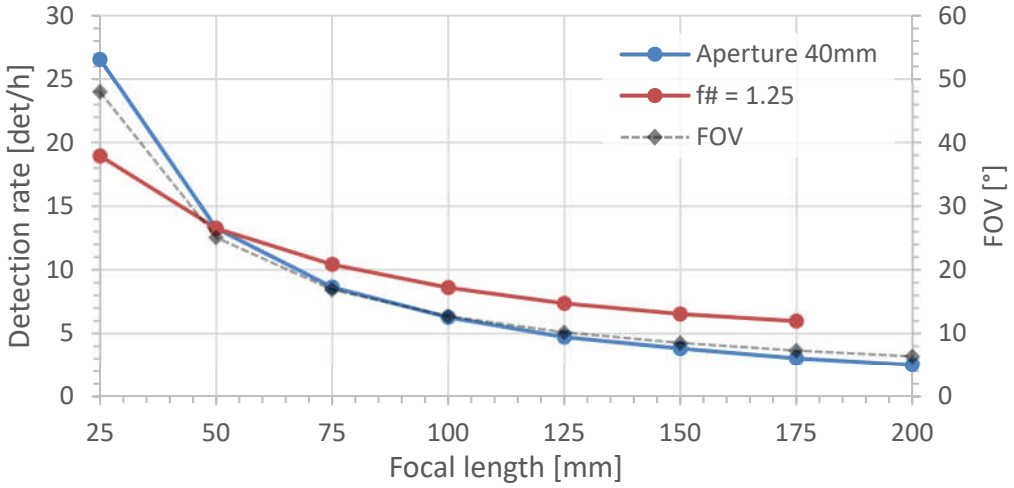

Figure 4.7: Detection rate depending on the optical system's focal length for a fixed optical aperture of 40 mm (blue) and a fixed f-number of 1.25 (red). The dashed line (grey) shows the corresponding FOV on the right axis.

For smaller focal length the FOV becomes larger. Consequently, a larger orbital volume is scanned and more objects can be detected within the same timeframe, as indicated by the increasing detection rate. The larger the aperture at the same focal length, the larger is the detection rate. Hence, the detection efficiency becomes higher for a larger aperture. This is shown in Figure 4.8. For systems with a fixed f-number, a longer focal length results in a larger aperture, hence a higher detection efficiency is observed. For systems with a fixed aperture diameter, the detection efficiency becomes lower for longer focal length, as this reduces the dwell time of the RSO on a single pixel.

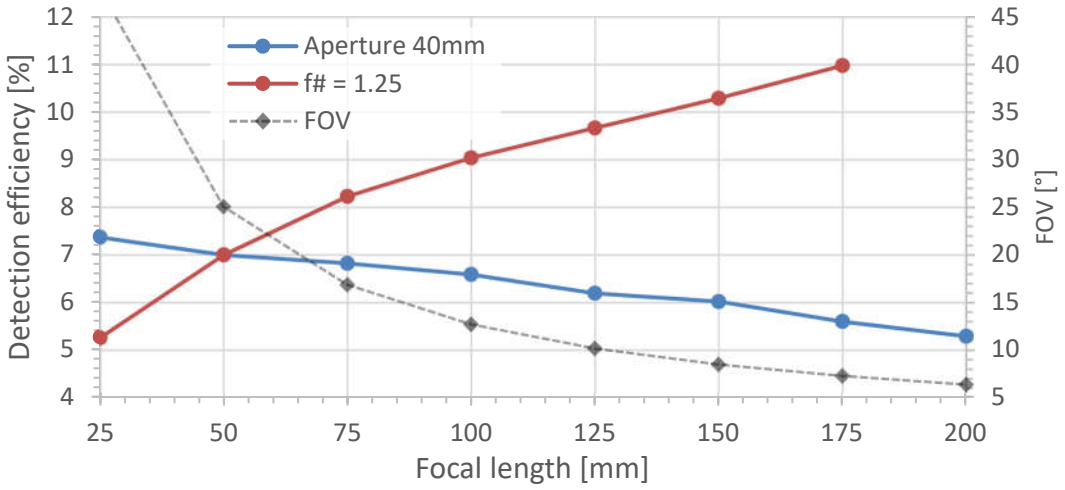

Figure 4.8: Detection efficiency depending on the focal length for a fixed optical aperture of 40 mm (blue) and a fixed f-number of 1.25 (red). The detection efficiency is the ratio of the detected RSO to the RSO crossing the FOV of the system. The dashed line (grey) shows the corresponding FOV on the right axis.

The total numbers of simulated RSO by PROOF depends on the actual RSO density, which is not uniform over the size nor the orbit height. This is why in the following the detection efficiency is calculated by relating detected to crossing objects depending on RSO diameter. In particular, this provides a metric for detectability of certain RSO size. Moreover, considering the experimental realization, a higher detection efficiency is the preferred property. For that, the detection efficiency in dependence of the RSO diameter is now analyzed.

Figure 4.9 shows exemplarily crossing and detected RSO by a PROOF simulation across one day depending on range and RSO diameter. The most obvious feature of this graph is that RSO smaller than 0.4 m in diameter clearly remain mostly undetected. Another characteristic is the correlation between RSO diameter and orbit height. For smaller diameter the density is highest around 800 km, while larger RSO are distributed more even across the ranges. When analyzing against RSO diameter, this correlation has to be kept in mind.

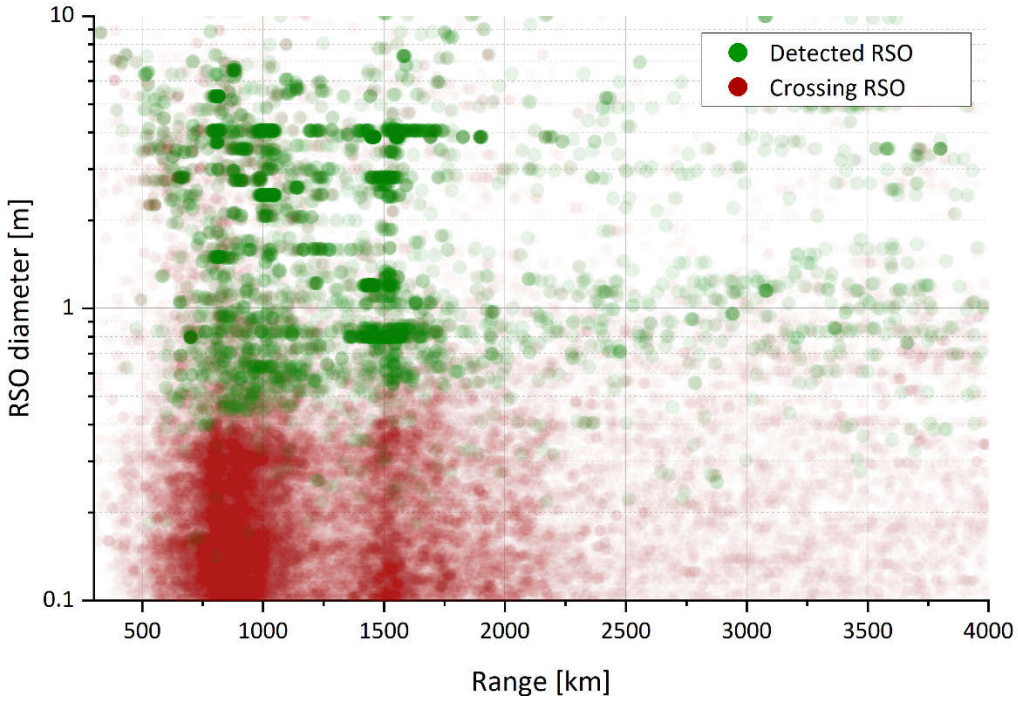

Figure 4.9: Detected RSO (green) and crossing RSO (red) depending on range to the RSO and RSO diameter. PROOF simulation of a single observation night of a FLI PL16803 camera and 135mm f2 lens with zenith LOS.

Note, that there is a distinct line between detected and crossing RSO which seems to be independent of orbit height. This line is located at about 0.4 m RSO diameter and later in Figure 4.13 is shown that 5% detection efficiency corresponds to this detection threshold. In contrast, the analytic link budget predicted a dependency on orbit height and resulted in a detection threshold that is 20% smaller at 800 km orbit height, see Figure 4.5 (top). The prediction from PROOF simulates the orbital environment more profoundly including the proper size density and actual illumination duration of RSO depending on orbital height. Thus, the vast majority of RSO at lower orbit height are counted as crossing but are not detected.

Figure 4.10 shows the detection efficiency of three systems with a fixed aperture diameter of 100 mm. The detection efficiency rises with larger RSO diameter up to 1 m, from then on it varies with a maximum of 45%. This results from the previously mentioned fact that the larger RSO diameter populate more often higher orbits, which reduces the detectability, and due to high background illumination during dusk and dawn. Note, that following the Poissonian error estimation $1/\sqrt{n}$, the error of the given detection efficiency rises with larger RSO diameter as the rate of absolute detections decreases with larger RSO diameter. Due to this systematic

statistical 'noise' the simulation results shown in this Chapter need to be compared relative to each other.

Figure 4.10 shows that the detection efficiency rises at the very last for the systems with longest focal length, as expected from the above discussion. This is in line with previous simulations in Section 4.2.1 which have shown larger RSO detection threshold for a larger focal length (see Figure 4.2). Still, the overall difference between the three systems is relatively small with a detection efficiency of 10% at 33 cm RSO diameter for *f'*=100 mm compared to 43 cm for 200 mm focal length. The small difference results from the fact that the aperture diameter has the strongest contribution to the detection efficiency, which has been kept constant for these three systems.

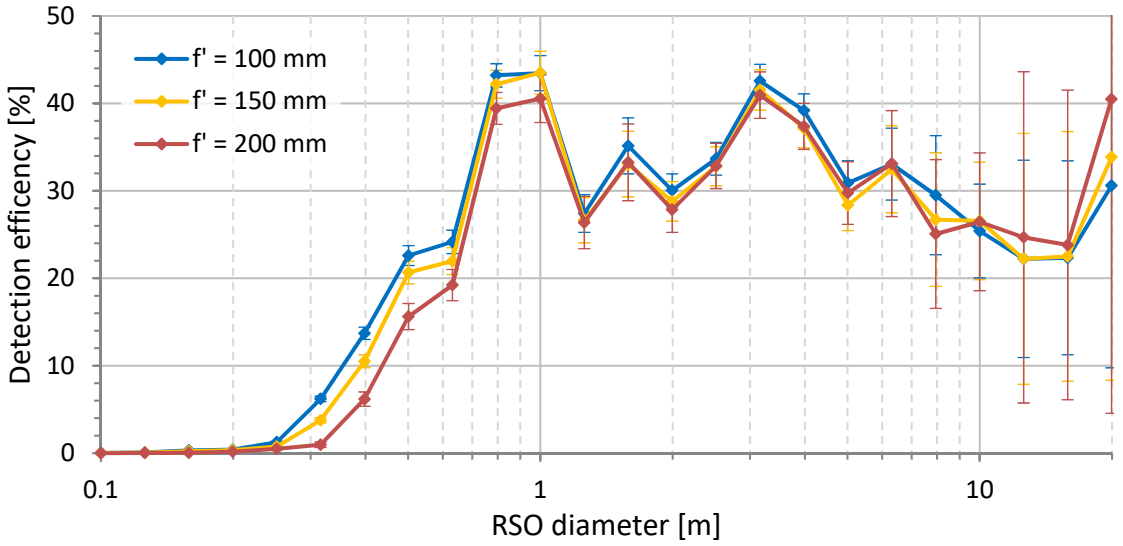

Figure 4.10: Detection efficiency depending on the RSO diameter for systems with a fixed aperture diameter of 100 mm and focal lengths of f' = 100 mm (blue), f' = 150 mm (yellow), and f' = 200 mm (red).

As the dependency on the aperture diameter is expected to be decisive, now the simulation varies the aperture diameter (AD) while leaving the system's focal length fixed. In Figure 4.11 it can be seen that the aperture diameter has a large effect on the detection threshold, in accordance with previous simulations in Section 4.2.1. It can be seen that the detection efficiency becomes clearly higher for smaller RSO diameter as the AD increases.

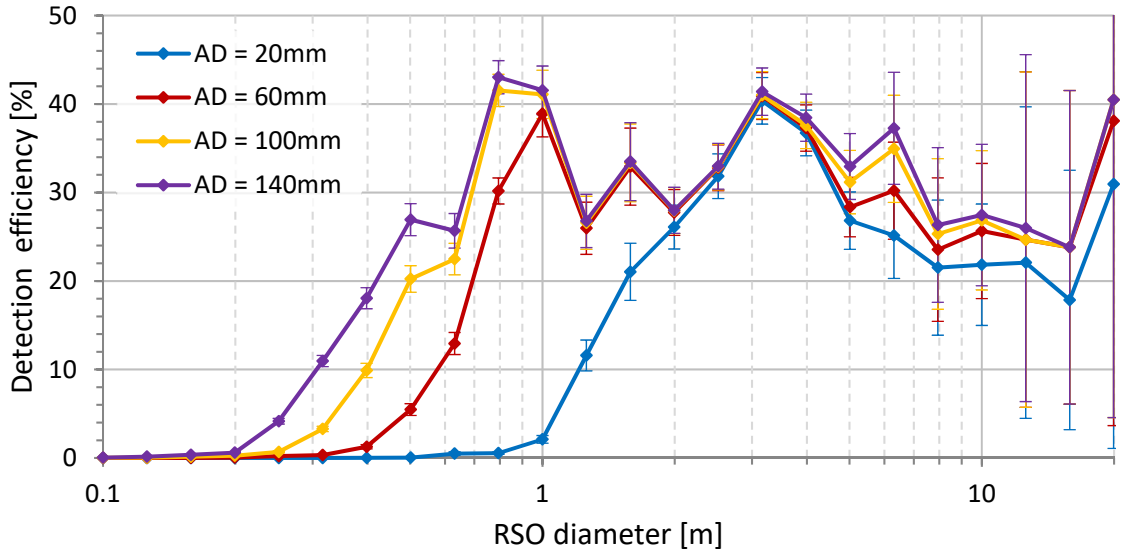

Figure 4.11: Detection efficiency depending on the RSO diameter for optical systems with a fixed focal length of 200 mm and aperture diameter of d_{optic} = 20 mm (blue), d_{optic} = 60 mm (red), d_{optic} = 100mm (yellow), and d_{optic} = 140 mm (purple).

For 100 mm aperture diameter and 200 mm focal length a detection threshold of 27 cm RSO diameter is calculated for 800 km orbit height (and d_{RSO}=32 cm in 1000 km) previously, while the PROOF simulation for the same system (yellow curve in Figure 4.11) crosses the 5% detection efficiency at 33 cm RSO diameter. Both calculations and simulations thus suggest about one third of a meter as a detection threshold.

4.2.2.3. Hardware simulations

The main design target for APPARILLO is to achieve the best detection efficiency within the hardware constraints (size, price) (see Section 4.3.3). The FOV of a system depends on the size of the camera sensor and the focal length (see Eq. (3.3)). The larger the FOV the larger is the observable volume in orbit, however a larger focal length allows a larger aperture diameter (available COTS lens designs are limited down to an f-number of 1.2 to 2). To take all system parameters into account, which depend on the sensor and lens, real combinations of available cameras and lenses are now compared. The list of available lenses with corresponding properties are listed in Table 4.5.

Lens	85mm f1.2	135mm f2	200mm f2	400mm f2.8
Product name	Canon EF 85mm f/1.2L II USM	Canon EF 135mm f/2L USM	Canon EF 200mm f/2L IS USM	Canon EF 400mm f/2.8L II IS USM
Focal length	85 mm	135 mm	200 mm	400 mm
Aperture diameter	70.8 mm	67.5 mm	100 mm	142.9 mm
F-number	1.2	2	2	2.8

Table 4.5: Properties of available COTS lenses which were used to perform PROOF simulations of possible real systems; [73], [74], [75], [76].

In Figure 4.12 simulations results are shown for three systems, the large area CCD (FLI), the low noise sCMOS (ZYLA), and the "low budget" CMOS (CMOSIS) sensor (see Table 4.3) combined with COTS lenses to provide the same FOV of about 5.5°. To match the same FOV for a camera with a smaller sensor, a smaller focal length is required. The f-number is selected as small as possible from available COTS lenses, which can be mounted to a Canon EF bayonet. The choices for this simulation were the 400mm f2.8 lens for the FLI PL0900 and the 135mm f2 for the ZYLA and CMOS sensors.

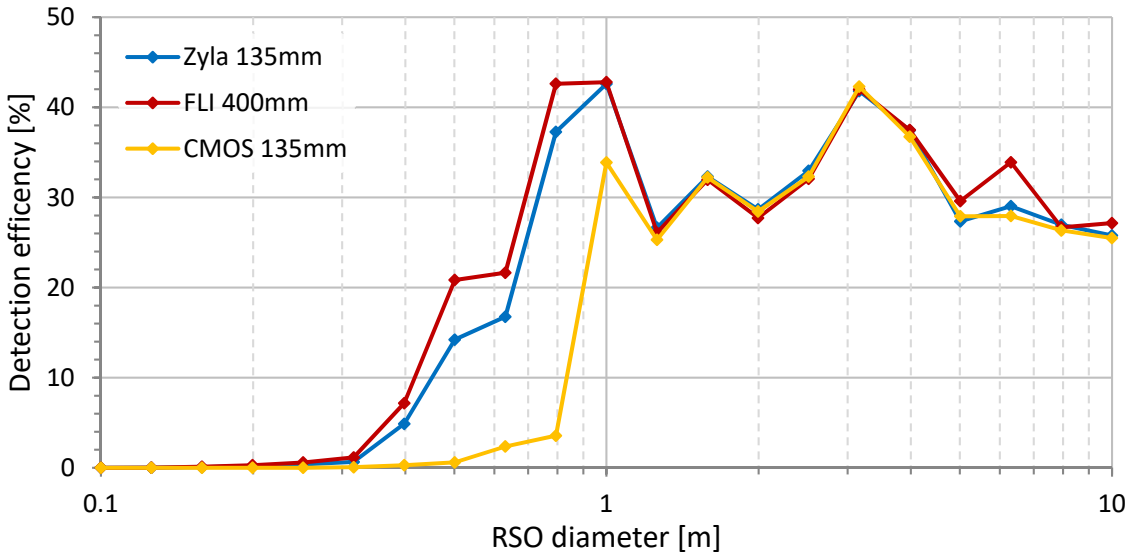

Figure 4.12: Detection efficiency depending on the RSO diameter for passive-optical systems with a fixed FOV of about 5.5°. The ZYLA (blue) and CMOS (yellow) cameras are combined with the 135mm f2 lens, which has an aperture diameter of 67.5 mm. The large format CCD camera FLI PL09000 (red) is combined with the 400mm f2.8 lens, which has an aperture diameter of 143 mm.

The detection efficiency comparison shows that the FLI camera provides the highest detection efficiency, while the CMOS performs worse especially below 1 m RSO diameter. This relates

to a larger sensor size, which allows using a larger aperture for the same FOV. Hence, the detection efficiency becomes better for smaller objects. Additionally, it can be seen that the low noise sCMOS sensor of the ZYLA performs better than the non-cooled CMOS. Due to the better performance of the large area CCD (FLI), it is suggested as the system of choice.

To converge the final hardware choice, a couple of camera lens combinations are simulated with the FLI PL09000 and ZYLA. Figure 4.13 shows that the detection efficiency over RSO diameter is again higher for systems with larger aperture, while the ZYLA tends to perform better when using the same lens as the FLI (compare 135mm f2). This can be explained by the shorter gap time, which is used for simulation with the ZYLA. Overall, camera properties have a small influence on noise level compared to the aperture diameter, if total noise is below 20 e^-, which is the case for all actively cooled cameras. Note, that the detection threshold observed in Figure 4.9 of 0.4 m (simulated using the FLI PL16803 and 135mm f2) corresponds to 5% detection efficiency.

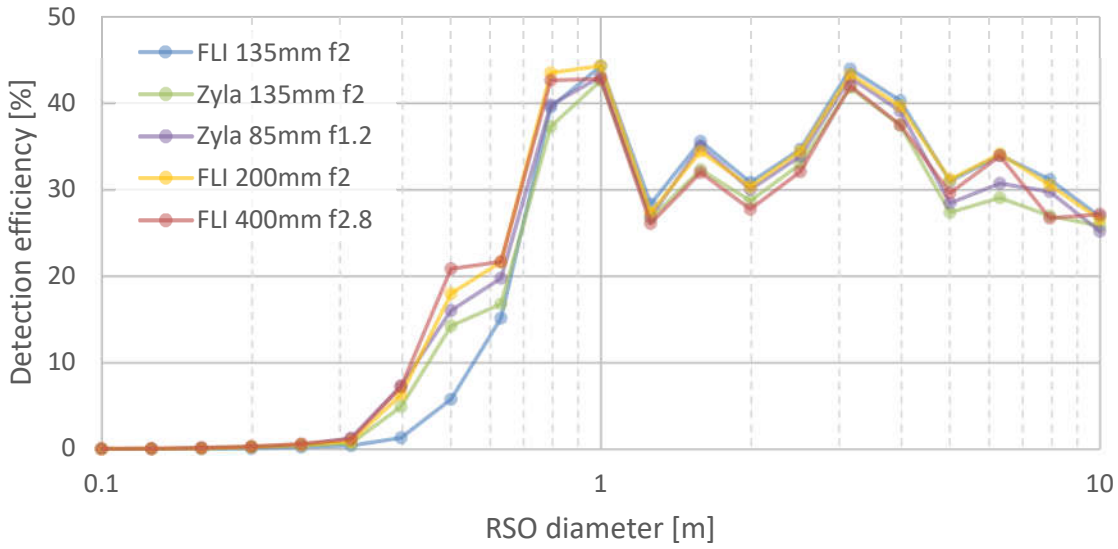

Figure 4.13: Detection efficiency according to PROOF simulations for selected COTS lenses (see Table 4.5) combined with the FLI PL09000 and ZYLA cameras.

Beside the detection efficiency, the absolute detection rates of the systems are an important property. The detection rates for the above considered systems (in Figure 4.13) are shown in Figure 4.14. To compare the detection rates between these systems with a special focus on the detection rate for smaller RSO, the detection rate below a certain RSO diameter is shown. For RSO diameter above 1 m the system with a larger FOV results in clearly higher detection rates. The 135mm f2 shows the highest total detection rates with up 16.5 det/h. However, for

smaller RSO diameter the detection rate deviate from the above case, here the FLI 135mm f2 system shows the lowest detection rate. Obviously, in this case the low detection efficiency for this system plays a significant role. Even though the FLI 400mm f2.8 has the largest aperture with highest detection efficiencies for smaller RSO, the detection rates are small compared to the other systems, due to the smaller FOV. The FLI 200mm f2 has the highest detection rates for smaller RSO and still the 2nd highest for larger RSO. This makes it most suitable to demonstrate the detectability of smaller RSO for the real system while still being useful for detecting larger RSO.

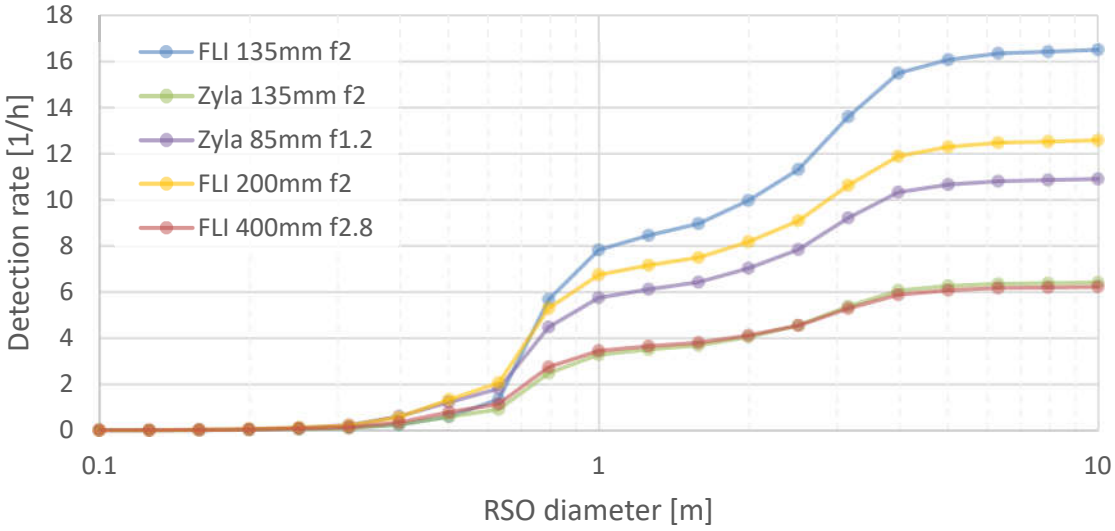

Figure 4.14: The cumulated detection rates of four systems with different FOV and aperture diameters.

Camera & lens	Detection threshold (5% detection efficiency)	Total detection rate (cumulated for $d_{RSO} \leq 0.5$ m)
FLI PL09000 & 135mm f2	0.5 m	16.5 obj/h (0.59 obj/h)
ANDOR ZYLA & 135mm f2	0.4 m	6.42 obj/h (0.59 obj/h)
ANDOR ZYLA & 85mm f1.2	0.35 m	10.9 obj/h (1.21 obj/h)
FLI PL09000 & 200mm f2	0.37 m	12.6 obj/h (1.33 obj/h)
FLI PL09000 & 400mm f2	0.35 m	6.22 obj/h (0.78 obj/h)

Table 4.6: PROOF simulation results of five different camera and lens combinations.

Table 4.6 lists the detection threshold, determined by the 5% detection efficiency, and detection threshold of the five simulated systems. Additional simulation results of various system combinations can be found in the Appendix 9.1.2.1.

4.2.2.4. Observation date and time

As explained in Chapter 3, a detection is not possible if the RSO is inside the Earth's shadow, which is also considered by PROOF. Simulating in 10 min time frames across the day for the entire year allows to evaluate the detectability of the staring system in different seasons. The following PROOF simulations (Figure 4.15, Figure 4.17, and Figure 4.18) are performed with zenith as LOS at DLR UFO observatory. As system the ZYLA equipped with the 135mm f2 lens is used. Simulations are performed for the first ten days in each given month between the years 2011 and 2015, and the results are averaged to reduce statistical fluctuations.

Figure 4.15 show the detection rate and efficiency over the day for four different months. The detection window, according to PROOF corresponds to a calculated Sun elevation α_{Sun} of -20° to -40° below the horizon. This is about 2 h after sunset and 2 h before sunrise.

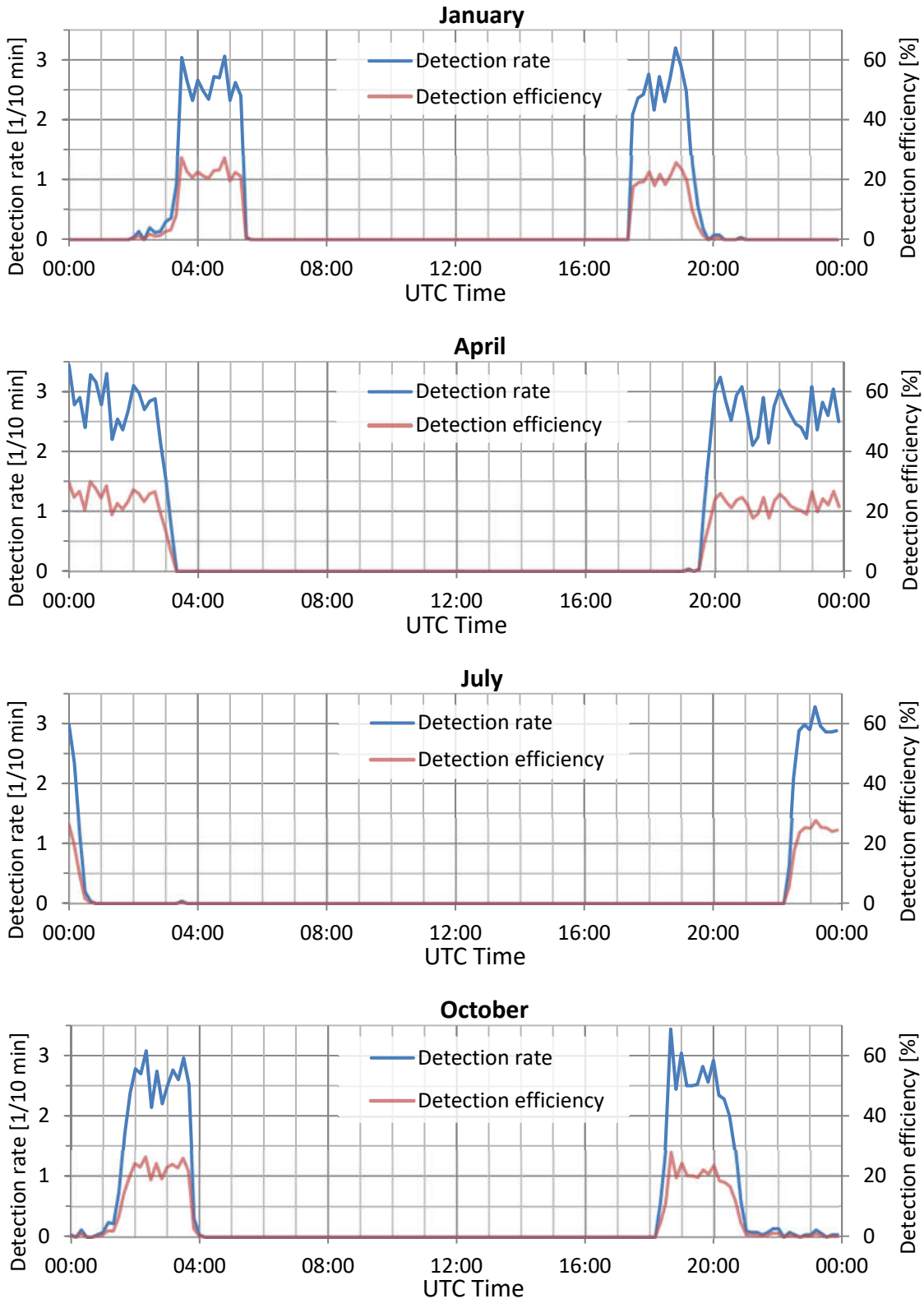

Figure 4.15: Detection rate (blue) and efficiency (red) over the time of the day (UTC) for four different months with zenith LOS. Simulations are performed in 10 min steps using the ANDOR ZYLA as camera and 135mm f2 as lens, located at the DLR's UFO observatory. The results are averaged over the first ten days of the given month for each year, between the years 2011 and 2015.

4.2.2.5. Observation LOS

Previous simulations in Section 4.2.2.2 to 4.2.2.4 are performed under a fixed zenith LOS. To determine the effect of smaller LOS elevations, the TLE database [15] is used to calculate the number of passing objects within a fixed FOV of 5.9° for four different compass directions, see Figure 4.16. The FOV corresponds to the ZYLA equipped with the 135mm f2 lens. As location UFO coordinates are used again (see Table 4.2) and the observation duration is one day, the first of April 2016. It can be seen that pointing the LOS of the camera system to low elevations for one specific azimuth increases the number of TLE objects in the FOV. This is due to a larger observed orbital volume under smaller elevations. Many LEO RSO are on polar synchronized orbits, which result in a larger number of passing objects in northern LOS direction (on the northern hemisphere, south on the southern hemisphere). Thus, the amount of crossing objects is lowest for southern and highest for northern azimuth. For East and West the number of crossing objects is equal while approaching the numbers for northern azimuth with increasing elevation. Note, that in comparison to PROOF the TLE analysis shows about half the number of crossing RSO. This is due to the fact that PROOF simulates the actual RSO distribution including not detected and not cataloged RSO, while the TLE catalog contains larger, cataloged RSO.

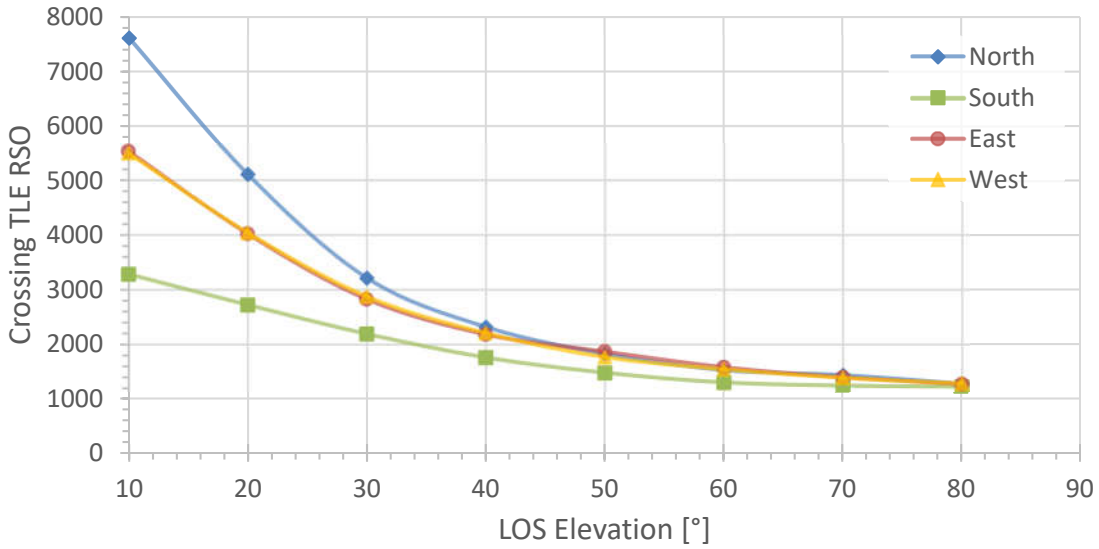

Figure 4.16: TLE objects in LEO crossing the FOV of 5.9° over 24 h based on the TLE catalog from April 1st 2016, for different cardinal directions with the origin at the DLR's UFO observatory.

For a more detailed investigation, PROOF simulations are performed under four different elevations for Western azimuth only. As observation time the first ten days of December for the years 2011 to 2015 were chosen instead of April, to emphasize the effect on the detection windows.

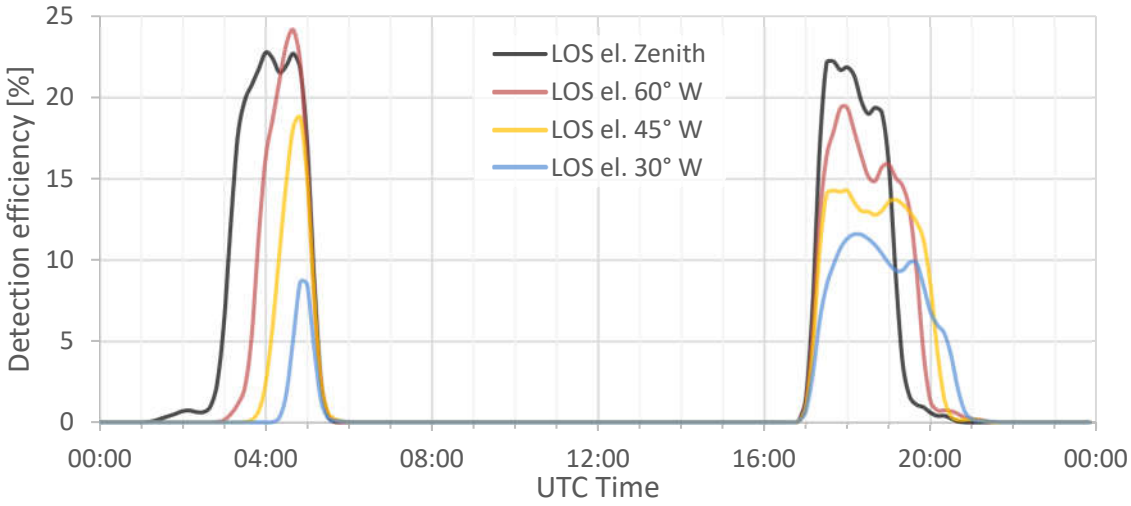

Figure 4.17: Detection efficiency over the time of the day for four different LOS elevations facing to the West (Ψ = 270°). Simulations are performed in 10 min steps using the ANDOR ZYLA as camera and 135mm f2 as lens located at the DLR's UFO observatory. The results are averaged over the first ten days in December for each year, between the years 2011 and 2015.

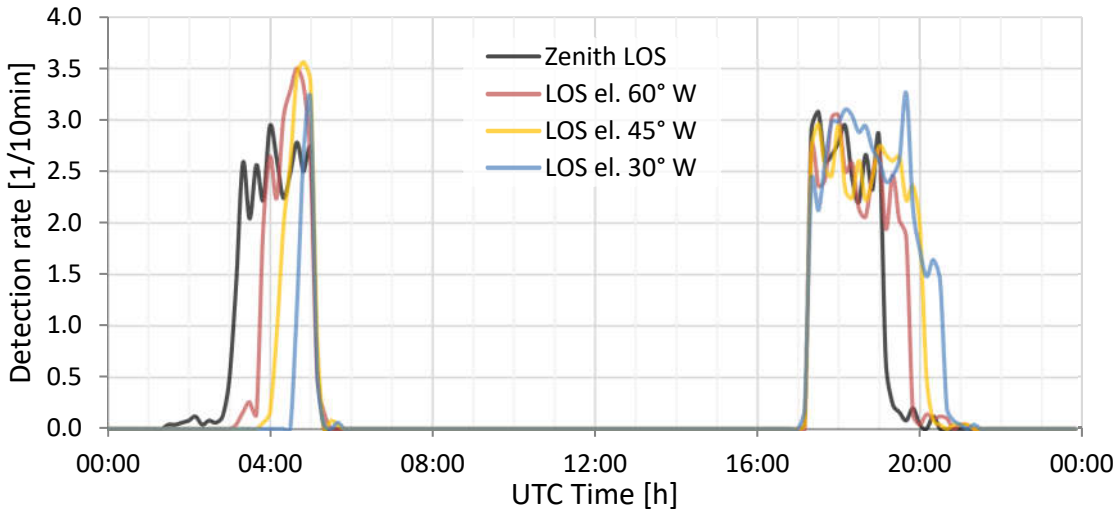

Figure 4.18: Detection rate over the time of the day for four different LOS elevations facing to the West (Ψ = 270°). Simulations are performed in 10 min steps using the ANDOR ZYLA as camera and 135mm f2 as lens located at the DLR's UFO observatory. The results are averaged over the first ten days in December for each year, between the years 2011 and 2015.

Figure 4.17 shows the detection efficiency across the day under zenith, α_{el} = 60°, α_{el} = 45°, and α_{el} = 30°. For lower elevations, the detection window (or time span) becomes larger during dusk, but shorter during dawn. The detection efficiency reduces with lower elevations, as the range to the RSO increases. This indicates that the detection threshold becomes larger with smaller elevations. However, the corresponding detection rate shown in Figure 4.18 is similar

for any elevation, once again that lower efficiency is compensated by the larger observed orbital volume.

4.2.2.6. Discussion

In this section the simulation showed how different focal length and aperture diameter combinations affect the detection rate and detection efficiency of a passive-optical system. A larger aperture is the most important parameter to achieve a larger detection efficiency for smaller RSO. As for the absolute detection rate a larger FOV is the critical parameter, due to the larger observed orbital volume. The PROOF simulations moreover show that a system consisting of COTS components can deliver high RSO detection rates. For a ground-based sensor located in

Europe detection rates up to 16 obj/h are expected with a detection efficiency of 25%, despite the strong seasonal dependence of observation time and LOS. However, these systems show fairly low detection efficiencies for RSO diameter below 0.5 m. A possible solution for this issue is discussed later in Chapter 5.3. Based on the simulations the possible camera and lens combinations have been evaluated to select the best performing system under consideration. More information about the camera and lens hardware selection are provided in Section 4.3.2 and 4.3.3 respectively.

4.3. HARDWARE SETUP

The hardware of the staring system is developed in three different stages. The core system consists of a camera, lens and a notebook, which is easy to set up and operate with low demands. This first system is called 'staring system', which is shown in Figure 4.19. It has been set up and tested in 2015, see Ref. [77]. In the second stage, the system was extended with a camera mounting for reliable camera pointing and a housing environmental protection. This second system is referred to as APPARILLO (AUTONOMOUS PASSIVE-OPTICAL STARING OF LEO FLYING OBJECTS), see Figure 4.30. Additionally, environmental data by a weather station is used to toggle camera acquisition. The final system, APPARILLO2, is an improvement of APPARILLO by introducing a more sophisticated weatherproofed housing with temperature-controlled compartments and a moveable sensor head instead of a fixed window. An image of APPARILLO2 during observations is shown in Figure 4.20. Additionally, the software is improved as well at this stage, which is explained in Section 4.4.

Figure 4.19: The FLI PL16803 and the Canon 135mm f2 lens used for staring observations. The first staring system was operated at UFO observatory, located at the Uhlandshöhe in Stuttgart, Germany.

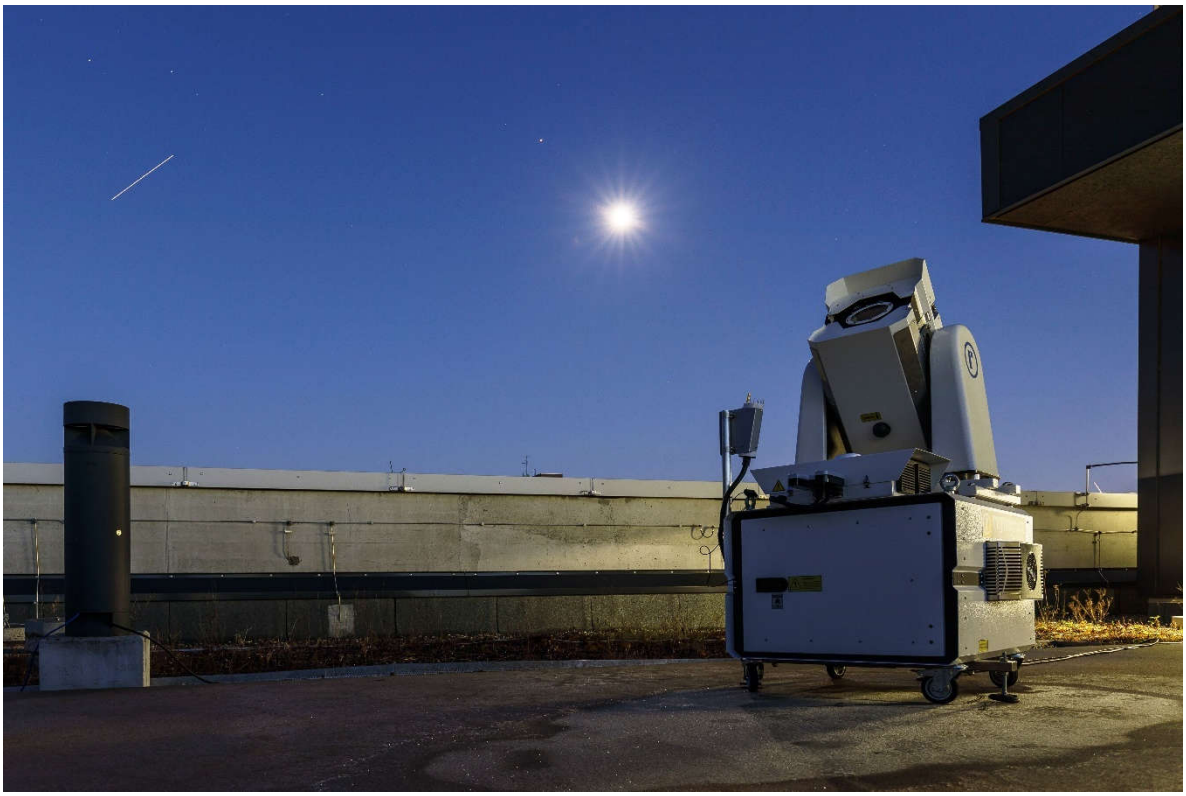

Figure 4.20: The APPARILLO2 staring sensor (bottom right) during observation in December 2020. The system has a movable sensor head and a cabinet. In the top left of the image is the ISS visible as a streak. The bright object in the center is the full moon and to the top left Mars is visible. The system is located on the top of the DLR's office building in Stuttgart, Germany.

These wide-angle staring systems are designed to identify any orbital objects in LEO. Each f the systems operates in staring mode by pointing the camera to a fixed section of the night sky (fixed horizontal coordinates) and recording continuously images. Due to high angular velocities of LEO objects as high as 1°/s (see Figure 3.13 in Section 3.6.1) the RSO are recorded as tracks, whereas stars are imaged as a point when using a 1 s long integration time. A sample composition of 20 recorded images showing three different objects is presented in Figure 4.21 and shows how RSO are recorded by the camera. The object's positions are measured by the streak's start and end points and transforming those camera coordinates to equatorial coordinates using astrometric calibration (see Section 3.4). Recording an object two or more times allows to determine the direction of flight. Measurements of each detected streak can be correlated to individual RSO using exposure time, track length, and orientation.

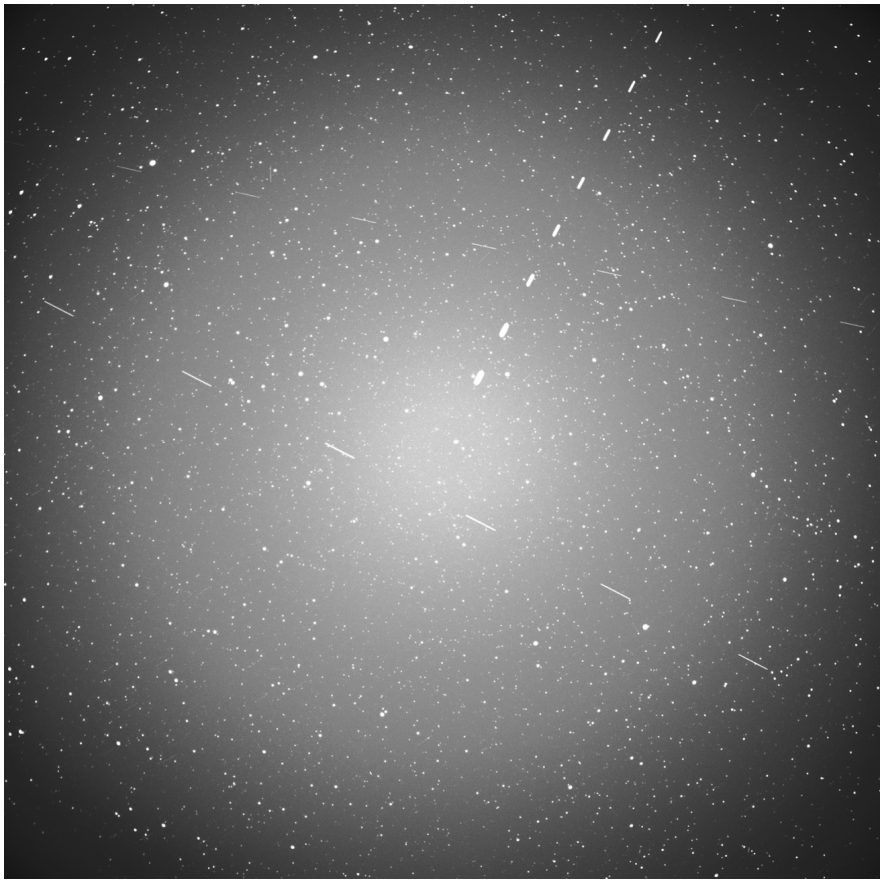

Figure 4.21: A composite image of 20 single frames recorded by the staring camera during 60 s observation time. Each image has an exposure time of 1 s using FLI PL16803 camera with Canon 135mm f2 lens under zenith LOS. It was recorded on April 17th 2014 20:46 (UTC) while three different LEO RSO were passing the FOV. The image moreover shows vignetting effect observable as radial dependence of brightness. Source: [77].

The following sections give further details on the hardware setup. First, the camera, second, the lens, 3rd, the GPS time synchronization is explained, 4th, the weather station hardware to measure the weather conditions, and 5th, the weatherproofed housing is presented. Further details of the used computer hardware as well as detailed specifications of any other hardware can be found in the Appendix 9.9.4. As operating system Linux (UBUNTU 18.4) is used, mainly due to the astrometric engine, for more details see Section 4.4. An overview of the components and their connections are shown in Figure 4.22.

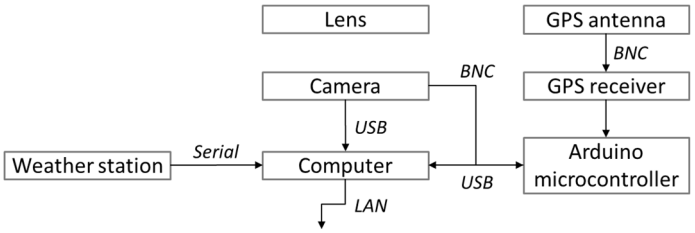

Figure 4.22: Schematic view of APPARILLO's system components and their electronic connection.

For the development of APPARILLO it is aimed that all components are commercial off-the-shelf (COTS), which reduces development investment and enables modularity. Moreover, the footprint of the camera and lens should be about 40 cm long and 15 cm wide with a weight below 6 kg, which a single operator can install. Additionally, the weatherproofed housing shall house the PC, GPS timer, power supplies, and provide a viewing window allowing an observation LOS between 30° and 90° elevation.

4.3.1. LOCATION

At a first stage, the observations with the staring system are performed at the DLR's UFO (UHLANDSHÖHE FORSCHUNGSOBSERVATORIUM), Sternwarte Stuttgart [77]. Later the APPARILLO system is operated on top of the roof of DLR's office building in Stuttgart Vaihingen, which allowed to setup and testing in the lab. Table 4.7 lists the geodetic position coordinates.

Properties	APPARILLO (1&2)	UFO
Latitude	48.74885° ± $5{\cdot}10^{-5}$ °	48.782390° ± $5{\cdot}10^{-6}$ °
Longitude	9.10257° ± $5{\cdot}10^{-5}$ °	9.196422° ± $5{\cdot}10^{-6}$ °
Altitude	486 m ± 6 m	351.3 m ± 0.5 m
Altitude reference frame	MSL (Mean sea level)	WGS84 (World Geodetic System)

Table 4.7: Geodetic position coordinates of the former UFO observatory and latest APPARILLO staring systems.

4.3.2. CAMERA

The previous simulations suggested to use an aperture diameter as large as possible to detect smaller RSO, while for obtaining a sufficiently large FOV a large sensor size is favorable. For the design constraints (which contains size, weight and cost), a sensor diagonal of about 50 mm was the largest available. Fortunately, this diameter enables using a wide range of COTS lenses. As explained above a relatively large exposure time of 1 s is used to image the objects as streaks. This makes identification of orbital objects simple and allows using large area CCD sensors. Due to their high resolution, the read-out speed is very slow. CMOS sensors on the other hand are fast but the dark noise dominates, which is why they should be cooled (compare CMOS to ZYLA in Table 4.3). Furthermore, the camera also needs to provide a trigger output to precisely synchronize the exposure time (see Section 4.3.4). During the system setup, only cameras equipped with CCD sensors were available in the desired sensor size while providing a trigger output. This is why, the PL16803 by FLI was selected for the first setup of the staring system. As an alternative, the sCMOS (Scientific CMOS) camera ZYLA by ANDOR was also available for testing.

Before final decisions were made on the camera, the PL16803 and ANDOR ZYLA were comprehensively tested including the use of our software (see Section 4.4). The ZYLA showed much faster image transfer and smaller gap times (< 1 s) and the global shutter in principle provides more precise time synchronization compared to the FLI camera. However, the small sensor size results in smaller detection rates. As for the FLI PL16803 the gap times are 4 s when using a binning of 2, and 9 s when using full image resolution. For the staring application those gap times are still small enough to record even fast objects two or more times within the 10° FOV of the staring camera. Its large pixel size implies a very good dynamic range of up to 100 ke^-, whereas the read-out and dark noise is very low with a total of 14 e^- per frame. There is also no pattern noise visible, which is typical for CMOS sensors.

For the later development on APPARILLO the FLI PL09000 was employed due to its nominal better performance, see Figure 4.23, while it shared the same physical properties, and interfaces (hardware and software) with the PL16803. The specifications of these cameras are listed in Table 4.8. Figure 4.23 shows that the detection threshold (5% detection efficiency) is 5 cm smaller for the PL09000 with 0.37 m compared to 0.42 m for the PL16803 combined with the 200mm f2 lens.

Properties	FLI PL16803	FLI PL09000	ANDOR ZYLA 5.5
Sensor	On Semi KAF-16803	On Semi KAF-09000	Fairchild
Sensor size: width x height, diagonal	36.8 mm x 36.8 mm, 51.7 mm		17.2 mm x 14 mm, 22.18 mm
Pixels	4096 x 4096	3056 x 3056	2650 x 2160
Pixel count	16.8 Mpx	9.3 Mpx	5.53 Mpx
Pixel size	9 μm	12 μm	6.5 μm
Full well capacity	100 000 e^-	110 000 e^-	30 000 e^-
Typical system noise	14 e^-	15 e^-	2.6 e^-
Dark noise (@-35°C)	0.005 e^-/s	0.02 e^-/s	0.14 e^-/s
Shutter	Mechanical blade shutter (UNIBLITZ CS-65)		Electronical: Rolling & Global
Common exposure speed	1 s		1 s
Common binning setting	2		1
Read-out rate	8 MHz		560 MHz
Peak QE	0.68	0.6	0.6
Transfer interface	USB 2.0		USB 3.0

Table 4.8: Camera specifications and exposure settings used by the APPARILLO system. [71], [70], [69], [78]. The QE of the cameras can be found in Appendix 9.9.1.

Despite being useful for staring, the downside of the FLI cameras is their relatively slow shutter with a total opening time of 54 ms and closing time of 52 ms [78]. This limits their use to long exposures only. The image read-out and transfer speeds are also slow, which results from the high resolution in combination with the CCD read-out architecture and the USB 2.0 interface.

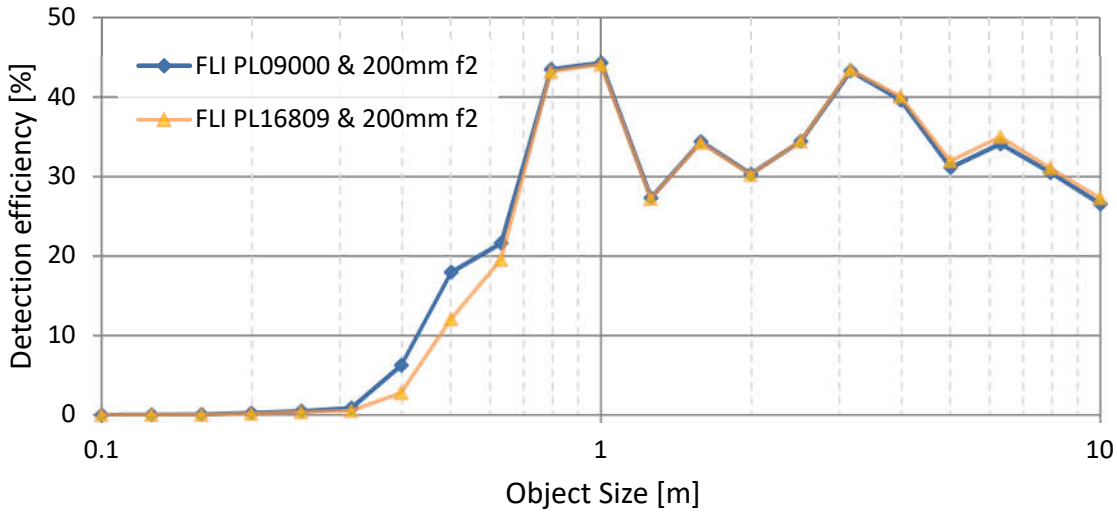

Figure 4.23: Comparison between the FLI PL16803 (orange) and FLI PL09000 (blue) camera according to PROOF simulations. The graph shows the simulated detection efficiency depending on the RSO diameter for the two staring systems equipped with the 200mm f2 lens.

4.3.3. LENS

Due to size and budget restrictions optics with an aperture larger than 100 mm and focal length larger than 300 mm were not suitable or available. Thus, refractive optics are the main choice and the COTS market of photography lenses has a large variety of lenses available. Furthermore, those lenses are relatively cheap due to mass production and have good image quality across a large image plane. The sensor size of previously presented cameras range up to 51.7 mm in diagonal. This makes lenses designed for Full-Frame[H] cameras still acceptable (shown later in this section). In Table 4.5 of previous Section 4.2.2.2 a preliminary selection of lenses was already presented (see Appendix 9.9.2 for full specifications of these lenses);

- 85mm f1.2
- 135mm f2
- 200mm f2
- 400mm f2.8

In the following the image quality of these lenses are investigated except the 400mm f2.8, which is too big, heavy, and expensive (see Appendix 9.9.2) to be used while the large focal length does not enable operation with a gap time of 9 s.

[H] Term commonly used in the consumer camera market, sensor measures 24 mm by 36 mm in width and height (43.6 mm diagonal). Also known as 35 mm format.

Two exemplary images of stars recoded by the FLI PL16803 in combination with the 85mm f1.2 are shown in Figure 4.24. It can be seen that the lens shows a large amount of spherical aberration. The PSF still results in a small measured FWHM. However, bright point sources (e.g. stars) are rendered as very large objects in the image while using a small binarization threshold. Furthermore, the PSF becomes very unsymmetrical in the image corners, which further degraded the image processing reliability.

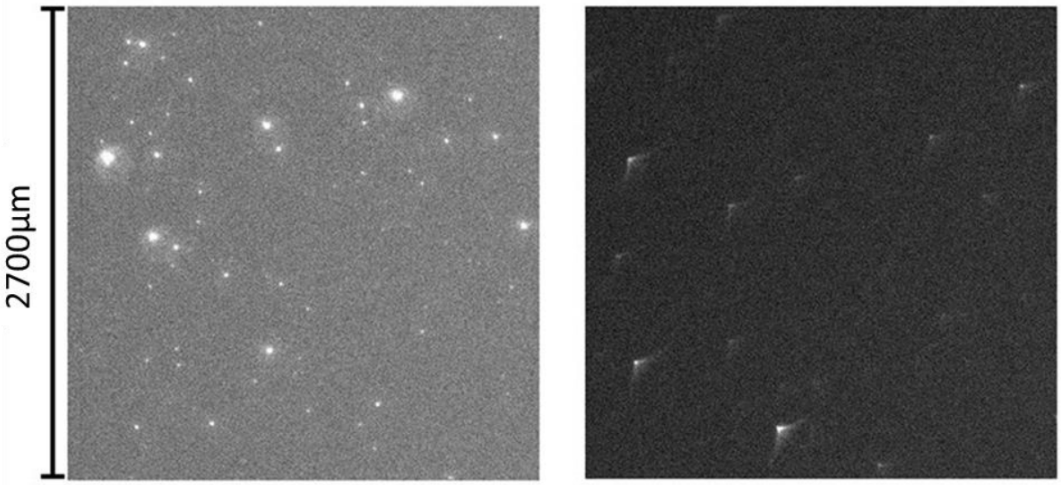

Figure 4.24: Cropped and enlarged frames of the image center (left) and outer image corner (right) using the 85mm f1.2 lens and FLI PL16803 camera at binning 1. Source: [79].

In Figure 4.25 and Figure 4.26 exemplary images of stars recoded by the FLI PL16803 in combination with the 135mm f2 and 200mm f2 are shown, respectively. Compared to the 135mm f2, the 200mm f2 lens has a much larger aperture and provides better image quality. In Figure 4.26 it is shown that stars are recorded by the 200mm f2 as symmetric points across the entire image, which is about 4 mm beyond its designed image radius. Using the 200mm f2, the measured FWHM of the PSF is 1.74 px using the PL16803 and 1.5 px using the PL09000. Additionally, the 200mm f2 lens shows less vignetting. As a downside, the price, size and weight are considerably larger for the 200mm f2 lens, but are still within the design constraints (see Appendix 9.9.2).

The 10 cm aperture of the 200mm f2 promises detecting objects as small as 40 cm in size according to PROOF (see Figure 4.13 in Section 4.2.2.2). The 200mm focal length results in a rectangular FOV of 10.4° by 10.4° when combined with the FLI CCD cameras. Table 4.9 lists the specifications of the 135mm f2 and 200mm f2 lenses which are used with the FLI cameras (see Table 4.8).

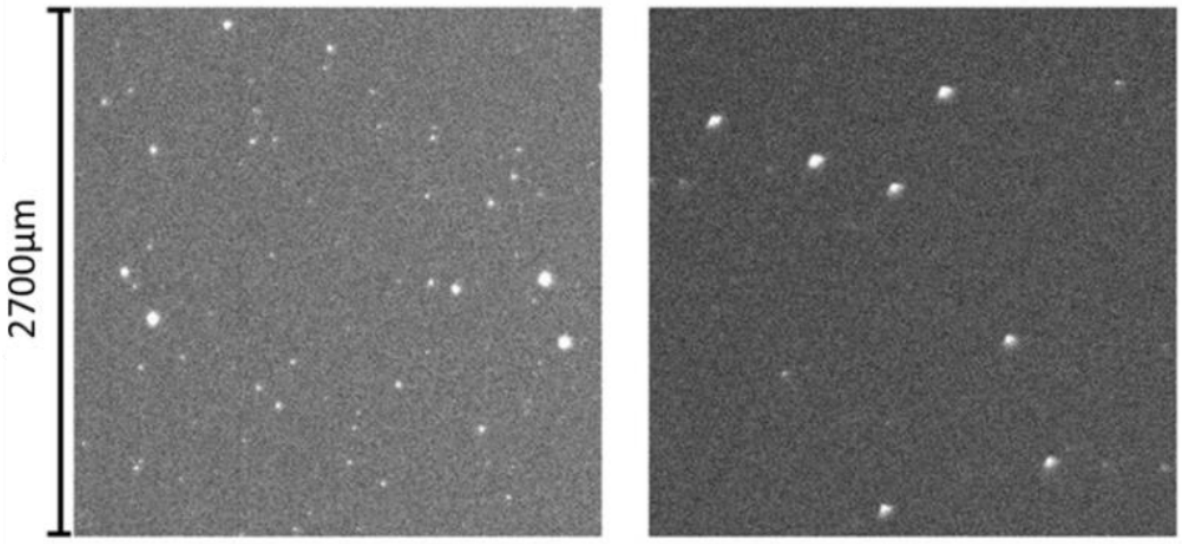

Figure 4.25: Cropped and enlarged frames of the image center (left) and outer image corner (right) using the 135mm f2 lens and FLI PL16803 camera at binning 1. Source: [79].

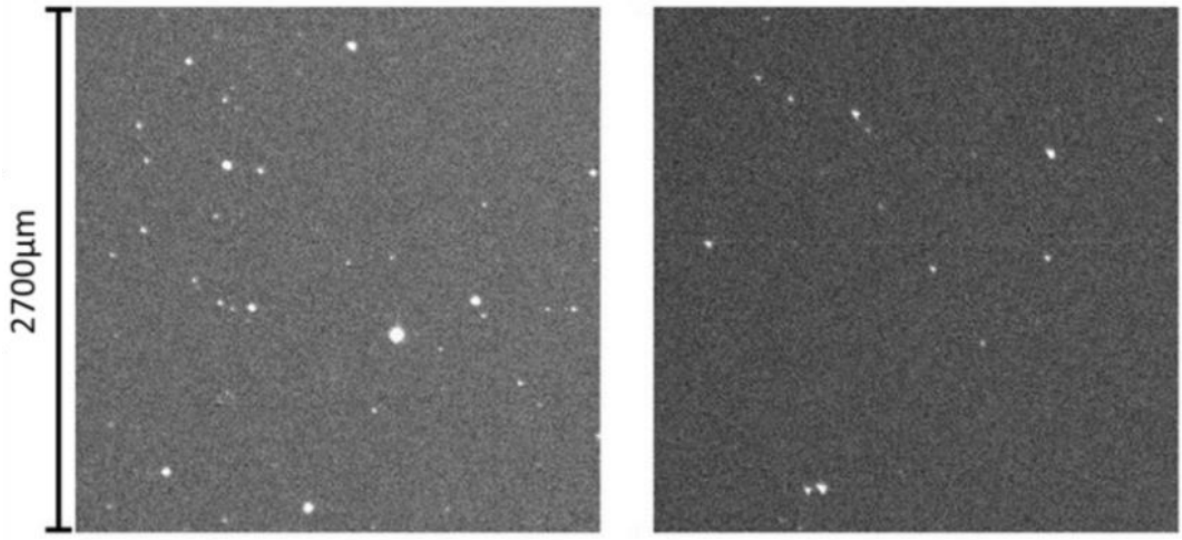

Figure 4.26: Cropped and enlarged frames of the image center (left) and outer image corner (right) using the 200mm f2 lens and FLI PL16803 camera at binning 1. Source: [79].

All lenses show an illumination fall-off to the image corner. This vignetting results mainly from the optical construction where the pupil is obscured by element borders, which is typical for lenses with a small *f*# [43]. The contribution by the cosine fourth power law is rather small for those telephoto lenses. According to the cosine fourth power law the intensity in the outer image corner drops by only 4% for a half angle of 7.5° (200mm f2 and FLI).

Lens	**135mm f2**	**200mm f2**
Model name	Canon EF 135mm f/2 L USM	Canon EF 200mm f/2 L IS USM
Bayonet	Canon EF	
Focal length	135 mm	200 mm
F-number	2	2
Aperture diameter	67.5 mm	100 mm
FOV: width x height / diagonal (@FLI)	15.2° x 15.2° / 21.0°	10.4° x 10.4° / 14.5°
Pixel scale (@PL16803)	13.8 arcsec/px (67 µrad/px)	9.3 arcsec/px (45 µrad/px)
Pixel scale (@PL09000)	18.3 arcsec/px (89 µrad/px)	12.4 arcsec/px (60 µrad/px)

Table 4.9: Lens specifications and properties used in combination with FLI cameras for staring observations, [74], [75].

Figure 4.27 shows the 200mm f2 lens and FLI PL0900 installed inside APPARILLO2's sensor head. An image of the FLI PL16803 and 135mm f2 is shown in Figure 4.19. Note, that the lenses are focused manually after installation.

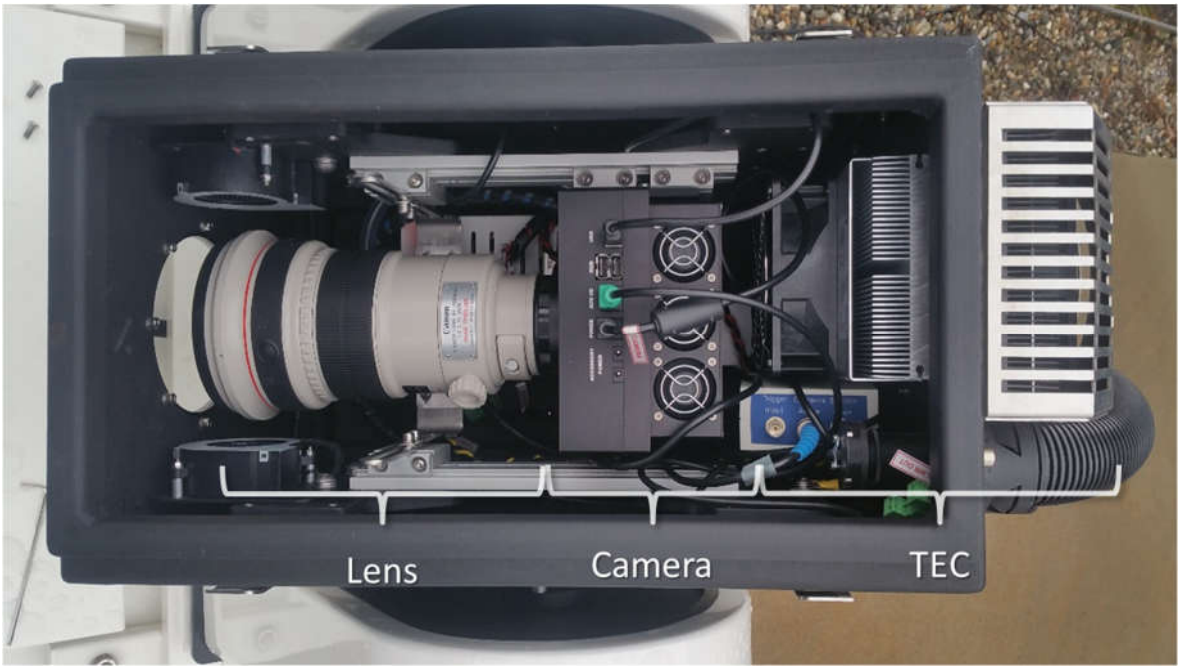

Figure 4.27: The FLI PL09000 Camera and Canon EF 200mm f/2 lens are mounted inside the sensor head of APPARILLO2 enclosure. Both lens and camera can be mounted on a rail. In the back of the sensor head is a thermo-electric cooler (TEC) (right in the image) and blowers in front of the window (left in the image) prevent condensation.

4.3.4. GPS SYNCHRONIZATION[I]

For GPS synchronization an ARDUINO based GPS timer is used, which consists of an ADAFRUIT ULTIMATE GPS receiver and an ARDUINO UNO microcontroller [80]. Figure 4.28 shows the inside of this GPS timer and the connected GPS antenna mounted on top of the weatherproofed housing. It can either be used to externally trigger the camera exposure by sending a TTL (transistor-transistor logic) pulse to the camera, or record the UTC time stamp of an incoming TTL pulse from the camera. The microcontroller compares the incoming TTL with the PPS signal provided by the GPS receiver. This way, it measures the time of a TTL signal with a nominal 100 μs precision [81].

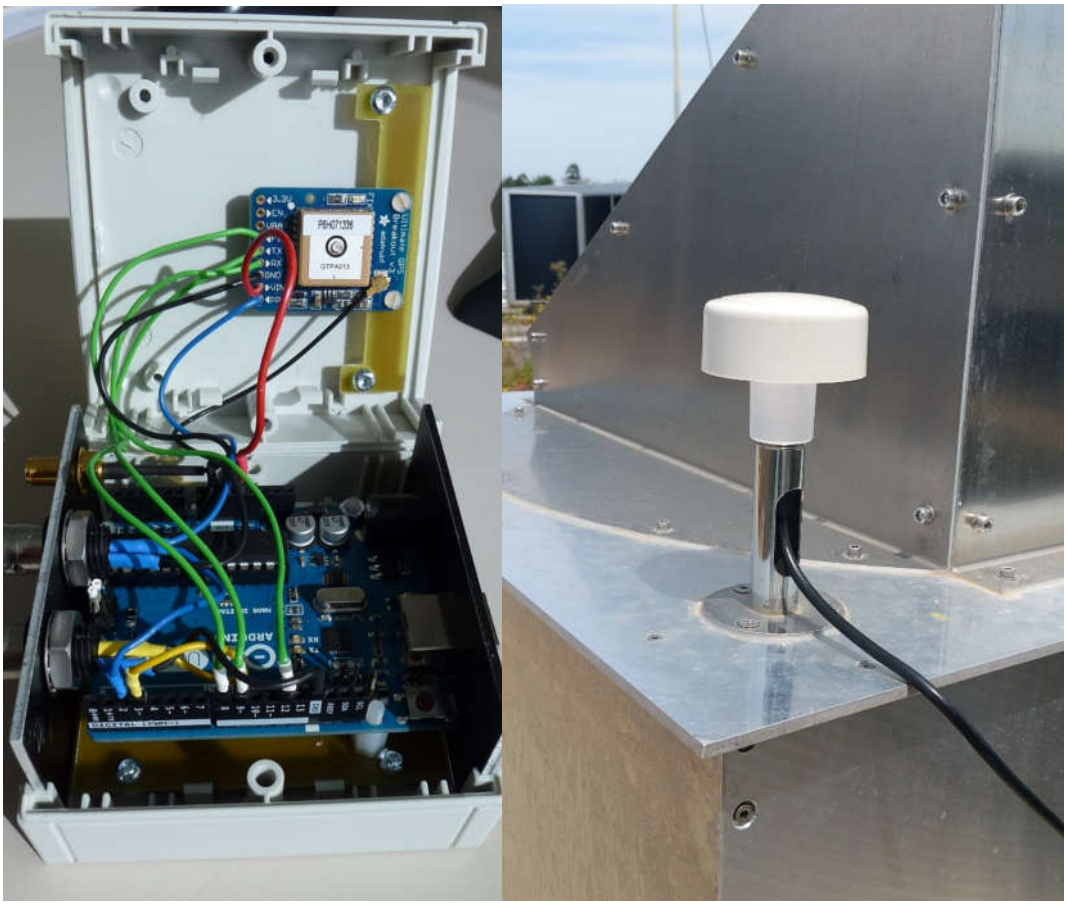

Figure 4.28: Left: Image of the GPS timer electronics, Source: [80]. Right: GPS antenna mounted on the APPARILLO enclosure.

[I] This section is reproduced in parts from [85]

4.3.5. WEATHER STATION

The task of the weather station is to support the autonomous operation of the staring system by toggling observations when a clear sky is present at night. As weather stations the BOLTWOOD CLOUDSENSOR II by DIFFRACTION LIMITED and the AURORA CLOUD SENSOR III by EUROTECH are used, see Figure 4.29. Both weather stations are connected over a serial connection to the PC, and only one station is used in each system. APPARILLO is equipped with the AURORA CLOUD SENSOR III and APPARILLO2 with the BOLTWOOD CLOUDSENSOR II. Both measure ambient temperature, humidity, dew point, light level, and difference between sky and ambient temperature. Furthermore, the BOLTWOOD records wetness, rain, and windspeed. The Aurora on the other hand measures only wetness *Wt*. This value is calibrated in the hardware interface to be larger than one when it is raining (to match the BOLTWOOD weather sensor). This enables using both sensors with the same threshold. The temperature difference between sky and ambient ΔT_{Sky} is used to measure cloud coverage. The light level L_{lvl} gives information about nighttime and acts as a fallback to the calculated nighttime (more details later under Section 4.4.1).

Figure 4.29: Left: EUROTECH's AURORA CLOUD SENSOR III mounted on the APPARILLO enclosure. Right: DIFFRACTION LIMITED's BOLTWOOD CLOUDSENSOR II mounted on the APPARILLO2 enclosure.

4.3.6. WEATHERPROOFED HOUSING

For reliable operation of the staring system a weatherproofed housing is mandatory. It needs to protect and house the required hardware from the environment. Its dimensions need to be smaller than 0.9 m by 1 m by 1.6 m in width, depth and height, and not more than a few hundred kg to ensure 'easy' transportation with a van, elevator and inside office buildings/labs. Rolls under the housing allow moving the housing easily and retractable feet securely keep the housing in a stable position during observation under stormy conditions. Moreover, condensation or accumulation of snow and ice on the viewing window must be prevented to maintain operation under any weather conditions. A plane glass as a window is the optimal choice to avoid additional image aberrations.

Figure 4.30: The first autonomous staring system APPARILLO was operated on the roof of DLR's office building in Stuttgart, Germany.

The first weatherproofed housing for APPARILLO, shown in Figure 4.30, was constructed and manufactured by the Institute of Technical Physics (DLR-TP) mechanical workshop. Its dimensions are 0.85 m by 0.85 m by 1.3 m to house all the components. Only a LAN and power connector are on the outside. The viewing window is tilted by 60° and measures 0.67 m by 0.31 m. This provides the desired observation between 30° and 90° elevation. Inside the

housing, a temperature-controlled fan heater is mounted under the window to prevent condensation and accumulation of snow and ice on the viewing window. A door gives access for installation or maintenance. An access port under the window allows to focus the lens after installation.

During operation, the APPARILLO housing proofed to be weather sealed under any weather condition occurred and the heater securely prevented any snow or ice accumulation. The only disadvantage is the accumulation of dirt/dust particles on the viewing window. The particles themselves are not causing any image degradation (e.g. aberration), but stray light when the Moon is bright enough. This stray light massively increases the background noise. In addition, the illuminated particles which are about 20 cm in front of the lens are imaged as round (defocused) bright circles on the image, see Figure 4.34 in Section 4.4.2. The solution to overcome this issue is delivered by a commercial housing.

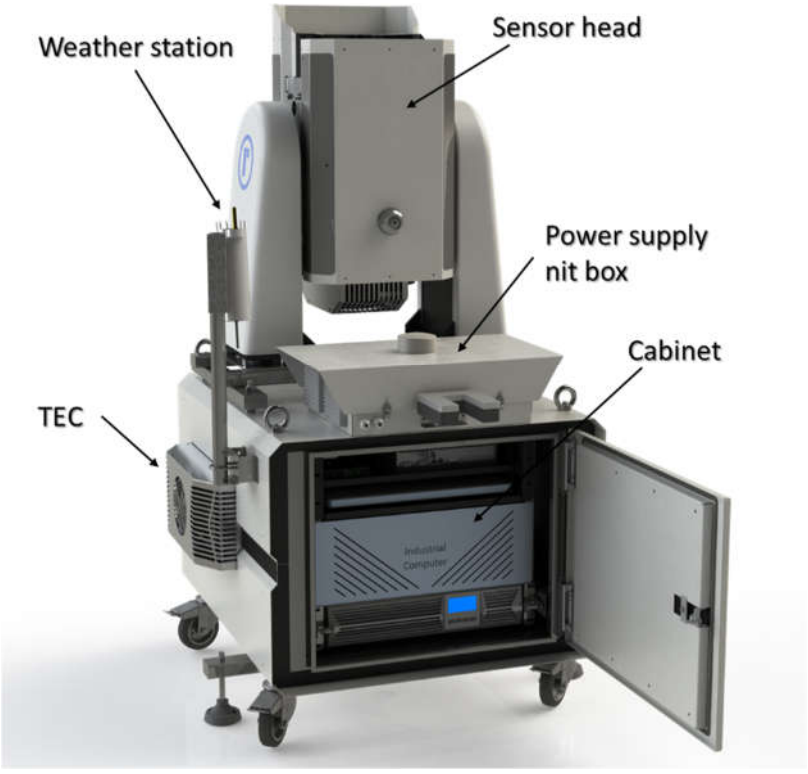

Figure 4.31: APPARILLO2 weatherproofed housing contains the camera and lens in the sensor head, while the computer and microcontroller are stored in the cabinet. TEC stabilize the temperature and prevent any condensation from the inside. The weather station, power supply nit bob, and GPS antenna are mounted on top of the cabinet. © RAYMETRICS

The second weatherproofed housing was developed by RAYMETRICS[J]. It is an adaption of a wind LIDAR system where the staring camera can be installed in the sensor head. Its IP68 rating protects the equipment from environmental influences. The sensor head contains the FLI PL09000 camera (see Section 4.3.2) and 200mm f2 lens (see Section 4.3.3), and is movable between -90° and 90° with respect to the horizon. It points upwards (to zenith or any other suitable elevation angle) during observation and moves the head pointing downwards when the observation is stopped. This protects the viewing window from any precipitation and the Sun accidently being focused on the image sensor or shutter blades of the camera. The head is weather sealed while blowers in front of the window as well as a thermo-electric cooler (TEC) controls the temperature and humidity preventing condensation on the window. Thus, all components are operated within their specifications. The viewing window measures 120 mm diameter which is sufficient for the 200mm f2 lens, while an anti-reflective (AR) coating prevents unwanted reflections. To mount camera and lens two rails are available on both sides inside the head. Using the FLI camera the lens can have a maximum length of 265 mm, which again is sufficient for the 200mm f2 lens. The main compartment contains the main controller of the enclosure (SMU200), a 1 U (rack unit) uninterruptible power supply (UPS), and a power distribution panel. These are mounted on a sliding 19" rack with a 4 U free space to accommodate a workstation computer. On top of the enclosure the weather station (BOLTWOOD CLOUDSENSOR II), the GPS antenna and a power supply nit box that provides direct current (DC) to the electronics camera and TEC units are mounted. Like the sensor head, the enclosure is also environmentally sealed and temperature controlled.

4.4. SOFTWARE ARCHITECTURE

The operation of APPARILLO is managed by the so-called Staring Daemon. This is a Python 3 program based on the Orbital Objects Observation Software (OOOS) package[K] [82]. The Staring Deamon handles the connected hardware:

- Weather station
- GPS Timer (Arduino microcontroller)
- Camera

[J] Raymetrics S.A., www.raymetrics.com.

[K] Orbital Objects Observation Software (OOOS): https://spacedebris.dlr.de/OOOS_software/index.html, Accessed Sep 26 2021.

- Weatherproofed housing (RAYMETRICS)

It starts the image acquisition (Section 4.4.1), manages the data transfer to the image processing (Section 4.4.2) and handles the data export. The optional data upload to the web server is performed by a seprate OOOS program, called Internet Daemon. The OOOS software is highly modular and not hardware bound, which allows a simple integration of the necessary software for the new hardware. Figure 4.32 shows how the Staring Daemon (green) is connected to the separate OOOS software components (purple), external software (red), and the hardware (blue). Data recording and transfer of files is shown in yellow. Weather information is recorded and saved by the Environment Daemon. The camera is controlled by the Acquisition Process, which is also connected to the GPS timer. The Staring Daemon itself is connected to those processes and daemons using high level commands. It reads the recorded weather data and toggles the image recording and sensor head position of the enclosure depending on the weather conditions and time. The Staring Daemon also handles the communication to the image processing program and hands over information and measurements to be uploaded to our website[L] by the Internet Daemon.

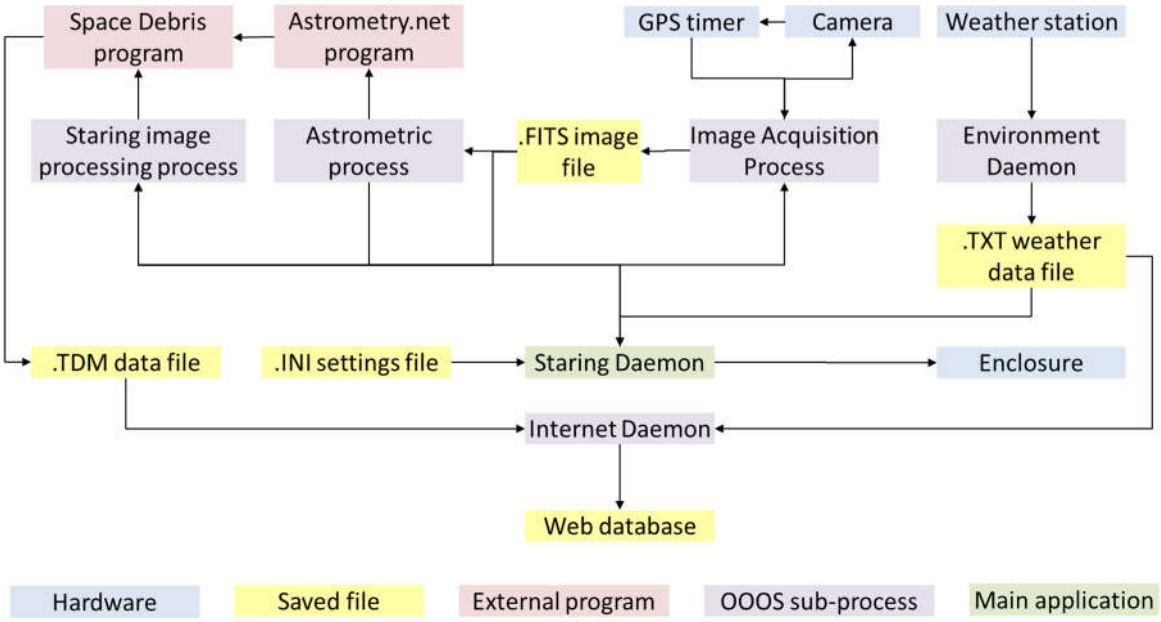

Figure 4.32: A schematic illustration how the different sub-processes (purple) and hardware interfaces (blue) are connected to the main program "Staring Daemon" (green). Data in- or output is shown in yellow and external software programs are marked in red.

[L] OOOS Web-Interface (2021): https://spacedebris.dlr.de/OOOS_web/index.php, Accessed Sep 26 2021.

4.4.1. IMAGE RECORDING

Image recording is the central process that interprets the conditions for starting and stopping the staring observations. The image recording itself is performed by the Image Acquisition Process which is connected to the camera hardware. It synchronizes the exposure start and end by the connected GPS Timer.

Images are saved in the FITS (Flexible Image Transport System) file format [83] and required meta data in the FITS file header by the Acquisition Process. Following information is required for follow up processing:

- Focal length
- Number of pixels in X- and Y-axis
- Pixel size
- Binning
- Exposure time
- Date
- GPS synchronized time of start and end of the exposure
- Geodetic coordinates

For automatic image recording, following environmental data from a weather station is required by the Staring Daemon:

- Temperature difference between sky and ambient: $\measuredangle T_{\mathrm{Sky}}$
- Light level: L_{lvl}
- Wetness/Rain: Wt

These values are used to determine the three conditions:

- *Clear sky*: is True, if ($\measuredangle T_{\mathrm{Sky}}$ < -28K)
- *Darkness*: is True, if (L_{lvl} < 10 a.u.)
- *Dry*: is True, if (Wt < 1)

$$Darkness_{\mathrm{meas}} = \begin{cases} 0: L_{\mathrm{lvl}} \geq 10a.u. \\ 1: L_{\mathrm{lvl}} < 10a.u. \end{cases}$$

$$Clear\ sky = \begin{cases} 0: \Delta T_{\mathrm{Sky}} \geq -28K \\ 1: \Delta T_{\mathrm{Sky}} < -28K \end{cases} \qquad (4.1)$$

$$Dry = \begin{cases} 0: Wt \geq 1 \\ 1: Wt < 1 \end{cases}$$

APPARILLO2 without any filters can perform observations under a Sun elevation of about -6° to the horizon. Thus, based on the geodetic coordinates for each night the time interval is calculated when the Sun is 6° below the horizon ($\alpha_{Sun} < -6°$), which serves as an additional condition. Note, that $\alpha_{Sun} < -6°$ is much higher than the Sun elevations determined using PROOF simulations ($\alpha_{Sun} < -20°$) in Section 4.2.2.4. Image recording *ImgAcq* is started if the above conditions $\alpha_{Sun} < -6°$, *Clear sky*, *Darkness* and *Dry* are true. All given thresholds are determined empirically and can be adjusted by the user.

$$Darkness_{\mathrm{calc}} = \begin{cases} 0: \alpha_{\mathrm{Sun}} \geq -6° \\ 1: \alpha_{\mathrm{Sun}} < -6° \end{cases}$$
$$ImgAcq = Darkness_{\mathrm{meas}} \wedge Clear\ sky \wedge Dry \wedge Darkness_{\mathrm{calc}} \quad (4.2)$$

If no environmental data is available, image recording is started based on the local time and the calculated Sun's elevation only,

$$ImgAcq = \begin{cases} 0: \alpha_{\mathrm{Sun}} \geq -6° \\ 1: \alpha_{\mathrm{Sun}} < -6° \end{cases}. \quad (4.3)$$

This requires, that the image processing can handle these situations, where images are recorded under 'bad' weather conditions. Images may contain clouds or other disturbances, might be overexposed, and hence may not contain (record) any stars or streaks.

4.4.2. IMAGE PROCESSING

The image processing reads the FITS files saved by the Acquisition Process and determines the RSO positions. The image processing needs to be as fast as the image recording to ensure 'stare and chase' operation. The actual system is operated with an image recording frequency of 0.2 Hz and fulfills the requirement of near real time processing.

The image processing is performed by a separate program written in C++. The software was designed and written in cooperation with KORMORAN TECHNOLOGIE[M] [84]. It reads in the recorded FITS image files and uses OpenCV[N] algorithms to process the images. A major challenge for the image processing is the presence of clouds, see Figure 4.33. Combined with stray light from artificial light sources, this has been a major source of false-positive detections by the first APPARILLO system. For autonomous operation with APPARILLO2 the new software was included and false-positive detection could mostly be suppressed successfully.

[M] KORMORAN TECHNOLOGIE GmbH, Prof. Dr. Rudolf Haussmann, www.kormoran-tech.com.

[N] OpenCV Website (2020): https://opencv.org, Accessed 24 Dec 2020.

To eliminate the background intensity profile, the brightness distribution in the intensity histogram is used to calculate the brightness thresholds in which the background intensities lie. All intensities below the lower threshold are excluded. Intensities above the upper threshold are considered as a star or streak (RSO). This threshold can be adopted by the user to fine tune the processing. The background image is obtained by replacing all pixels with intensities above the upper threshold by an inpainting method. This is based on intensity values of their surroundings obtained by a fast-marching algorithm. The final step is to smooth the background image by applying a box filter iteratively. All parameters of these filters may be adjusted by the user. Figure 4.34 shows the result of the final background image (right) subtracted from the original image (left).

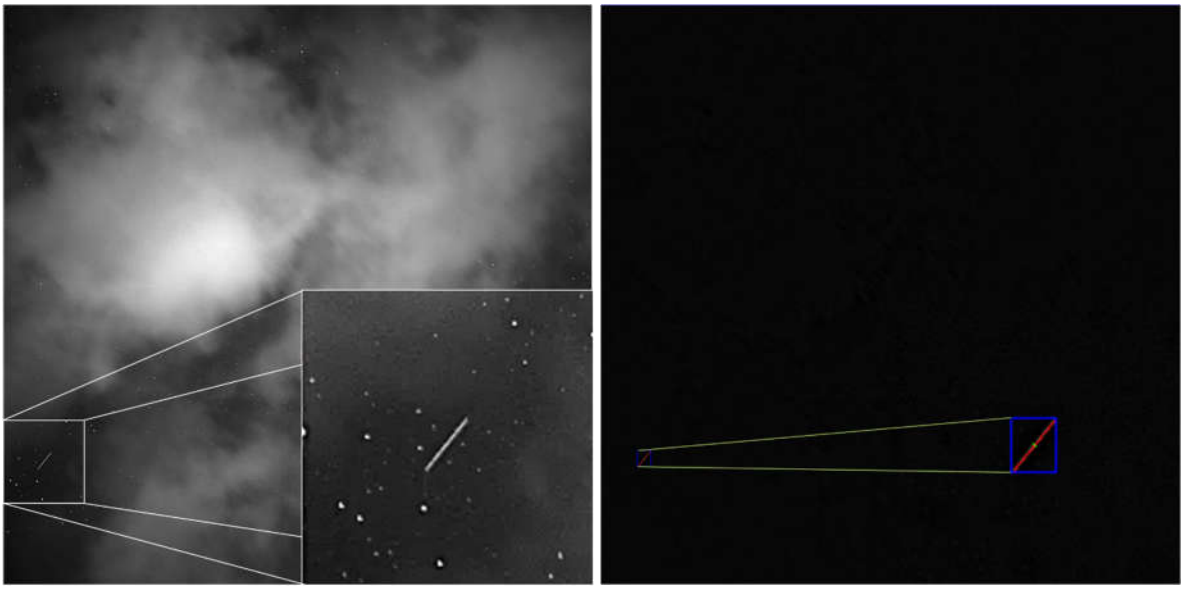

Figure 4.33: Sample image acquired by the staring sensor during partly cloudy sky (left). The software is designed to handle clouds and still detect orbital objects recorded as streaks (right). As long as there is a detectable dozen of stars to perform astrometric calibration, the measured streak position can be transformed to equatorial coordinates. Source: [85].

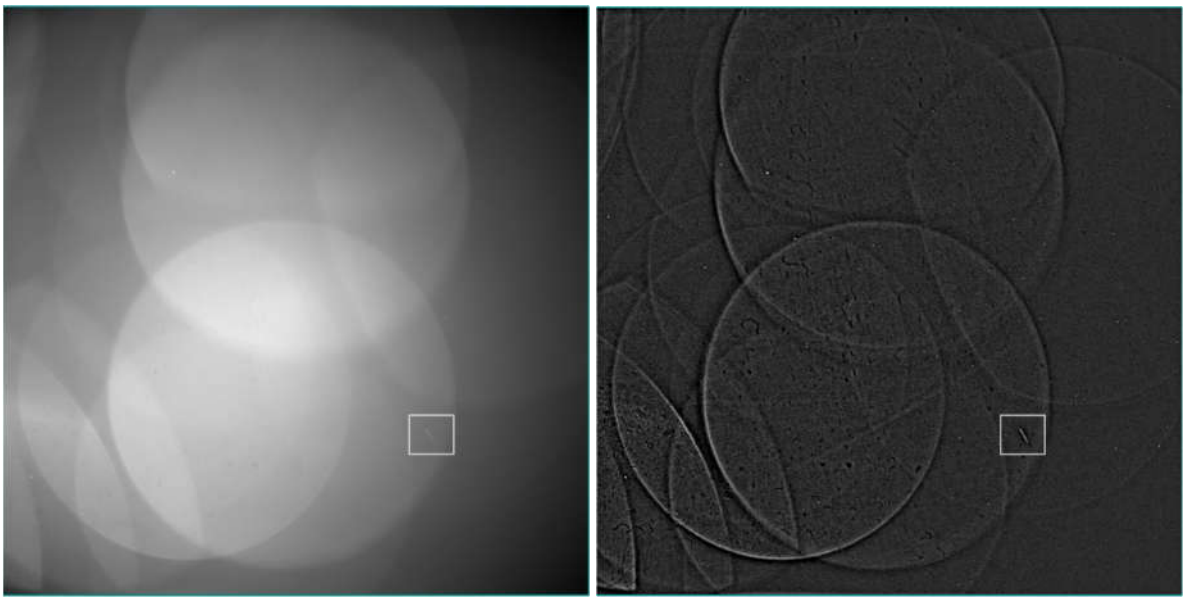

Figure 4.34: Left: Original image taken by APPARILLO with disturbing stray light induced by the Moon. The stray light results from dust particles on the window of the enclosure. Right: The processed image after background subtraction. The location of the streak is marked with a white box. Source: [84].

Due to the fast processing capabilities simple Binary Large Object (BLOB) detection (also called labelling)[O] is used by binarizing the image and performing BLOB detection in it. To identify objects in the image, areas above the upper threshold are investigated by their connected pixels. For each BLOB the pixel count, first, and second moment is measured. For each one, user defined star and streak thresholds are given to categorize the BLOB in the image. If the measured properties do not meet both requirements the BLOB is rejected and is not be considers as an RSO or star. If the minor and major axes of the second moments are almost equal, it is categorized as a star, however if the major axis is very large, it counts as a streak. The positions of the stars are measured by the first moments, while for the streaks the start and end points are determined. To improve accuracy of the streak's start and end point determination, an intensity distribution function is fitted onto the pixel values of the streak's area. By a minimization calculation, the parameter of the underground intensity, amplitude, position, length and orientation are optimized. Furthermore, the algorithm handles outliers, like stars next to the streak, and performs a robust solution to determine streak's start and end positions, see Figure 4.35.

[O] BLOB detection refers to modules to detect connected regions in a binary image and measure their properties, which allows to distinguish between different BLOB shapes and sizes.

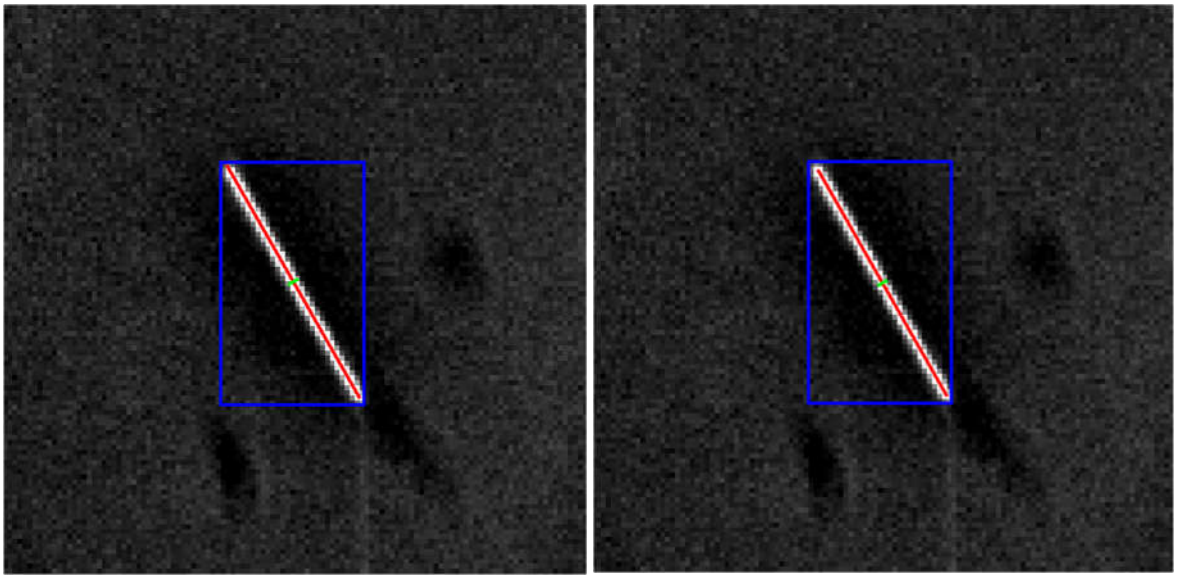

Figure 4.35: Enlarged section of the white box in the image shown in Figure 4.34 right. The bounding box of the detected streak is blue. The streak's measured position (red line) before (left) and after (right) applying an intensity fit function. Source: [84].

The star positions are used to perform astrometric calibration, which allows transforming the streak's coordinates into equatorial coordinates, see Section 4.4.3. Each image is processed individually and the bunch of determined streaks are correlated to individual RSO (see Section 4.4.4). Note, images recorded with APPARILLO2 can be processed under 1 s with available PC hardware (see Appendix 9.9.4). More processing intense techniques presented by Milani [86] or Vananti et al. [87] allow improved detectability and smaller SNR extraction thresholds of streaks, however they are not feasible for 'near real time' processing required by this autonomous sensor.

4.4.3. ASTROMETRIC CALIBRATION

The astrometric calibration transforms measured RSO coordinates into equatorial coordinates using stars as reference. An astrometric engine detects the stars automatically and generates a plate (model of the transformation), which allows to transforms any camera coordinates into equatorial coordinates.

The very first staring system and the first APPARILLO were operated under Windows using PINPOINT software [56] for astrometric calibration. APPARILLO2 is operated under Linux (UBUNTU 18.4), while ASTROMETRY.NET [54] is used as astrometric engine (installed as a separate program). Compared to PINPOINT, ASTROMETRY.NET has a much more robust engine

which can handle difficult images, overcoming the limitations of PINPOINT for autonomous operation. For instance, ASTRONOMY.NET does not require initial conditions compared to PINPOINT. With the latest image processing software by KORMORAN-TECHNOLOGIES [84], the measured positions of detected stars (see section 4.4.2) are fed into ASTROMETRY.NET to perform astrometric solving. This procedure further improved the performance and reliability of the solving.

4.4.4. OBJECT CORRELATION

The final step of the image processing is to combine measured equatorial coordinates from the observed streaks of several different images for each observed RSO. During this process following approximations are assumed. First, the observed orbit section of the RSO is approximately on a straight line in the equatorial system. Second, the RSO orbits on a great circle, which lies on the equatorial sphere with the orbital plane located at the center point of this sphere. The normal vector of this plane parameterizes this great circle uniquely.

To proceed with the object correlation, the normal vectors of all streaks are calculated and compared within certain tolerances for clustering. The second criterium to group the detected streaks to objects is the velocity, which is obtained by the lengths of the streaks and exposure time of the image. After a user defined time interval, no more streaks are grouped to an RSO and the group is closed. The interval of 300 s is motivated by the time an RSO above LEO in 4000 km orbit height is crossing the diagonal FOV of 15° (see Figure 3.13 in Section 3.6.1), which is sufficient to cover all objects of interest in LEO. If the group contains only two pairs of equatorial coordinates, that are determined by one streak, the calculation is dismissed as it does not provide the direction of flight. Finally, a least-squares fit is performed to all streaks of a single RSO. This allows to calculate the root-mean-square (RMS) deviation and to reject outliers by a threshold given by the user.

The extracted equatorial coordinates and corresponding time are written into a TDM file [88] including meta data. This enables simple data sharing with other existing stations or databases. TDM files recorded by APPARILLO2 are uploaded directly to our web database using the Internet Daemon. This interchange of the data is important to enable APPARILLO2 to be used as an SSA surveillance sensor. To analyze the measurements, the measured RSO are identified within the post processing later. An object is correlated with the latest available TLE predictions by CELESTRAK [15] after the image processing is finished each night. An RSO is considered as identified when all measured coordinates divert less than 1° from the predicted TLE coordinates.

5. RESULTS

In this Chapter the results of several observation campaigns during the setup of the system are shown. The performances of the very first staring system and APPARILLO2 are quantified and compared to each other and previous simulations. First, the results of the first staring sensor are presented which were performed 2016, followed by observations performed by the latest APPARILLO2. Data from the first APPARILLO is not analyzed due to problematic images (see Figure 4.34).

5.1. FIRST STARING CAMPAIGN 2016

In 2015 and 2016 the first operational staring system was only operated manually during pristine weather and observation conditions. As already mentioned in Section 4.4.2 the image processing of the early system was only able to handle images of a clear sky. More details of the image processing pipeline of this staring system are presented in Ref. [77]. Table 5.1 lists the hardware and recording settings of the observation campaign performed in the first half of 2015 and August 2016. In 2015 the 135mm f2 lens was used, which has been replaced for observations in 2016 with the 200mm f2 lens.

The results of the very first observations from 2015 are published in Ref. [77]. During this campaign observations were performed during dusk where maximum detection rates are observed. Across the year a total observation time of almost 24 h have been accumulated. In total 568 RSO have been detected which results in a detection rate of 24.2 obj/h. 412 of those could be identified using the TLE database, which results in a significant amount of 28% of uncatalogued RSO.

The next campaign in August 2016 was performed over a few nights which resulted in 156 detected objects during 11 h total observation time. This results in a detection rate of 14 obj/h, which is about 58% lower compared to the first campaign in 2015. In the August 2016 campaign 21% of the detected objects could not be identified using the TLE catalog [15].

PROOF predictions shown in previous Section 4.2.2 predicted a detection rate of 12.6 obj/h using the 200mm f2 lens and 16.5 obj/h using the 135mm f2 lens. This results in 47% larger measured detection rate compared to simulations in 2015, and only 11% larger in 2016. One reason for the higher rates are due to that the measurement are recorded during pristine

conditions only, while PROOF simulations were averaged from sunrise to sunset. Table 5.2 lists the results from these two campaigns and compares to the simulations.

Parameter	**2015**	**August 2016**
Camera	FLI PL16803 (see Table 4.8)	
Lens	Canon EF 135mm f/2 L USM (see Table 4.9)	Canon EF 200mm f/2 L IS USM (see Table 4.9)
FOV	15.2° x 15.2°	10.4° x 10.4°
Diameter of aperture	67.5 mm	100 mm
Exposure time	1 s	1 s
Frame rate	0.2 Hz	0.2 Hz
Binning	2	2
Pixel scale	0.0077°/px (27.6 arcsec/px or 134 μrad/px)	0.005°/px (18.6 arcsec/px or 90 μrad/px)
Observation period	23.471 h	11 h
LOS	Zenith	
Geodetic coordinates:		
Latitude	48.782390° ± $5 \cdot 10^{-6}$ °	
Longitude	9.196422° ± $5 \cdot 10^{-6}$ °	
Altitude (MSL)	399 m ± 5 m	

Table 5.1: Configuration and settings of the first staring system campaigns in 2015 and August 2016.

	2015	**August 2016**
Detected RSO	568	156
Detection rate	24.2 obj/h	14 obj/h
Simulated detection rate (avg., see Section 4.2.2.2)	16.5 obj/h	12.6 obj/h
Measurement/Simulation	147%	111%
Identified TLE RSO	412	123
Unidentified amount	28%	21%

Table 5.2: Results of the first staring system from campaigns performed in 2015 and August 2016 in comparison.

Identified RSO using CELESTRAK's NORAD TLE predictions [15] and the SATCAT [3] database allows to group detected objects with regard to their size. In Figure 5.1 the total number of crossing RSO according to TLE predictions is compared to the detected RSO depending on their RCS from measurements of the campaign in August 2016. The relation of detected TLE objects to crossing TLE objects gives the detection efficiency, which is shown in the bottom half of Figure 5.1. It can be seen that the cumulated detection efficiency down to RCS 2 m² is about 95%, which means that large RSO are well detected by the system. For RCS between 0.8 m² and 2.25 m² the detection efficiencies of about 50% are well above the predictions by PROOF simulations. This is a consequence of observations limited to pristine observation conditions while PROOF simulations (see Figure 4.23) are performed from sunset to sunrise. The smallest RSO is found to be at an RCS of 0.1 m². More details on the August 2016 campaign can be found in Ref. [79].

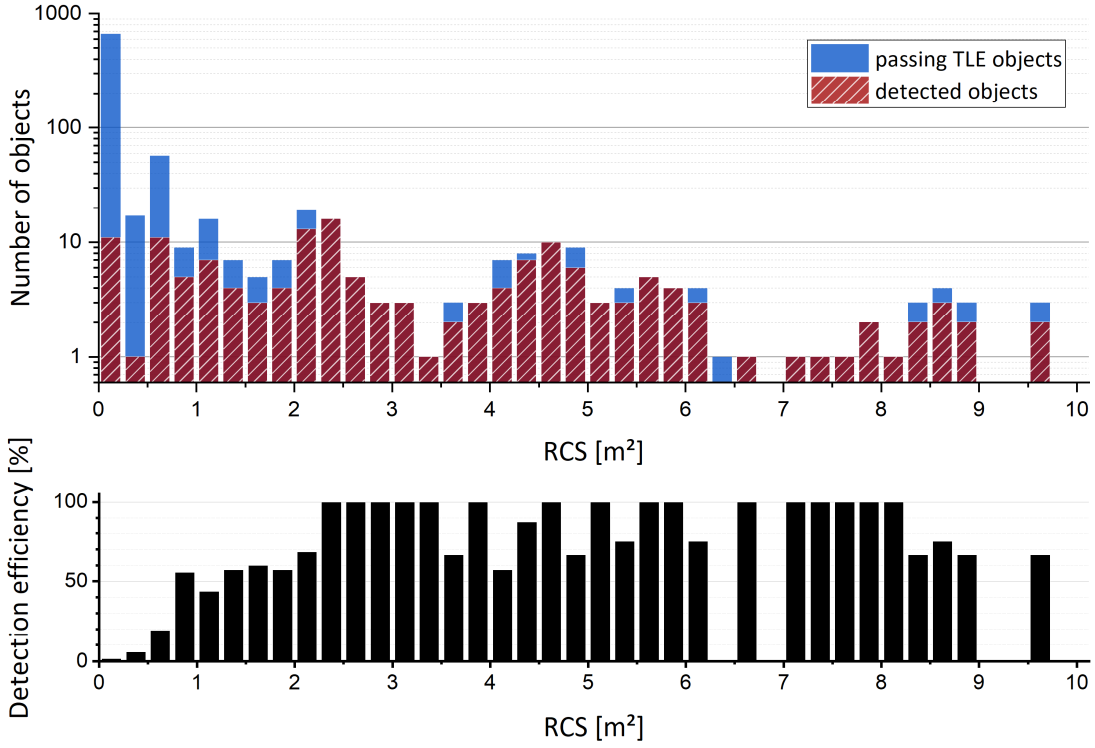

Figure 5.1: Measurements of the first staring system using the FLI PL16803 camera and 200mm f2 lens during 11 h of observation time in August 2016. Depending on the RSO's RCS (according to SATCAT [3]), the number of detected RSO (red) and crossing RSO according to the TLE catalog (blue) is shown in the top, while in the bottom the corresponding detection efficiency (black) is shown. Source: [79].

5.2. APPARILLO2

In contrast to observation campaigns using the staring system in 2015 and 2016, operational campaigns using APPARILLO2 are performed 24/7 with automatic image acquisition and image processing as presented under Section 4.4. During these campaigns APPARILLO2 was placed on top of the roof of our office building as shown in Figure 4.20. The configuration parameters of APPARILLO2 are listed in Table 5.3 and details of the five observation campaigns are listed in Table 5.4.

Parameter	Value
Camera	FLI PL09000 (see Table 4.8)
Lens	Canon EF 200mm f/2 L IS USM (see Table 4.9)
FOV	10.4° x 10.4°
Diameter of aperture	0.1 m
Exposure time	1 s
Frame rate	0.2 Hz
Binning	2
Pixel scale	0.0069°/px (24.8 arcsec/px or 120 μrad/px)
Geodetic coordinates:	
Latitude	48.74885° ± $5 \cdot 10^{-5}$ °
Longitude	9.10257° ± $5 \cdot 10^{-5}$ °
Altitude	486 m ± 6 m

Table 5.3: APPARILLO2 configuration and settings during campaigns between November 2020 and August 2021. The geodetic position is derived from the GPS timer.

Campaign	Date	Nominal LOS	Astrometric determined Alt / Az
#1 December	20.11.2020 - 23.12.2020	Zenith	88°/144°
#2 February	18.02.2021 - 08.03.2021	45° N	47°/3°
#3 March	09.03.2021 - 29.03.2021	45° W	46°/273°
#4 April-June	30.03.2021 - 04.07.2021	45° N	46°/5°
#5 July	05.07.2021 - 19.08.2021	Zenith	89°/194°

Table 5.4: APPARILLO2 configuration of campaigns between November 2020 and August 2021. Configuration and settings are listed in Table 5.3.

By November 2020 the software was ready to perform autonomous operation and the first results of the December 2020 campaign were published in Ref. [85]. During these campaigns the system operated under various weather conditions, which included:

- Frost (down to -5°C on 20.11.2020)
- Heavy snowfall
- Glaze frost
- Storm
- Fog
- Thunderstorm (including hail)
- Heavy rainfall
- High temperatures (up to 38°C ambient recorded by the weather service)

Before analysis of the campaigns, sample pictures taken by the camera during operation are presented. As an example, Figure 5.2 shows a series of 89 images combined across 13.5 min duration where 10 RSO passed the FOV. The images are realigned to the stars for better visibility. Figure 5.2 contains low altitude LEO RSO as long streaks, high altitude LEO RSO as short streaks, and rotating RSO are spotted through their intensity variations.

Figure 5.2: 89 images by APPARILLO2 merged from observation between 04:57:18 to 05:04:44 on November 26th 2020. Ten different RSO passed the FOV over the 13.5 min of observation duration. Images were realigned to match the star background for better visibility. Source: [85].

Two more RSO are shown in each image in Figure 5.3. Again, a series of images is combined to show how an RSO is recorded by the sensor. The object in the left image has a constant brightness and passes in front of two galaxies M81 and M82. The right image in Figure 5.3 shows the object GLOBALSTAR M015 which is rotating, thus a change in the streak's brightness is visible.

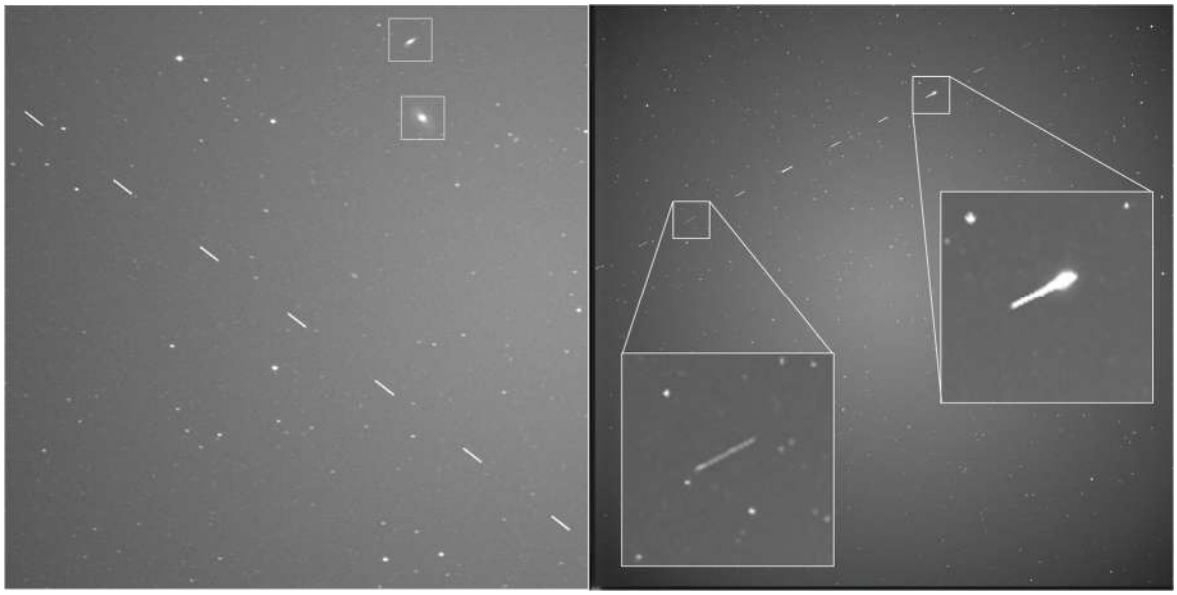

Figure 5.3: Left: Cropped image showing SL-12 Rocket body (NORAD: 24829) as streaks passing in front of the galaxies M81 and M82, which are visible in the upper right of the image. 8 images are merged, which are recorded between 03:09:00 and 03:09:36 on December 17th 2020. Right: 12 images, which are recorded between 03:29:21 and 03:30:02 on November 26th 2020, are combined to show intensity variations of the rotating object GLOBALSTAR M015 (NORAD=25308). Two streaks are enlarged to show typical intensity variations of the rotating RSO. Adopted from: [85].

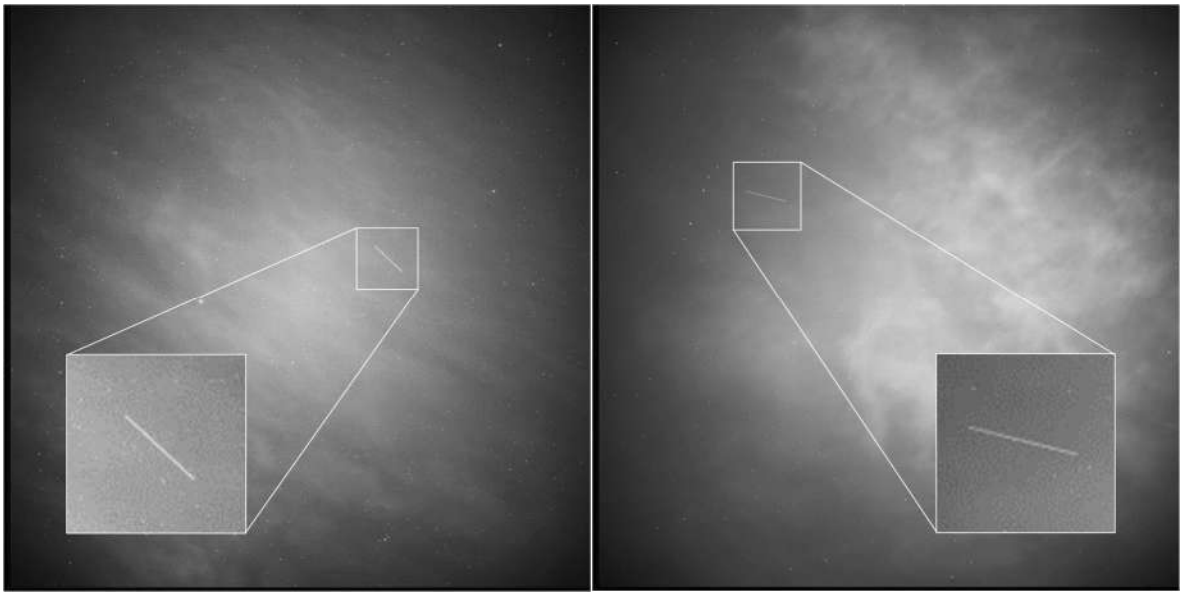

Figure 5.4: Two images each showing a high cloud layer and a LEO RSO in the image. Left: USA 25 (NORAD=18025) recorded on December 11th 2020 05:52:39:514. Right: STARLINK-1312, (NORAD=45398) recorded on December 17th 2020 06:12:06:970. Adopted from: [85].

The sky is not always perfectly clear during observations as already shown in Figure 5.2 and Figure 5.3. Often semi-transparent high clouds are present in the sky and observed by the system alongside with RSO, which is shown in the two sample images in Figure 5.4. These images are a particularly good example to demonstrate the capability of the latest image processing, which handles these background intensity fluctuations and reliably detects the RSO.

The image processing provides a lot of parameters to be adjusted (see Appendix 9.2.2) which affect sensitivity, false-negative, and false-positive detection rates. The settings are chosen to have no false-positive detections. This was validated for the first (December 2020) campaign by reviewing the corresponding images of each detected object [85]. An analysis of false-negative detections reveals that faint objects or rotating RSO with large intensity variations are the missed by the image processing. These intensity variations induce higher moments of the grayscale streak, which causes rejection by the 'fast-marching algorithm'. However, this adjustment of the algorithm is necessary to prevent the detection of misplaced streak's start and end positions due to close background stars. An exact number of the actual false-negative rate cannot be given as the human observer is unreliable in detecting streaks from a stack of images which range up to 8500 images per night. Reviewing 15% of the data by a human observer showed a false detection rate of 4% by the image processing. On the other hand, it should be noted that the human missed about the same number of streaks, especially short streaks, which the software did detect correctly. For subsequent campaigns the data was only reviewed randomly or when the system showed unusually high or low detection rates. That streaks are identified as good as the human observer, consequently implies that the streak detection can be trusted at this point.

In the next Section 5.2.1 the recorded TDM data are analyzed to review the detection performance of APPARILLO2 in more detail.

5.2.1. DETECTION PERFORMANCE

The number of detected RSO by APPARILLO2 is measured by the number of TDM files saved by the system. Furthermore, a correlation with the TLE catalog [15] is performed using the TDM data once the image processing is finished. An object is considered as identified when all measured coordinates divert less than 1° from the predictions.

Figure 5.5 to Figure 5.9 show the number of recorded TDM (blue) and correlated TLE objects (red) of each night as a histogram for each campaign. Depending on the observation LOS and month, the maximum number of detected objects per night substantially varies; being 138

detected objects per night during campaign #1 December, 406 obj during campaign #2 February, 485 obj during campaign #3 March, 562 obj during campaign #4 April-June, and 248 obj during campaign #5 July. Comparing campaign #1 December and #5 July, which are observed under zenith LOS, it can be seen that the amount of recorded TDM increases to the summer, although the observation time window is about the same (see Figure 5.5 and Figure 5.9). This is potentially caused by the better weather conditions and optimal phase angle. In winter high transparent clouds as shown in Figure 5.4 are often present. Due to a larger observing orbital volume at lower LOS elevation of 45°, the maximum number of detected RSO increases up to a factor of 3 compared to zenith LOS, see Figure 5.6 and Figure 5.8. Smaller numbers of recorded TDM or no detections, in the graphs shown in Figure 5.5 to Figure 5.9, are related to bad weather conditions. This shows the critical dependency of APPARILLO's performance on the weather conditions.

It is worth mentioning, that the system's overall performance in judging the weather conditions is very reliable and the system successfully operated the whole time autonomously only by a few exceptions. Between December 23rd and February 18th in 2021 APPARILLO2 needed to be serviced, due to a power supply failure of the RAYMETRICS enclosure. Another error occurred between May 22nd and June 16th where the weather station constantly recorded 0 K as temperature difference between sky and ground. Thus, the software interpreted this as cloudy condition and no observation were performed, resulting in a large observation gap, see Figure 5.8. A restart of the weather station and environment daemon fixed this behavior. This is why a different weather station with a better hardware interface is recommended in the future.

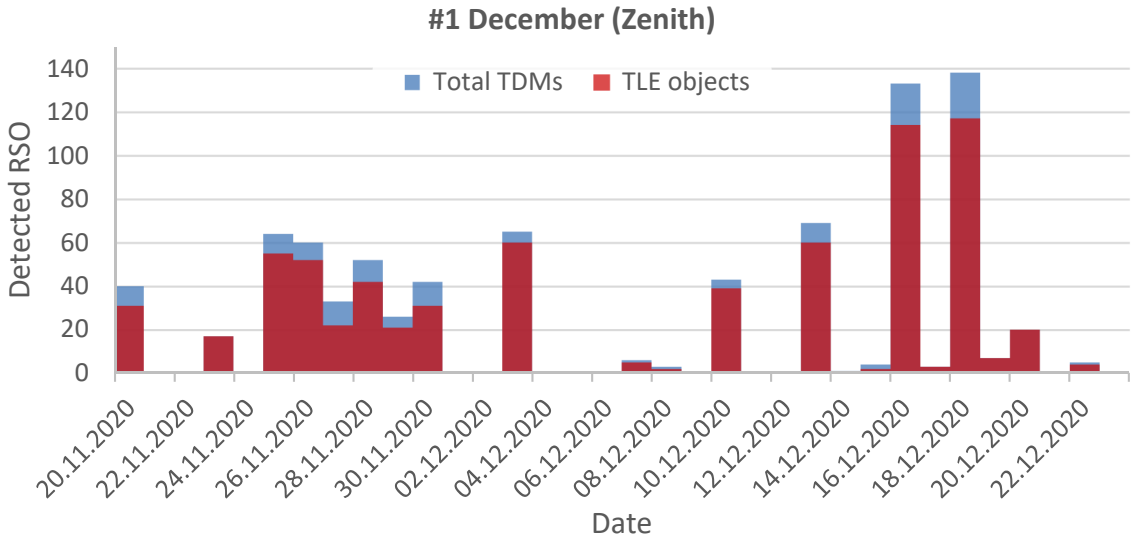

Figure 5.5: Number of recorded TDM files (blue) and correlated TLE objects of each night during campaign #1 December under zenith LOS.

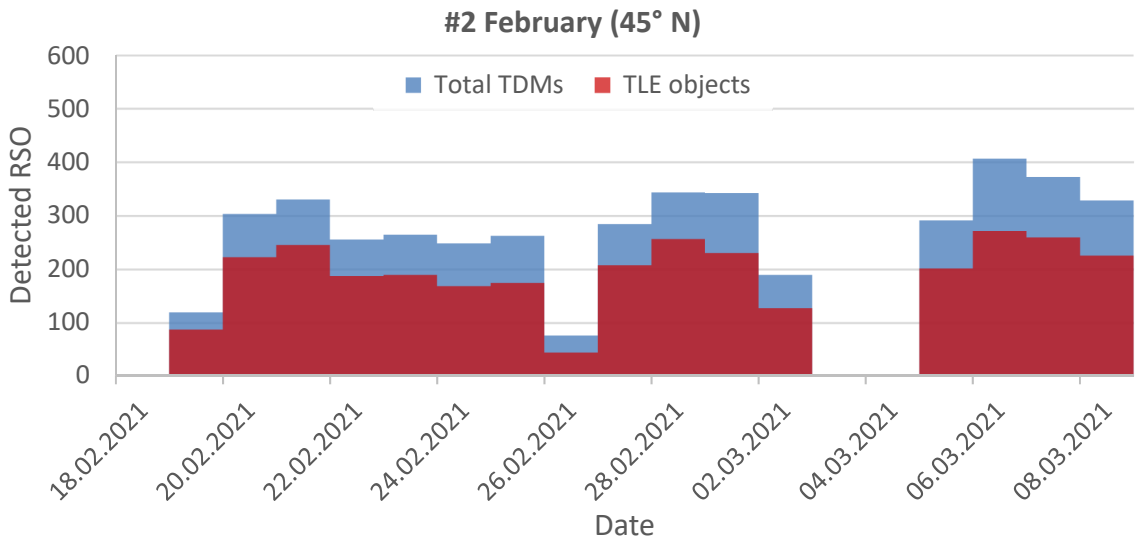

Figure 5.6: Number of recorded TDM files (blue) and correlated TLE objects of each night during campaign #2 February under 45° North LOS.

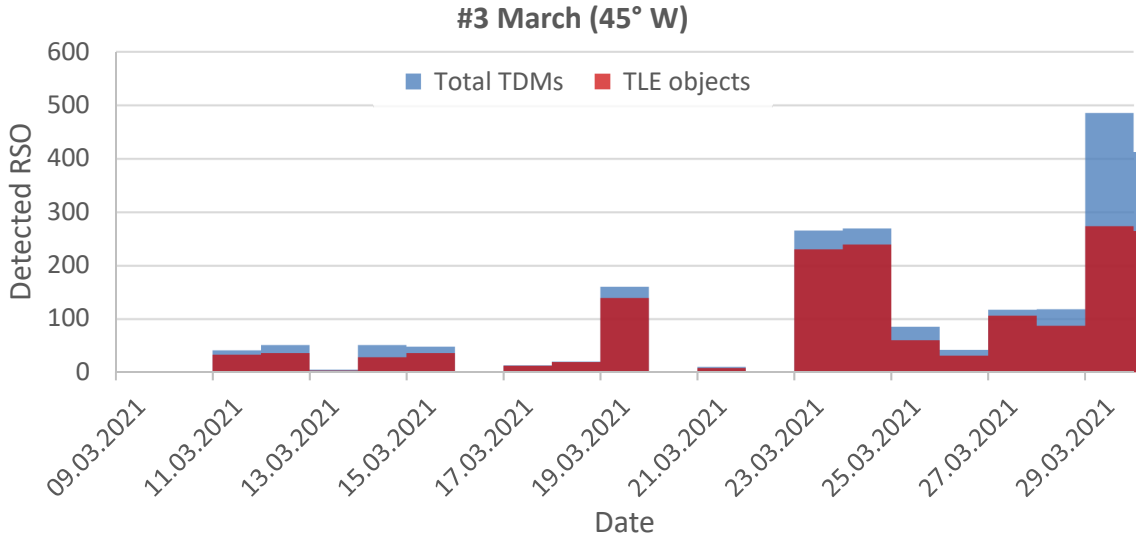

Figure 5.7: Number of recorded TDM files (blue) and correlated TLE objects of each night during campaign #3 March under 45° West LOS.

Due to network issues no TLE catalog could be downloaded for a few days in campaigns #4 and #5, hence no correlation with the TLE catalog could be performed (blue pillars within the histogram). Table 5.5 summarizes the number of detected objects and correlated TLE objects for each campaign, respectively. It can be seen that during observations performed in winter (campaign #1 and #2) the percentage of correlated objects are higher than during observations in summer.

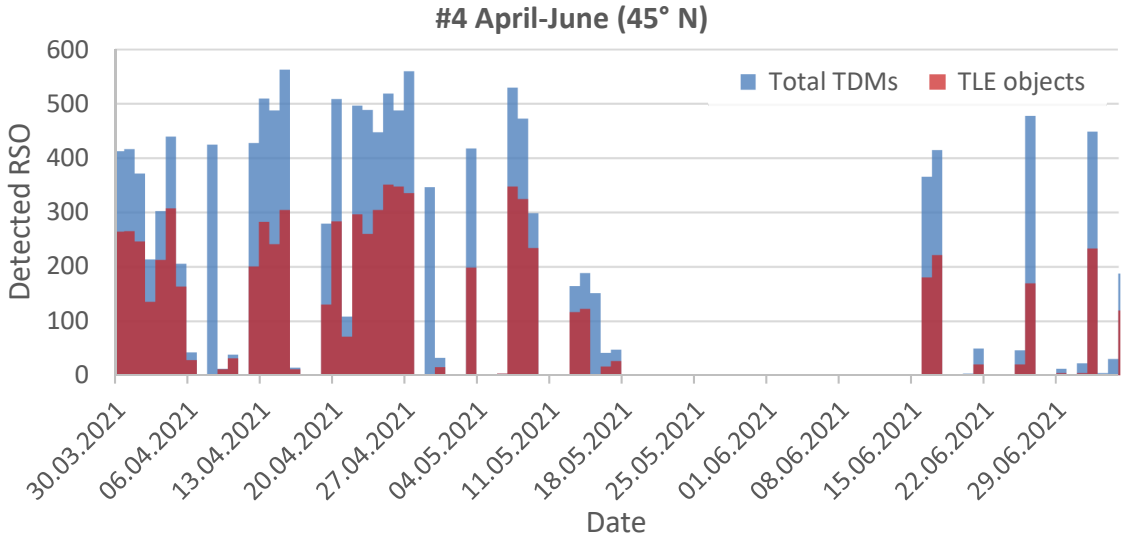

Figure 5.8: Number of recorded TDM files (blue) and correlated TLE objects of each night during campaign #4 April-June under 45° North LOS.

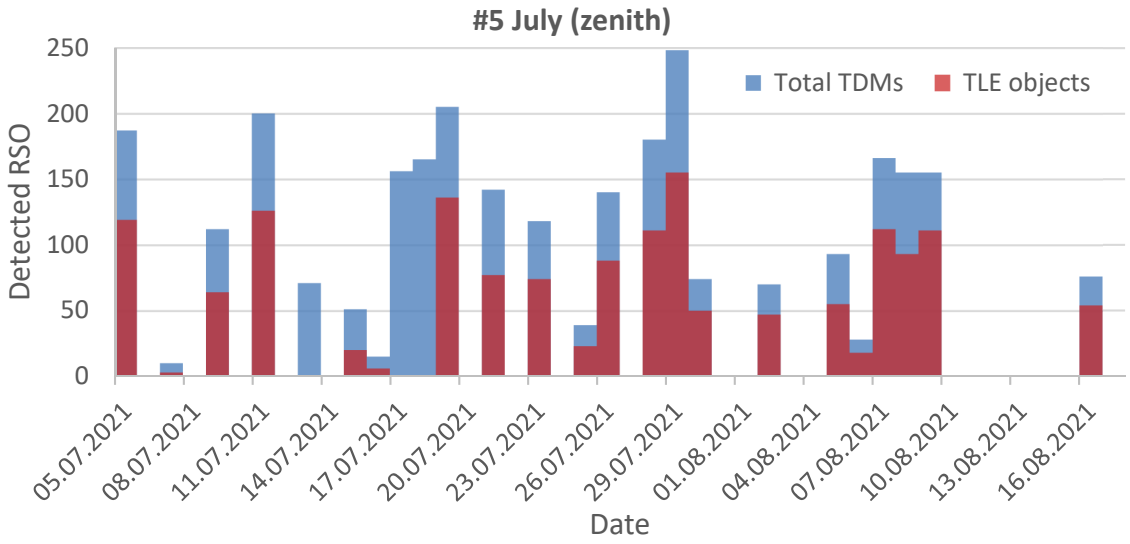

Figure 5.9: Number of recorded TDM files (blue) and correlated TLE objects of each night during campaign #5 July under zenith LOS.

At zenith LOS 20% more objects could not be identified in summer compared to winter (compare campaign #1 to #5), while under 45° N 10% more objects could not be identified (compare campaign #2 to #4). With increasing absolute number of detected RSO, which is a result of higher detection efficiency related to weather and observation conditions, the percentage of unidentified RSO increases as well. This points towards the assumption that unidentified RSO are more likely smaller objects, which are the better detected, the higher the detection efficiency.

In total 36% of all detected object could not be identified by the TLE catalog. It can be seen that the value of 40% unpublished objects in the TLE catalog [1] is confirmed very well with 36% of uncorrelated RSO measured by APPARILLO2.

Campaign	Date	Nominal LOS	Detected RSO (TDM files)	Identified TLE RSO	Percentage of unidentified RSO
#1 December	20.11.2020 - 23.12.2020	Zenith	831	704	15.28
#2 February	18.02.2021 - 08.03.2021	45° N	4717	3315	29.72
#3 March	09.03.2021 - 29.03.2021	45° W	1780	1340	24.72
#4 April-June	30.03.2021 - 04.07.2021	45° N	13423	7913	41.05
#5 July	05.07.2021 - 19.08.2021	Zenith	2418	1512	37.47
Total			23356	14903	36.19

Table 5.5: Number of detected RSO, correlated RSO with the TLE catalog [15] and percentage of unidentified RSO for each campaign.

In the following, the detection rates are analyzed for each LOS individually from data taken in campaigns #1 to #5, and compared to PROOF simulations.

Zenith LOS:

Figure 5.10 shows the hourly detection rate of the first campaign between November 20th to December 23rd under zenith LOS. It can be seen that the system does not show any detections around midnight, as predicted by PROOF simulations, but high detection rates of up to 37 obj/h after sunset and before sunrise (terminator phase). The two observed detection windows are each about 3 h long, while PROOF predicted a duration of 2 h for each detection window. Low detection rates are caused by weather conditions limiting the observation window. The highest detection rate measured 37 objects per hour on 14th of December, while detection rates mostly ranged between 25 and 30 objects per hour.

Figure 5.11 shows the hourly detection rate for the last campaign #5 July. It can be seen that the detection window ranges over the entire night without a gap between 8 pm and 2 am UTC. The observed detection window of the system is 3 times larger, with 6 h, compared to 2 h simulated by PROOF, see Figure 4.15. The maximum detection efficiency for campaign #5 is much higher with 49 obj/h compared to the #1 December campaign with 36 obj/h. However,

a raise in the detection rate to the summer was not predicted by the simulations, which indicates that circumstances not considered by PROOF play a significant role for the real detection efficiency.

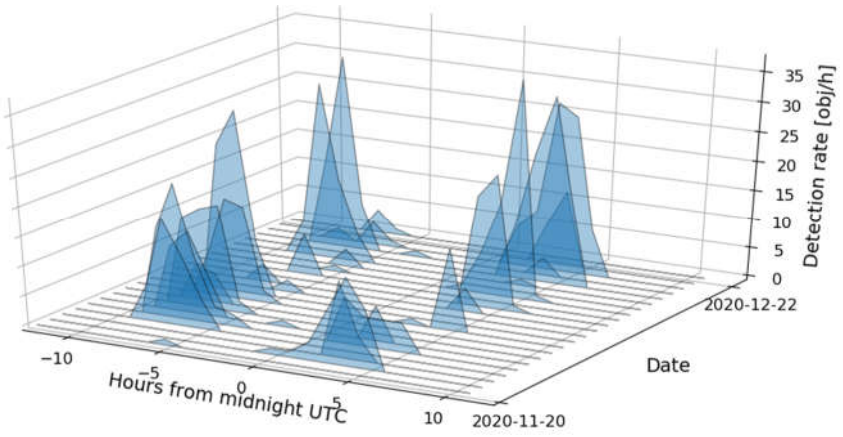

Figure 5.10: Waterfall plot of the detection rates per hour measured from UTC midnight during campaign #1 December under zenith LOS. Days without any detections are excluded.

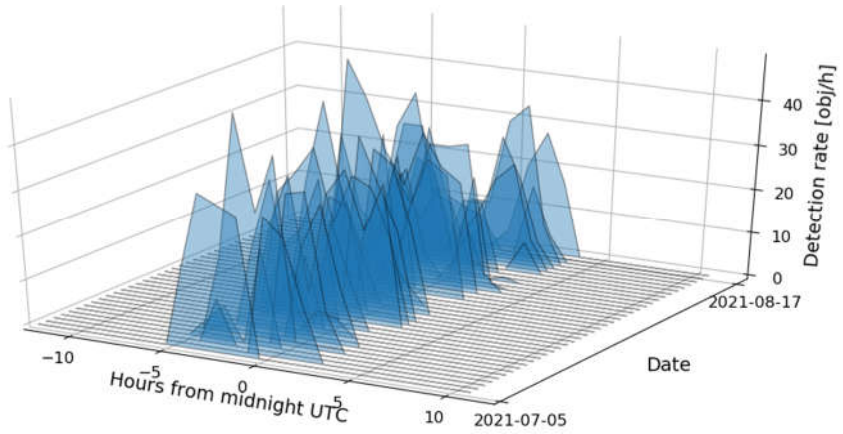

Figure 5.11: Waterfall plot of the detection rates per hour measured from UTC midnight during campaign #5 July under zenith LOS. Days without any detections are excluded.

Figure 5.12 and Figure 5.13 show how the system interpreted the weather conditions by the weather station across the days from December 3rd to 23rd, and the resulting detection rate (blue). It can be seen that the system correctly interprets good observation conditions by the weather sensor, consequently the detection rate rises. The only unexpected behavior, which is observed, was wrong recording of the $\measuredangle T_{Sky}$ when the weather sensor became wet. This can be seen as fine lines (orange) in the clear sky condition in those figures. This caused the system to start observation falsely for a few minutes. However, the image processing handled those situations without a single false-positive detection.

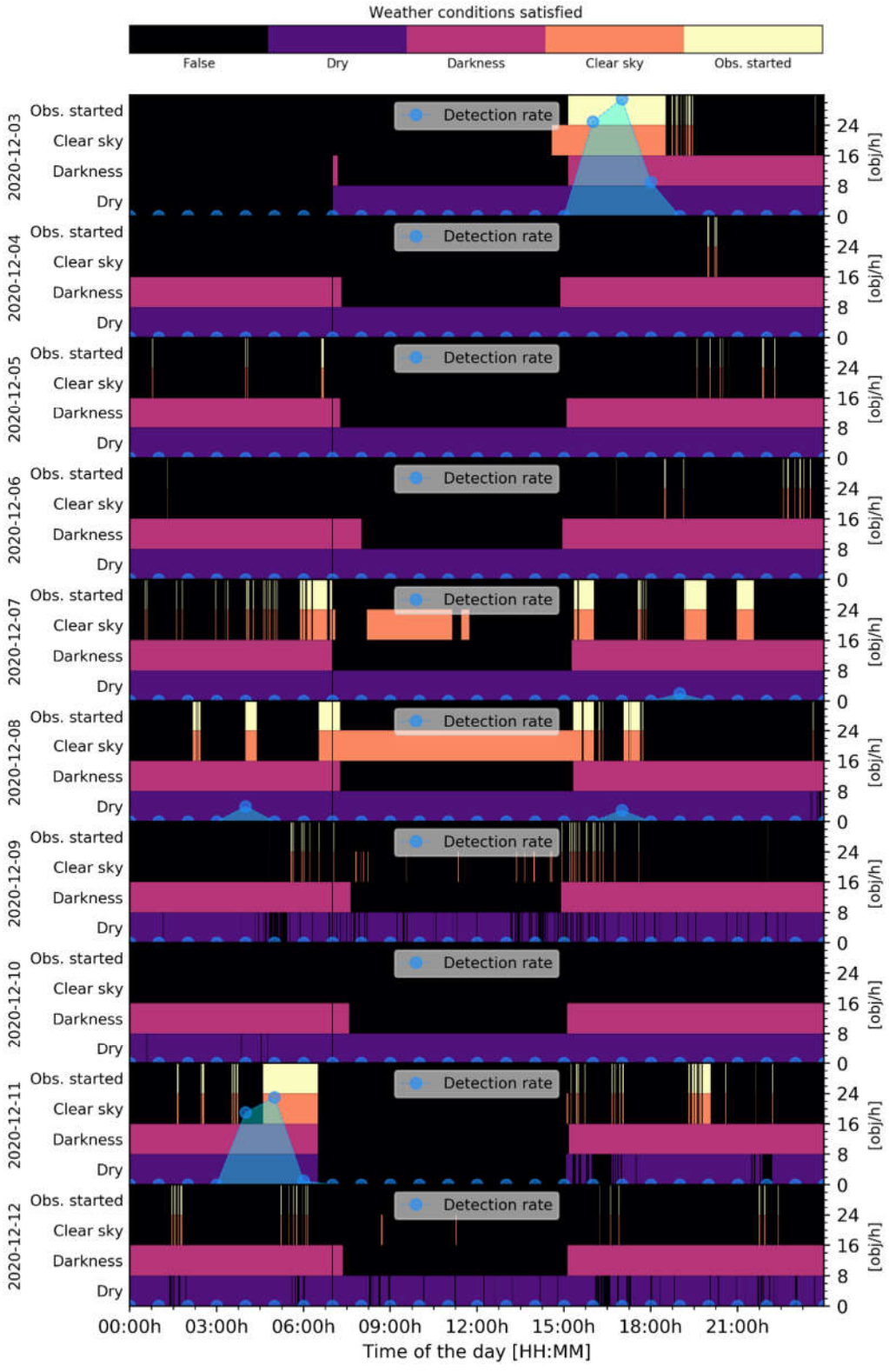

Figure 5.12: Measured weather conditions and the corresponding detection rate of the APPARILLO2 system between December 3rd to 12th. Each of the ten days is shown in a separate row. Within each the conditions: Dry (purple), Darkness (magenta), Clear sky (orange) and Observation started (yellow) are shown in four separate rows over the UTC time of the day. If any condition is not satisfied it is shown in black. On the right axis the hourly detection rate is shown in blue over the time of the day. Source: [85].

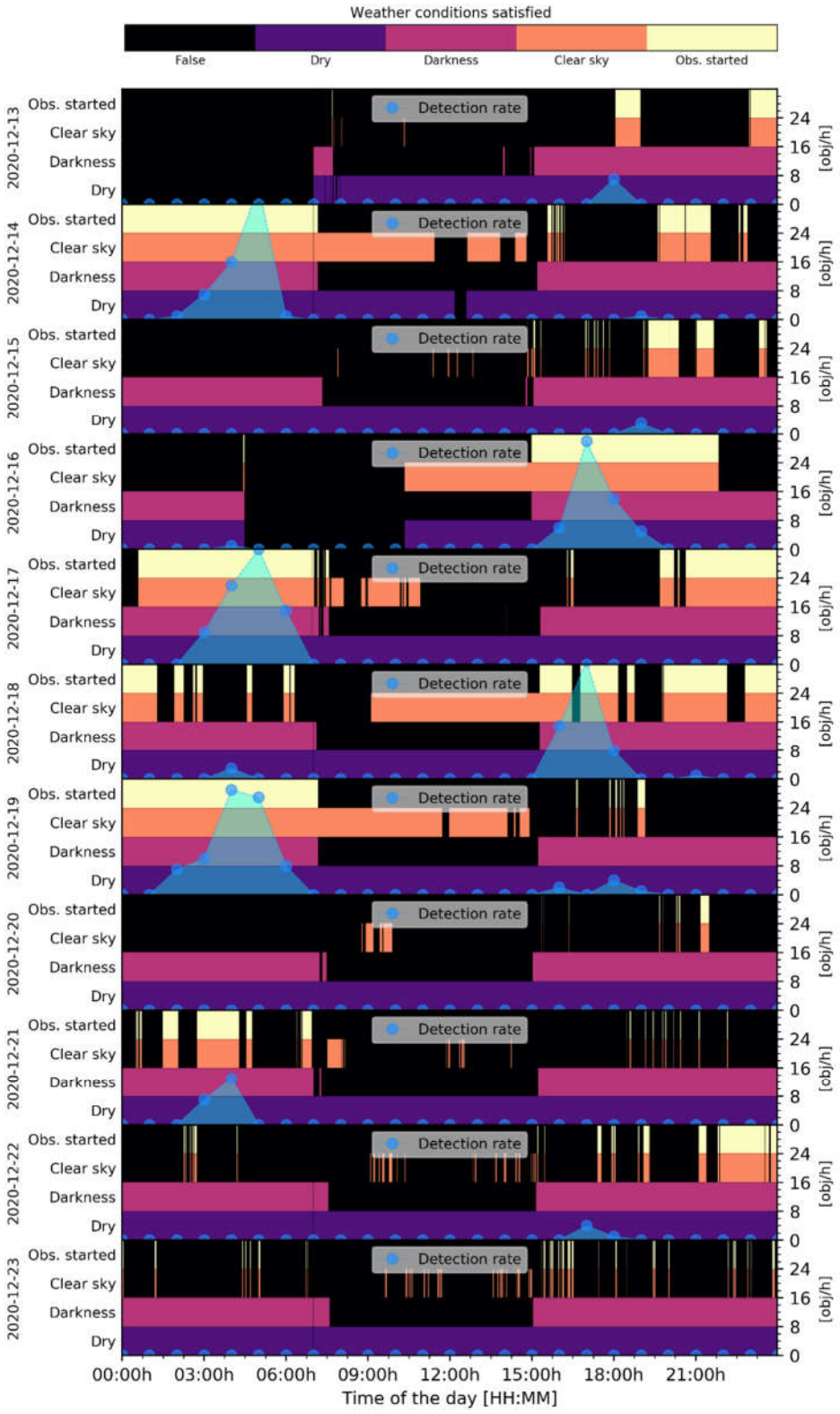

Figure 5.13: Measured weather conditions and the corresponding detection rate of the APPARILLO system between December 13th to 23rd. Each of the 11 days is shown in a separate row. Within each the conditions; Dry (purple), Darkness (magenta), Clear sky (orange) and Observation started (yellow) are shown in four separate rows over the UTC time of the day. If any condition is not satisfied it is shown in black. On the right axis the hourly detection rate is shown in blue over the time of the day. Source: [85].

45° West LOS:

Figure 5.14 shows the hourly detection rate under 45° W LOS during campaign #3 March. Compared to simulations the detection windows are slightly longer with about 2 h before sunset and 3.5 h after sunset, while PROOF predicted 1 h and 3 h, see Figure 4.18. The measured detection rate rises and falls over a duration of about 2 h while PROOF showed a steeper rise and fall of less than 30 min. This indicates that PROOF is not properly simulating the Earth shadow. The detection rate before sunrise is about 2 times higher than after sunset, where PROOF predicted only 20% higher rates. Compared to zenith LOS, the larger detection rates under 45° LOS result from the larger observed orbital volume, as already indicated by PROOF.

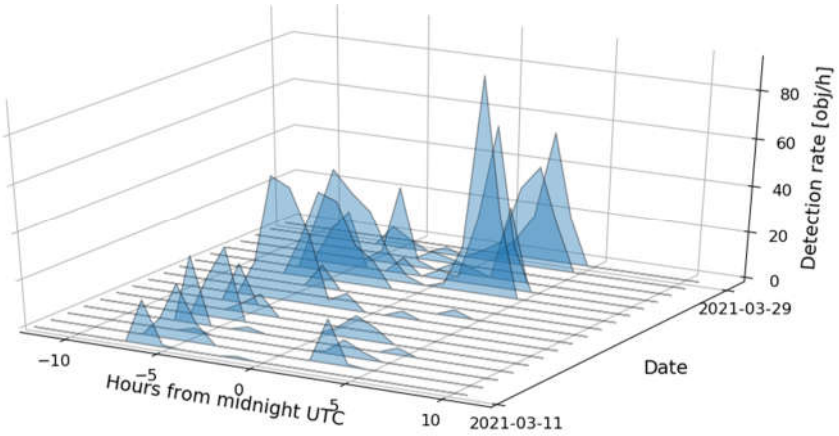

Figure 5.14: Waterfall plot of the detection rates per hour measured from UTC midnight during campaign #3 March under LOS to 45° W. Days without any detections are excluded.

45° North LOS:

For the analysis of data taken under 45° N LOS the campaigns #2 February and #4 April-June are used. At 45° N LOS it becomes more noticeable, compared to 45° W LOS, that detection rates are much higher compared to zenith LOS. Detection rates during campaign #2 February are as high as 90 obj/h and detection windows before sunrise and after sunset are each about 4 h long. Detection rates from all campaigns performed under 45° N LOS are shown in Figure 5.15 as a waterfall plot. It can be seen that the two detection windows merge to a single detection window. When comparing campaign #2 February to campaign #4 April-June, the peak detection rate is once again higher to the summer. The two detection windows in winter merge to a single one by the end of April, reaching a duration of 5.5 h until June. In contrast, PROOF predicted a single detection window by the beginning of April, while the detection window reaches 2.5 h in June (see Figure 9.18 in Appendix 9.1.2.2).

Simulations in Figure 4.16 have predicted the same number of detectable RSO for 45° N and 45° W, while the number increased from 1200 under zenith to 2000 under 45°. In contrast, the measurements show much more detected objects under 45° N LOS compared to 45° W and about three times more detections compared to zenith LOS. These results are explainable by the larger observed orbital volume and the fact that a lot of LEO RSO are located on polar orbits.

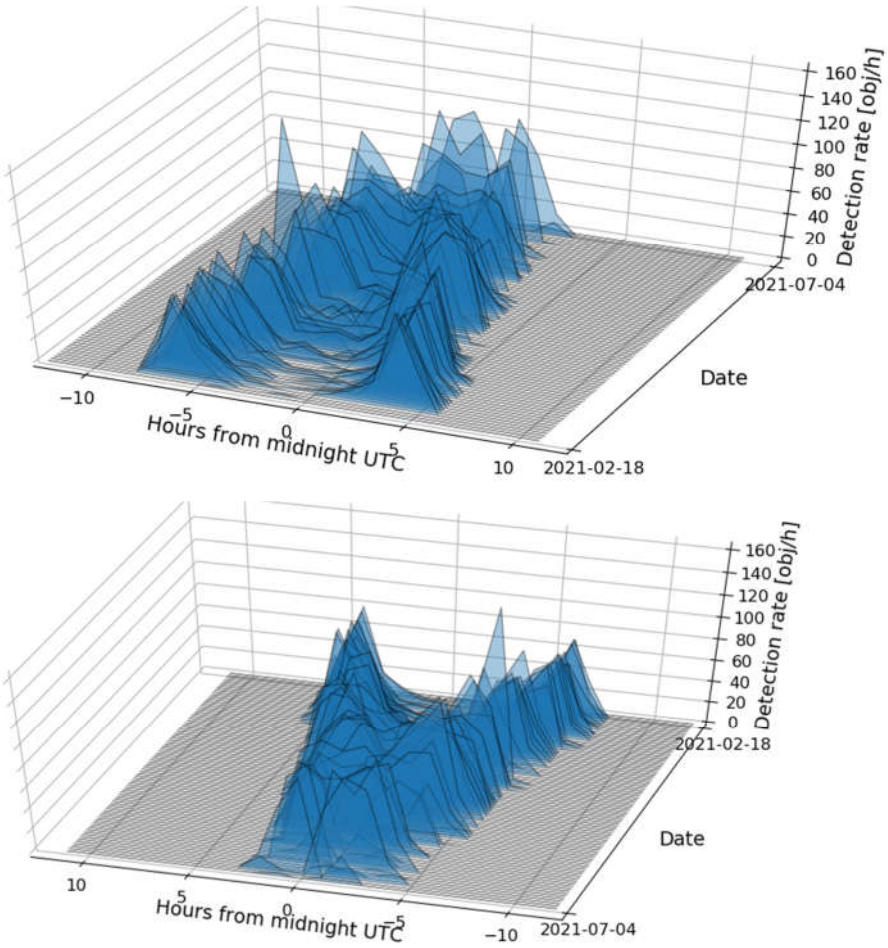

Figure 5.15: Waterfall plot of the detection rates per hour measured from UTC midnight during campaigns #2 February and #4 April-June under LOS to 45° N from two different perspectives. Days without any detections are excluded

Table 5.6 sums up the results of this section and lists the measured peak detection rates compared to the simulated detection rates (if available), as shown in Figure 4.15 under Section 4.2.2.4. A better comparison of detection rate graphs of the campaigns and simulations can be found in Appendix 9.2.3 (Figure 9.30 & Figure 9.31 for zenith LOS, Figure 9.37 for 45° W LOS, and Figure 9.45 & Figure 9.46 for 45° N LOS) and 9.1.2.2 respectively (Figure 9.13 to Figure 9.24).

Campaign	Date	Nominal LOS	Measured peak det. rate (morning/evening) [obj/h]	Simulated peak det. rate [obj/h]
#1 December	20.11.2020-23.12.2020	Zenith	37 / 33	18 / 18
#2 February	18.02.2021-08.03.2021	45° N	90 / 80	-
#3 March	09.03.2021-28.03.2021	45° W	92 / 53	21 / 18
#4 April-June	29.03.2021-04.07.2021	45° N	106 / 162	-
#5 July	05.07.2021-19.08.2021	Zenith	40/49	18 / 18

Table 5.6: Comparison between measured peak detection rate by APPARILLO2 and corresponding simulations of each campaign between November 2020 and August 2021.

5.2.2. DETECTION EFFICIENCY

Again, identified RSO using CELESTRAK NORAD TLE predictions [15] and the SATCAT [3] database are used to group detected objects with regard to their sizes (RCS). For convenient comparison, the equivalent circular diameter is calculated from the RCS using Eq. (3.39). In order to assess performance of APPARILLO2, the detected identified TLE RSO can be compared to all crossing RSO according to the TLE catalog, which gives the detection efficiency. This analysis is only performed using identified RSO, where the RCS is available in the SATCAT database. Any other recorded TDM is not included in this analysis. Again, graphs shown in Figure 5.16 to Figure 5.19 are grouped by the observed LOS of the campaigns; first zenith, second 45° W, and third 45° N.

All four graphs (Figure 5.16 to Figure 5.19) have in common that the number of small objects is highest for the crossing TLE RSO and almost constantly decreasing with larger object diameter. The amount of detected small objects on the other hand is very low, however increases exponentially up to RSO diameter of 2 m to 3 m. For even larger RSO the absolute numbers of RSO is decreasing, hence, fewer objects are detected by the system.

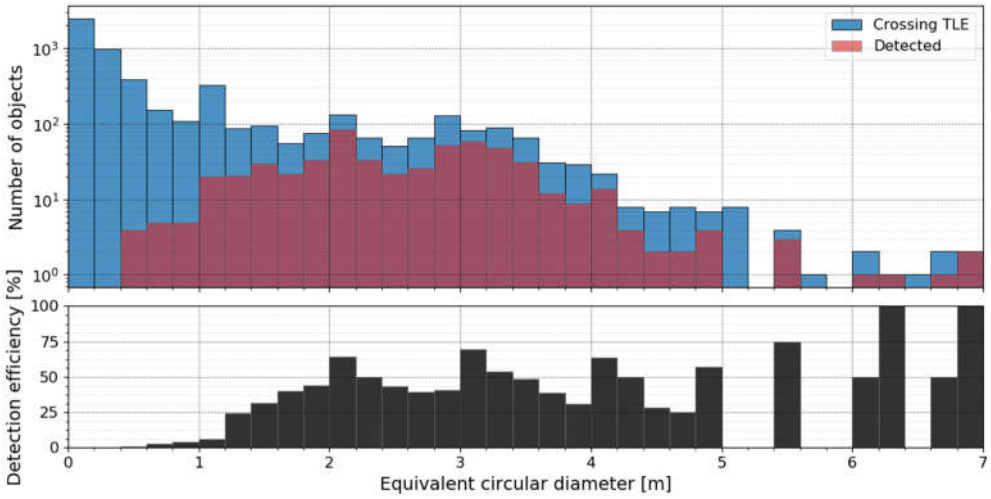

Figure 5.16: Top: Histogram of detected RSO by APPARILLO2 (red) and crossing TLE RSO (blue) according to CELESTRAK's NORAD TLE predictions grouped by equivalent circular RCS diameter. Bottom: The corresponding detection efficiency (black) grouped by equivalent circular RCS diameter. The objects were recorded during the campaign #1 December under zenith LOS.

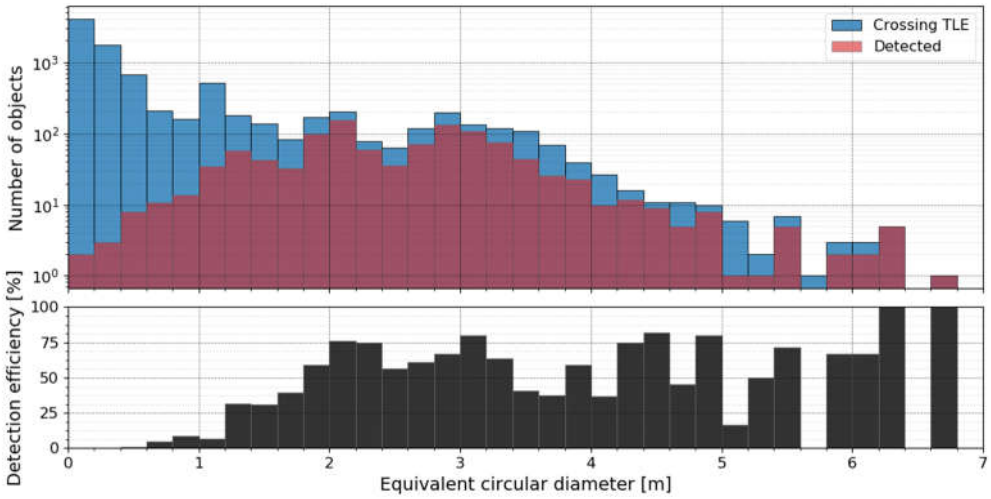

Figure 5.17: Top: Histogram of detected RSO by APPARILLO2 (red) and crossing TLE RSO (blue) according to CELESTRAK's NORAD TLE predictions grouped by equivalent circular RCS diameter. Bottom: The corresponding detection efficiency (black) grouped by equivalent circular RCS diameter. The objects were recorded during the campaign #5 July under zenith LOS.

The total amount of crossing objects varies between observation due to different observation duration, thus the detection efficiency provides the better comparison. The relation between detected and crossing TLE object gives the detection efficiency and is shown in the bottom part in Figure 5.16 to Figure 5.19.

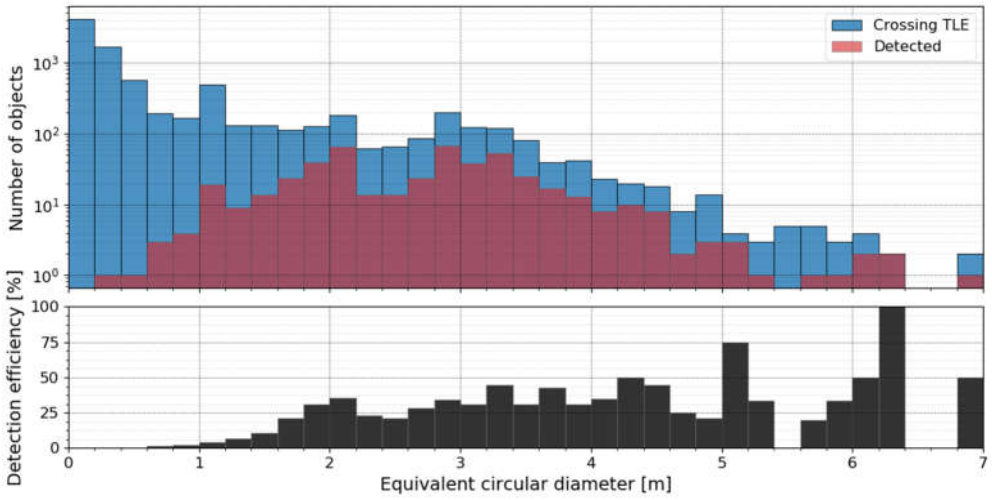

Figure 5.18: Top: Histogram of detected RSO by APPARILLO2 (red) and crossing TLE RSO (blue) according to CELESTRAK's NORAD TLE predictions grouped by equivalent circular RCS diameter. Bottom: The corresponding detection efficiency (black) grouped by equivalent circular RCS diameter. The objects were recorded during the campaign #3 March under 45° W LOS.

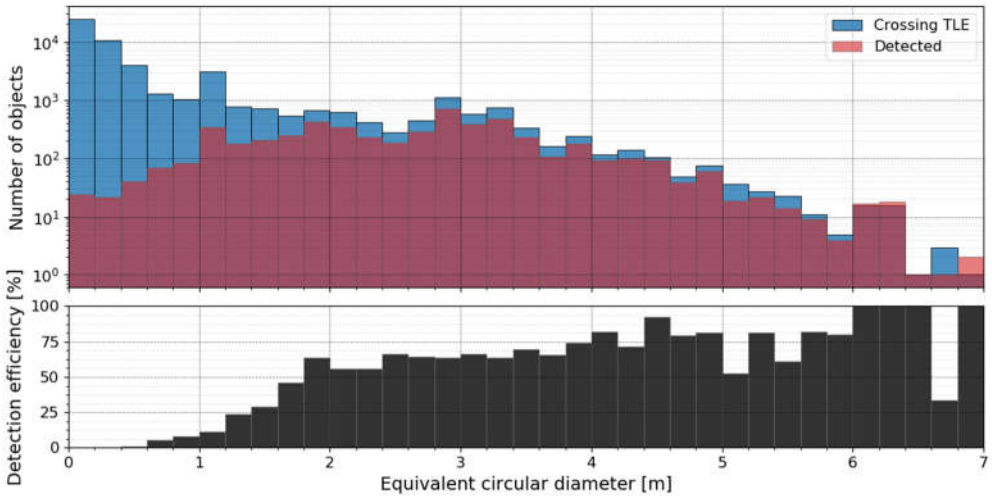

Figure 5.19: Top: Histogram of detected RSO by APPARILLO2 (red) and crossing TLE RSO (blue) according to CELESTRAK's NORAD TLE predictions grouped by equivalent circular RCS diameter. Bottom: The corresponding detection efficiency (black) grouped by equivalent circular RCS diameter. The objects were recorded during the campaigns #2 February and #4 April-June under 45° N LOS.

It can be seen that the detection efficiency of detected RSO by APPARILLO2 is smaller with smaller object size and becomes larger with larger object size reaching a detection efficiency of about 50%. This relation was predicted by the PROOF simulations shown previously in Figure 4.13 under Section 4.2.2.2, however the RSO diameter where the detection efficiency reaches its peak is much larger in the measurements with 2 m compared to the predicted 0.6 m. The

reason for the smaller detection threshold predicted by PROOF is its idealistic sensor model, which does not consider any weather conditions and artificial background light sources. In addition, for larger RSO the measured detection efficiency is again higher than the 45% by PROOF predictions, reaching up to 100%. However, due to few events for RSO larger than 4 m the given efficiencies possess a high statistical uncertainty. The overall observed higher detection efficiencies compared to PROOF simulation results from the fact that PROOF predicted a much shorter detection windows compared to the observed detection window duration.

Over all campaigns, the 10% detection efficiency is reached at about 1.2 m ±0.2 m and 50% detection efficiency at about 1.8 m ±0.2 m (except under 45° W). Under 45° N higher detection efficiencies for smaller objects are observed compared to zenith and 45° W LOS. This behavior was not predicted by the simulations shown in Figure 4.5 under Section 4.2.1.3. Additionally, the detection efficiencies under 45° N of RSO larger than 2.25 m are higher as well compared to 45° W LOS and even zenith LOS. This observation may result from better illumination conditions of the RSO under 45° N LOS. As already mentioned, an obvious performance boost to the summer season is visible when comparing campaigns #1 and #5, see Figure 5.16 and Figure 5.17.

Comparing observations of the first staring system in 2016 to APPARILLO2 campaign #5 it is noticeable that the overall detection efficiency is lower, see Figure 9.25 in Appendix 9.2.3. At an RCS of 1 m² APPARILLO2 has a detection efficiency of about 35%, while the first staring system shows 50%. At 2.25 m² the efficiency rises to 75% using APPARILLO2 and 100% using the first staring system. This results from the fact that the first staring system was operated under pristine conditions only, while APPARILLO2 operated 24/7. Thus, clouds or higher background illumination were existent from time to time, reducing the overall detection efficiency. The efficiency of RSO smaller than an RCS of 0.5 m² is very similar with about 10% for both systems. This points towards the fact, that the sensitivity is not affected by the latest image processing deployed with APPARILLO2.

5.2.3. DETECTION THRESHOLD

To obtain physical properties and optical cross section (OCS) of detected RSO, ESA's DISCOS catalog [89] is used. This information allows evaluating the system's detectability in dependence on RSO dimensions, OCS and mass. The catalog does not provide information for every identified TLE object, which limits the amount of analyzed RSO. To evaluate the

physical dimensions of detected RSO all objects are sorted according to their volume in ascending order for each LOS, see Figure 5.20 to Figure 5.25. Analyzing the smallest RSO in volume with respect to OCS and RCS, delivers the dimensions of the smallest detected objects (detection threshold).

Zenith LOS:

For zenith LOS all detected and identified RSO's volume and mass during campaigns #1 December and #5 July are shown in Figure 5.20. A histogram on each axis shows the corresponding distributions.

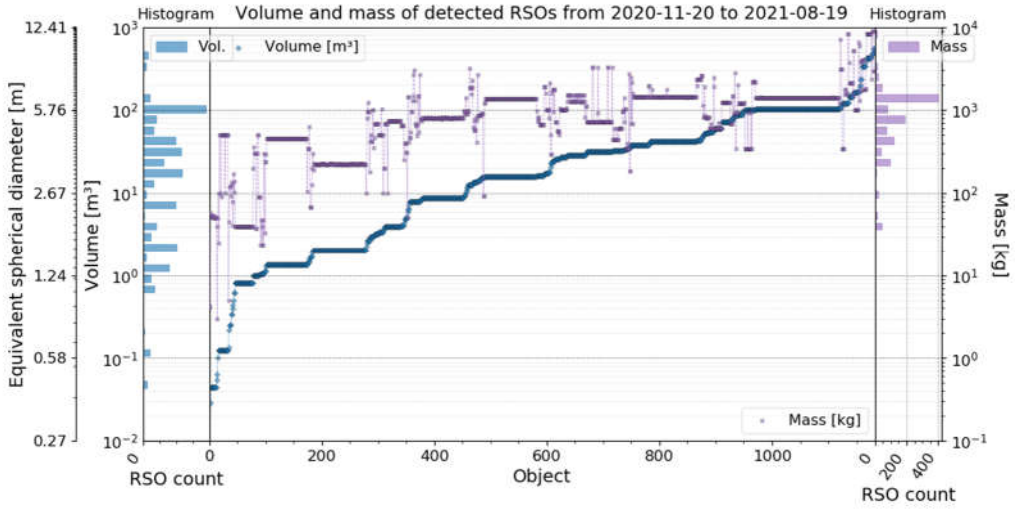

Figure 5.20: Every object recorded during campaigns #1 December and #5 July sorted according to their volume in ascending order. The volume (blue) and mass (purple) according to DISCOS [89] is shown for each RSO. The corresponding mass distribution is shown on the right y-axis and volume distribution on the left y-axis.

Figure 5.21 shows the dimensions as well as the equivalent spherical and circular diameter for the smallest objects within the same dataset. The distributions of the equivalent spherical diameter of the volume and equivalent circular diameter of the RCS and OCS are presented to the right. The 50 smallest RSO according to their volume detected during campaign #1 December and #5 July, according to their volume are shown in Figure 5.21 (bottom).

The smallest 8 RSO are thin but long objects, between 0.2 m to 0.5 m in height and length, and more than 4 m in depth. Their equivalent OCS circular diameter is considerably larger than the equivalent spherical diameter calculated from their volume. The smallest cube shaped RSO are 0.37 m by 0.37 m by 0.5 m and their equivalent circular diameter from the OCS is similar to

the equivalent spherical diameter with about 0.5 m and 0.6 m (object 9 and 10). Hence, one can conclude that 0.5 m is the detection threshold of APPARILLO2 for zenith LOS. This detection threshold is about the same threshold PROOF simulations predicted at a detection efficiency of 5% for the FLI PL0900 and 200mm f2 lens (see Figure 4.23).

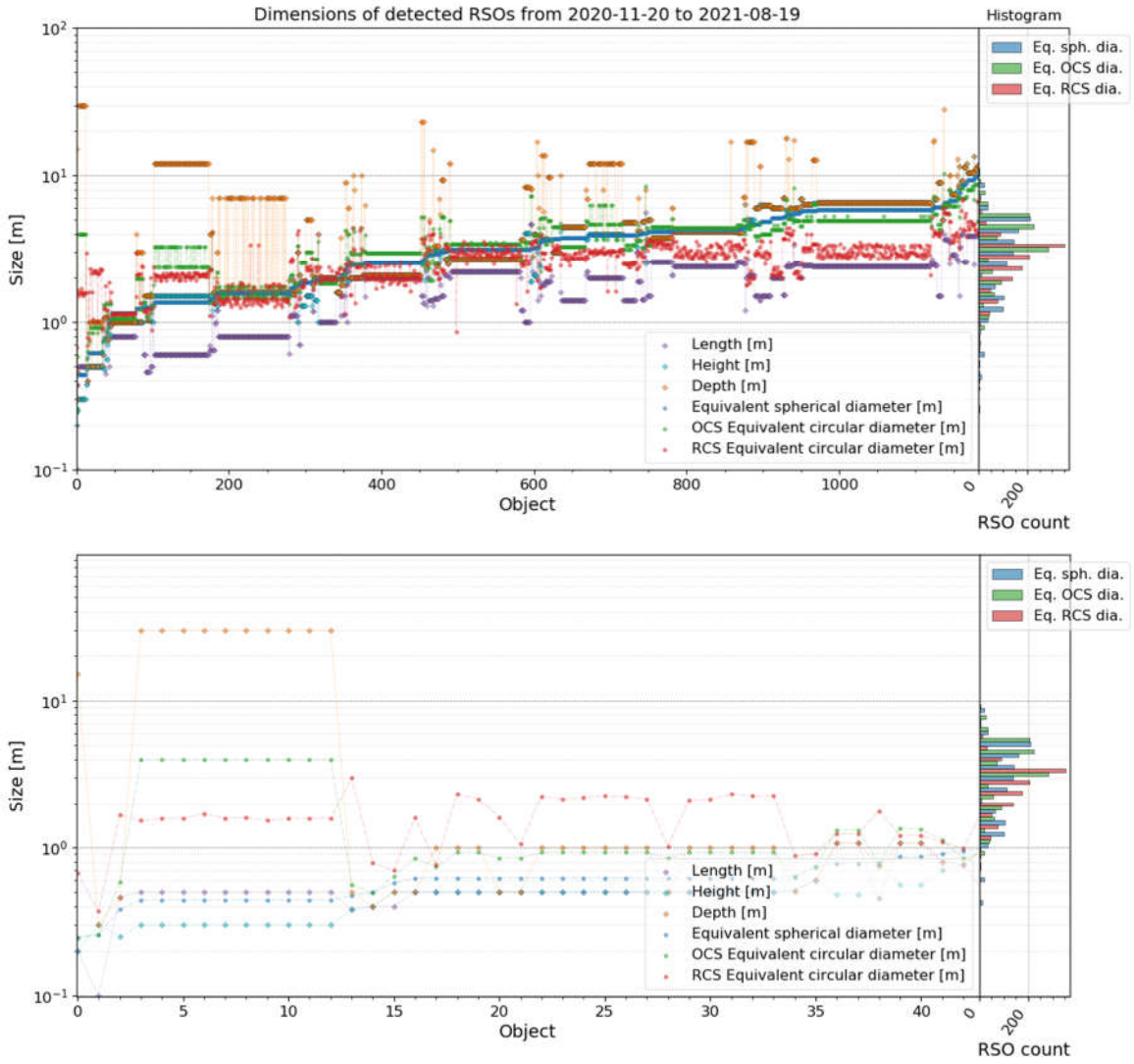

Figure 5.21: The dimensions, equivalent cross sectional and spherical diameters of every identified object (top) recorded during campaigns #1 December and #5 July under zenith LOS, sorted according to its volume in ascending order. In the bottom graph only the smallest objects are shown. The RSO's length (purple), height (cyan), depth (orange), equivalent spherical diameter (blue), equivalent circular OCS (green), and RCS diameter (red) is shown left. The corresponding distributions of the last three equivalent diameter is shown in the same colors on the right y-axis.

45° West LOS:

In Figure 5.22 and Figure 5.23 it can be seen that under 45° W LOS the distribution of detected RSO is very similar to zenith LOS. However, only 4% of the detected RSO are smaller 1 m³ compared to 6% under zenith LOS (Figure 5.20). The dimensions of the smallest detected cube shaped object (object 3 in Figure 5.23) is 0.5 m by 0.6 m by 0.6 m with an equivalent spherical diameter of 0.65 m, see Figure 5.23 (bottom). This detection threshold is larger than under zenith LOS but might result from the smaller dataset from just 550 compared to 950 analyzed objects.

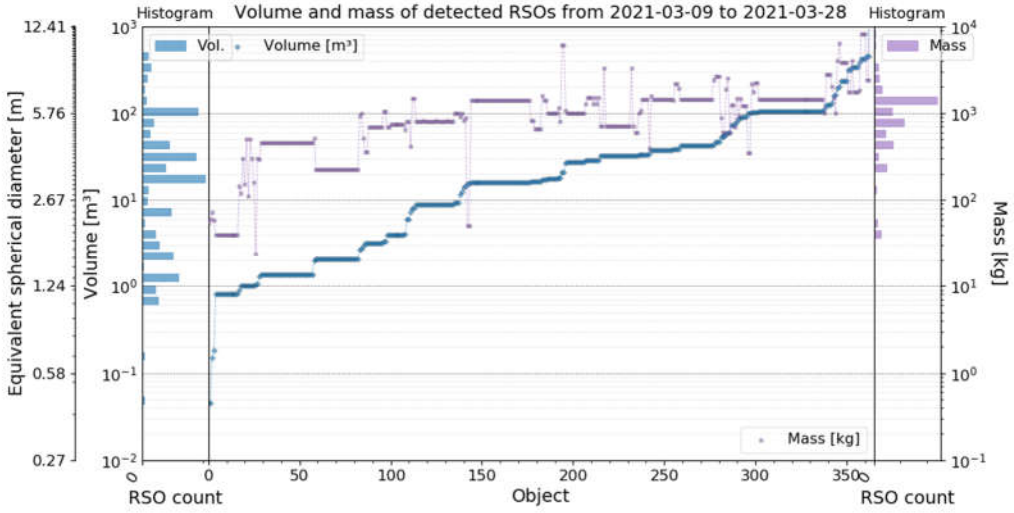

Figure 5.22: Every object recorded during campaign #3 March sorted according to their volume in ascending order. The volume (blue) and mass (purple) according to DISCOS [89] is shown for each RSO. The corresponding mass distribution is shown on the right y-axis and volume distribution on the left y-axis.

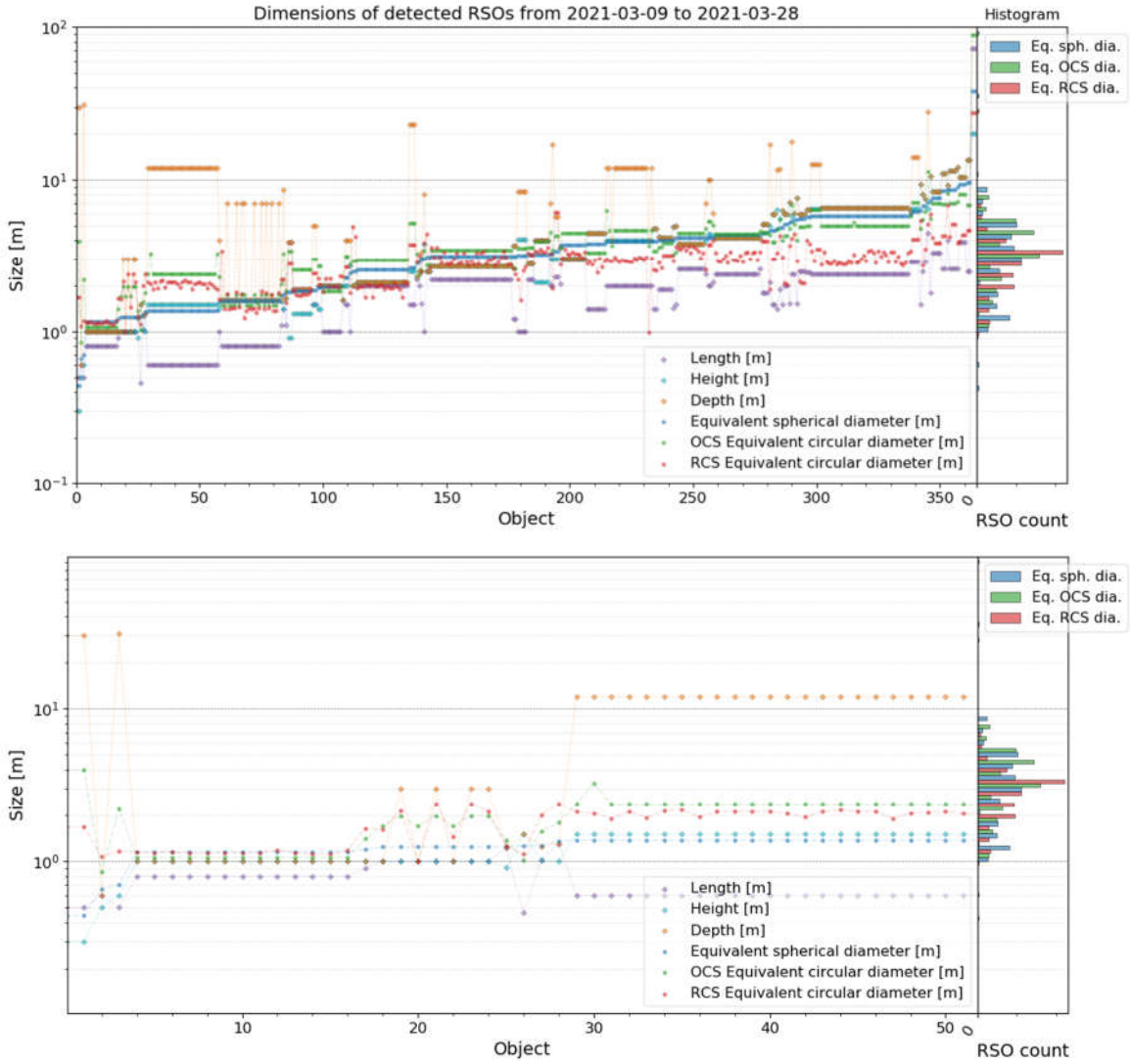

Figure 5.23: The dimensions, equivalent cross sectional and spherical diameters of every identified object (top) recorded during campaign #3 March under 45° W LOS, sorted according to its volume in ascending order. In the bottom graph the smallest objects are shown. The RSO's length (purple), height (cyan), depth (orange), equivalent spherical diameter (blue), equivalent circular OCS (green), and RCS diameter (red) is shown left. The corresponding distributions of the last three equivalent diameter is shown in the same colors on the right y-axis.

45° North LOS:

Figure 5.24 shows the volume & mass and Figure 5.25 the dimensions & equivalent diameters of the detected objects within campaigns #2 February and #4 April-June. Under 45° N LOS the dimensions of the smallest detected cube shaped RSO is 0.2 m by 0.3 m by 0.4 m (object 2 in Figure 5.25) with an equivalent spherical diameter of about 0.3 m. Another big cluster is visible in the bottom graph of Figure 5.25 from object 7 to 24, were the detected RSO measure 0.25 m by 0.45 m by 0.45 m with an equivalent spherical diameter of 0.4 m. This shows that this object size can repeatedly be detected by APPARILLO2 under 45° N LOS.

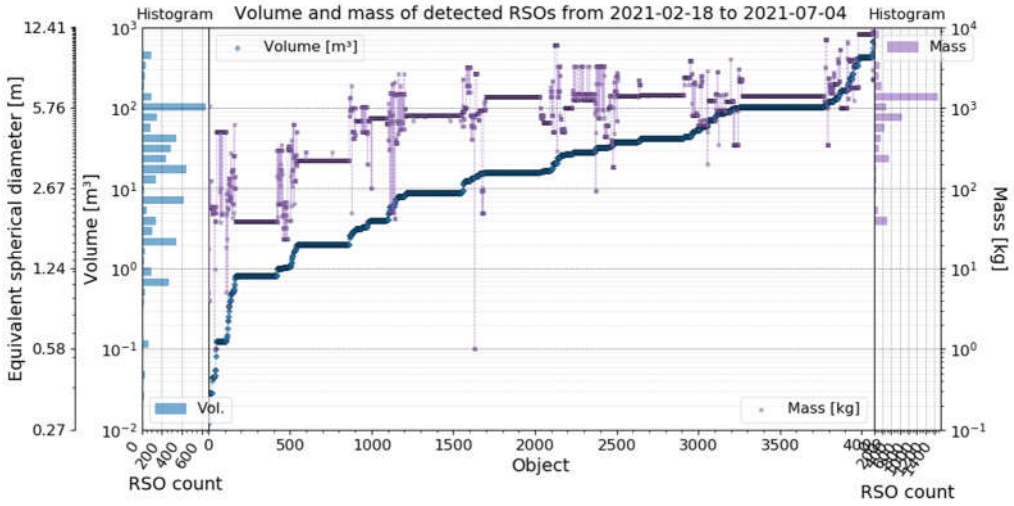

Figure 5.24: Every object recorded during campaign #2 February and #4 April-June sorted according to their volume in ascending order. The volume (blue) and mass (purple) according to DISCOS [89] is shown for each RSO. The corresponding mass distribution is shown on the right y-axis and volume distribution on the left y-axis.

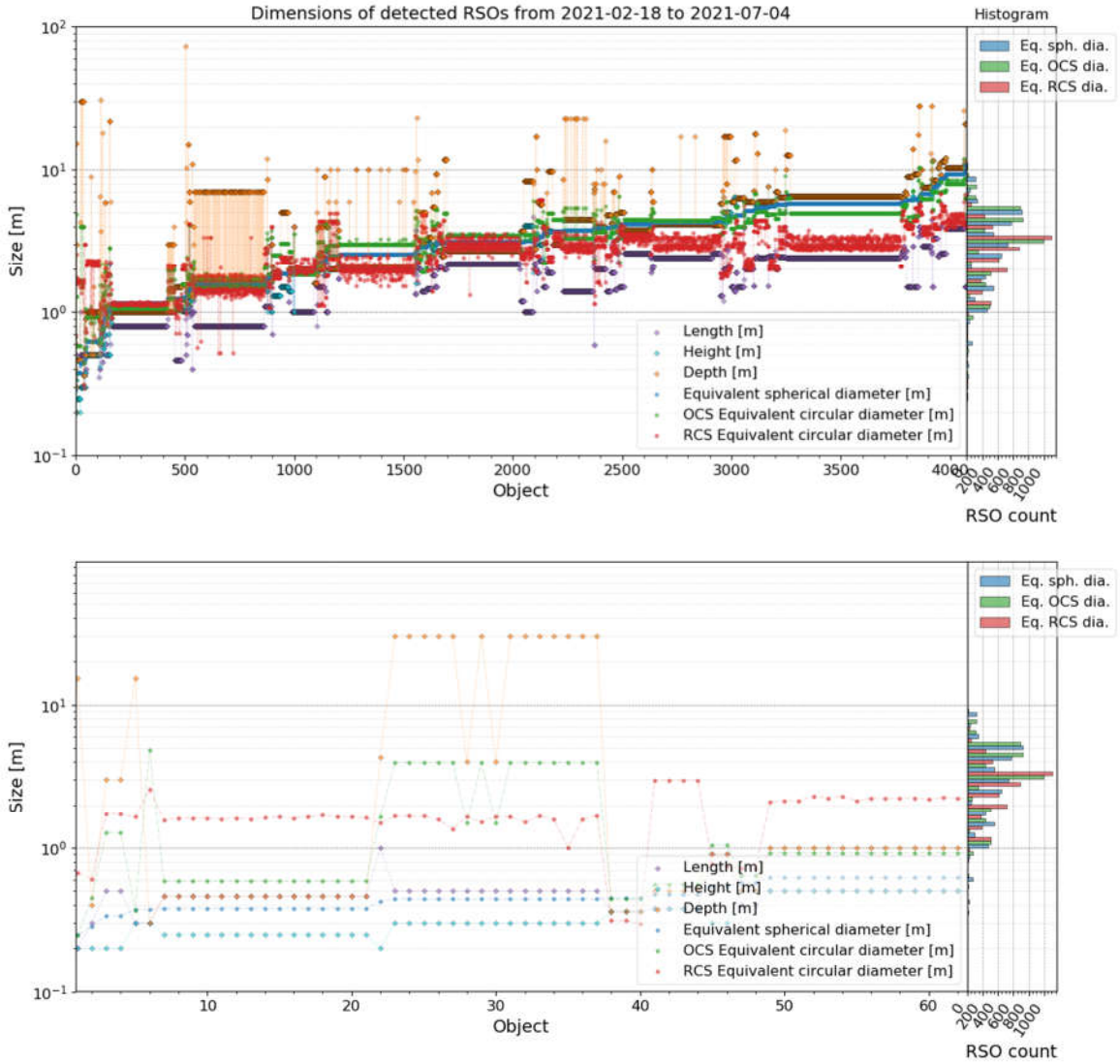

Figure 5.25: The dimensions, equivalent cross sectional and spherical diameters of every identified object (top) recorded during campaigns #2 February and #4 April-June under 45° N LOS, sorted according to its volume in ascending order. In the bottom graph the smallest objects are shown. The RSO's length (purple), height (cyan), depth (orange), equivalent spherical diameter (blue), equivalent circular OCS (green), and RCS diameter (red) is shown left. The corresponding distributions of the last three equivalent diameter is shown in the same colors on the right y-axis.

To provide a comparison between the preceding RSO volume distributions, the percentage of detected objects smaller than 0.1 m³ and 1 m³ are listed in Table 5.7.

Figure 5.26 to Figure 5.28 show the histograms of the equivalent diameters as already shown for each LOS in the right panels of Figure 5.21, Figure 5.23, and Figure 5.25, respectively. Directly comparing these histograms reveals, that under 45° N noticeably more smaller objects

could be detected than under zenith LOS. However, the smallest detected objects of both have 0.25 m in equivalent diameter. Under 45° W, no objects smaller 0.4 m equivalent spherical diameter were detected. Hence, the detection threshold is almost equal between zenith LOS and 45° N, while under 45° W the detection threshold is larger. This may result from the better illumination conditions of the RSO under 45° N LOS compared to 45° W or zenith LOS. Table 5.7 lists the detection thresholds according to different measures for each observed LOS.

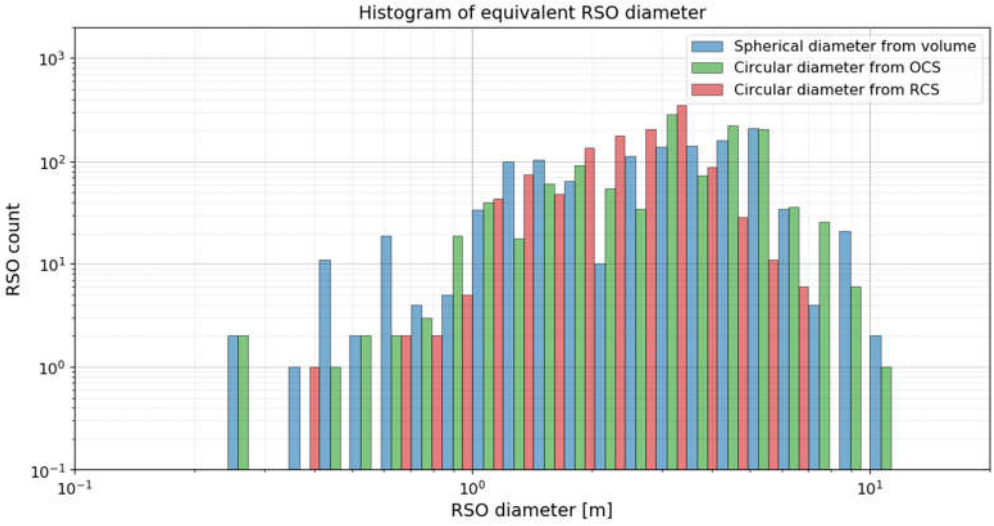

Figure 5.26: Histogram of equivalent circular OCS & RCS, and spherical diameter of all detected RSO during campaigns #1 December and #5 July observed under zenith LOS. The green and red bars are shifted to the right for better visibility.

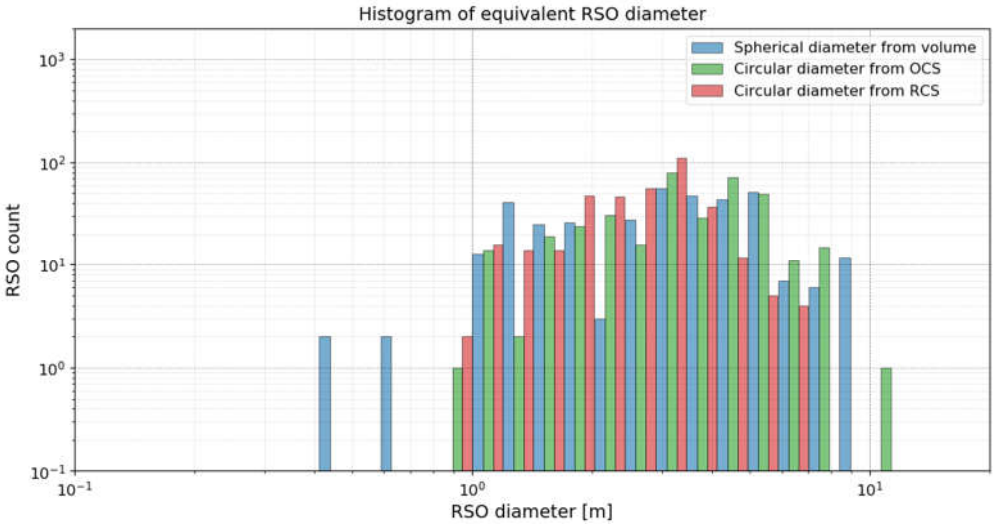

Figure 5.27: Histogram of equivalent circular OCS & RCS, and spherical diameter of all detected RSO during campaign #3 March observed under 45° W LOS. The green and red bars are shifted to the right for better visibility.

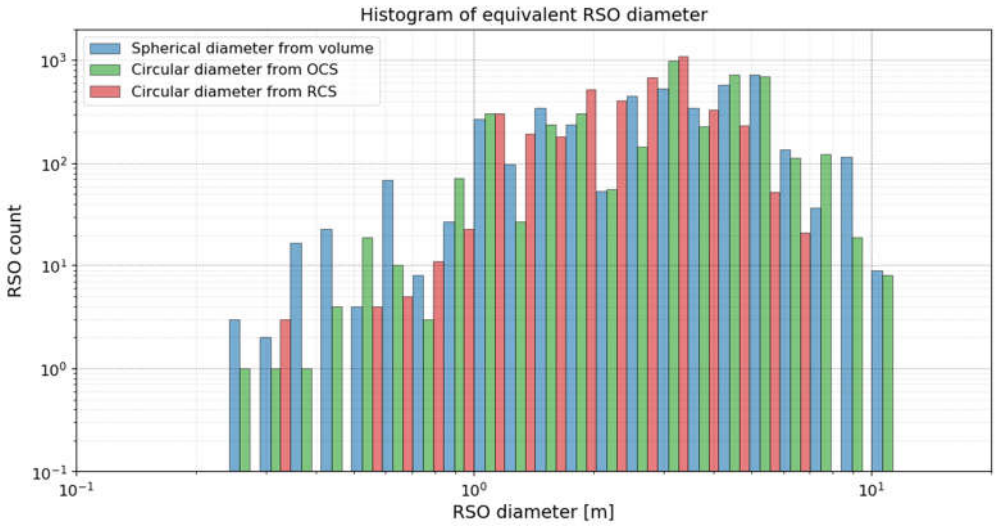

Figure 5.28: Histogram of equivalent circular OCS & RCS, and spherical diameter of all detected RSO during campaigns #2 February and #4 April-June observed under 45° N LOS. The green and red bars are shifted to the right for better visibility.

The analytical link budget model shown in Figure 4.5 under Section 4.2.1.3 predicts a lower detection threshold with lower orbit height. However, the smallest (box shaped) objects have been detected at 1000 km orbit height or above, see Figure 9.28 for zenith LOS and Figure 9.43 for LOS 45° N in Appendix 9.2.3. This may result from the fact that lower objects enter the Earth shadow sooner, hence, it is less likely to detect them. This behavior is also predicted by PROOF simulations, see Figure 4.9 under Section 4.2.2.2.

Note, that the analytical detection threshold in 1000 km orbit height is close to the observed detection threshold with 0.32 m. However, the link budget model also predicts a larger detection threshold at an elevation of 45°, which is strongly depended on the visibility (see Figure 4.5 bottom). In contrast, the observed detection threshold is smaller under 45° N LOS. To account for this behavior, the analytic model can be adopted by a better visibility condition than the assumed 10 km (Section 5.3.1).

Additional figures of the physical property distributions for each campaign can be found in the Appendix 9.2.3. Furthermore, an overview graph over the equivalent spherical diameter depending on the equivalent circular diameter of RCS and OCS is presented, which shows the linearity between OCS and equivalent spherical diameter.

LOS	Zenith	45° W	45° N
Percent RSO < 0.1 m³	1.08%	0.18%	0.90%
Percent RSO < 1 m³	6.16%	3.96%	9.00%
Det. threshold eq. sph. diameter of cubic RSO	0.5 m	0.65 m	0.4 m
Det. threshold eq. OCS diameter	0.25 m	0.9 m	0.25 m
Det. threshold eq. sph. Diameter	0.25 m	0.4 m	0.25 m
RCS detection efficiency of 10%	1 m	1.4 m	1.2 m

Table 5.7: Detection threshold results of APPARILLO2 of all campaigns (#1-#5) for each observing LOS.

5.2.4. ANGULAR RESOLUTION

In the following, the precision of the measurements is analyzed by comparing the extracted equatorial coordinates of RSO to the available TLE predictions [15]. Two exemplary visualizations from a random subset of detected RSO are shown in Figure 5.29 and Figure 5.30. They each show the measured equatorial coordinates (red cross) of about two dozens RSO and their corresponding predicted position (blue circle) calculated using TLE data from that night. The presented RA (γ) and Dec (δ) cover the entire range of observed equatorial coordinates for this night. Overall, the matching between TLE and measurements is very consistent. Any angular distance between observed and predicted positions is encoded into the size of the symbols. Notably, there is an offset displacement between measured and predicted positions, which is similar in magnitude and angular direction for positions of each object.

Equatorial coordinates

Figure 5.31 and Figure 5.32 show the angular displacement distributions between measurement and TLE prediction of a subset of RSO from campaign #5 July for each equatorial coordinate in a separate graph. For the data points of each RSO, the distribution of displacements to predictions are depicted in those two graphs, color coded according to the mean radial angular displacement.

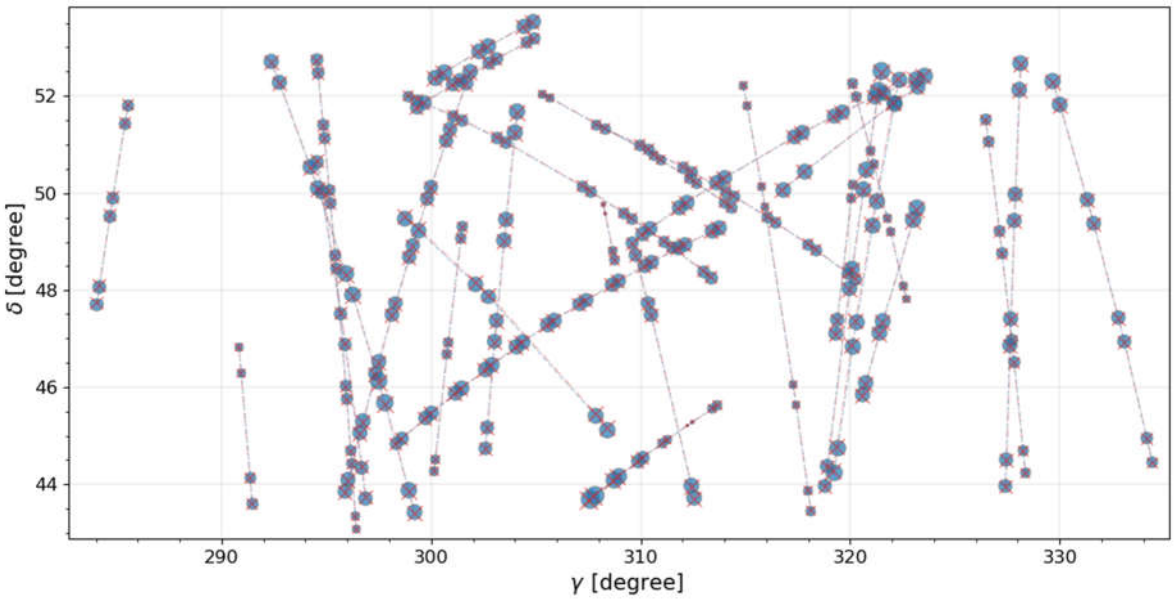

Figure 5.29: Equatorial positions of a subset of detected RSO by APPARILLO2 (red cross) on July 9th 2021 and the corresponding TLE objects (blue circle). The sizes of the markers show the relative angular displacement between measurements and predictions.

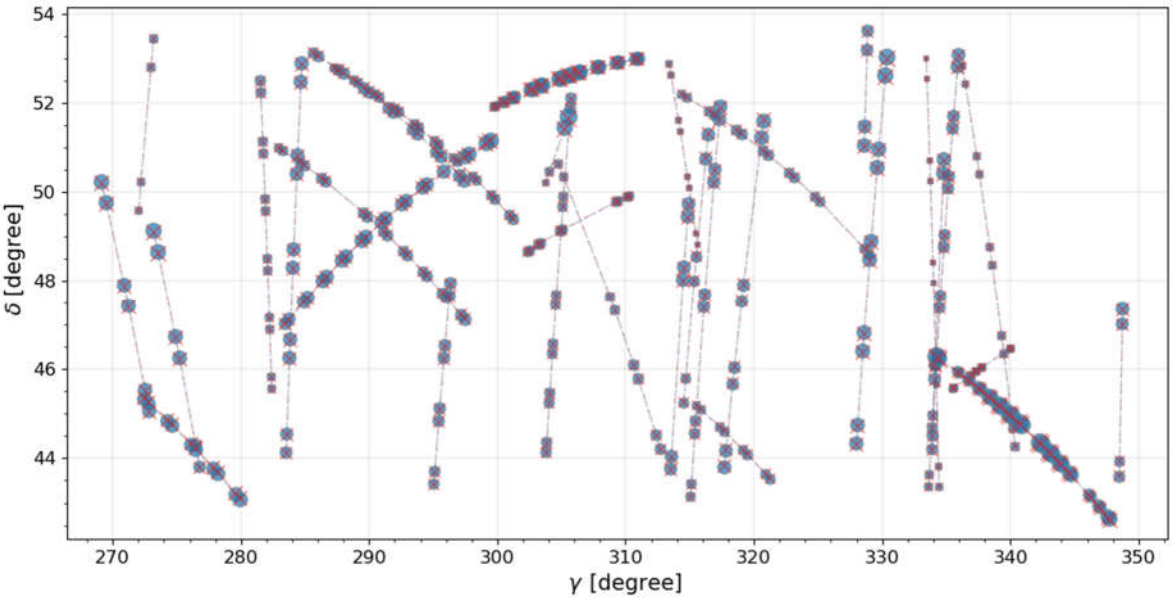

Figure 5.30: Equatorial positions of a subset of detected RSO by APPARILLO2 (red cross) on August 5th 2021 and the corresponding TLE objects (blue circle). The sizes of the markers show the relative angular displacement between measurements and predictions.

A histogram of all measurements taken under zenith LOS for the equatorial coordinates are shown in Figure 5.33. The two histograms show that the angular distance of measurements to the TLE predictions is almost Gaussian distributed with a deviation of about 0.025° and scatter around zero.

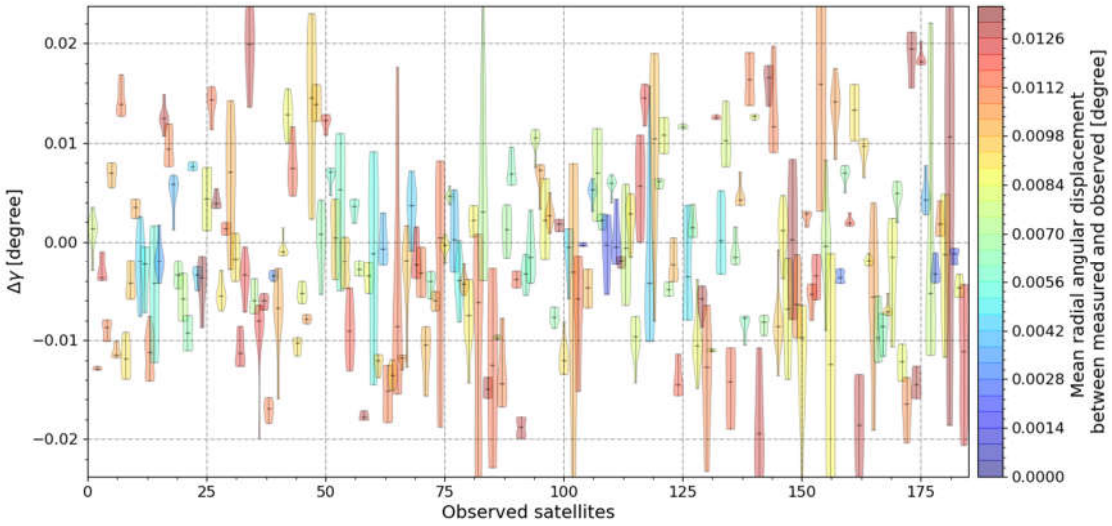

Figure 5.31: RSO's ⊿γ between measured object positions and their TLE predictions. The color corresponds to the mean radial angular displacement of each object to the TLE prediction (not just mean angular displacement in γ), from small values colored in blue to large values colored in red. Presented data is from a subset of measured objects under zenith LOS during campaign #5 July.

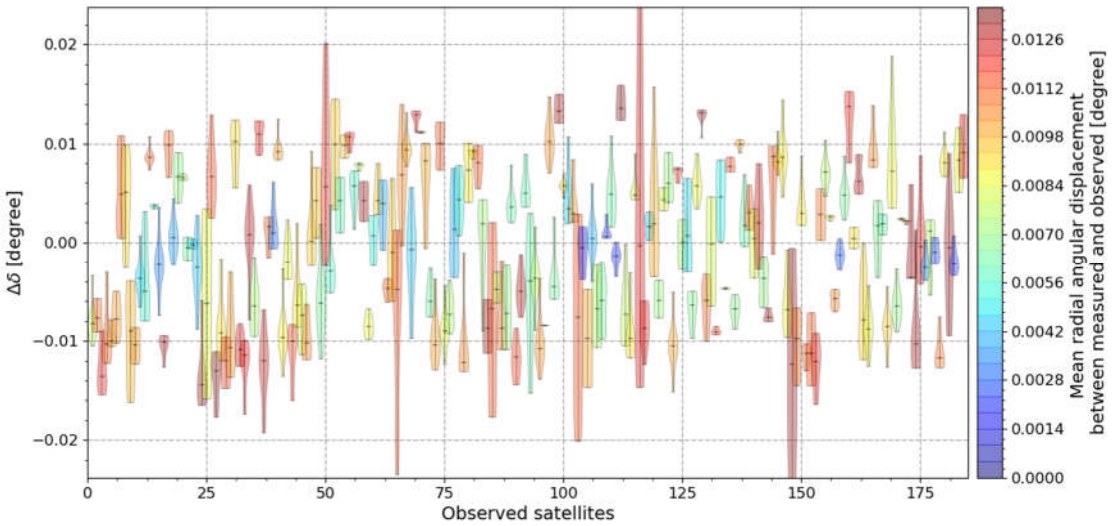

Figure 5.32: RSO's ⊿δ between measured object positions and their TLE predictions. The color corresponds to the mean radial angular displacement of each object to the TLE prediction (not just mean angular displacement in δ), from small values colored in blue to large values colored in red. Presented data is from a subset of measured objects under zenith LOS during campaign #5 July.

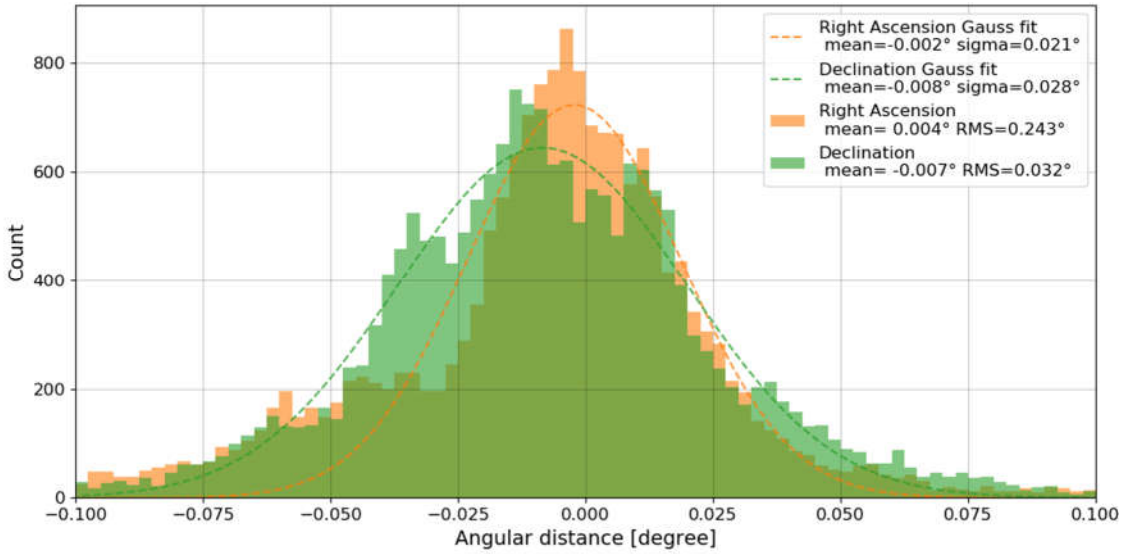

Figure 5.33: Histogram of ∠Ιγ (orange) and ∠Ιδ (green) between measured RSO positions and their TLE predictions. Presented data is from all measured and correlated RSO under zenith LOS during campaigns #1 December and #5 July.

Radial angular displacement

The equatorial coordinates are not equidistant for observations under different LOS. To provide a comparable measure, the radial angular distance is calculated. Under the assumption that the TLE predictions define the real positions, the angular resolution of APPARILLO2 can be determined. Figure 5.34 to Figure 5.36 show the radial angular displacement histograms from all measurements of each observed LOS. The obtained RMS of the angular displacements range between 0.040° and 0.058° yielding to the system's angular resolution.

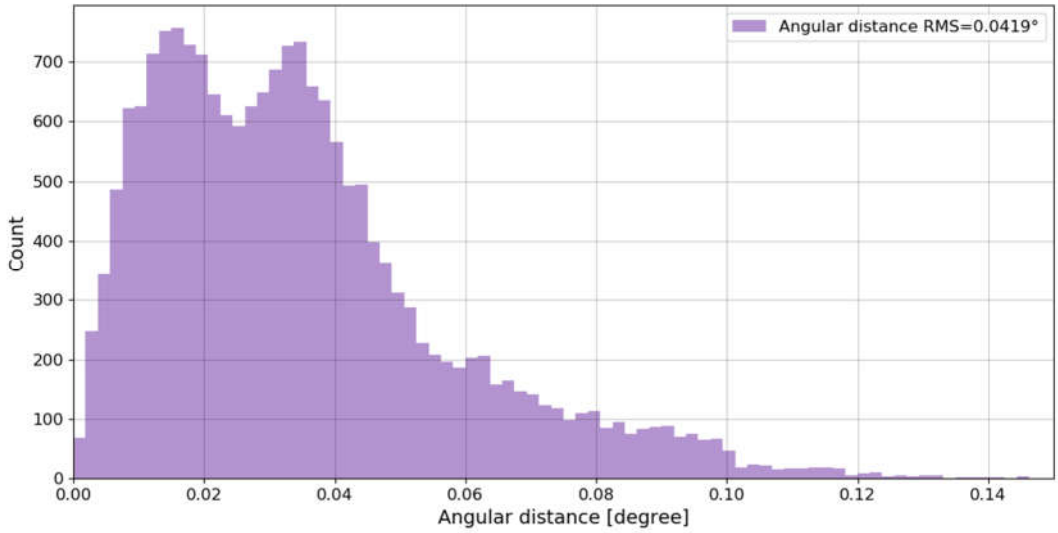

Figure 5.34: Histogram of radial angular displacement between measured RSO positions and their TLE predictions. Presented data is from all measured and correlated RSO under zenith LOS during campaigns #1 December and #5 July.

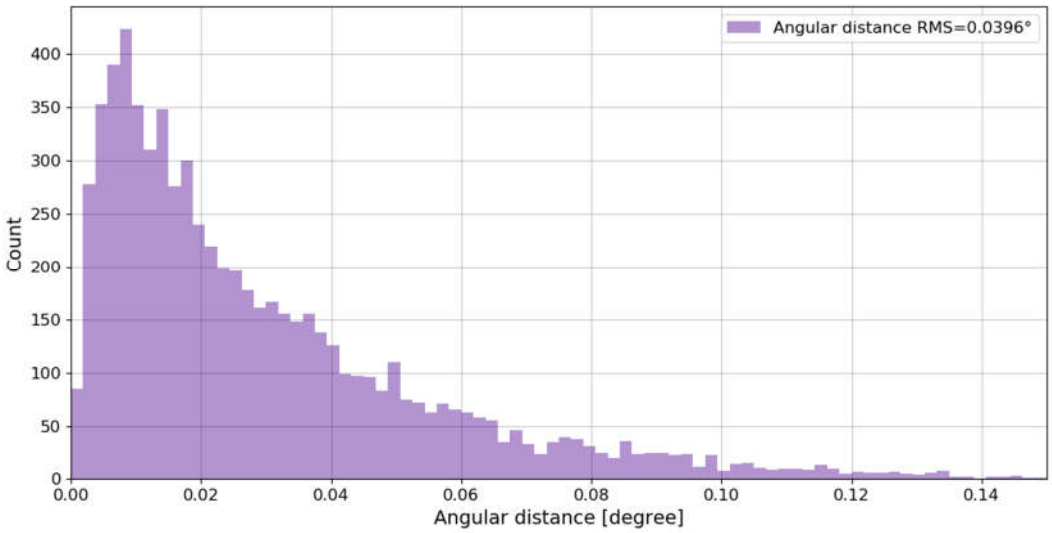

Figure 5.35: Histogram of radial angular displacement between measured RSO positions and their TLE predictions. Presented data is from all measured and correlated RSO under 45° W LOS during campaigns #3 March.

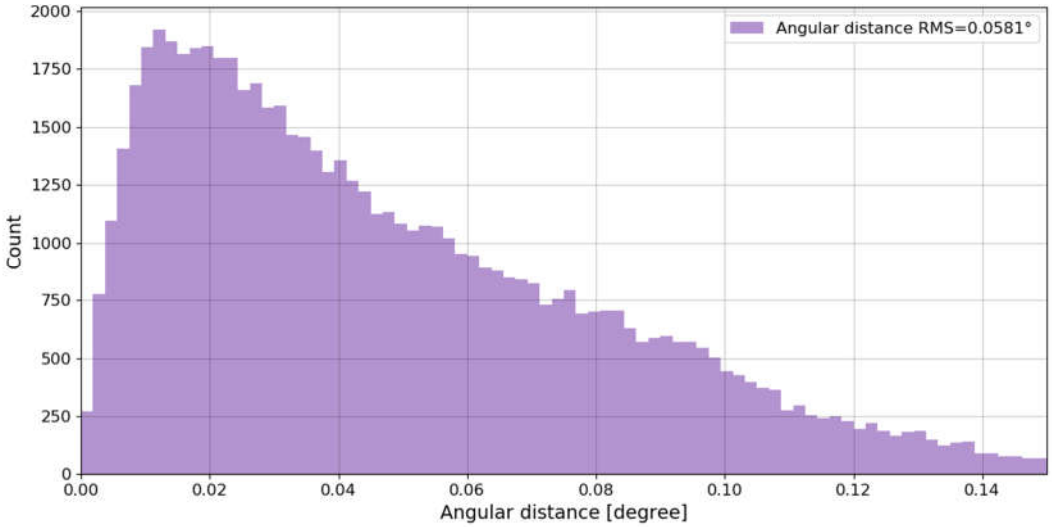

Figure 5.36: Histogram of radial angular displacement between measured RSO positions and their TLE predictions. Presented data is from all measured and correlated RSO under 45° N LOS during campaigns #2 February and #4 April-June.

Figure 5.37 to Figure 5.39 show the radial displacement between measurements and predictions for each identified RSO depending on RSO's RCS and range, for measurements of zenith, 45° W and 45° N LOS, respectively. It can be seen that the radial displacement is not depending on RSO's RCS. However, more green and yellow objects are visible at closer range. This dependency could result from larger prediction uncertainties in the TLE predictions due to atmospheric drag and higher velocities. Note, the same angular displacement corresponds to a smaller Along- or Cross-Track error for closer range.

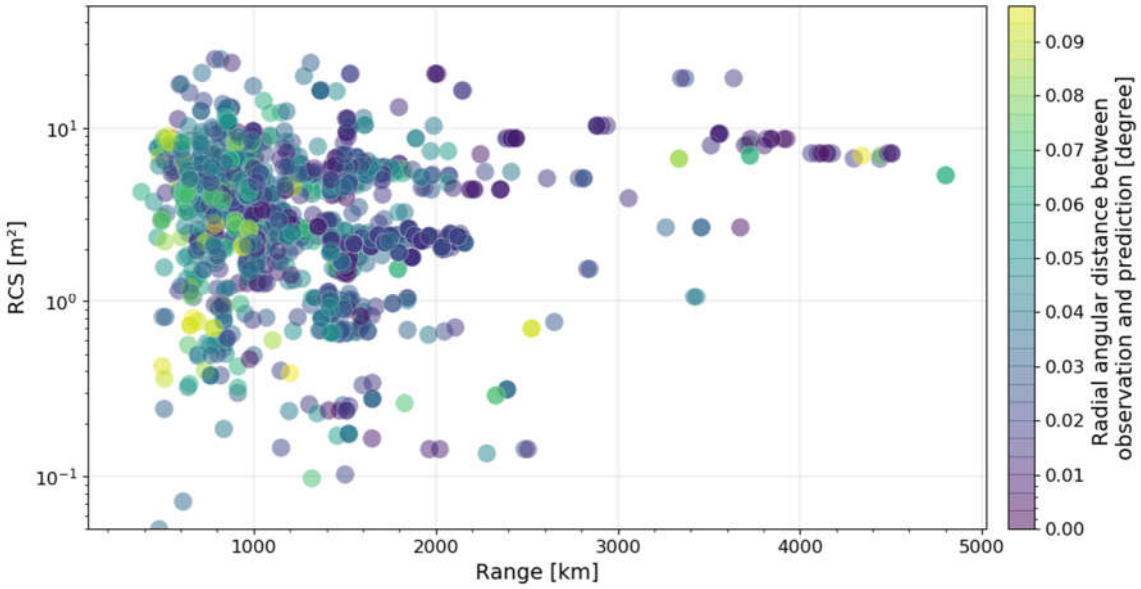

Figure 5.37: Mean radial angular displacement between measured and predicted RSO positions depending on RSO's RCS and range. Color coded from 0° (deep blue) to 0.1° (yellow) for all identified objects detected during campaigns #1 December and #5 July. All objects are observed under zenith LOS with the APPARILLO2 system.

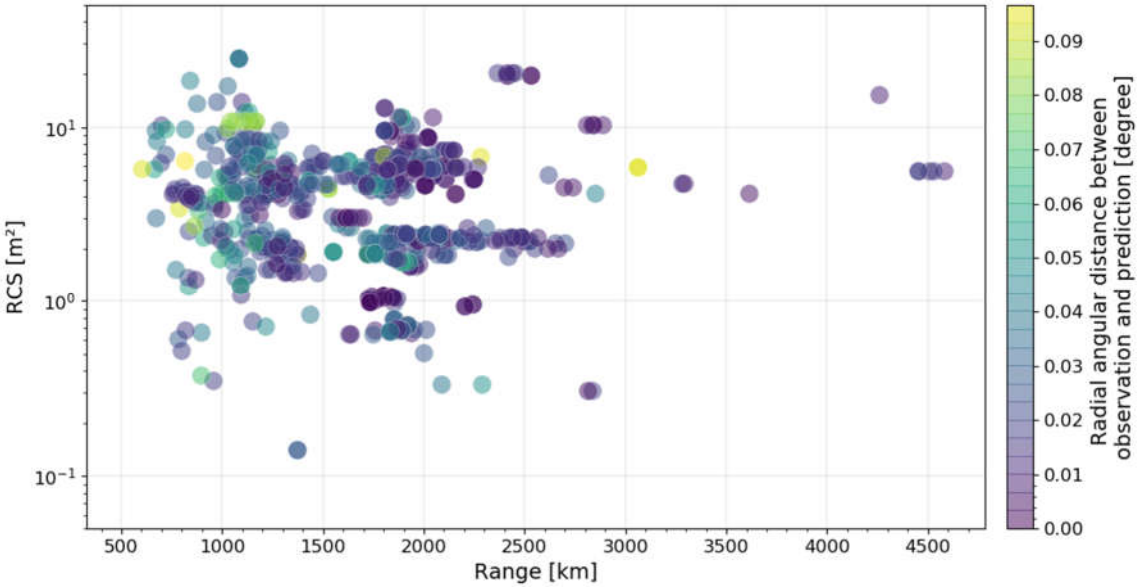

Figure 5.38: Mean radial angular displacement between measured and predicted RSO positions depending on RSO's RCS and range. Color coded from 0° (deep blue) to 0.1° (yellow) for all identified objects detected during campaign #3 March. All objects are observed under 45° W LOS with the APPARILLO2 system.

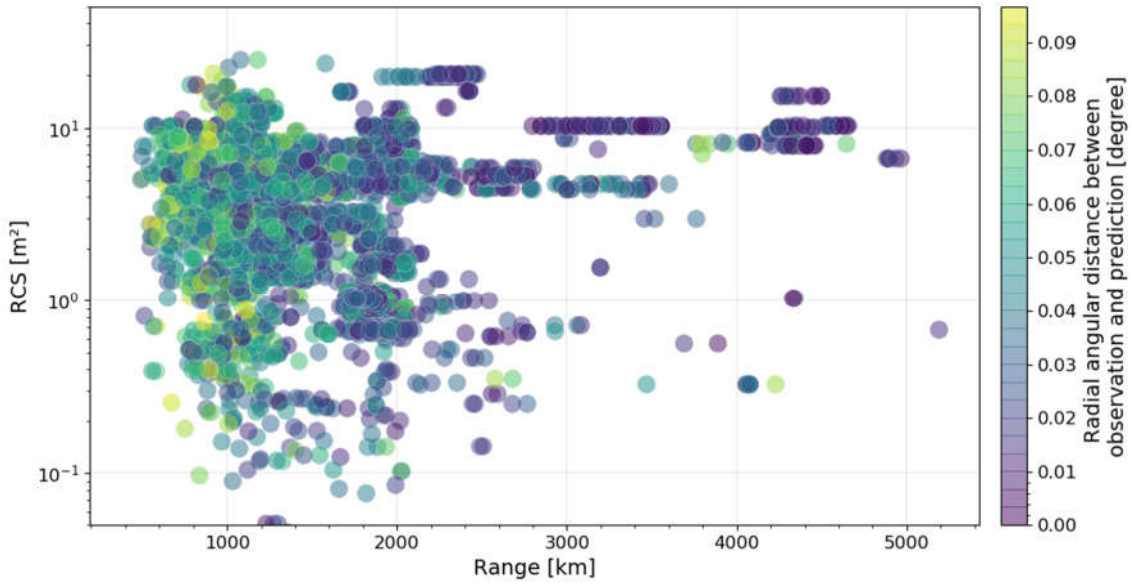

Figure 5.39: Mean radial angular displacement between measured and predicted RSO positions depending on RSO's RCS and range. Color coded from 0° (deep blue) to 0.1° (yellow) for all identified objects detected during campaigns #2 February and #4 April-June. All objects are observed under 45° N LOS with the APPARILLO2 system.

Along- and Cross-Track error

To analyze the displacements in more detail, the angular displacement is considered in terms of the Along-Track and Cross-Track angular displacement in the RSW (the Radial/Along-Track/Cross-Track system). First, RSO and station coordinates are transformed into cartesian coordinates using Eq. (3.43) and (3.40). The station vector $\overrightarrow{r_{\text{station}}}$ has its origin at the Earth center (ECI) and is added to the measured RSO $\overrightarrow{r_{\text{RSO}}}$ and predicted $\overrightarrow{r_{\text{TLE}}}$ coordinates to obtain the Earth centered vector of the measured object $\vec{r_{\text{S}}}$ and of the predicted objects position $\vec{r_{\text{P}}}$. The error vector $\vec{r_{\Delta}}$ is the difference between those two vectors.

$$\begin{aligned}
\overrightarrow{r_{\text{RSO}}} &= \begin{pmatrix} X_{\text{RSO}} \\ Y_{\text{RSO}} \\ Z_{\text{RSO}} \end{pmatrix} \\
\overrightarrow{r_{\text{station}}} &= \begin{pmatrix} X_{\text{station}} \\ Y_{\text{station}} \\ Z_{\text{station}} \end{pmatrix} \\
\vec{r_{\text{S}}} &= \overrightarrow{r_{\text{station}}} + \overrightarrow{r_{\text{RSO}}} \\
\vec{r_{\text{P}}} &= \overrightarrow{r_{\text{station}}} + \overrightarrow{r_{\text{TLE}}} \\
\vec{r_{\Delta}} &= \vec{r_{\text{P}}} - \vec{r_{\text{S}}}
\end{aligned} \tag{5.1}$$

To obtain the Along-Track vector a singular value decomposition (SVD) is performed on all measured points $\boldsymbol{M}_{\text{S}}$. The resulting matrix $\boldsymbol{V}^{H}$ gives the eigenvectors, of which the first is the

vector pointing Along-Track to the measured points. Hence, the Along-Track vector $\overrightarrow{r_{\text{Along-Track}}}$ is the first row of matrix $\boldsymbol{V}^H$.

$$\begin{aligned} \boldsymbol{USV}^H &= \text{SVD}(\boldsymbol{M}_S) \\ \overrightarrow{r_{\text{Along-Track}}} &= \boldsymbol{V}^H[0] \end{aligned} \tag{5.2}$$

The Cross-Track vector $\overrightarrow{r_{\text{Cross-Track}}}$ is normalized to unity and perpendicular to the Along-Track vector $\overrightarrow{r_{\text{Along-Track}}}$, and the radial vector $\overrightarrow{r_{\text{Radial}}}$. $\overrightarrow{r_{\text{Radial}}}$ is the normalized RSO vector $\overrightarrow{r_S}$.

$$\begin{aligned} \overrightarrow{r_{\text{Radial}}} &= \frac{\overrightarrow{r_S}}{\|\overrightarrow{r_S}\|} \\ \overrightarrow{r_{\text{Cross-Track}}} &= \frac{\overrightarrow{r_{\text{Along-Track}}} \times \overrightarrow{r_{\text{Radial}}}}{\|\overrightarrow{r_{\text{Along-Track}}} \times \overrightarrow{r_{\text{Radial}}}\|} \end{aligned} \tag{5.3}$$

Then, Along- $d_{\text{Along-Track}}$ and Cross-Track $d_{\text{Cross-Track}}$ errors can be calculated as follows,

$$\begin{aligned} d_{\text{Along-Track}} &= \overrightarrow{r_\Delta} \cdot \overrightarrow{r_{\text{Along-Track}}}, \\ d_{\text{Cross-Track}} &= \overrightarrow{r_\Delta} \cdot \overrightarrow{r_{\text{Cross-Track}}}. \end{aligned} \tag{5.4}$$

Using this calculation, the Along- and Cross-Track error is analyzed in the graphs shown in Figure 5.40 to Figure 5.44. Figure 5.40 and Figure 5.41 show the Along- and Cross-Track error distributions for each RSO of the same subset of objects as presented in Figure 5.31 and Figure 5.32.

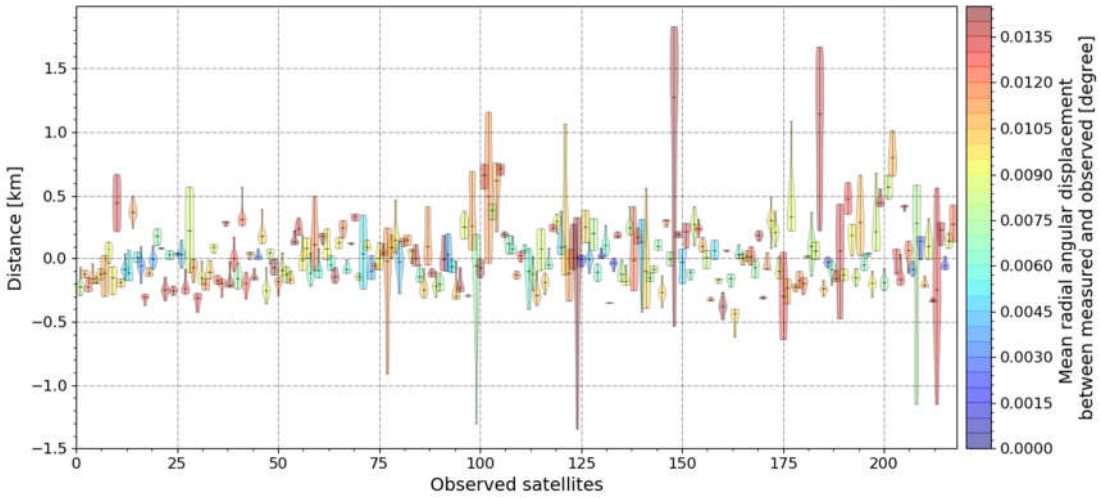

Figure 5.40: Along-Track displacement distributions between measured object positions and their TLE predictions as a distribution for each object. The color corresponds to the mean angular distance of each object to the TLE prediction, from small values colored in blue to large values colored in red. Presented data is from a subset of measured objects under zenith LOS during campaign #5 July.

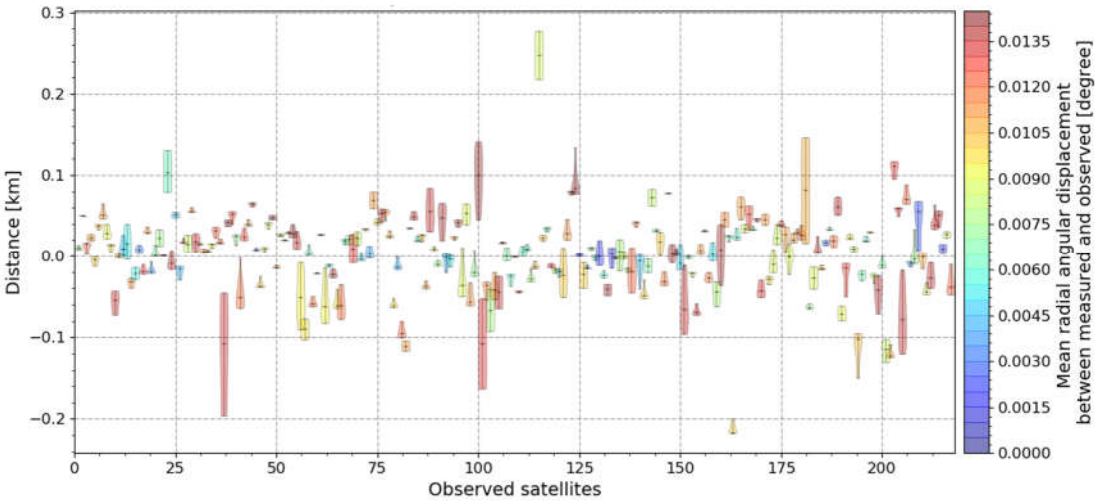

Figure 5.41: Cross-Track displacement distributions between measured object positions and their TLE predictions for each object. The color corresponds to the mean angular displacement of each object to the TLE prediction, from small values colored in blue to large values colored in red. Presented data is from a subset of measured objects under zenith LOS during campaign #5 July.

A histogram of Along- and Cross-Track distances for all measurements taken under zenith LOS is shown in Figure 5.42. The Histograms for Along- and Cross-Track error under LOS 45° W and 45° N are shown in Figure 5.43 and Figure 5.44, respectively. These histograms show that the Along-Track displacement to the TLE predictions is about ten times larger than the Cross-Track displacement. Both Along- and Cross-Track are almost Gaussian distributed. Histograms of the Along-Track displacements show a slight positive offset while the Cross-Track displacements scatter around zero. The Along-Track error is larger for observations under 45° LOS, since the distance to measured objects is larger.

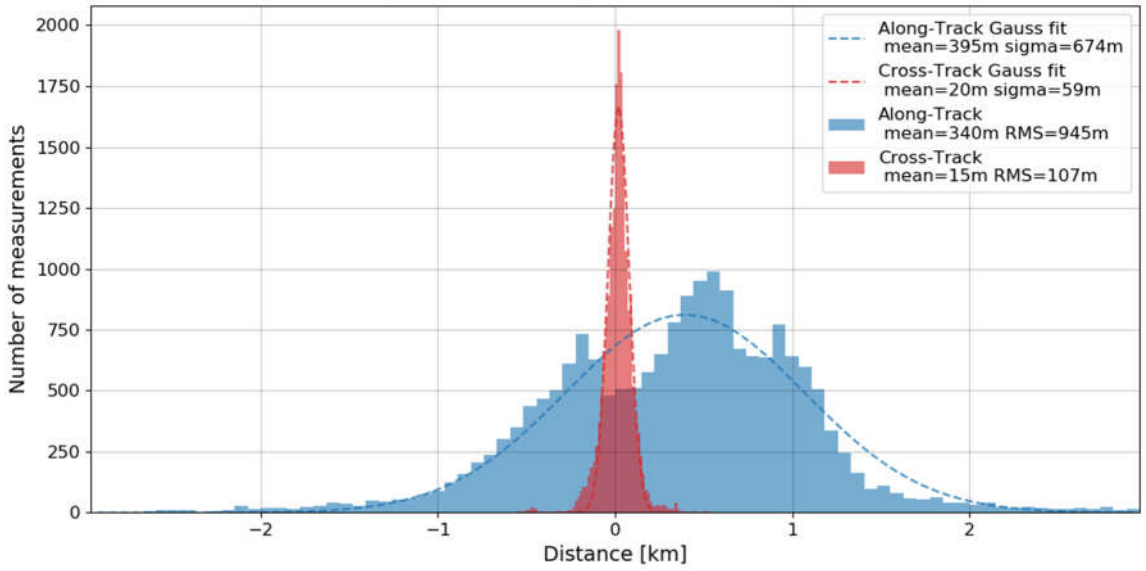

Figure 5.42: Histogram of Along- and Cross-track displacements between measured RSO positions and their TLE predictions. Presented data is from all measured and correlated RSO under zenith LOS during campaigns #1 December and #5 July.

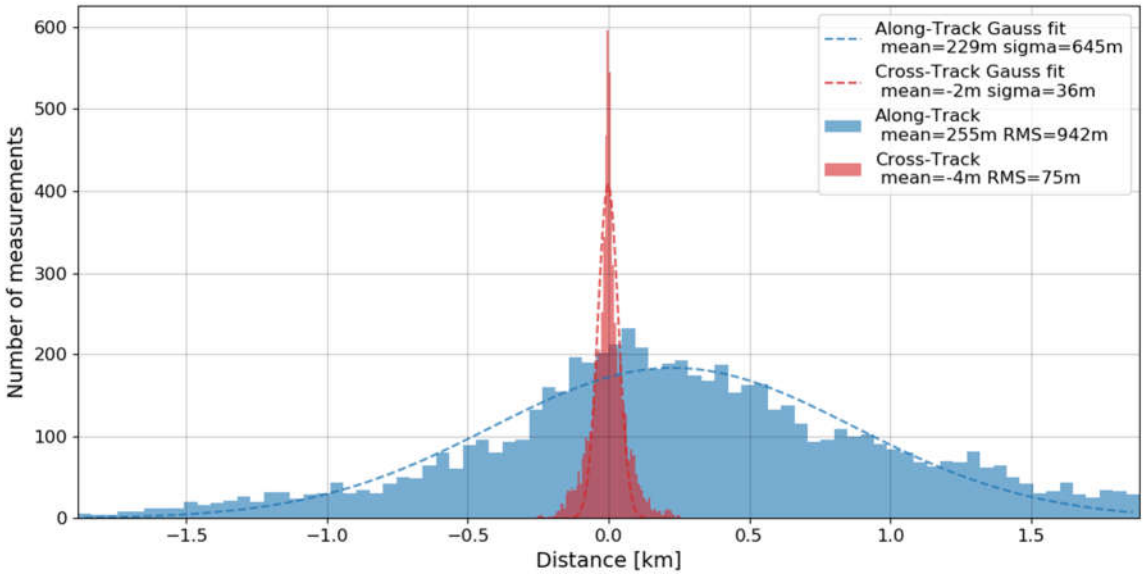

Figure 5.43: Histogram of Along- and Cross-Track displacements between measured RSO positions and their TLE predictions. Presented data is from all measured and correlated RSO under LOS 45° W during campaign #3 March.

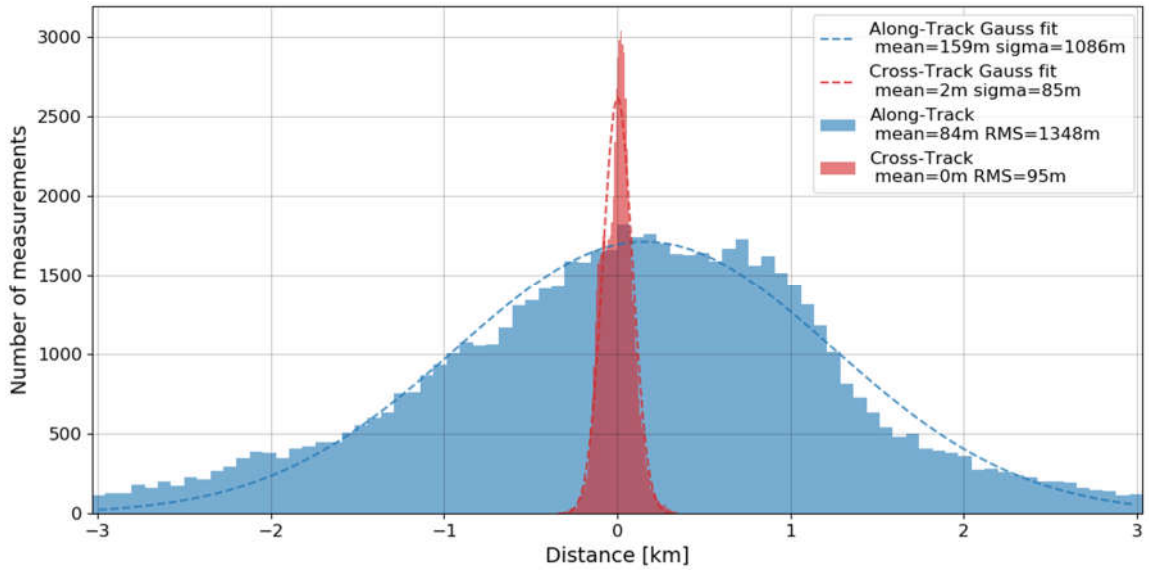

Figure 5.44: Histogram of Along- and Cross-Track displacements between measured RSO positions and their TLE predictions. Presented data is from all measured and correlated RSO under LOS 45° N during campaigns #2 February and #4 April-June.

Table 5.8 lists the angular, Along-, and Cross-Track errors for each LOS. The radial angular displacement is mainly determined by the Along-Track error. The Cross-Track error on the other hand is about ten times smaller, which results from the fact that the fit algorithm captures the Cross-Track components of a streak much easier. More crucial is the impact of a time bias, which does not affect the Cross-Track component, but strongly the Along-Track one.

LOS	**Zenith**	**45° W**	**45° N**
Along-Track RMS error	945 m	942 m	1348 m
Cross-Track RMS error	107 m	75 m	95 m
Radial RMS error	0.042°	0.040°	0.058°

Table 5.8: Radial angular, Along-, and Cross-Track RMS errors of each observed LOS by APPARILLO2 system, derived by comparing all measurements to predicted positions based on TLE.

CPF prediction analysis

However, to determine the absolute precision of the system, more precise orbit predictions are required. Therefore, the Along- and Cross-Track errors are analyzed with regard to more precise CPF predictions [37] of each RSO for which these predictions are available. Under zenith LOS, seven detected RSO, that have been measured during campaigns #1 December and #5 July, could be compared to CPF predictions. The Along- and Cross-Track error distribution of each RSO gained in this analysis is shown in Figure 5.45. It can be seen that the

Along- and Cross-Track errors are significantly lower compared to the analysis using TLE predictions in Figure 5.42. For these seven detections the Along-Track errors are always positive, while the Cross-Track errors are distributed around zero. Remarkably, the dispersion of the four JASON3 detections compares well to the error of a single detection event. This fact supports the ascertainment of the determined errors to constitute the system's performance. Especially, the determined errors do not show a particular dependency on orbit height (compare JASON 3 at h_{RSO} = 1337 km and GRACEFO 1 & 2 at h_{RSO} = 490 km).

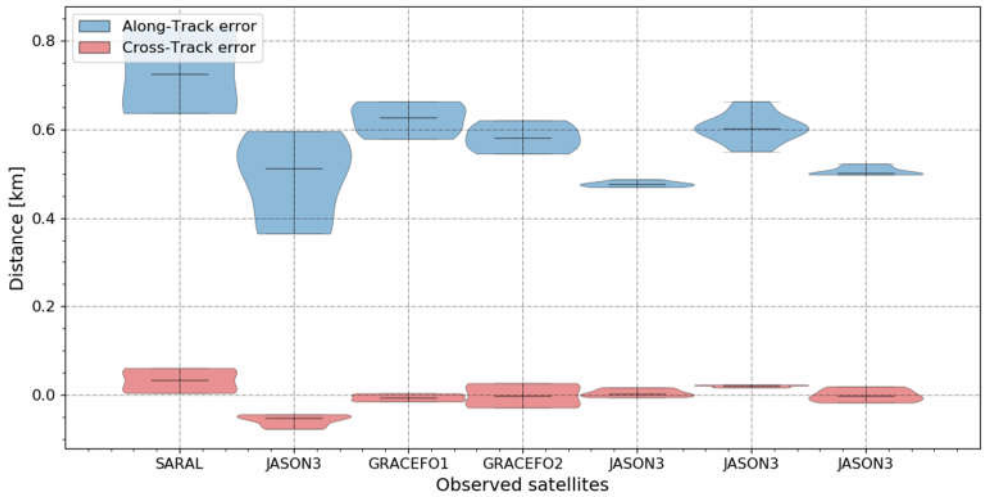

Figure 5.45: Along-Track (blue) and Cross-Track (red) error distributions between measured and predicted RSO positions using CPF prediction files [37]. The first two RSO were measured during campaign #1 December and the last five during campaign #5 July, observed under zenith LOS. The Along-Track RMS error of these objects is 574 m and the Cross-Track error is 30 m.

During campaigns #2 February and #4 April-June eight RSO, observed under LOS 45° N, could be compared to precise CPF predictions. The Along- and Cross-Track error distributions of each RSO are shown in Figure 5.46. It can be seen that six of the detections show a two to three times larger Along-Track error than shown in Figure 5.45 previously. Thus, the Along-Track RMS error with 1386 m is closer to the results from the analysis using TLE predictions. However, the Cross-Track RMS error with 32 m remains similar to CPF results from zenith LOS observations. This points towards the previously observed behavior that LOS 45° N bears a difficulty for precise Along-Track measurements. Again, similar errors independent of orbit height are observed (compare CRYOSAT 2 at h_{RSO} = 720 km to KOMPSAT 5 at h_{RSO} = 553 km), which underlines that the LOS is the determining factor of the Along-Track error. One reason lies in the angular velocities which depend on LOS. Longer streaks on the image allow to determine the start and end coordinates more precisely relative to the streak length.

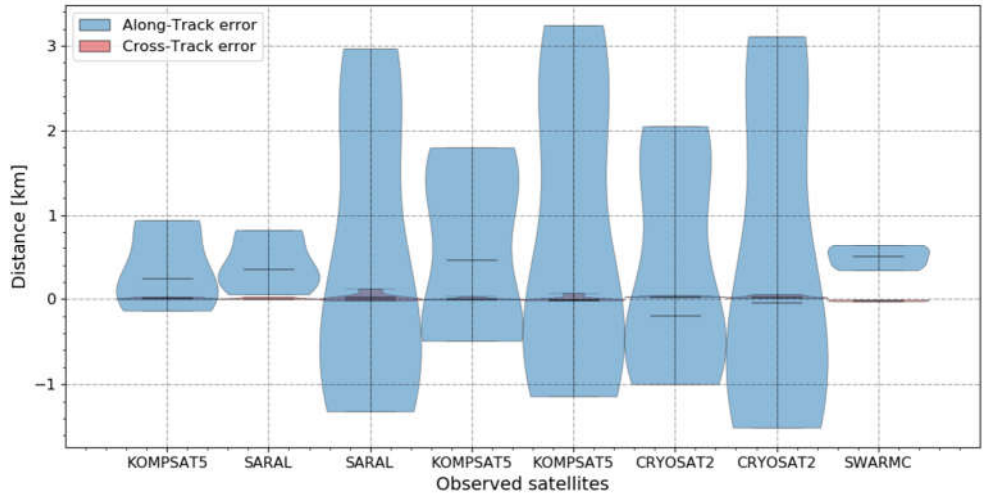

Figure 5.46: Along-Track (blue) and Cross-Track (red) error distributions between measured and predicted RSO positions using CPF prediction files [37]. The first five RSO were measured during campaign #2 February and the last three during campaign #4 April-June, observed under 45° N LOS. The Along-Track and Cross-Track RMS errors of these objects are 1386 m and 32 m, respectively.

Still, the overall low Cross-Track error reveals that TLE predictions are indeed less precise than CPF and that the observed Cross-Track errors within the TLE evaluation (see Table 5.8) are not due to measurement uncertainties. Indeed, the absolute Cross-Track error around 30 m matches APPARILLO's theoretical pixel scale of 120 µrad/px (see Table 5.3), which determines streak Cross-Track component with subpixel accuracy.

The fact that the Along-Track error is more than ten times larger than the Cross-Track error indicates that the time synchronization is unprecise. An Along-Track error of 700 m corresponds to a timing error of about 100 ms. The velocity aberration (see Section 3.7) with up to 15 ms and the shutter opening and closing time with a total of 106 ms partly explain the occurrence of a large Along-Track error. In a future system a more precise time synchronization is recommended by using cameras with a global electronic shutter and a direct GPS time synchronization.

The performed error analysis delivers the final system's precision values to be consistent with theoretical performance measures. The analysis using TLE and CPF predictions show that the LOS plays a dominant role for the Along-Track error, while the Cross-Track error seems unaffected and matches the angular resolution of the system. The determined errors using TLE predictions turn out clearly higher than the analysis using CPF predictions. This shows that APPARILLO2 is indeed capable of revealing TLE's intrinsic larger uncertainties and in principle can provide sufficiently precise angular measurements to perform subsequent passive-optical closed-loop tracking.

5.3. PROSPECTS

In Section 5.3.1, the previously determined detection threshold (under Section 5.2.3) is used to adopt the analytical link budget calculations to fit the observations of APPARILLO2. Then, this is used to estimate required system performance for a passive-optical sensor to detect RSO as small as 10 cm. This necessitates an advanced image processing technique, *synthetic tracking*, which is introduced in Section 5.3.2.

A laser ranging system needs a priori information to track and measure the distance to an object. The combination of the presented staring system and a ranging system allows to detect new RSO in LEO and provide accurate distance measurements for a precise orbit determination, which is mandatory for keeping it in a catalog. The first step in this direction is the handover of the angular position information to a tracking telescope. Such a subsequent handover to a separate tracking station is presented in Section 5.3.3.

A method to determine range information by using two staring systems is the parallax configuration. In Section 5.3.4 an estimation for the expected range uncertainties of such a sensor combination is presented.

5.3.1. PROJECTED STARING SENSOR PERFORMANCE

In Section 5.2.3 APPARILLO2's detection threshold is derived from the measurements. These results are used to adopt a few parameters of the analytical model to fit the experimental observations.

Due to better detection performance under 45° N LOS compared to zenith LOS, the visibility V has to be set to 40 km, which corresponds to 90% transmission under 45° elevation and 93% under zenith. The background noise L_b is increased to the largest feasible value with 15 mag/arcsec², which is a typical value for a large city with light pollution [49]. Furthermore, the upper and lower threshold values of APPARILLO2's image processing vary depending on the background it needs to remove. Thus, setting a larger SNR of 6 is feasible. Any other parameters used for simulations within this Section are given by the hardware, the FWHM of the PSF is set to its measured value of 1.5 px. Table 5.9 lists the updated parameters for following simulations. These parameters result in a detection threshold matching the measurements and Figure 5.47 shows APPARILLO2's detection threshold depending on orbit height and elevation using the updated parameters.

Parameter	Value	Description
QE (eff.)	0.55	Quantum efficiency
τ_{optic}	0.85	Transmission of the optical system
τ_{atm}	0.93	Transmission of the atmosphere (el90°)
V [km]	40	Visibility
d_{optic} [m]	0.1	Diameter of the optical aperture
y_{pix} [µm]	12	Pixel size
e_{read} [e^-]	15	Read out noise of the image sensor
f' [m]	0.2	Focal length of the optical system
FWHM [px]	1.5	FWHM of the PSF
τ_{px}	0.32	Pixel coupling efficiency
L_b [mag/arcsec²]	15	Background brightness
SNR	6	Signal to noise ratio
h_{RSO} [km]	1000	Orbit height of the RSO
ϱ_{spec}, ϱ_{diff}	0.175	Specular and diffuse reflectivity of the RSO
ψ	75°	Phase angle between the RSO, the observer and the Sun
f#	2	f-number of the optical system
t_{exp} [s]	1	Exposure time
α_{el}	90°	Angle between horizon and observer's line of sight
$h_{station}$ [m]	500	Station height

Table 5.9: List of parameters and their values used for the calculation of the passive-optical link equation to represent measured results of APPARILLO2.

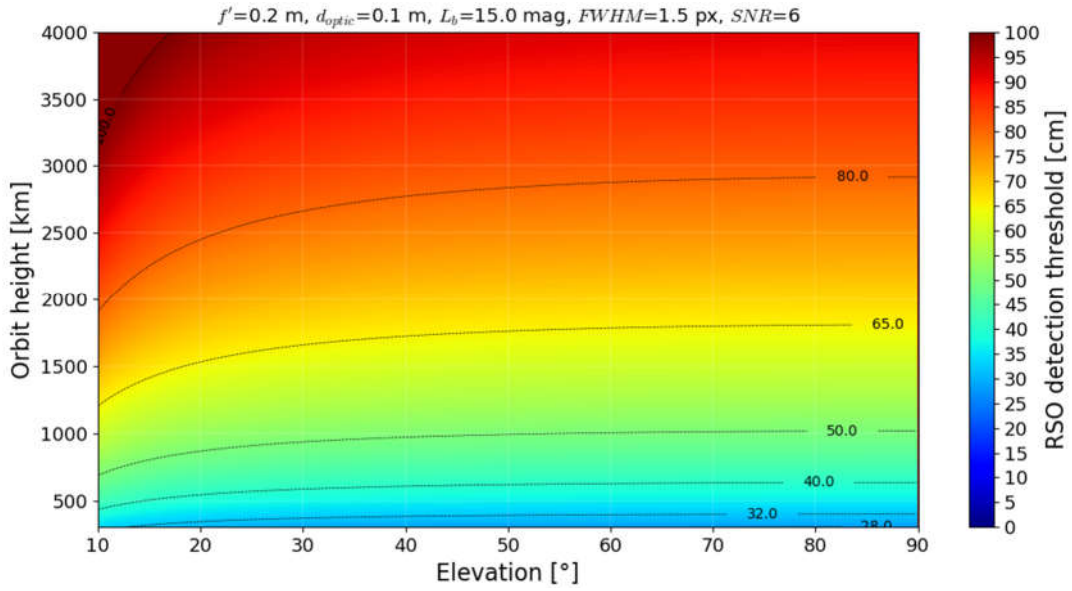

Figure 5.47: The detectable RSO diameter depending on the LOS elevation and RSO orbit height for a system with 10 cm aperture and an f# of 2. The parameters are selected to match APPARILLO2 measured performance under zenith LOS, see Table 5.9.

With the parameters well matching the experimental conditions and observations, the link budget simulation can now be used to estimate system properties to detect objects as small as 10 cm. Figure 5.48 shows the detection threshold depending on aperture diameter and f-number *f#* under 90° observation elevation. It can be seen that, under these conditions even a 2 m aperture can only detect objects with a size of 12 cm and larger.

To be able to detect smaller objects it is recommended to first reduce the *SNR* required to extract and detect an object in the image. Figure 5.49 shows the linear relation of SNR and aperture diameter on the detection threshold for an optical system with a fixed *f#* of 2 of an RSO in 1000 km orbit height, observed under 90° elevation. It can be seen that reducing the *SNR* of 6 by a factor of ten, will enable APPRILLO2 to detect objects as small as 14 cm. The alternative, increasing the aperture diameter well above 1 m, is connected with a dramatic increase in cost, weight, and size. Thus, the investment in image processing techniques to reduce SNR is much more feasible than a hardware investment. Furthermore, a larger aperture diameter typically results in a larger focal length, which implies a smaller FOV.

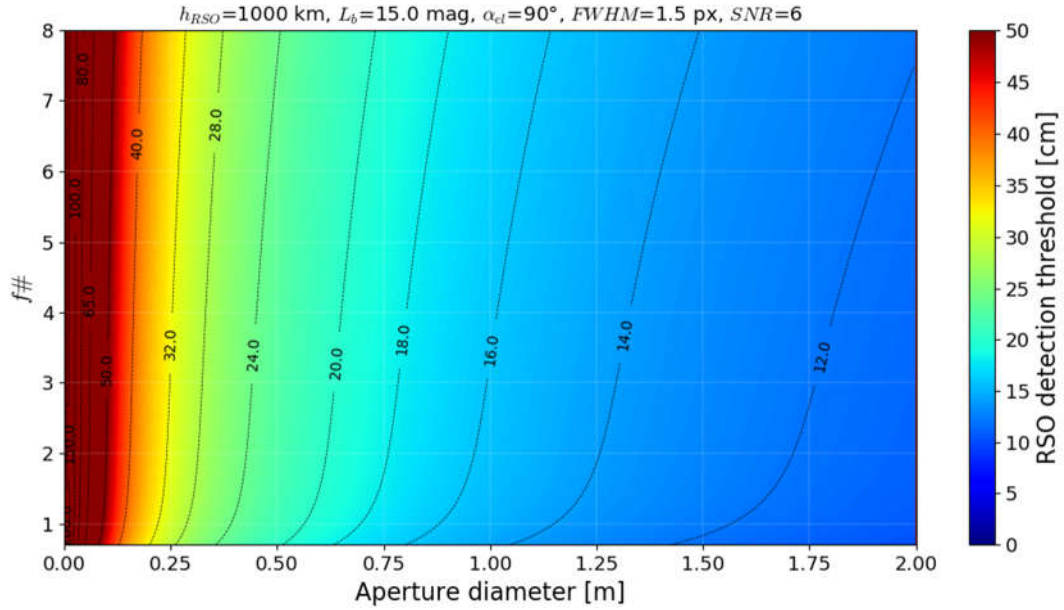

Figure 5.48: The detectable RSO size in 1000 km orbit height depending on aperture diameter and f# under 90° elevation. The parameters are chosen to match APPARILLO2 results using the parameters listed in Table 5.9.

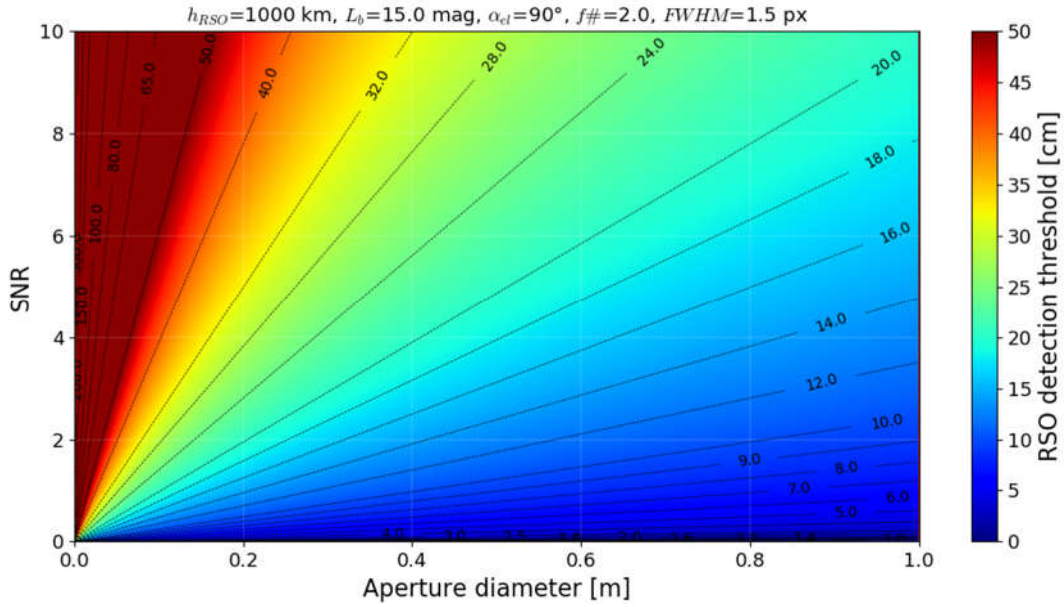

Figure 5.49: The minimum detectable RSO diameter depending on the SNR detection threshold and aperture diameter under 90° elevation. The parameters are chosen to match APPARILLO2 results, see Table 5.9.

Figure 5.50 shows the detection threshold depending on aperture diameter and *f#* using a *SNR* of 0.6, to sketch the potential of a reduced *SNR* to detected and extract an RSO in an image. Using a small *SNR* of 0.6, smaller telescopes can be used to achieve detection of objects smaller than 10 cm. According to the model a 25 cm aperture with an *f#* of 2 is sufficient to detect objects smaller than 10 cm.

In the next Section 5.3.2 preliminary results of an image processing algorithm are presented, which has the potential to reduce *SNR* up to the desired regime well below 1.

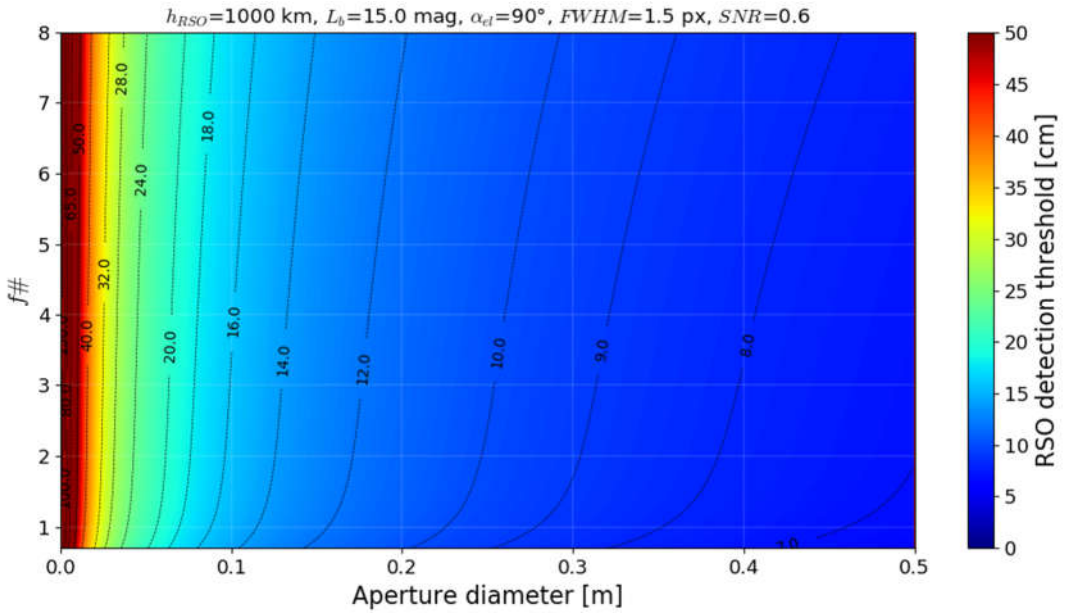

Figure 5.50: The detectable RSO size in 1000 km orbit height depending on aperture diameter and f# under 90° elevation. The SNR is reduced to 0.6 to show improvement in the detection threshold by optimizing the image processing sensitivity. Any other parameters are chosen to match APPARILLO2 results, see Table 5.9.

5.3.2. SYNTHETIC TRACKING

Synthetic tracking (ST) is an image processing technique, which provides a magnitude higher sensitivity to extract small signals in a noisy background using the same optical system. ST simulates the behavior of a tracking camera, but instead of mechanically continuously tracking the camera, a series of images is used to realign those images to simulate the tracking. The base algorithm behind ST is the so-called Shift-and-Add method and was already used in speckle astronomy to compensate atmospheric turbulence by adding a series of short exposures and shifting them such that the bright objects in each image are aligned to each other [90]

The resulting ST images I_{ST} is calculated from a series of *n+1* images (I_1, I_2, …, I_n), shifted by the shift vector *v* (v_x, v_y). The input images recorded with a constant frame rate need to be ordered timewise. The intensity of I_{ST} at its coordinates *x* and *y* depending on the shift vector components in x and y coordinates (v_x, v_y) is given by,

$$I_{ST}(x, y, v_x, v_y) = \sum_{i=0}^{n} I_i(x + \frac{iv_x}{n}, y + \frac{iv_y}{n}). \quad (5.5)$$

Where *n* is the number of images of the stack. An illustration how the shift vector affects the stack of images is shown in Figure 5.51. Figure 5.52 shows that the signal of an object add-up onto a single pixel if it moves through the image with a constant velocity that is equal to the shift vector. In ST the shift vector is varied in any sensible direction to detect an object, which is not detectable in an individual image. In case of a LEO RSO the shift vector would correspond to a value between 1.2°/s and 0.05°/s in any direction.

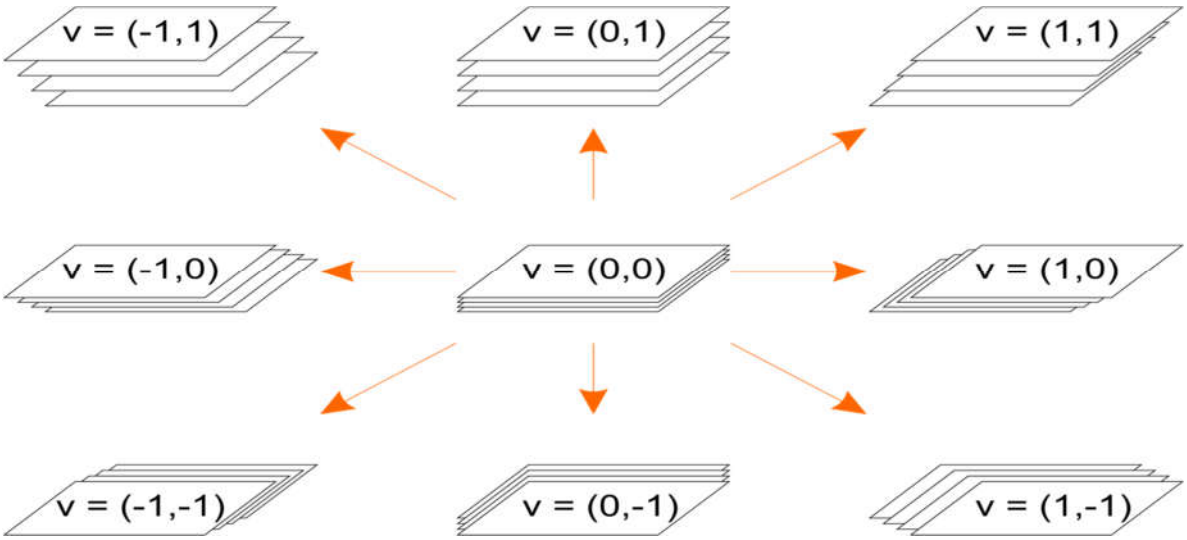

Figure 5.51: Illustration of shifts by the shift vector v on a stack of images. Source: [91].

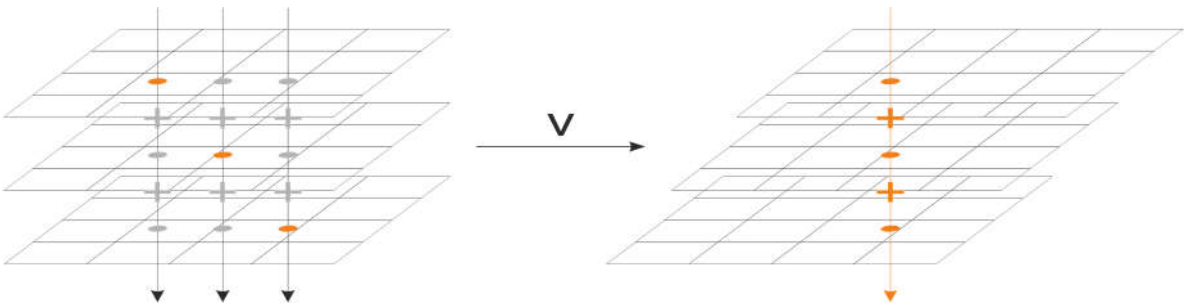

Figure 5.52: Illustration of adding up intensity values from a stack of images by an object (orange) that moves with the same apparent velocity through the focal plane as the shift vector v. Source: [91].

ST was first introduced to detect faint Near-Earth Asteroids (NEA) and by stacking 60 images the SNR could be increased by a factor of 20 to 40 compared to streak detection [92]. Due to low apparent angular velocity of NEA, ST could be performed in post processing. With increasing computer performance (esp. utilizing GPU processing performance) a real-time realization is feasible for LEO RSO detection. Hereby, the challenge is to perform the processing within a few seconds to allow subsequent 'stare and chase' operation and as fast as the data is taken by the camera to enable continuous operation of the staring sensor.

To demonstrate the feasibility, a computer code is written as implementation of an algorithm to perform ST on a stack of simulated images [91]. The simulator reproduces an image which contains stars and RSO as point sources. The point source is blurred by a Gaussian function to reproduce the PSF width, which results from aberrations and turbulence. Background noise is added by modelling photon shot noise as random Poisson distribution of the intensities. Additionally, vignetting is added to the final image. A simulated image is shown in Figure 5.53.

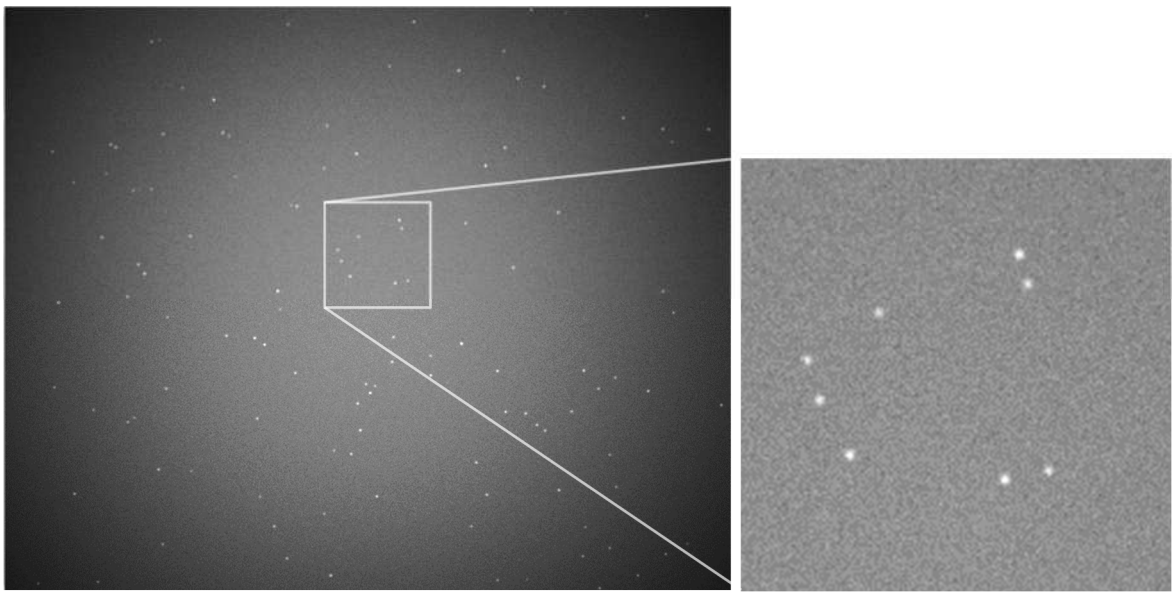

Figure 5.53: On the left an exemplary simulated image to be used for ST that incorporates background noise, vignetting, and Gaussian PSF. To the right is an enlarged section of the center of the simulated image. Adopted from source: [91].

The Shift-and-Add algorithm is implemented to be executed on a GPU by using NVIDIA's CUDA (Compute Unified Device Architecture) application programming interface (API).

Hereby, the star positions are assumed to be known in the simulated images, such that they can be masked and replaced by the surrounding background noise.

Figure 5.54 shows an object in a single image (top) and after ST (bottom). It can be seen that after processing a stack of 100 images using the ST algorithm, the signal strength is massively improved.

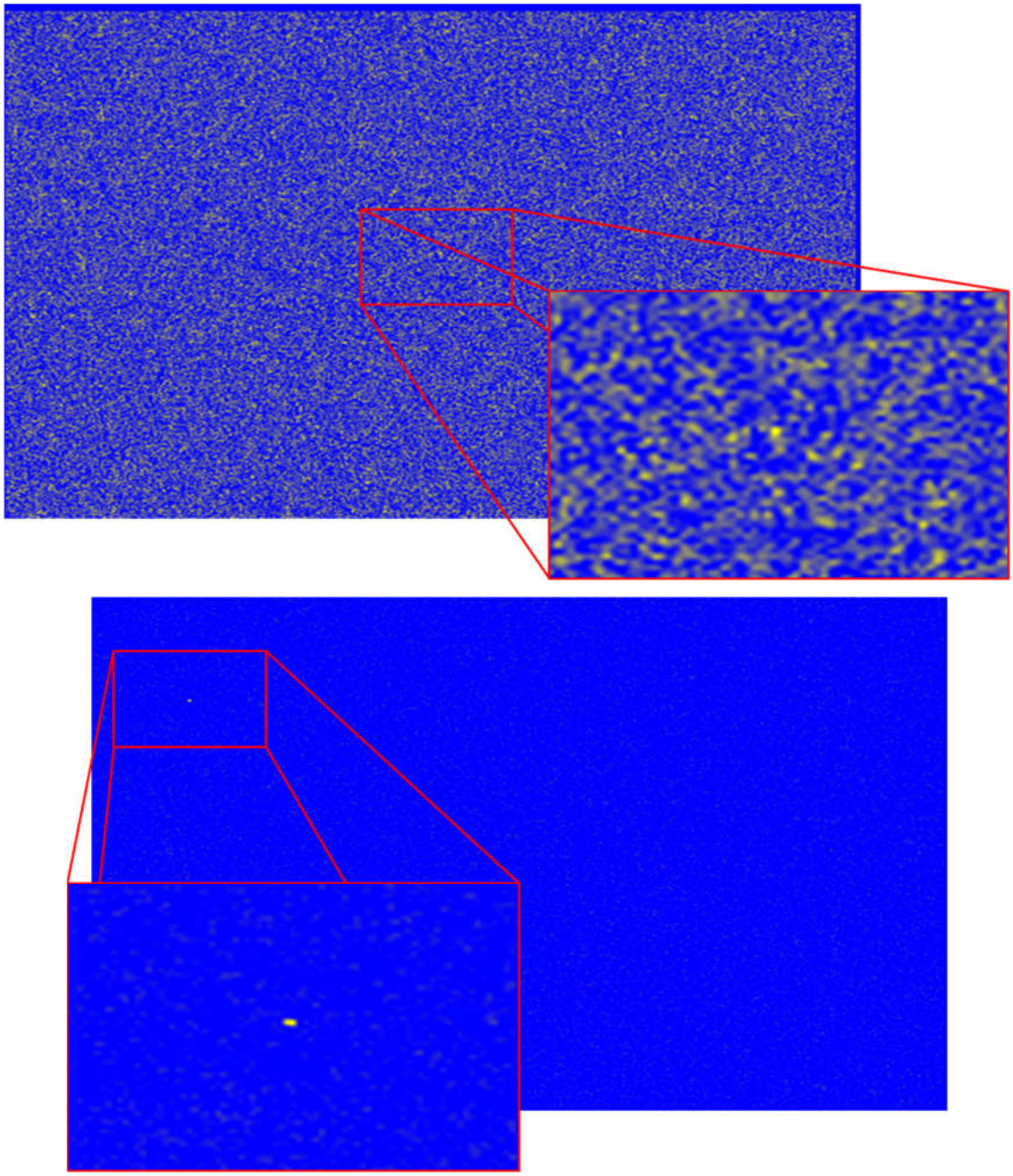

Figure 5.54: Top: A single simulated image with background stars removed is shown, which contains an RSO in the enlarged section. Bottom: An exemplary shift image after processing shows that the SNR of same RSO is improved massively by the ST algorithm. The brightness values are normalized independent for each image for better visualization. Source: [91].

To determine the detected RSO in a stack of processed images, the brightest intensity value is saved with its corresponding shift vector. Figure 5.55 shows an example result of the maximum intensities depending on the vector shift in *x* and *y* direction when three different RSO are present in the original image series. For each matching shift vector, the diagram shows a distinct intensity maximum.

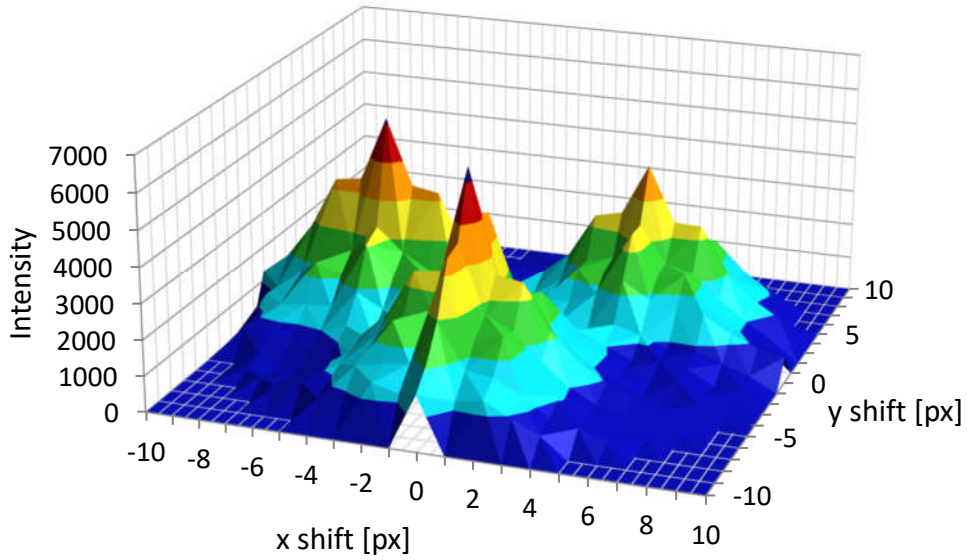

Figure 5.55: Maximum intensity values depending on shift vector components after processing 100 images. The shift diagram shows three RSO as local maxima. From left to right, the shift vectors of these are (-7, 0), (0, -7), and (5, 3) with the corresponding SNRs of 0.41, 0.41 and 0.38, respectively. The noise mean value is 132. Diagram obtained by subtracting the offset for illustration. Adopted from source: [93].

The implemented ST algorithm reliably detects objects down to an *SNR* of 0.4 in a stack of 100 images [93]. This result show that ST potentially allows an order of magnitude smaller *SNR* to detect RSO. Figure 5.50 shows that assuming a *SNR* detection threshold of 0.6, objects as small as 10 cm could be detected with an aperture size of 25 cm and an *f*# of 2. A realization of such a system using ST has a projected performance approaching RADAR sensitivity.

Furthermore, it is shown in Ref. [93] that a near real-time realization is feasible on current COTS GPU by optimizing the search area, reducing the image's resolution, and the number of images in the stack. Future increase in GPU computing performance potentially provides higher sensitivity by larger image stacks and higher resolutions.

5.3.3. STARE AND CHASE

The 'stare and chase' campaign was only performed in 2016 using the first staring system at DLR's UFO observatory. As software, the DLR-TP internal software tool to control the telescope and camera hardware is used. The basic principle of the employed software is the same as OOOS, except the former does not export equatorial coordinates in the TDM format. Instead, the equatorial coordinates are directly used to perform a linear extrapolation (see Figure 5.58) and predict the future position of the detected RSO. Then the tracking telescope is directed by the software to the predicted location and performs observations. By capturing a series of images, the RSO can be redetected. This process is called 'stare and chase' and is illustrated in Figure 5.56.

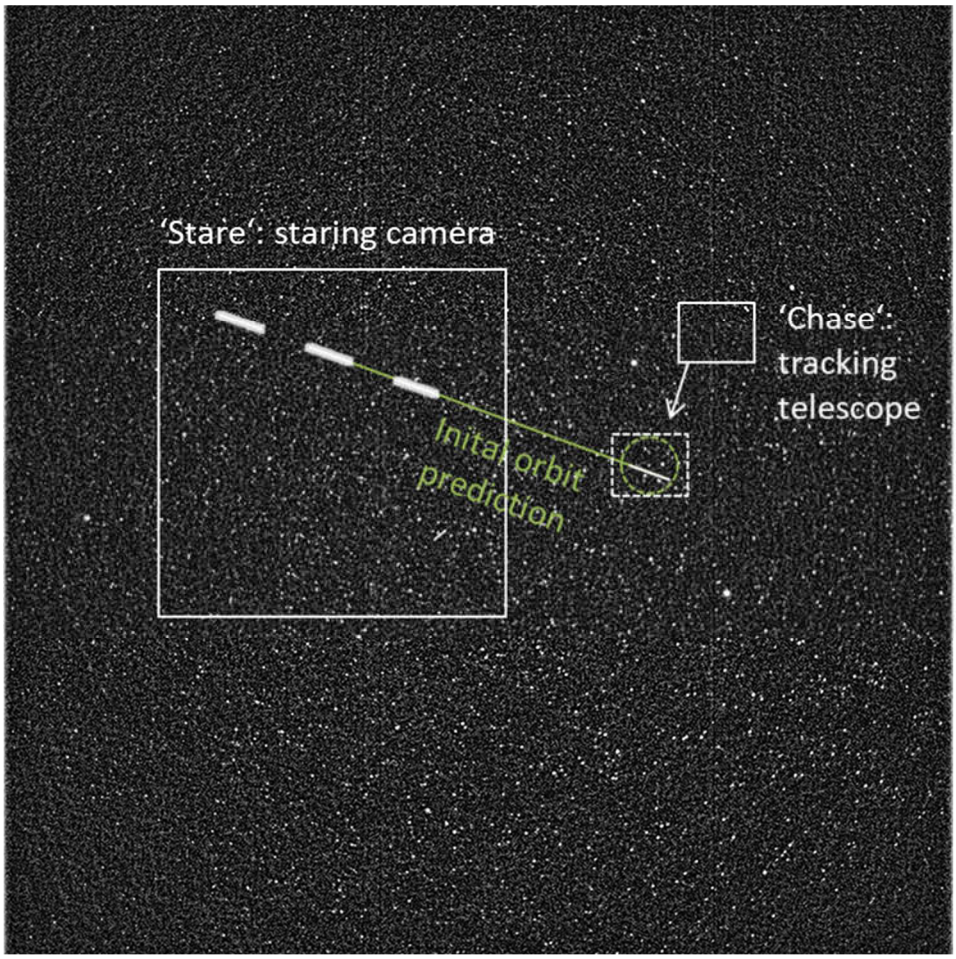

Figure 5.56: Illustration of the 'stare and chase' operation. The staring sensor (illustrated by the larger left white box) detects and measures one RSO two or more times. Then, an initial orbit prediction (green) is performed to capture this object with the tracking telescope (illustrated by the smaller right white box). Adopted from source: [62].

As tracking telescope, the PLANEWAVE CDK 17, mounted on an ASTELCO NTM-500 German equatorial mount, is used. The tracking camera is an ANDOR ZYLA, which results in a FOV of 0.32° by 0.27° [81]. Figure 5.57 shows the tracking telescope and staring camera at the UFO observatory. A detailed description of the setup can be found in Ref. [79]. See Appendix 9.9.3 for hardware specifications.

Figure 5.57: The 'stare and chase' setup at DLR's UFO laser ranging station. The staring camera equipped with the 135mm f2 lens is shown on the left, and the PLANEWAVE CDK 17 tracking telescope is shown on the right. Source: [94].

Figure 5.58 shows how the measurements of an RSO from two subsequent images taken by the staring camera are used to calculate a trajectory by a linearly extrapolating the equatorial coordinates. A fast calculation and handover are crucial to redetect the object before it disappears behind the Earth horizon. For the presented system the position of the RSO is predicted between 10 s to 15 s after its detection and handed over to the tracking telescope. The tracking telescope is directed to this predicted position and a series of images is taken at the desired time to recapture the object.

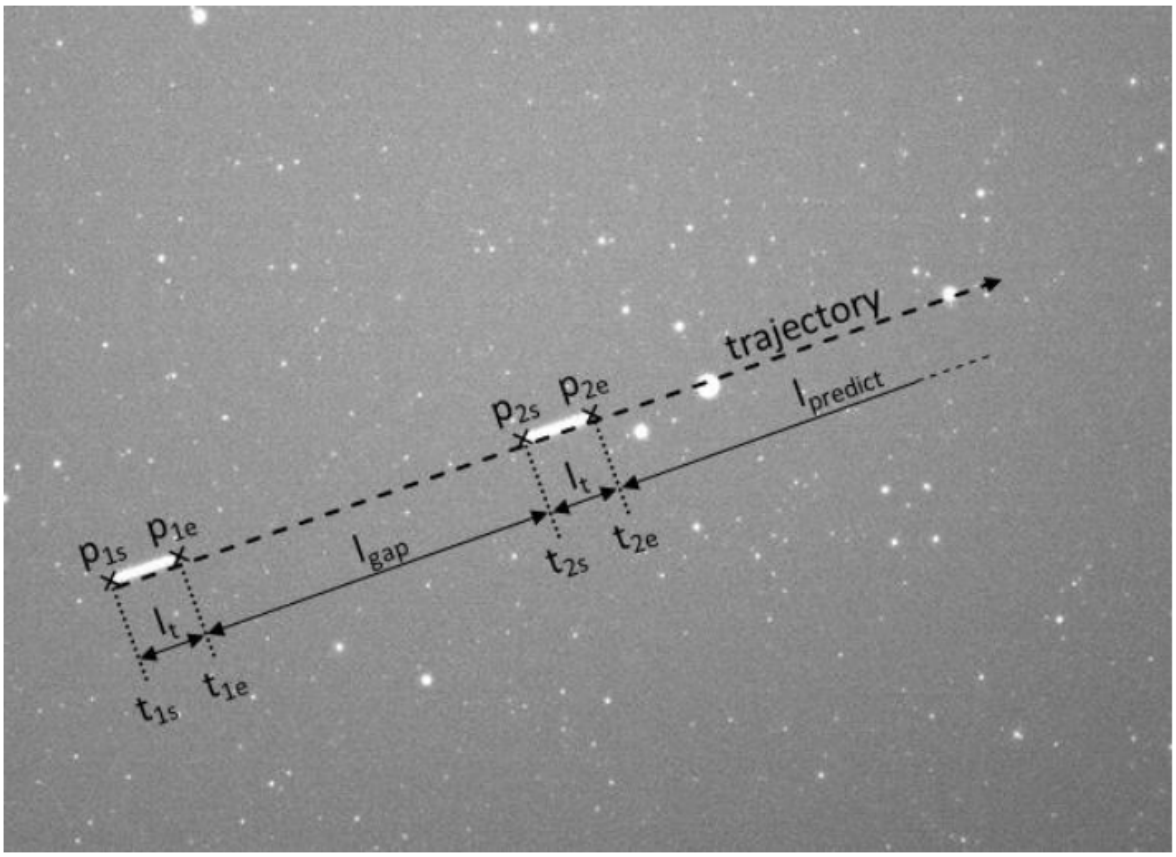

Figure 5.58: Overlay of two images by the staring sensor containing an RSO. Using the measured streak positions (p_{1s}, p_{1e}, p_{2s}, p_{2e}), corresponding observation times (t_{1s}, t_{1e}, t_{2s}, t_{2e}), information about the gap length l_{gab}, and track length l_t a prediction $l_{predict}$ is calculated. Source: [79].

As staring cameras not only the FLI PL16803 (1 s long exposure time) but also the ANDOR ZYLA is used with a shorter exposure time of 0.1 s. Both staring cameras are equipped with the 135mm f2 lens and time synchronization is performed with the ARDUINO GPS timer (see Section 4.3.4). Figure 5.59 and Figure 5.60 show each a successful 'stare and chase' measurement with the presented systems. In Figure 5.59 a successful operation observing GLOBALSTAR M003 on January 25th 2016 is shown using the FLI as staring camera. Figure 5.60 shows a 'stare and chase' recapture of CZ-4C R/B on June 22nd 2016 using the ZYLA as staring camera. The measurements deliver a prediction uncertainty of 722 arcsec (0.2°), which is within the limits to recapture the RSO with the tracking telescope. This demonstrates the capability of a successful handover by the presented staring systems to a tracking sensor and in principle allows subsequent laser ranging. Following our successful 'stare and chase' operation (more details and results can be found under Ref. [79]), the additional laser ranging for such a system was demonstrated by Steindorfer et al., see Ref. [64].

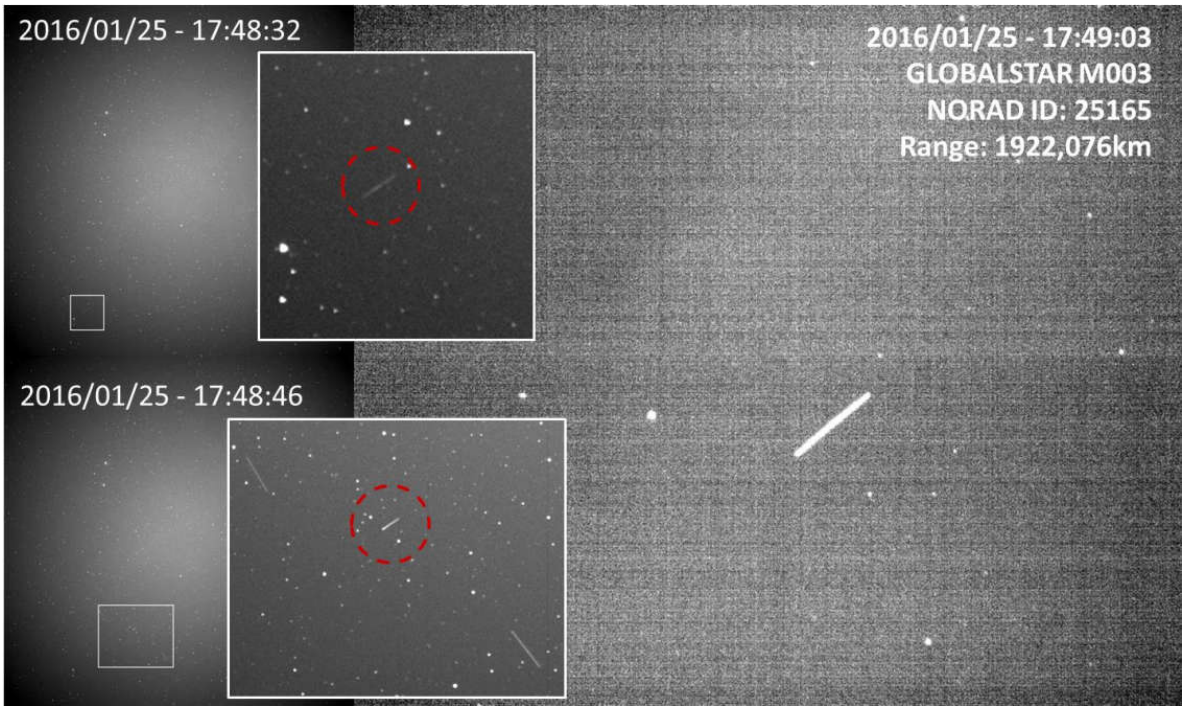

Figure 5.59: Left: Two successive images (t_{exp} = 1 s) by the staring camera (FLI PL16803 & 135mm f2) of the passing RSO recorded as streaks (red circle). Right: Subsequent 'chase' image of the satellite GLOBALSTAR M0003 (NORAD ID: 25165) taken by thetracking telescope. Source: [79].

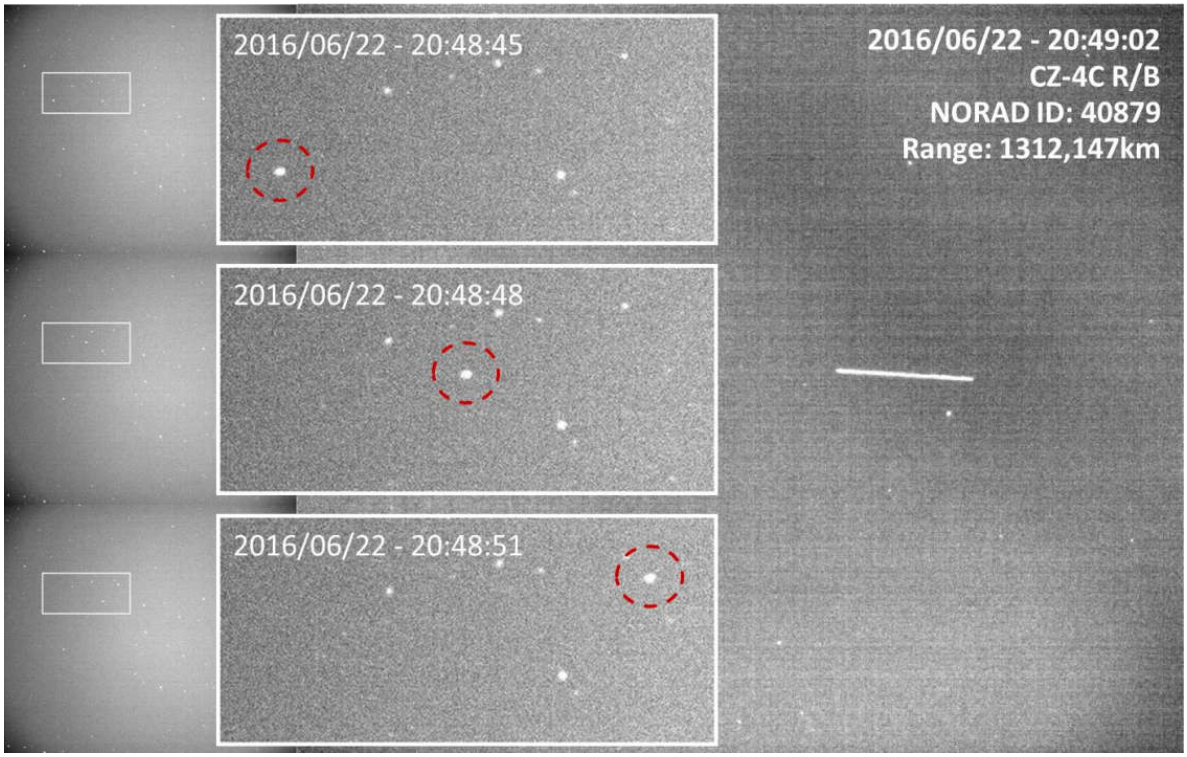

Figure 5.60: Left: Three successive images (t_{exp} = 0.1 s) by the staring camera (ANDOR ZYLA & 135mm f2) with the RSO recorded as points (red circle). Right: Subsequent 'chase' image of the space debris object CZ-4C R/B (NORAD ID: 40879) taken by the UFO tracking telescope. Source: [79].

5.3.4. DISTANCE DETERMINATION BY A PARALLAX PASSIVE-OPTICAL SYSTEM

By simultaneously measuring the angular position to an RSO by two passive-optical sensors, which are spatially separated, the range to the RSO can be determined by a parallax configuration. This will improve IOD (Initial orbit determination) and is recommended for future investigation. A first error estimation of the determined height shall be given in the following for the gained parameters of APPARILLO2.

To estimate the parallax height uncertainty $\measuredangle h$, it is assumed that the RSO is measured in an isosceles triangle between observer *1* and *2*. It has the baseline b between the two observers and h is the altitude of the RSO.

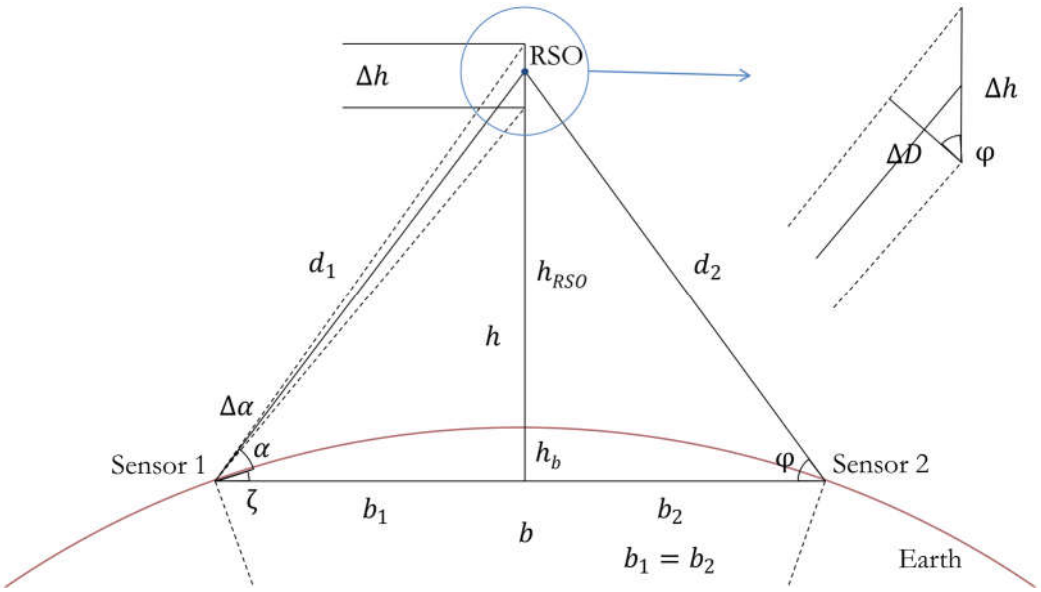

Figure 5.61: Geometric relations in an isosceles triangle between two passive-optical sensors on the Earth surface and an RSO to estimate the height uncertainty $\measuredangle h$ of the RSO.

The height uncertainty $\measuredangle h$ results from the angle φ and the corresponding lateral distance $\measuredangle D$,

$$\Delta h = \frac{\Delta D}{\cos(\varphi)}. \tag{5.6}$$

Thereby, $\measuredangle D$ results from the angular measurement uncertainty $\measuredangle \alpha$ and the distance to the RSO $d_{1/2}$,

$$\frac{\Delta D}{d_1} = \arctan(\Delta\alpha) = \Delta\alpha. \tag{5.7}$$

The distance to the RSO d_1 can be calculated from the baseline b and the height of the RSO to the baseline h.

$$d_1 = \sqrt{\frac{b^2}{4} + h^2} \tag{5.8}$$

Where the height h is the sum of the orbit height h_{RSO} and the height of the circular segment h_b. The height of the segment h_b can be calculated from the Earth radius R_E and h. Therefore, h can be calculated as follows,

$$h = h_{RSO} + h_b = h_{RSO} + R_E - \sqrt{{R_E}^2 - \frac{b^2}{4}} \tag{5.9}$$

The angle φ results from the height h and baseline b,

$$\varphi = \arctan\left(\frac{2h}{b}\right). \tag{5.10}$$

This gives the approximate height uncertainty $\measuredangle h$ with given angular uncertainty $\measuredangle\alpha$, distance between the sensors b, and height h.

$$\Delta h = \frac{\Delta\alpha\sqrt{\frac{b^2}{4} + h^2}}{\cos\left(\arctan\left(\frac{2h}{b}\right)\right)} \tag{5.11}$$

The corresponding elevation α_{el} under which the two sensors observe the RSO can be calculated from h, b and R_E,

$$\alpha_{el} = \varphi - \zeta = \arctan\left(\frac{2h}{b}\right) - \arcsin\frac{b}{2R_E} \tag{5.12}$$

The resulting height uncertainty $\measuredangle h$ is shown as a function of the baseline for three different angular uncertainties $\measuredangle\alpha$ in Figure 5.62. For the angular uncertainty three choices have been evaluated: the pixel scale of the APPARILLO2 system (green), three times the pixel scale (red), and the angular uncertainty observed by the APPARILLO2 system (blue). For each angular uncertainty the height uncertainty is shown for 800 km and 1200 km orbit height. With increasing baseline, $\measuredangle h$ becomes smaller and reaches a limit above 500 m. Furthermore, it can be seen that $\measuredangle h$ is not improving by a baseline larger than 2000 km. For the given angular measurement uncertainty of APPARILLO2 the height uncertainty is a few kilometers large. However, an improvement of the system's measurement precision can push the height uncertainty down to a few hundred meters.

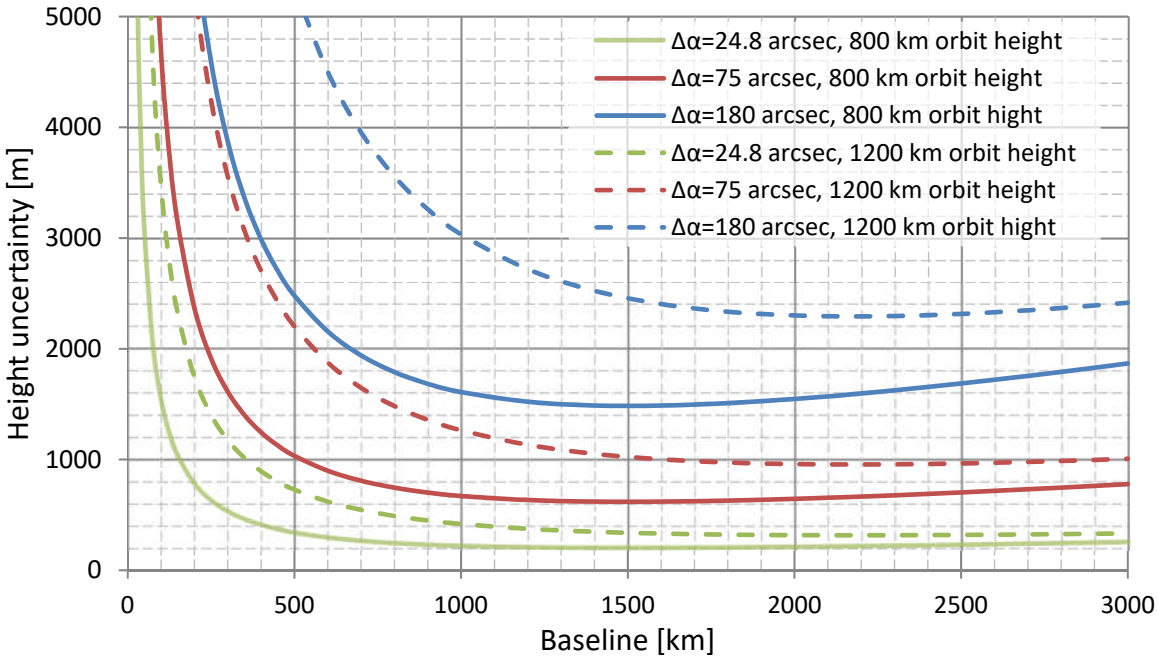

Figure 5.62: Estimated height uncertainty ⊿h for parallax passive-optical sensor configuration depending on the two observer's baseline. The angular measurement uncertainty ⊿α are selected according to the pixel scale of the APPARILLO2 (see Table 4.9 under Chapter 4.3.3), 3 times the pixel scale, and the estimated angular measurement uncertainty of the system (see Table 5.8 under Chapter 5.2.4), respectively. For each angular uncertainty the height uncertainty is shown for an RSO on a circular orbit in 800 km (solid) and 1200 km (dashed) orbit height.

Figure 5.63 shows the elevation under which the two passive optical sensors need to observe the RSO under the presented condition. It can be seen that the observing elevation for a baseline of 3000 km is already very low with 30°, which is why a baseline smaller 2000 km is recommended for observations.

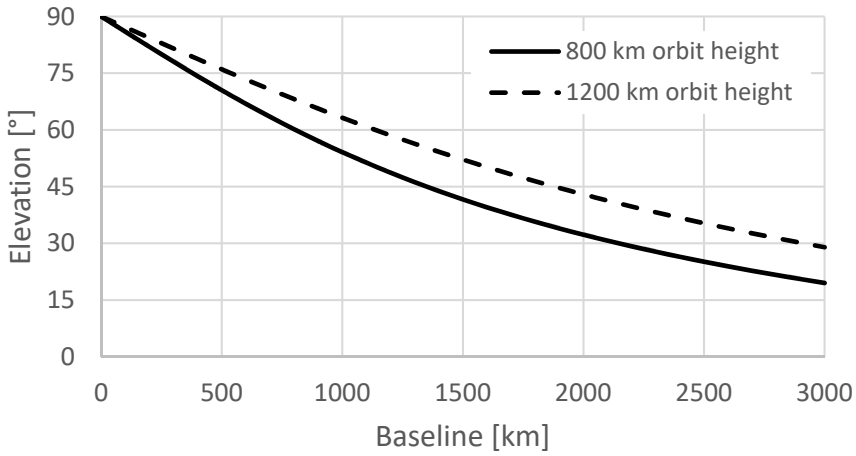

Figure 5.63: Corresponding elevation α_{el} (to Figure 5.62) depending on the baseline b of two sensors observing 800 km (solid) and 1200 km (dashed) orbit height in a parallax configuration.

6. SUMMARY

Laser ranging systems require a-priori orbital information of the RSO (residential space objects) in order to track the target of interest. Thus, they rely on a separate surveillance network to operate. Currently, RADAR (radio detection and ranging) sensors perform this task and enable to maintain a catalog of orbit predictions for RSO down to a size of 10 cm in LEO (Low Earth Orbit). However, operation of these systems is very expensive. In contrast, a passive-optical sensor is a cost-effective and easy to operate system to detect and measure orbital objects in LEO to provide an IOD (initial orbit determination) suitable for laser ranging systems. A large number of such small systems can enable operating a network of several sensors across the globe to overcome local weather dependency and the limited observation time of a single sensor. Within this thesis the development and functionality of APPARILLO2 (AUTONOMOUS PASSIVE-OPTICAL STARING OF LEO FLYING OBJECTS 2) is described in Chapter 4, which autonomously performs accurate observations with high efficiencies continuously since November 2020. The measurements deliver angular positions of RSO saved in standardized TDM (Tracking Data Message) format, which are uploaded to the webserver[P]. This way necessary information to perform IOD for laser ranging systems is provided globally.

To design the staring system made from COTS (commercial off-the-shelf) components, an analytical model is presented to examine the influence of hardware properties on the detection performance. Furthermore, the deterministic simulation software PROOF (Program for Radar and Optical Forecasting) is used to simulate detection rates and efficiencies of various system configurations. On this basis, the hardware design was refined in three stages. The final system APPARILLO2 is equipped with a large format CCD (charge coupled device) camera and 10 cm aperture, which results is a FOV (field of view) of 10° by 10°. One important aspect of the autonomously operating system is the software, that automatically toggles the image acquisition and processes the data (Section 4.4). Based on the measurements performed under different LOS (line-of-sight) within several campaigns, the detection rates and efficiencies have been evaluated, and the detection threshold been determined. Furthermore, the angular

[P] OOOS Web-Interface (2021): https://spacedebris.dlr.de/OOOS_web/observations_log.php, Accessed Sep 26 2021.

resolution of the system is investigated by comparing the measurements to orbital predictions provided by CELESTRAK's NORAD (North American Aerospace Defense Command) TLE (Two-Line Elements) [15] and ILRS's (International Laser Ranging Service) CPF (Consolidated Laser Ranging Prediction Format) [37] predictions. The analysis of the overall system performance allows to work out a perspective to push the passive-optical sensor to be able to detect RSO down to 10 cm in size.

Operational campaigns

Within the time period of November 2020 and October 2021, five campaigns under three different LOS have been performed to observe the impact of season and LOS on APPARILLO2's performance. The observed LOS are zenith, 45° West (W), and 45° North (N), respectively. As shown within this thesis, passive-optical sensors like APPARILLO2 take advantage from the illumination of the RSO by the Sun, while the observer needs to be in the Earth shadow. This implies that during good weather conditions the detection windows are limited to a few hours each night. During winter the two detection windows before sunrise and after sunset are each about 3 h long, which merge to a single window towards summer. It has been found that the experimental detection window is about 50% longer than predicted by PROOF simulations (Section 5.2.1). APPARILLO2 consistently assesses the weather conditions (Section 4.3.5) and toggles observations under clear sky at night (Section 4.4.1).

Detection rates and efficiencies

The measured detection rate is found to be higher in summer compared to winter. This effect is not indicated by PROOF and presumably results from better weather conditions. Under zenith LOS the maximum detection rate is 37 obj/h in campaign #1 December, while in campaign #5 July the maximum observed detection rate is 49 obj/h. Under 45° N LOS the maximum detection rate is 90 obj/h in campaign #2 February, while in campaign #4 April-June the maximum observed detection rate is significantly higher with 162 obj/h. The observed detection rates under 45° W are strongly phase angle dependent compared to 45° N, reaching a maximum detection rate of 92 obj/h before sunrise and only 53 obj/h after sunset. The larger detection rates at 45° N LOS can be related to the larger observed orbital volume and the fact that a lot of LEO RSO are located on polar orbits. This is in contrast to simulations, which have predicted the same number of detectable RSO for 45° N and 45° W LOS. With regard to the detection windows, the simulations again do not agree with measurements. The actual measurements can be performed over a duration of 5.5 h in June,

while the simulated detection window is only 2.5 h long. Consequently, the detection efficiency determined by PROOF tends to be lower, compared to the observed detection efficiencies. However, for RSO smaller than 2 m in diameter, the observed efficiencies are generally smaller than predicted by PROOF simulations (Section 5.2.2). Measured detection efficiencies remain below 10% for RSO smaller than 1 m in diameter, while detection efficiencies for larger RSO of 2 m upwards rise up to 60% - 75% in all campaigns, except under 45° W where it remains below 40%.

Detection threshold

Using information about physical properties derived from the DISCOS (Database and Information System Characterizing Objects in Space) catalog allows to derive the actual detection threshold, which is compared to simulations in Section 5.2.3. The determined detection threshold of APPARILLO2 is an RSO diameter of 0.5 m under zenith, 0.65 m under 45° W, and 0.4 m under 45° N LOS. This contradicts the analytical simulations, which predicted a larger detection threshold under smaller elevations. The lower detection threshold coincides with higher measured detection rates and reinforce the more favorable LOS to northern direction. The smallest RSO are detected at 1000 km orbit height. The reason for that can be seen in the general lower detection efficiencies for lower orbital heights, and the characteristic correlation between RSO diameter and orbit height. For smaller RSO diameter, the density is highest at around 800 km, while larger RSO are distributed more evenly across the ranges. In accordance to the previously mentioned fact that efficiencies for smaller RSO diameter are predicted higher than the actual measurement efficiencies, the simulated thresholds by the analytical model and PROOF turn out to be slightly smaller with about 0.35 m compared to the measured 0.5 m under zenith LOS.

Reasons why the analytical model and PROOF simulations show a better detection threshold are following idealizations:

- The photon flux irradiates the center of the pixel.
- The sensitive/active area of a pixel is assumed to be a square with the width to be the same as the pixel spacing.
- The calculation of the photon flux from the RSO and background illumination might not match with the spectral response of the detector.
- The PSF approximation using Gaussian distribution does not reflect the actual power distribution due to aberrations or diffraction.

- This SNR assumption implies that a large number of pixels are utilized to accurately characterize the background noise levels. This assumption leads to exaggerated values of limiting magnitude for small FOV sensors or for frames containing crowded star fields [49].
- Not all noise sources are considered: photoelectric or flicker noise, fixed-pattern noise, reset noise [43].
- Higher background noise due to artificial light and clouds/humidity.

Measurement resolution

The observation of LEO RSO is performed by pointing the camera and lens to a fixed direction with respect to the horizon. Using the exposure time of one second, stars are recorded as points, while LEO RSO are recorded as streaks. The image processing measures the streak's start and end positions and transforms the measured camera coordinates into equatorial coordinates using astrometric calibration. These coordinates, saved in TDM format, are compared with orbit predictions based on TLE and CPF predictions to derive APPARILLO2's measurement uncertainty.

The determined angular resolution of the system using TLE predictions as reference is 0.042° under zenith, 0.04° under 45° W, and 0.058° under 45° N LOS. The LOS plays a dominant role for the Along-Track error, while the Cross-Track error seems unaffected and matches the angular resolution of the system. Generally, the observed Along-Track error is, with 1000 m, more than ten times larger than the Cross-Track error with about 90 m (Section 5.2.4). The Along-Track error is mainly driven by the uncertainty of the time synchronization, which has probably its main contribution from the mechanical shutter opening and closing duration of about 100 ms. In a future system this may be improved to reduce the Along-Track error. Comparison with CPF predictions consistently revealed a Cross-Track error about three times smaller than by TLE predictions. This reveals the sub-pixel measurement accuracy of the image processing, while the Along-Track error remains large. This further shows that the designed system reveals TLE's intrinsic larger uncertainties. The systems accuracy is in principle sufficient for precise angular measurements to perform subsequent passive-optical closed-loop tracking.

Perspective

A passive-optical sensor measures LEO RSO optically, which adds another source of information to currently RADAR based catalogued RSO. OCS (Optical cross section) and RCS (Radar cross section) are often not equal for an RSO, which results from the fact that the RCS depends more on the RSO materials and size, while the OCS depends highly on the object orientation to the light source, the material, and size of the visible surface. Recent developments in the satellite industry, for instance using wood [95] or black paint [96], favor SSA (Space situational awareness) networks with complementary sensor properties. Materials like wood reduce the RCS, while the OCS is not affected. On the other hand, a black painted satellite has reduced OCS but maintains its RCS. This is why a passive-optical staring sensor, as demonstrated here, can play a major role in future SSA sensor networks. Furthermore, such a system may especially be used to detect objects larger than 0.5 m in order to relieve surveillance systems, such that precise RADAR sensors can focus on detecting smaller or critical RSO.

Over all campaigns, 36% of detected RSO could not be identified using CELESTRAK's TLE catalog, see Section 5.2.1. This confirms the often-stated number of 40% of the known RSO by the US SSN remain unpublished [1], and underlines the ability of a passive-optical staring system to detect unknown orbital objects. Hence, substantial contribution of a passive-optical staring system can be expected to an SSA network.

Passive-optical systems suffer from two main downsides when used for cataloging newly detected objects. One is the relatively low angular resolution, which results from the compromise of a large FOV and consequently relatively small focal length. Secondly, the system only measures two dimensions over a relatively small arc. This is why this system is developed to be combined with a laser ranging system. Such a 'stare and chase' handover of a preliminary orbit prediction from a detected RSO obtained by the staring sensor to a tracking station has been successfully demonstrated within this thesis (Section 5.3.3).
To determine the range to an RSO, two passive-optical sensors can be combined in a parallax setup. The expected range uncertainty is dependent on baseline distance, orbital altitude, and angular resolution, which is calculated to be at least 1400 m for the given system (Section 5.3.4).

The path to push the detection performance to the desired regime around 10 cm RSO diameter has been considered through a hardware and software solution. To propose a system the parameter of the analytical link budget is adopted using the experimental results. The calculation reveals that an aperture diameter of far more than 2 m is necessary to detect RSO smaller than 12 cm. On the other hand, by introducing synthetic tracking as image processing algorithm, the required SNR of an RSO recorded on the image can be reduced from 6 to 0.6 (Section 5.3.2). This eventually allows to detect RSO as small as 14 cm in diameter using APPARILLO2. Further increasing the aperture diameter to 25 cm pushes the detection threshold even below 10 cm (Section 5.3.1).

It can be concluded, that cost-effective easy-to-operate passive-optical sensors as presented in this work, could be utilized to approach uncatalogued regimes, delivering valuable positional information for subsequent laser tracking, and thereby fill a crucial gap in current SSA networks.

7. REFERENCES

[1] H. Klinkrad, "Space Object Catalogs," in *SSA Conference*, Colorado Springs, 2006.

[2] NASA Orbital Debris Program Office, "Orbital Debris Quarterly News Vol 23 Q1-2," vol. 23, no. 1&2, 2019.

[3] CelesTrak, "SATCAT online satellite database," 2021. [Online]. Available: https://celestrak.com/satcat/boxscore.php. [Accessed 28 Aug 2021].

[4] ESA, 2021. [Online]. Available: https://www.esa.int/Safety_Security/Space_Debris/Space_debris_by_the_numbers. [Accessed 28 Aug 2021].

[5] T. Flohrer, H. Krag and R. Klinkrad, "Assessment and categorization of TLE orbit errors for the US SSN catalogue," in *Technical proceedings of 9th AMOS conference*, Maui, 2008.

[6] J. Degnan, "Satellite laser ranging in the 1990s," in *Report of the 1994 Belmont workshop*, Belmont, 1994.

[7] C. Bamann and U. Hugentobler, "Accurate orbit determination of space debris with laser tracking," in *Proc. 7th European conference on space debris*, Darmstadt, 2017.

[8] H. Krag, S. Setty, A. Di Mira, I. Zayer and T. Flohrer, "Groundbased laser for tracking and remediation - an architectural view," in *Proceedings of the 69th international astronautical congress (IAC)*, Bremen, 2018.

[9] Inter-Agency Space Debris Coordination Committee, "IADC Space Debris Mitigation Guidelines," 09 2007. [Online]. Available: https://orbitaldebris.jsc.nasa.gov/library/iadc_mitigation_guidelines_rev_1_sep07.pdf. [Accessed 28 Aug 2021].

[10] NASA Orbital Debris Program Office, "Orbital Debris Quarterly News Vol 24 Q1," vol. 24, no. 1, 2020.

[11] H. Klinkrad, Space Debris - Models and Risk Analysis, 1 ed., Berlin: Springer, 2006.

[12] ESA Space Debris Office, ESA's Annual Space Environment Report, vol. 3.1, Darmstadt: ESOC, 2019.

[13] NASA Orbital Debris Program Office, "Orbital Debris Quarterly News Vol 24 Q4," vol. 24, no. 4, Nov 2020.

[14] H. Klinkrad and H. Sdunnus, "Concepts and applications of the MASTER space debris environment model," *Adv. Space Res.,* vol. 19, no. 2, p. 227–280, 1997.

[15] CelesTrak, "NORAD Two-Line Element Sets," 2020. [Online]. Available: www.celestrak.com/NORAD/elements/. [Accessed 05 Dec 2020].

[16] K. Chang, "Astronauts on SpaceX Flight Encounter Space Junk Danger," 23 Apr 2021. [Online]. Available: https://www.nytimes.com/2021/04/23/science/space-junk.html. [Accessed 28 Aug 2021].

[17] A. Kooser, "Orbital debris strikes ISS robotic arm, leaves a mark," CNET, 28 May 2021. [Online]. Available: https://www.cnet.com/news/orbital-debris-strikes-iss-robotic-arm-leaves-a-mark/. [Accessed 28 Aug 2021].

[18] Office of Safety and Mission Assurance, Guidelines and Assessment Procedures for Limiting Orbital Debris, Washington, D.C.: NASA, 1995.

[19] D. J. Kessler and B. G. Cour-Palais, "Collision frequency of artificial satellites: The creation of a debris belt.," *Journal of Geophysical Research: Space Physics,* vol. 83, no. 6, p. 2637–2646, 1978.

[20] NASA Orbital Debris Program Office, "LEGEND," 2021. [Online]. Available: https://orbitaldebris.jsc.nasa.gov/modeling/legend.html. [Accessed 28 Aug 2021].

[21] International Organization for Standardization, "ISO 24113: Space systems - Space debris mitigation requirements," 2019. [Online]. Available: https://www.iso.org/standard/72383.html. [Accessed 03 Jan 2021].

[22] S. Mathewson, "ESA partners with startup to launch first debris removal mission in 2025," Space.com, 16 May 2021. [Online]. Available: https://www.space.com/esa-startup-clearspace-debris-removal-2025. [Accessed 28 May 2021].

[23] D. McKnight, R. Witner, F. Letizia, S. Lemmens, L. Anselmo, C. Pardini, A. Rossi, C. Kunstadter, S. Kawamoto, V. Aslanov, J.-C. D. Perez, V. Ruch, H. Lewis, M. Nicolls and L. Jing, "Identifying the 50 statistically-most-concerning derelict objects in LEO," *Acta Astronautica,* vol. 181, p. 282–291, 2021.

[24] S. Scharring, H. Dreyer, G. Wagner, J. Kästel, P. Wagner, E. Schafer, W. Riede, C. Bamann, U. Hugentobler, T. Suchodolski, W. Promper, T. Flohrer, S. Setty and I. Zayer, "Conceptual Study on Laser Networks for Near-Term Collision Avoidance for Space Debris in the Low Earth Orbit," in *Proc. of High Power Laser Ablation*, 2021.

[25] M. Schmitz, S. Fasoulas and J. Utzmann, "Performance model for space-based laser debris sweepers," *Acta Astronautica,* vol. 115, p. 376–383, 02 06 2015.

[26] ESA, "Declaration on the Space Situational Awareness (SSA) Preparatory Programme," ESA, Darmstadt, 2008.

[27] T. Floher, "Optical Survey Strategies and their Application to Space Surveillance," in *Geodätisch-geophysikalische Arbeiten in der Schweiz,* vol. 87, S. G. Kommission, Ed., Zürich, ETH Zürich, 2012, p. 178.

[28] Wikipedia, "Phased array animation," 2021. [Online]. Available: https://upload.wikimedia.org/wikipedia/commons/4/4a/Phased_array_animation_with_arrow_10frames_371x400px_100ms.gif. [Accessed 22 May 2021].

[29] C. Bonnal and D. S. McKnight, IAA situation report on space debris. International Academy of Astronautics, 2016., Paris: IAA, 2016.

[30] Defense Logistics Agency, "Contract No: 838-11," US Department of Defense, Washington D.C., 2011.

[31] Wikipedia, "Eglin AFB Site C-6," 2021. [Online]. Available: https://en.wikipedia.org/wiki/Eglin_AFB_Site_C-6. [Accessed 28 Aug 2021].

[32] U.S. Air Force, "AN-FPS-85 radar aerial view," AN/FPS-85 U.S. Air Force Fact Sheet, [Online]. Available: https://upload.wikimedia.org/wikipedia/commons/f/f9/AN-FPS-85_radar_aerial_view.jpg. [Accessed 19 May 2017].

[33] H. Fiedler, J. Herzog, M. Prohaska and T. Schildknecht, "SMARTnet - An Update," in *Proc. 1st NEO and Debris Detection Conference*, Darmstadt, 2019.

[34] NASA Headquarters Office of Safety and Mission Assurance, "Handbook for Limiting Orbital Debris," NASA, Washington, D.C., 2008.

[35] L. Combrinck, "Satellite laser ranging," *Sciences of Geodesy-I,* p. 301–338, 2010.

[36] NASA GFSC, "Potsdam3: General information web page," 2020. [Online]. Available: https://ilrs.gsfc.nasa.gov/network/stations/active/POT3_station_info.html. [Accessed 22 May 2021].

[37] TU München:, "Satellites tracked by ILRS," 2020. [Online]. Available: https://edc.dgfi.tum.de/en/satellites/. [Accessed 29 Aug 2021].

[38] G. Kirchner, F. Koidl, F. Friederich, I. Buske, U. Völker and W. Riede, "Laser measurements to space debris from Graz SLR station," *Advances in Space Research,* vol. 51, no. 1, pp. 21-24, 2013.

[39] S. Riepl, J. Eckl, F. Sproll, D. Hampf, P. Wagner, W. Riede, G. Kirchner, F.Koidl, M. Steindorfer, P. Wang, U. Schreiber, C. Bamann, U. Hugentobler, T. Flohrer und Q. Funke, „First results from an ESA study on accurate orbit determination," in *Proc. 7th European Conference on Space Debris*, Darmstadt, Germany, 2017.

[40] Austrian academy of science, "Laser ranging research group web page," 2020. [Online]. Available: https://www.oeaw.ac.at/en/iwf/research/research-groups/satellite-laser-ranging. [Accessed 22 May 2021].

[41] H. Klinkrad, *ESA Space Debris Course,* 2018.

[42] G. D. Badhwar and P. D. Anz-Meador, "Relationship of Radar Cross Section to the Geometric Size of Orbital Debris," in *AIAA/NASA/DOD Orbital Debris Conference*, Baltimore, Maryland, 1990.

[43] H. Gross, Handbook of optical systems, vol. Vol. 1. Fundamentals of Technical Optics, Weinheim: WILEY-VCH Verlag GmbH & Co. KGaA, 2005.

[44] Nick84, "File:Solar spectrum en.svg," 14 Feb 2013. [Online]. Available: https://commons.wikimedia.org/wiki/File:Solar_spectrum_en.svg. [Accessed 22 May 2021].

[45] J. R. Shell, "Optimizing orbital debris monitoring with optical telescopes," in *Proc. of AMOS*, Maui, HI, 2010.

[46] J. R. Tower, P. Swain, F.-L. Hsueh, R. Dawson, P. Levine, G. Meray, J. Andrews, V. Frantz, M. Grygon, M. Reale and T. Sudol, "Large Format backside Illuminated CCD Imager for Space Surveillance," *IEEE Transactions on Electron Devices,* vol. 50, no. 1, pp. 218-224, 2003.

[47] D. W. J. Streuber and E. I. Bailis, "Imaging Charge-Coupled Devices for Deep-Space Surveillance," in *Proc. Soc. Photo-opt. Instr. Eng., Smart Sensors II*, 1980.

[48] mostlymissiledefense, "Space Surveillance: The Visual Brightness and Size of Space Objects," 21 Aug 2012. [Online]. Available: mostlymissiledefense.com/2012/08/21/space-surveillance-the-visual-brightenss-and-size-of-space-objects-august-21-2012/. [Accessed 22 May 2021].

[49] R. Coder and M. Holzinger, "Multi-objective design of optical systems for space situational awareness," *Acta Astronautica,* vol. 128, p. 669–684, 06 07 2016.

[50] J. Degnan, "Millimeter Accuracy Satellite Laser Ranging: A Review," *Contributions of Space Geodesy to Geodynamics: Technology.,* pp. 133-162, 1993.

[51] R. M. Pierce, J. Ramaprasad and E. C. Eisenberg, "Optical attenuation in fog and clouds," in *Proc. SPIE 4530, Optical Wireless Communications IV*, 2001.

[52] K. Fischer, M. Witiw and E. Eisenberg, "Optical attenuation in fog at a wavelength of 1.55 micrometers," *Atmospheric Research,* vol. 87, no. 3-4, pp. 252-258, 2008.

[53] G. Ruppersberg und R. Schallhase, „Slant meteorological visibility," *Journal of Modern Optics,* Bd. 26, Nr. 5, 1979.

[54] Astrometry.net project, "Astrometry.net astrometric engine," 2020. [Online]. Available: http://astrometry.net/use.html. [Accessed 08 Feb 2021].

[55] D. W. Hogg and M. Blanton, "Automated Astrometry," *Astronomical Data Analysis Software and Systems XVII, ASP Conference Series,* vol. 394, 2008.

[56] DC-3 Dreams, *PinPoint Engine V6.0 Reference Guide,* Advances Observatory Software, 2012.

[57] K. F. Wakker, Fundamentals of Astrodynamics, D. U. o. Technology, Ed., Delft: Faculty of Aerospace Engineering, 2015.

[58] B. Hofmann-Wellenhof, H. Lichtenegger and J. Collins, GPS - theory and practice, vol. 5th, Wien: Springer, 1997, p. 382.

[59] N. Sneuuw, *Dynamic Satellite Geodesy,* Stuttgart: University of Stuttgart, 2006.

[60] D. A. Vallado, Fundamentals of Astrodynamics and Applications, 3rd ed., Berlin: Springer, 2007.

[61] U. Renner, J. Nauck and N. Balteas, Satellitentechnik: Eine Einführung, Berlin: Springer Verlag, 2013.

[62] P. Wagner, T. Hasenohr, D. Hampf, F. Sproll, L. Humbert, J. Rodmann and W. Riede, "Detection and laser ranging of orbital objects using optical methods," in *Proc. of Remote Sensing System Engineering VI*, San Diego, 2016.

[63] P. Wagner, D. Hampf, F. Sproll, L. Humbert and T. Hasenohr, "System zur Bestimmung und/oder Vorhersage einer Position und/oder einer Flugbahn von orbitalen Objekten im Weltraum". Germany Patent DE 20 2017 101 831 U1, 29 March 2017.

[64] M. Steindorfer, G. Kirchner, F. Koidl, P. Wang, A. Anto, J. Sánchez and K. Merz, "Stare and chase of space debris targets using real-time derived pointing data," *Adv. Space Res.,* vol. 60, pp. 1201-1209, 2017.

[65] J. Gelhaus, S. Flegel and C. Wiedemann, "Program for Radar and Optical Observation Forecasting," European Space Agency, Braunschweig, 2011.

[66] Thorlabs, "Camera Lenses for Machine Vision," 2021. [Online]. Available: https://www.thorlabs.com/images/tabimages/MVL75M1.xlsx. [Accessed 22 Sep 2021].

[67] M. Schubert, L. Böttcher, E. Gamper, E. Stoll and P. Wagner, "Detectability of Space Debris Objects in the Infrared Spectrum," *Advances in Space Research,* 2021.

[68] H. Krag, A Method for the Validation of Space Debris Models and for the Analysis and Planning of Radar and Optical Surveys, Vols. Berichte aus der Luft- und Raumfahrttechnik, I. o. S. S. a. t. T. Braunschweig, Ed., Aachen: Shaker Verlag, 2003.

[69] Andor, "Andor Zyla for life sciences specifications," 2021. [Online]. Available: https://andor.oxinst.com/assets/uploads/products/andor/documents/andor-zyla-for-life-sciences-specifications.pdf. [Accessed 26 Sep 2021].

[70] Finger Lakes Instruments:, "ProLine 09000 data sheet," 2018. [Online]. Available: http://www.flicamera.com/spec_sheets/archive/PL09000.pdf. [Accessed 28 Aug 2021].

[71] FLI, "ProLine PL16803," 2015. [Online]. Available: http://www.flicamera.com/spec_sheets/archive/PL16803.pdf. [Accessed 26 Sep 2021].

[72] E. Optics, "GS3-U3-41C6NIR-C 1" FLIR Grasshopper 3 USB 3.0 Hochleistungskamera, NIR," 2016. [Online]. Available: https://www.edmundoptics.de/p/GS3-U3-41C6NIR-C-1-Grasshopper-USB-30-NIR-Camera/31998/. [Accessed 18 June 2016].

[73] B. Carnathan, "Canon EF 85mm f/1.2L II USM Lens Specifications and Measurements," The-Digital-Picture.com, 2021. [Online]. Available: https://www.the-digital-picture.com/Reviews/Lens-Specifications.aspx?LensComp=0&Lens=397. [Accessed 22 May 2021].

[74] B. Carnathan, "Canon EF 135mm f/2L USM Lens Specifications and Measurements," The-Digital-Picture.com, 2021. [Online]. Available: https://www.the-digital-picture.com/Reviews/Lens-Specifications.aspx?LensComp=0&Lens=108. [Accessed 22 May 2021].

[75] B. Carnathan, "Canon EF 200mm f/2L IS USM Lens Specifications and Measurements," The-Digital-Picture.com, 2021. [Online]. Available: https://www.the-digital-picture.com/Reviews/Lens-Specifications.aspx?Lens=458. [Accessed 22 May 2021].

[76] B. Carnathan, "Canon EF 400mm f/2.8L IS II USM Lens Specifications and Measurements," The-Digital-Picture.com, 2021. [Online]. Available: https://www.the-digital-picture.com/Reviews/Lens-Specifications.aspx?LensComp=0&Lens=741. [Accessed 22 May 2021].

[77] P. Wagner, D. Hampf and W. Riede, "Passive optical space surveillance system for initial LEO object detection," in *Proceedings of 66th international astronautical conference (IAC)*, Jerusalem, 2015.

[78] Vincent Associates, "Uniblitz CS65 datasheet," 2020. [Online]. Available: https://www.uniblitz.com/wp-content/uploads/2020/05/uniblitz-cs65-datasheet.pdf. [Accessed 05 Nov 2021].

[79] T. Hasenohr, "Initial detection and tracking of objects in low earth orbit," University of Stuttgart, Stuttgart, 2016.

[80] D. Hampf, *GPS camera timer,* DLR, 2016.

[81] D. Hampf, P. Wagner and W. Riede, "Optical technologies for observation of low earth orbit objects," in *Proceedings of 65th international astronautical conference (IAC)*, Toronto , 2014.

[82] D. Hampf, F. Sproll and T. Hasenohr, "OOOS: a hardware-independent SLR control system. In ILRS technical workshop," in *ILRS technical workshop*, Riga, 2017.

[83] NASA/GSFC, "FITS Support Office," 2021. [Online]. Available: https://fits.gsfc.nasa.gov/fits_home.html. [Accessed 28 Aug 2021].

[84] R. Haussmann, P. Wagner and T. Clausen, "Streak detection of space debris by a passive optical sensor," in *Proc. of 8th European conference on space debris*, Darmstadt, 2021.

[85] P. Wagner and T. Clausen, "APPARILLO: a fully operational and autonomous staring system," *CEAS Space Journal,* pp. 1-24, 5 Jul 2021.

[86] A. Milani, "Discovery of very small asteroids by automated trail detection," *Earth, Moon, and Planets,* vol. 72, p. 257–262, 1996.

[87] A. Vananti, K. Schild and T. Schildknecht, "Improved detection of faint streaks based on a streak-like spatial filter," *Adv. Space Res.,* vol. 65, no. 1, p. 364–378, 2020.

[88] CCSDS, "Tracking Data Message - RECOMMENDED STANDARD CCSDS 503.0-P-1.1.," 2018. [Online]. Available: https://public.ccsds.org/Lists/CCSDS%205030P11/503x0p11.pdf. [Accessed 21 Dec 2020].

[89] ESA, "DISCOSweb," 2021. [Online]. Available: https://discosweb.esoc.esa.int/. [Accessed 29 Jan 2021].

[90] N. Baba, S. Isobe, Y. Norimoto and M. Noguchi, "Stellar speckle image reconstruction by the shift-and-add method," *Applied Optics,* vol. 24, no. 10, pp. 1403-5, 1984.

[91] J. Zscheile, "Synthetic optical tracking of objects in Low Earth Orbit in real-time," TU Dresden, Dresden, 2019.

[92] M. Shao, B. Nemati, C. Zhai, S. Turyshev and J. Sandhu, "Finding Very Small Near-Earth Asteroids using Synthetic Tracking," *In The Astrophysical Journal,,* vol. 782, no. 1, 2014.

[93] J. Zscheile, P. Wagner, R.-A. Lorbeer and B. Guthier, "Synthetic tracking for orbital object detection in LEO," in *Proc. of 1st NEO and Debris Detection Conference*, Darmstadt, 2019.

[94] T. Hasenohr, D. Hampf, P. Wagner, F. Sproll, J. Rodmann and L. Humbert, "Initial detection of low earth orbit objects through passive optical wide angle imaging systems," in *Proc. of Deutscher Luft- und Raumfahrtkongress*, 2016.

[95] J. Timmer, "New wooden satellite is part advertising, part student project," Ars Technica, 14 April 2021. [Online]. Available: https://arstechnica.com/science/2021/04/finland-may-beat-japan-in-the-wooden-satellite-space-race/. [Accessed 05 Sep 2021].

[96] A. Wood, "SpaceX dark coating successfully cuts Starlink satellite reflectivity," New Atlas, 08 Dec 2020. [Online]. Available: https://newatlas.com/space/spacex-starlink-satellite-reflectivity-astronomy/. [Accessed 05 Sep 2021].

[97] M. Iqbal, An introduction to solar radiation, 9 ed., Academic Press Canada, 1983.

[98] G. Seeber, Satellite geodesy: foundations, methods, and applications., Berlin, Boston: Walter de Gruyter, 2003.

[99] M. Henriksson, "Detection probabilities for photon-counting avalanche photodiodes applied to a laser radar system," *Applied optics,* vol. 44, no. 25, pp. 5140-5147, 2005.

[100] D. A. Arnold, "Transfer Function of the LARES Retroreflector Array, 2015.," in *ILRS Technical Workshop*, 2015.

[101] D. Jenn, "Laser Cross Section (Ch 9)," Nov 2011. [Online]. Available: http://faculty.nps.edu/jenn/EC4630/LCSV2.pdf. [Accessed 10 Nov 2020].

[102] W. E. Krag, "Visible Magnitude of Typical Satellites in Synchronous Orbits," Massachusetts Institute of Technology, Cambridge, 1974.

[103] F. Moeller, "Optics of the lower atmosphere," *Applied Optics,* vol. 3, no. 2, 1964.

[104] R. Hadfield, "Single-photon detectors for optical quantum information applications," *Nature photonics,* vol. 3, no. 12, pp. 696-705, 2009.

[105] C. Kießling, "Development of digital imaging methods for an autonomous system for detection and mapping of orbital objects," Johannes Gutenberg-University Mainz, Mainz, 2018.

[106] W. Commons, „File:Comparison satellite navigation orbits.svg," 2021. [Online]. Available: https://commons.wikimedia.org/wiki/File:Comparison_satellite_navigation_orbits.svg. [Zugriff am 29 Sep 2021].

[107] NASA, "Process for Limiting Orbital Debris," NASA, 2019.

[108] Raymetrics S. A., *Camera Enclosure Instruction manual,* 2019.

[109] ASTELCO Systems, *New-Technology-Montierung NTM-500,* 2010.

[110] PlaneWave Instruments, "PlaneWave CDK17," 2008. [Online].

[111] D. Arnold, „Method of calculating retroreflector-array transfer functions," SAO Special Report 382, 1979.

[112] D. Arnold, „Cross section of ILRS satellites," in *ILRS Technical Workshop*, 2003.

[113] M. Shao, "Finding Very Small Near-Earth Asteroids using Synthetic Tracking," *The Astrophysical Journal,* 10 Feb 2014.

[114] T. Flohrer and H. Krag, "Space Surveillance and Tracking in ESA's SSA Programme," in *Proceedings 7th European Conference on Space Debris*, Darmstadt, 2017.

[115] P. Wagner, D. Hampf, F. Sproll, T. Hasenohr, L. Humbert, J. Rodmann and W. Riede, "Passive optical link budget for LEO space surveillance," in *Technical proceedings of 18th AMOS conference*, Maui, 2017.

[116] C. Á. Arroyo-Parejo, N. Sánchez-Ortiz and R. Domínguez-Gonzalez, "Effect of Mega-Constellations on Collision Risk in Space," in *Proc. of 8th European Conference on Space Debris*, Darmstadt, 20–23 April 2021.

[117] R. R. Bate, D. D. Mueller and J. E. White, Fundamentals of Astrodynamics, New York: Dover Publications Inc., 1971, p. 455.

[118] E. Stansberry, „Characterizing the Space Debris Environment with a Variety of SSA Sensors," in *Space Situational Awareness and its Relationship with Science (PSW2)*, Bremen, 2010.

8. PUBLICATIONS

Partial/intermediate results of this thesis were previously published in:

8.1. JOURNAL PAPER

1) *P. Wagner and T. Clausen* (2021) "APPARILLO: a fully operational and autonomous staring system for LEO debris detection". CEAS Space Journal. Springer. DOI: 10.1007/s12567-021-00380-6, ISSN 1868-2502
2) *D. Hampf, E. Schafer, F. Sproll, T. Otsubo, P. Wagner and W. Riede* (2019) "Satellite Laser Ranging at 100 kHz Pulse Repetition Rate". CEAS Space Journal. Springer. doi: 10.1007/s12567-019-00247-x. ISSN 1868-2502
3) *M. Schubert, L. Böttcher, E. Gamper, E. Stoll and P. Wagner*, "Detectability of Space Debris Objects in the Infrared Spectrum", submitted to Elsevier 15. February 2021
4) *D. Hampf, F. Sproll, P. Wagner, L. Humbert, T. Hasenohr and W. Riede,* (2016) "First successful satellite laser ranging with a fibre-based transmitter". Advances in Space Research, 58 (4), pp. 498-504. Elsevier. doi: 10.1016/j.asr.2016.05.020. ISSN 0273-1177
5) *L. Humbert, D. Hampf, P. Wagner, F. Sproll and W. Riede* (2015) "Innovative laser ranging station for orbit determination of LEO objects with a fiber-based laser transmitter", CEAS Space Journal, (pp. 1-5), ISSN 1868-2502

8.2. PATENTS

(1) Patent: DE 10 2015 106 481.2, "Optische Einrichtung (Strahlteiler für Instrumente mit optischer Vergrößerung)", *Buske, Ivo; Wagner, Paul; Hampf, Daniel* (Filing date: Oct 2015).
(2) Gebrauchsmusterschrift, DE 20 2017 101 831 U1 "System zur Bestimmung und/oder Vorhersage einer Position und/oder einer Flugbahn von orbitalen Objekten im Weltraum", *Wagner, Paul; Hampf, Daniel; Sproll, Fabian; Humbert, Leif; Hasenohr, Thomas,* (29 March 2017), https://patents.google.com/patent/DE202017101831U1/en (https://register.dpma.de/DPMAregister/pat/PatSchrifteneinsicht?docId=DE202017101831U1), Accessed 22 January 2021
(3) Patent application DE 102019126336.0, „Kompaktes System zur Laserentfernungsmessung zu Satelliten ‚miniSLR'", *Wagner, Paul; Hampf, Daniel.*

8.3. CONFERENCE PAPER

1) *Wagner, Paul and Hasenohr, Thomas and Hampf, Daniel and Sproll, Fabian and Humbert, Leif and Rodmann, Jens and Riede, Wolfgang* (2017) Passive optical link budget for LEO space surveillance. 2017 AMOS Conference, 19.-22. Sep. 2017, Maui, HI, USA

2) *Wagner, Paul and Hampf, Daniel and Sproll, Fabian and Hasenohr, Thomas and Humbert, Leif and Rodmann, Jens and Riede, Wolfgang* (2016) "Detection and laser ranging of orbital objects using optical methods". In: Proceedings of SPIE - The International Society for Optical Engineering. SPIE Optical Engineering and Applications, 28. Aug.-01. Sep. 2016, San Diego, CA, USA. doi: 10.1117/12.2236919

3) *Wagner, Paul and Hampf, Daniel and Riede, Wolfgang* (2015) "Passive optical space surveillance system for initial LEO object detection". In: Proceedings of the International Astronautical Congress, IAC. 66th International Astronautical Congress, 12.-16. Oct. 2015, Jerusalem, Israel

4) *Wagner, Paul and Schröder, Helmut and Riede, Wolfgang* (2014) "In-situ laser-induced contamination monitoring using long-distance microscopy". In: Proceedings of SPIE - The International Society for Optical Engineering. SPIE Laser Damage 2014, 27.-30. Sep. 2014, Boulder, USA.

5) *Scharring, Stefan and Dreyer, Heiko and Wagner, Gerd and Kästel, Jürgen and Wagner, Paul and Schafer, Ewan and Riede, Wolfgang and Bamann, Christoph and Hugentobler, Urs and Lejba, Pawel and Suchodolski, Tomasz and Döberl, Egon and Weinzinger, Dietmar and Promper, Wolfgang and Flohrer, Tim and Setty, Srinivas and Zayer, Igor and Di Mira, Andrea and Cordelli, Emiliano* (2021) "Conceptual Study on Laser Networks for Near-Term Collision Avoidance for Space Debris in the Low Earth Orbit". High Power Laser Ablation, 13.-15. Apr. 2021, virtual.

6) *Hampf, Daniel and Riede, Wolfgang and Bartels, Nils and Schafer, Ewan and Wagner, Paul* (2021) "A path towards low-cost, high-accuracy orbital object monitoring". 8th European Conference on Space Debris, 20.-23. Apr 2021, Darmstadt.

7) *Haussmann, Rudolf and Wagner, Paul and Clausen, Tim* (2021) "Streak detection of space debris by a passive optical sensor". 8th European Conference on Space Debris, 20.-23. April 2021, Darmstadt, Germany.

8) *Scharring, Stefan and Dreyer, Heiko and Wagner, Gerd and Riede, Wolfgang and Schafer, Ewan and Kästel, Jürgen and Wagner, Paul and Bamann, Christoph and Hugentobler, Urs and Suchodolski, Tomasz and Lejba, Pawel and Döberl, Egon and Weinzinger, Dietmar* (2020) "Final Presentation: Laser Ranging and Momentum Transfer Evolution Study (LARAMOTIONS)". Final Presentation: Laser Ranging and Momentum Transfer Evolution Study (LARAMOTIONS), 17. Dez. 2020, online.

9) *Wagner, G., Wagner, P., Schafer, E., Hampf, D., & Riede, W.* (2019). "Mobile Station for Orbit Determination of Satellites and Space Debris"., In Proc. of the 1st IOC, 09-12. Dec 2019, Sugarland, TX, USA.

10) *Zscheile, Josua and Wagner, Paul and Lorbeer, Raoul-Amadeus and Guthier, Benjamin* (2019) "Synthetic tracking for orbital object detection in LEO". ESA NEO and Debris Detection Conference, 22.-24.01.2019, Darmstadt, Deutschland.

11) *Hampf, Daniel and Wagner, Paul and Schafer, Ewan and Riede, Wolfgang* (2018) "Concept for a new minimal SLR system". In: 21st International Laser Ranging Workshop. 21st International Laser Ranging Workshop, 5.-9. Nov 2018, Canberra, Australia

12) *Hampf, Daniel and Wagner, Paul and Schafer, Ewan and Mösbauer, Pascal and Lützen, Pia and Riede, Wolfgang* (2018) "MiniSLR: A fully automated miniature satellite laser ranging groand station". In: Proceedings of the International Astronautical Congress, IAC. 69th International Astronautical Congress, 1.-5. Okt. 2018, Bremen

13) *Rodmann, Jens and Hampf, Daniel and Hasenohr, Thomas and Humbert, Leif and Riede, Wolfgang and Sproll, Fabian and Wagner, Paul* (2017) "Precise short- and long-term propagation of orbits and uncertainties using the Hermite integration scheme for LEO space debris objects". KePASSA 2017 – 3rd International Workshop on Key Topics in Orbit Propagation Applied to Space Situational Awareness, 25.-27. July 2017, Noordwijk, NL

14) *Humbert, Leif and Hampf, Daniel and Sproll, Fabian and Wagner, Paul and Hasenohr, Thomas and Rodmann, Jens and Riede, Wolfgang* (2017) "Innovative Technolohies for Optical Ground Stations". 7th European Conference on Space Debris, 18 - 21 April 2017, Darmstadt, Deutschland.

15) *Rodmann, Jens and Hampf, Daniel and Hasenohr, Thomas and Humbert, Leif and Riede, Wolfgang and Sproll, Fabian and Wagner, Paul* (2017) Precise orbit propagation for space debris objects using the Hermite integration scheme. 7th European Conference on Space Debris, 18.-21. Apr. 2017, Darmstadt, Deutschland

16) *Stefan Riepl et al.,* (2017) "First Results from an ESA Study on Accurate Orbit Determination with Laser Tracking of Uncooperative Targets", In Proc. of 7th European Conference on Space Debris, Darmstadt, Germany

17) *Hasenohr, Thomas and Hampf, Daniel and Wagner, Paul and Sproll, Fabian and Rodmann, Jens and Humbert, Leif and Herkommer, Alois and Riede, Wolfgang* (2016) "Initial Detection of Low Earth Orbit Objects through Passive Optical Wide Angle Imaging Systems". Deutscher Luft- und Raumfahrtkongress, 13.15. Sep. 2016, Braunschweig, Germany

18) *Hampf, Daniel and Sproll, Fabian and Wagner, Paul and Humbert, Leif and Hasenohr, Thomas and Riede, Wolfgang and Rodmann, Jens* (2016) "Satellite Laser Ranging with a fibre-based transmitter". In: 20th International Laser Ranging Conference. 20th International Laser Ranging Conference, 9-14 Oct 2016, Potsdam.

19) *Sproll, Fabian and Hampf, Daniel and Wagner, Paul and Riede, Wolfgang and Eckl, Johann and Riepl, Stefan and Schreiber, Ulrich and Bamann, Christoph and Hugentobler, Urs and Kirchner, Georg and Koidl, Franz and Steindorfer, Michael* (2016) "Two-color and multistatic space debris laser tracking". 20th Int. Workshop on Laser Ranging, 9.-14. Oct 2016, Potsdam, Deutschland.

20) *Hippler, Markus and Wagner, Paul and Schroeder, Helmut and Riede, Wolfgang* (2016) "Laser-induced contamination of space borne laser systems: impact of organic contamination and mitigation by oxygen". In: Proceedings of SPIE - The International Society for Optical

Engineering, 9952, 99520N-1. Systems Contamination: Predictions, Control, and Performance 2016, 28. Aug. - 01. Sept. 2016, San Diego, USA

21) *Hasenohr, Thomas and Hampf, Daniel and Wagner, Paul and Sproll, Fabian and Rodmann, Jens and Humbert, Leif and Herkommer, Alois and Riede, Wolfgang* (2016), "Initial detection of low earth orbit objects through passive optical wide angle imaging systmes", Deutscher Luft- und Raumfahrtkongress, 13.15. Sep. 2016, Braunschweig, Germany

22) *Gouy, Yann and Wagner, Paul and Sproll, Fabian and Hampf, Daniel and Riede, Wolfgang and and Steck, Emilie and Sanchez, Crisanto and Salter, Michael and Wang, Qin and Michalkiewicz, Aneta and Krezel, Jerzy and Debowska, Anna and d'Humières, Benoît and Thueux, Yoann* (2016) "The C3PO Project: a Laser Communication System Concept for Small Satellites". 4S Symposium, 01. June. 2016, Valletta, Malta.

23) *Riede, Wolfgang and Buske, Ivo and Hampf, Daniel and Sproll, Fabian and Wagner, Paul and Walther, Andreas and Humbert, Leif* (2016) "Laseroptische Nachführsysteme für Anwendungen in der Luft- und Raumfahrt". DWT Tagung Angewandte Forschung für Verteidigung und Sicherheit in Deutschland, 22.-24. Februar 2016, Bonn Bad Godesberg, Deutschland

24) *Hampf, Daniel and Riede, Wolfgang and Wagner, Paul and Sproll, Fabian and Humbert, Leif* (2015) "Orbital Debris Laser Ranging Station Stuttgart". ILRS Technical Workshop, 26. - 30. Oct. 2015, Matera, Italy.

25) *Hampf, Daniel and Wagner, Paul and Riede, Wolfgang* (2014) "Optical technologies for observation of low Earth orbit objects". In: Proceedings of the International Astronautical Congress, IAC. 65th International Astronautical Congress 2014, 29. Sep - 03. Okt 2014, Toronto, Canada

26) *Wagner, Paul and Hampf, Daniel and Sproll, Fabian and Humbert, Leif and Riede, Wolfgang* (2015) "Passiv und aktiv optische Detektion und Vermessung von Weltraumschrott". mn Seminar (invited talk), 15. Dez. 2015, Hochschule Darmstadt, Darmstadt, Deutschland

27) *Riede, Wolfgang and Hampf, Daniel and Wagner, Paul and Giesen, Adolf* (2014) "Active-optical debris detection: a means for highly accurate position determination of space debris orbits". Workshop on Space Debris Modeling and Remediation in Paris, 16.-18.Juni 2014, Paris.

28) *Schroeder, Helmut and Wagner, Paul and Kokkinos, Dimitris and Riede, Wolfgang and Tighe, Adrian* (2013) "Laser-induced contamination and its impact on laser damage threshold". In: 45rd Annual Laser Damage Symposium on Optical Materials for High Power Lasers, 8885. Laser-Induced Damage in Optical Materials 2013, 22.-25. Sept. 2013, Boulder, USA.

9. APPENDIX

9.1. SIMULATIONS

9.1.1. PASSIVE-OPTICAL LINK BUDGET

Following graphs from Figure 9.1 to Figure 9.6 use the passive-optical link budget parameters listed in Table 4.1.

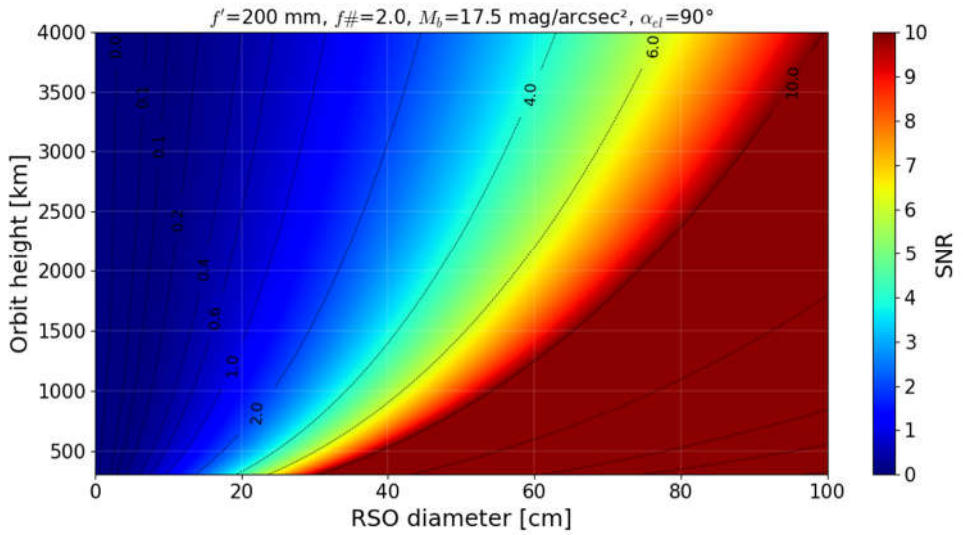

Figure 9.1: The SNR depending on the RSO orbit height and RSO diameter at M_b=17.5 mag/arcsec² background brightness. All simulation parameters are listed in Table 4.1. (Note, that the colors are chosen to show the detectability: red – very high, green – high, blue – low)

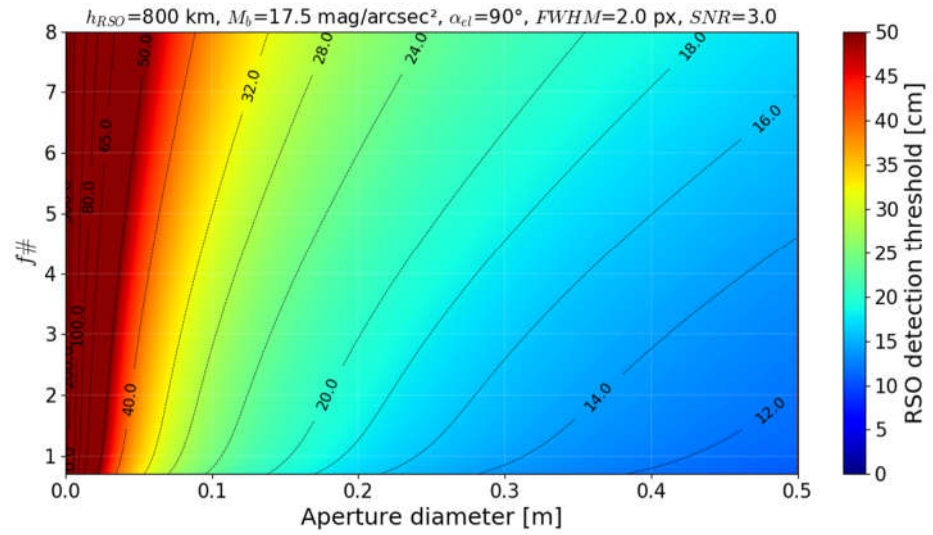

Figure 9.2: The detectable RSO size in 800km orbit height depending on aperture diameter and f-number. All simulation parameters are listed in Table 4.1.

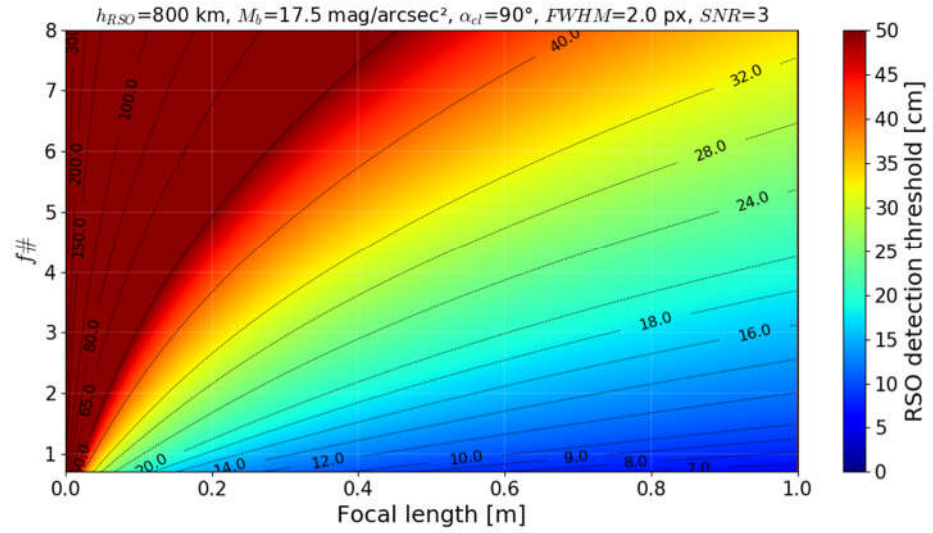

Figure 9.3: The detectable RSO size in 800km orbit height with background illumination of 17.5 mag/arcsec² depending on the optical system's focal length and f-number. All simulation parameters are listed in Table 4.1.

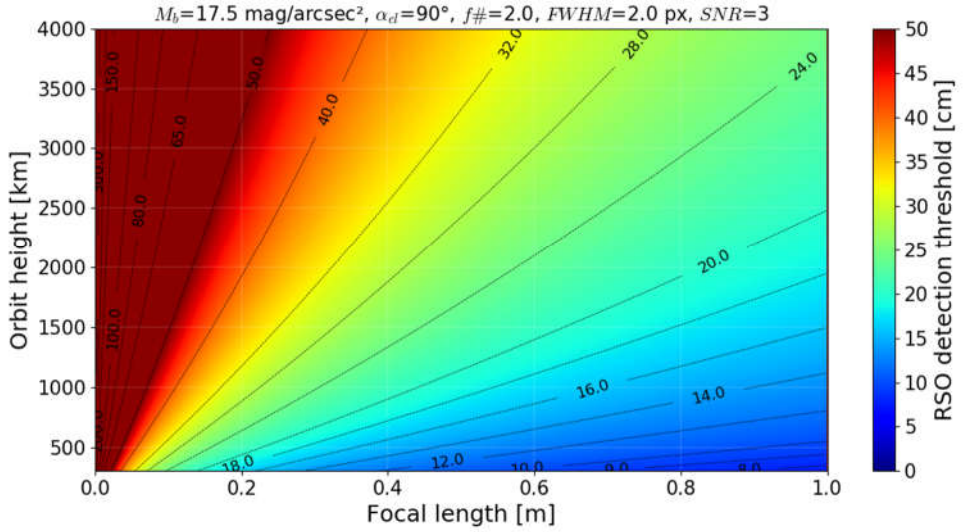

Figure 9.4: The detectable RSO at diffrent orbit height depending on the focal length. All simulation parameters are listed in Table 4.1.

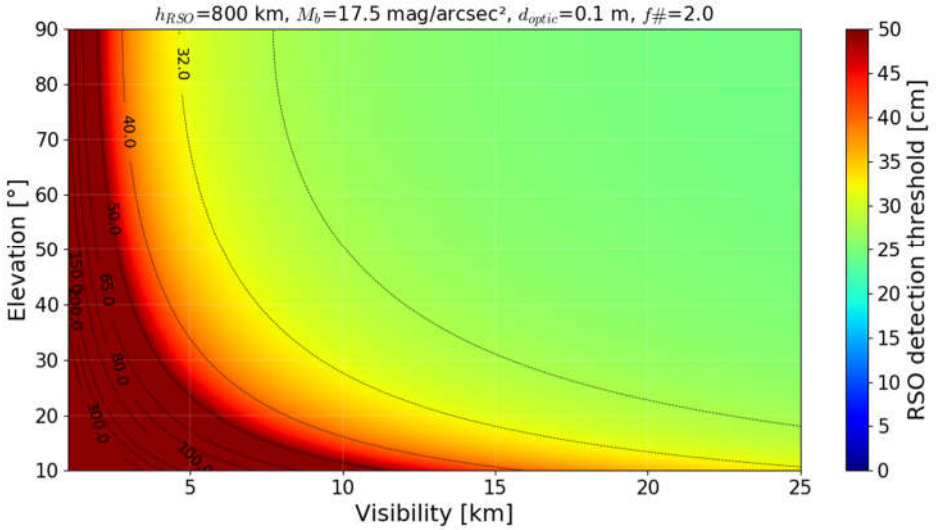

Figure 9.5: The detectable RSO size in 800km orbit height depending on the visibility and LOS elevation. All simulation parameters are listed in Table 4.1.

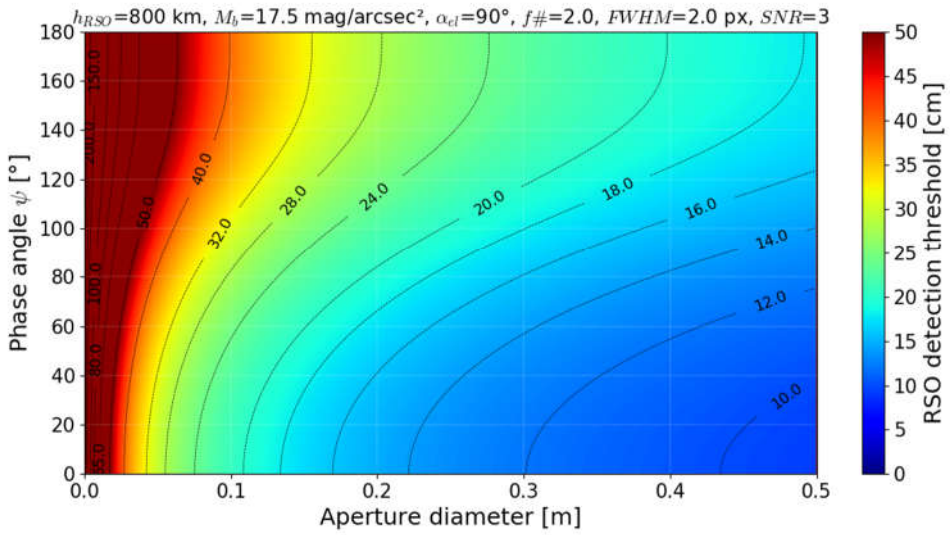

Figure 9.6: The detectable RSO size in 800km orbit height depending on aperture diameter and the phase angle at the RSO between Sun and observer. All simulation parameters are listed in Table 4.1.

9.1.2. PROOF

Under Chapter 4.2.2.1 the setup of PROOF simulations is explained, where Table 4.2 lists the general PROOF settings, Table 4.3 the camera parameters, and Table 4.5 the lens properties, which are used for PROOF simulations in Figure 9.7 to Figure 9.24.

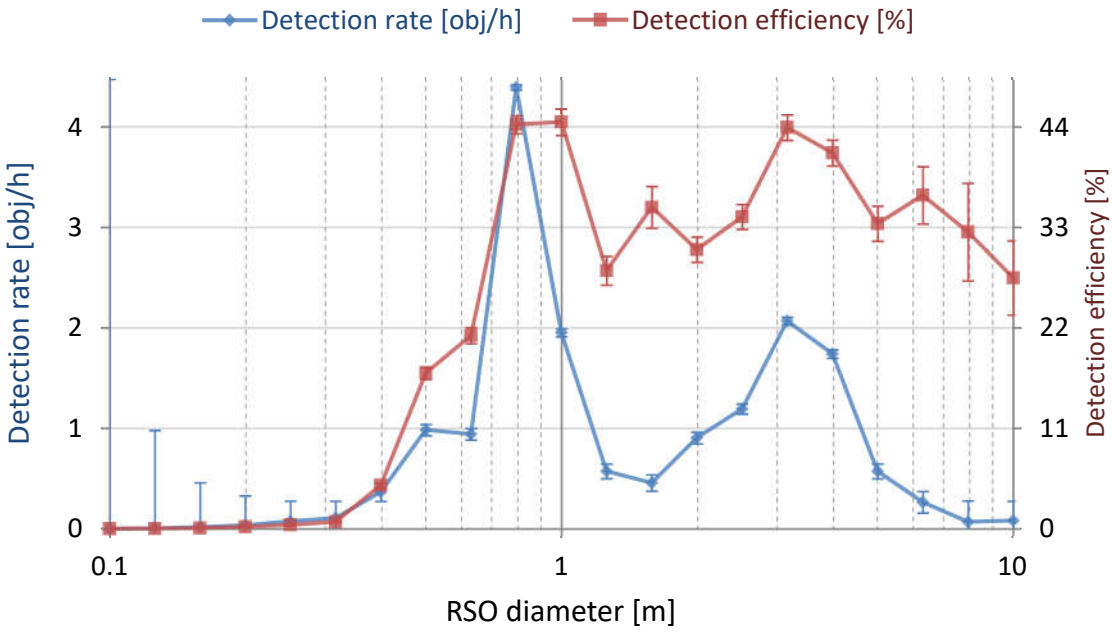

Figure 9.7: Detection rate per RSO diameter (blue) and corresponding detection efficiency using the FLI PL16803 and 135mm f2 lens.

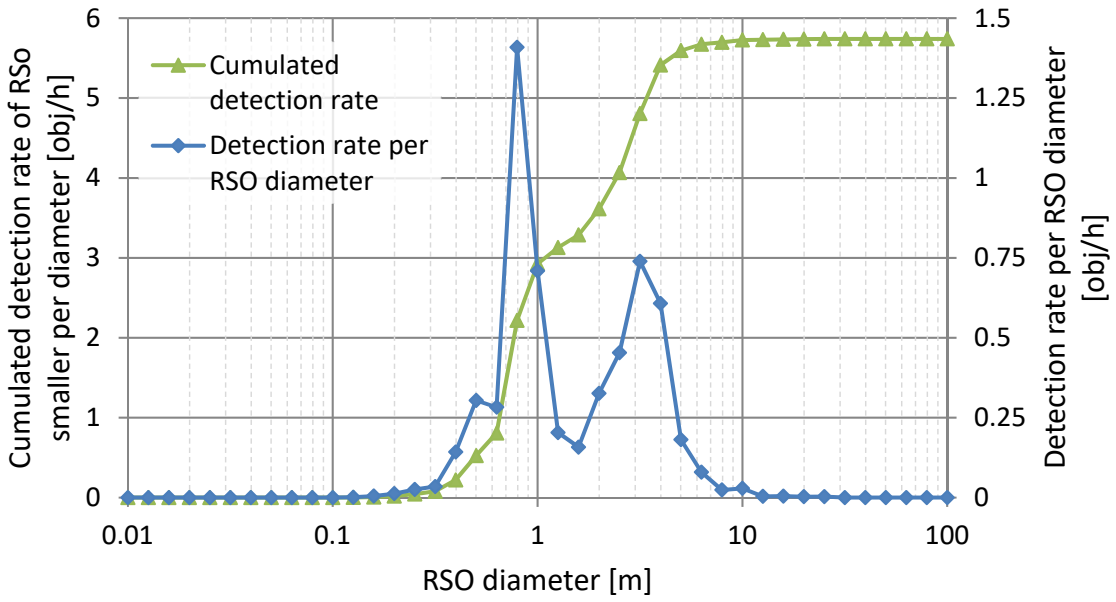

Figure 9.8: Cumulated detection rate for RSO with smaller diameter (green) and detection rate per RSO diameter (blue) simulated with the ANDOR ZYLA camera and 135mm f2 lens.

9.1.2.1. System comparison

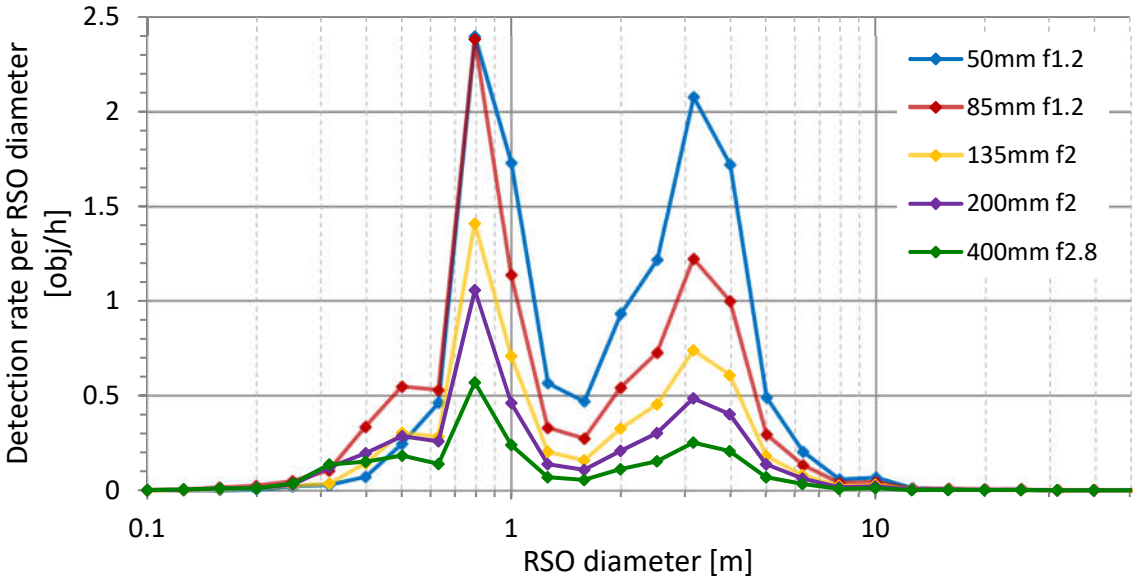

Figure 9.9: Detection rate per RSO diameter using ANDOR ZYLA camera and different lenses.

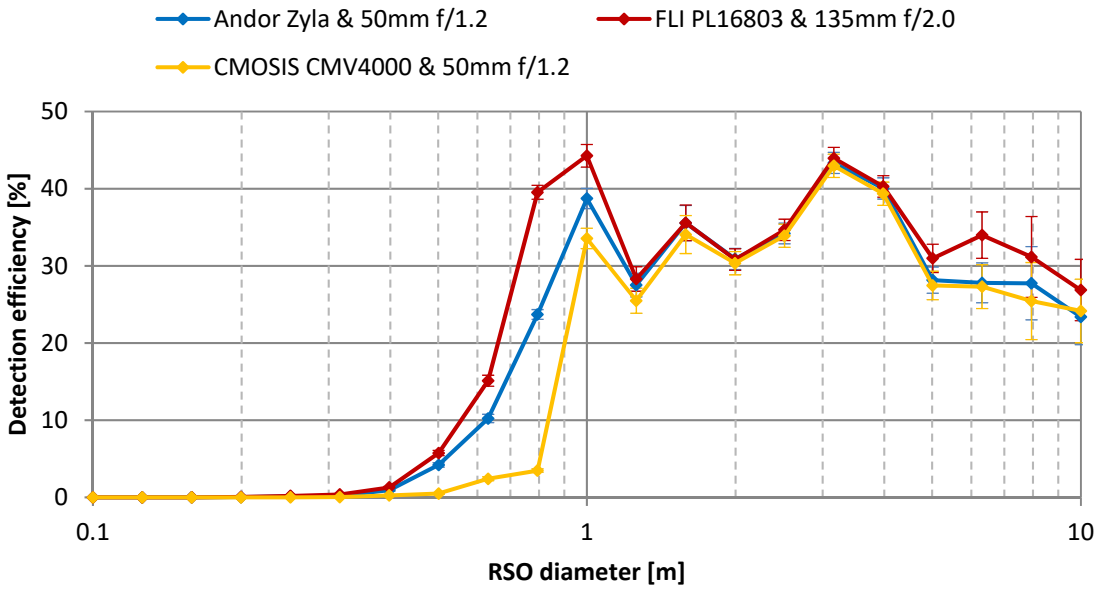

Figure 9.10: Detection efficiency of three different staring systems with a FOV of 15°.

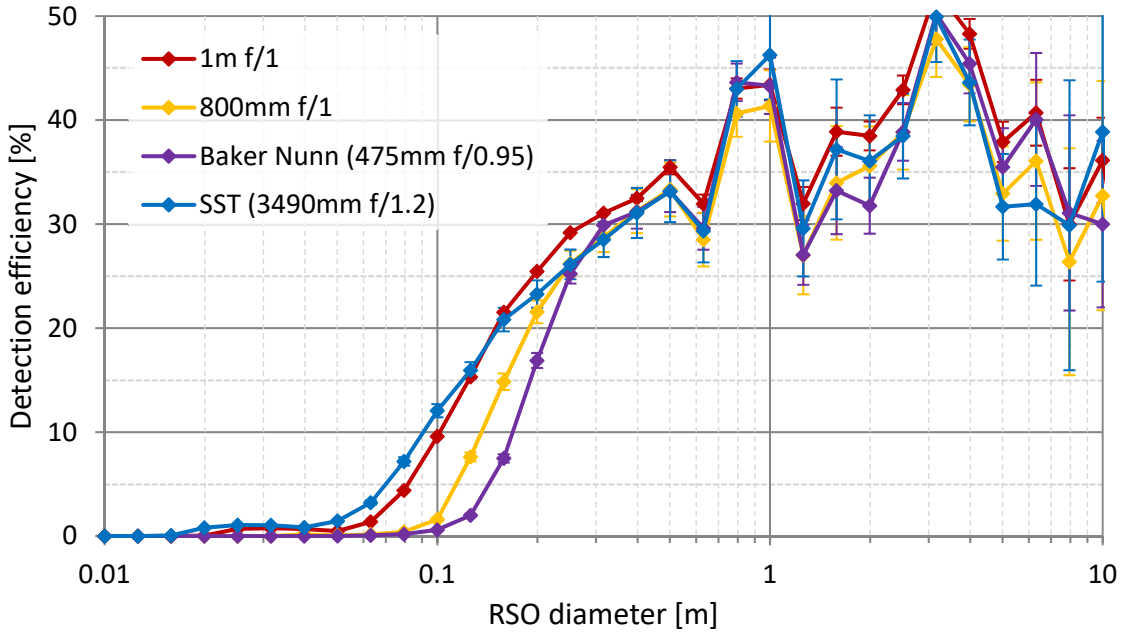

Figure 9.11: Detection efficiency depending on RSO diameter of large aperture staring systems. Two theoretical staring systems with a focal length of 1 m (red) and 800 mm (yellow) both with an f# of 1 been simulated as well as two real system, the Baker Nunn and the Space Surveillance Telescope (SST).

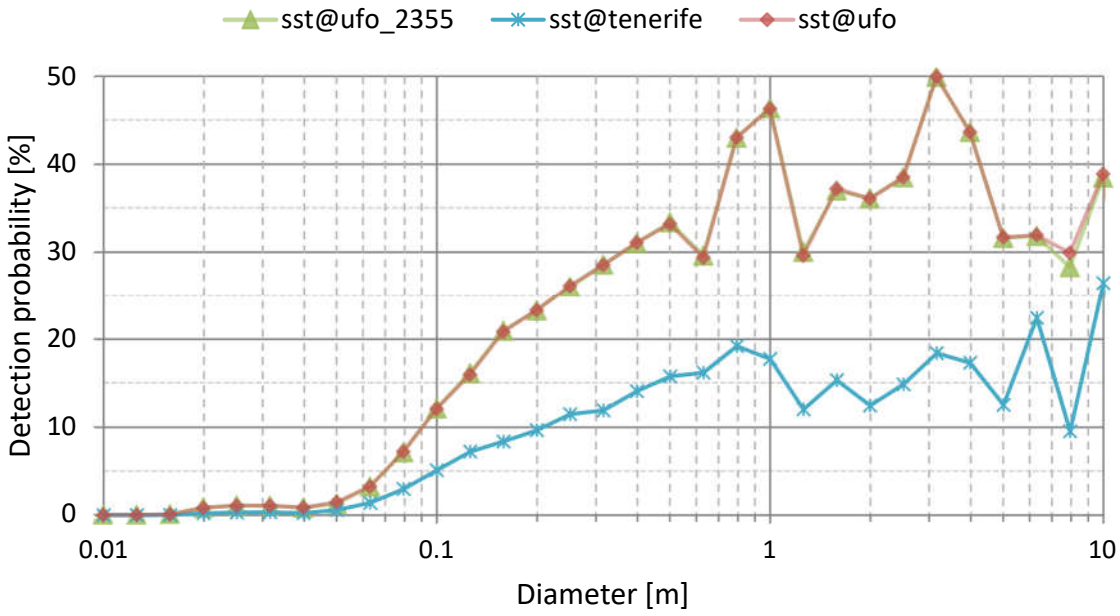

Figure 9.12: Observer location variation using the Space Surveillance Telescope as a staring system at DLR's UFO location, at UFO location with 2355 m altitude and ESA's OGS location.

9.1.2.2. Detection windows of each month

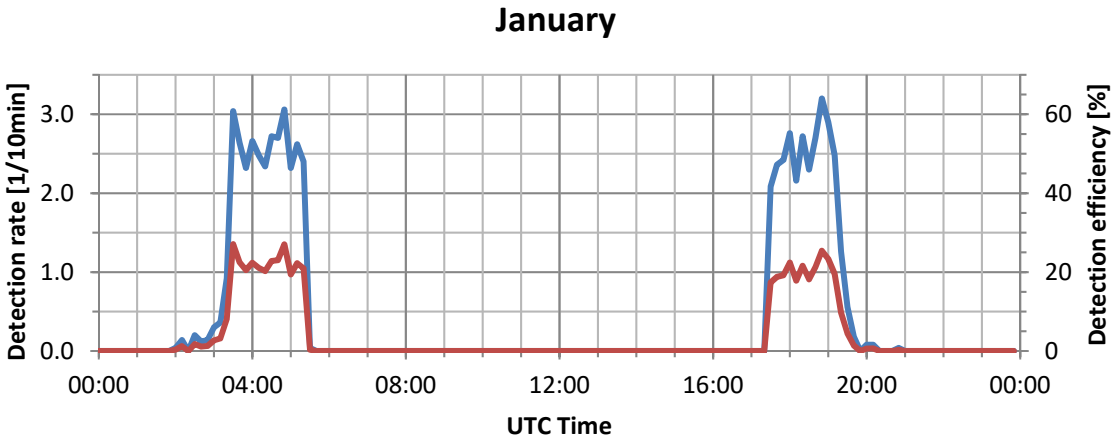

Figure 9.13: Detection rate (blue) and efficiency (red) over the time of the day (UTC) for four different months with zenith LOS. Simulations are performed in 10 min steps using the ANDOR ZYLA as camera and 135mm f2 as lens located at the DLR's UFO observatory. The results are averaged over the first ten days of the given month for each year, between the years 2011 and 2015.

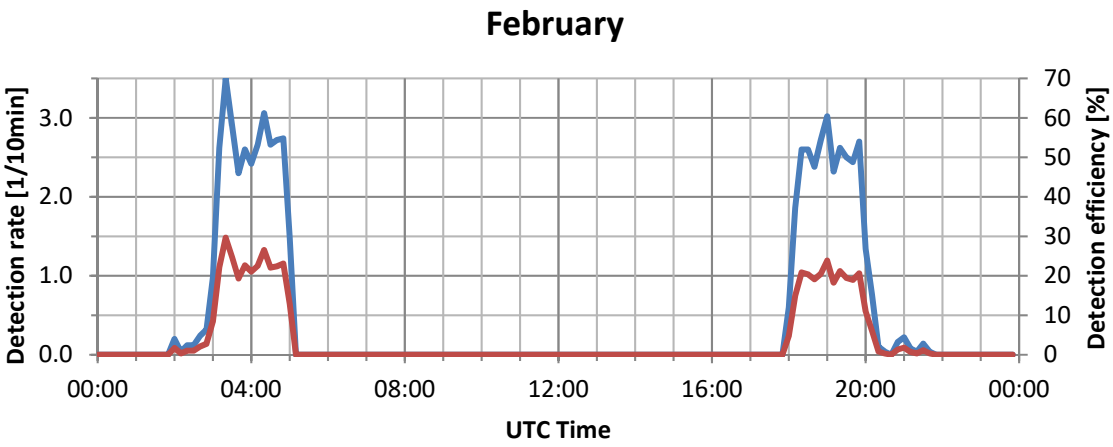

Figure 9.14: Detection rate (blue) and efficiency (red) over the time of the day (UTC) for four different months with zenith LOS. Simulations are performed in 10 min steps using the ANDOR ZYLA as camera and 135mm f2 as lens located at the DLR's UFO observatory. The results are averaged over the first ten days of the given month for each year, between the years 2011 and 2015.

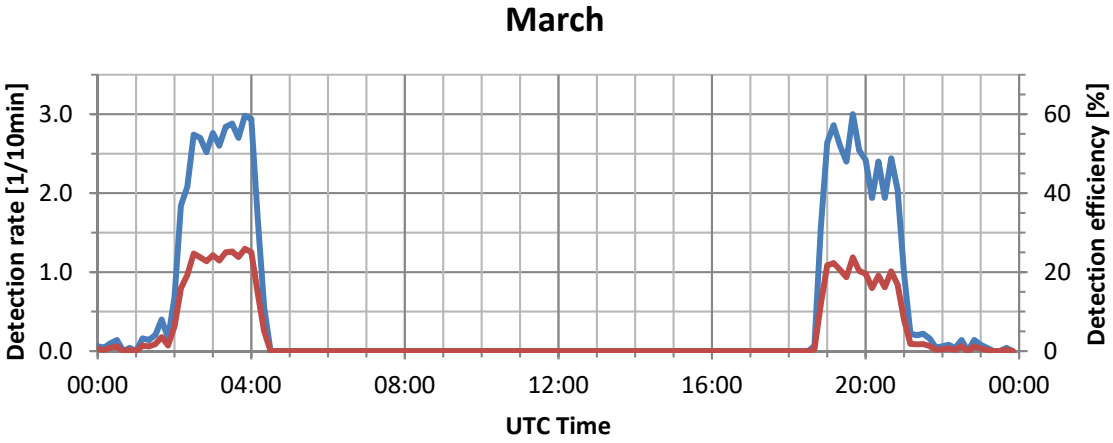

Figure 9.15: Detection rate (blue) and efficiency (red) over the time of the day (UTC) for four different months with zenith LOS. Simulations are performed in 10 min steps using the ANDOR ZYLA as camera and 135mm f2 as lens located at the DLR's UFO observatory. The results are averaged over the first ten days of the given month for each year, between the years 2011 and 2015.

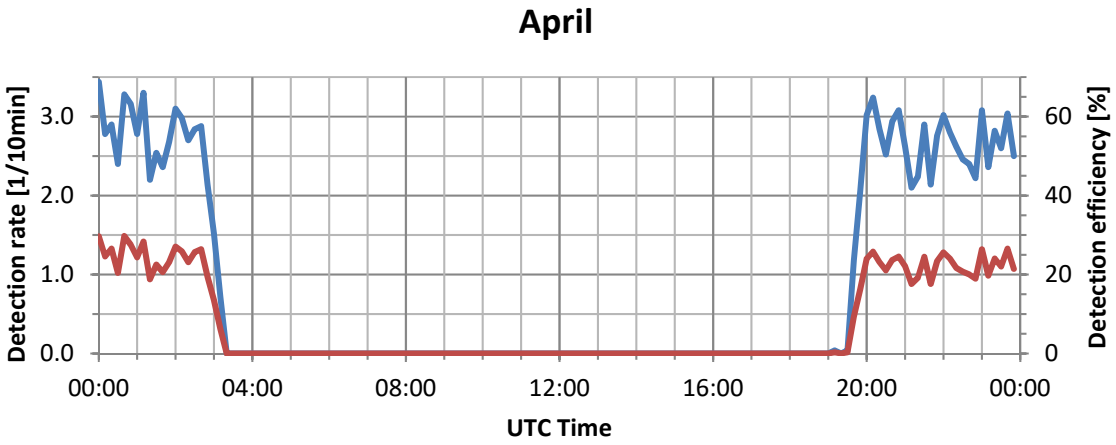

Figure 9.16: Detection rate (blue) and efficiency (red) over the time of the day (UTC) for four different months with zenith LOS. Simulations are performed in 10 min steps using the ANDOR ZYLA as camera and 135mm f2 as lens located at the DLR's UFO observatory. The results are averaged over the first ten days of the given month for each year, between the years 2011 and 2015.

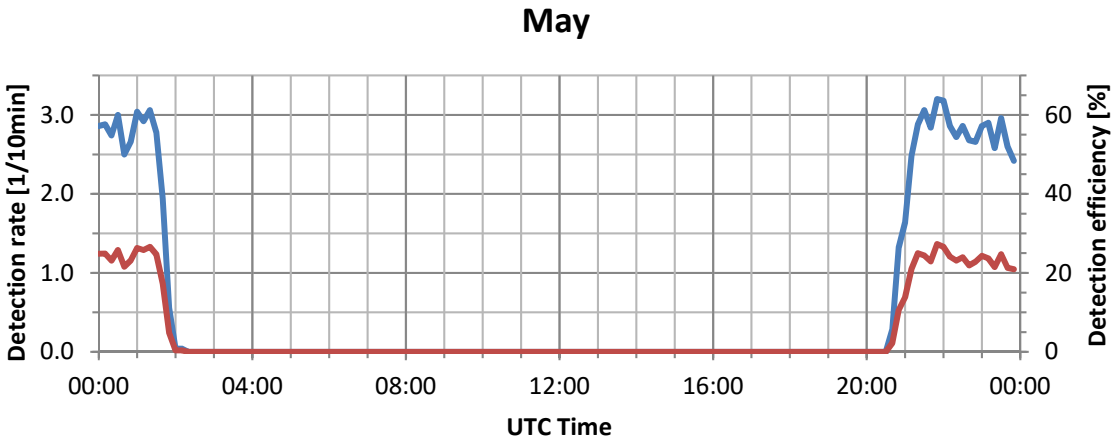

Figure 9.17: Detection rate (blue) and efficiency (red) over the time of the day (UTC) for four different months with zenith LOS. Simulations are performed in 10 min steps using the ANDOR ZYLA as camera and 135mm f2 as lens located at the DLR's UFO observatory. The results are averaged over the first ten days of the given month for each year, between the years 2011 and 2015.

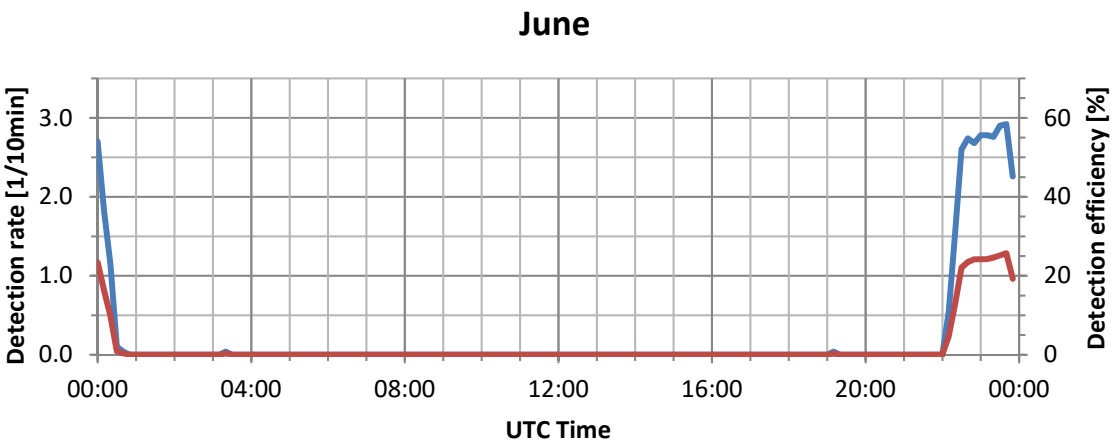

Figure 9.18: Detection rate (blue) and efficiency (red) over the time of the day (UTC) for four different months with zenith LOS. Simulations are performed in 10 min steps using the ANDOR ZYLA as camera and 135mm f2 as lens located at the DLR's UFO observatory. The results are averaged over the first ten days of the given month for each year, between the years 2011 and 2015.

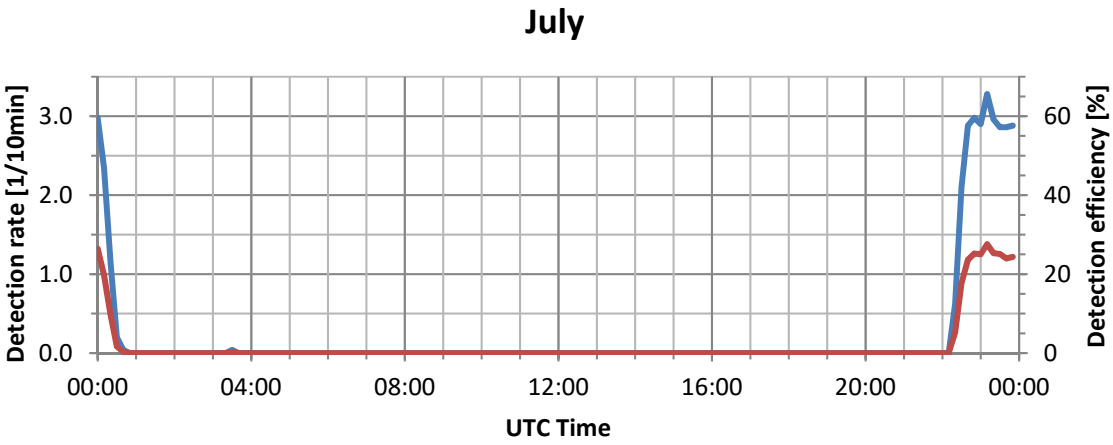

Figure 9.19: Detection rate (blue) and efficiency (red) over the time of the day (UTC) for four different months with zenith LOS. Simulations are performed in 10 min steps using the ANDOR ZYLA as camera and 135mm f2 as lens located at the DLR's UFO observatory. The results are averaged over the first ten days of the given month for each year, between the years 2011 and 2015.

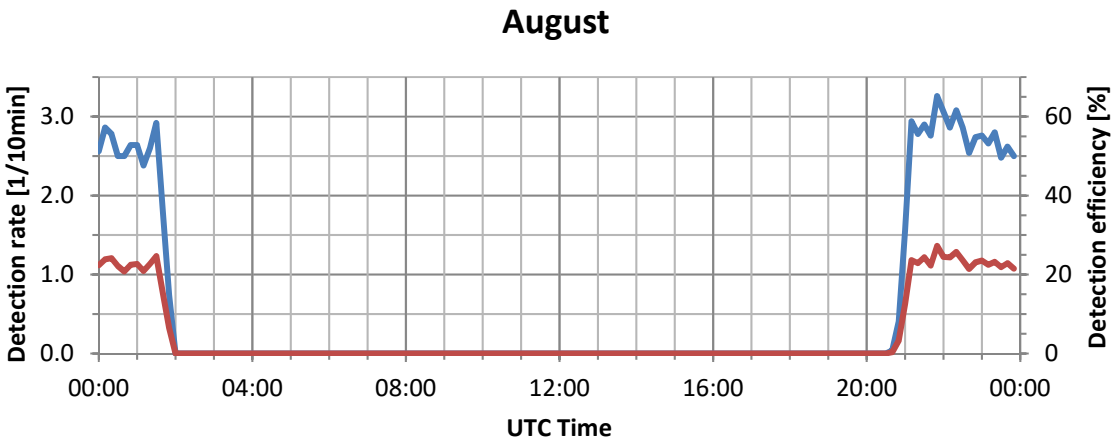

Figure 9.20: Detection rate (blue) and efficiency (red) over the time of the day (UTC) for four different months with zenith LOS. Simulations are performed in 10 min steps using the ANDOR ZYLA as camera and 135mm f2 as lens located at the DLR's UFO observatory. The results are averaged over the first ten days of the given month for each year, between the years 2011 and 2015.

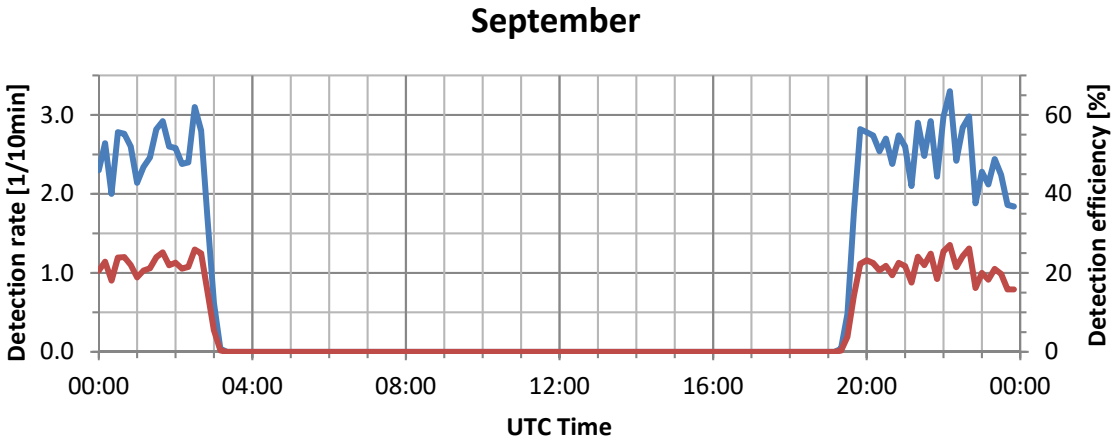

Figure 9.21: Detection rate (blue) and efficiency (red) over the time of the day (UTC) for four different months with zenith LOS. Simulations are performed in 10 min steps using the ANDOR ZYLA as camera and 135mm f2 as lens located at the DLR's UFO observatory. The results are averaged over the first ten days of the given month for each year, between the years 2011 and 2015.

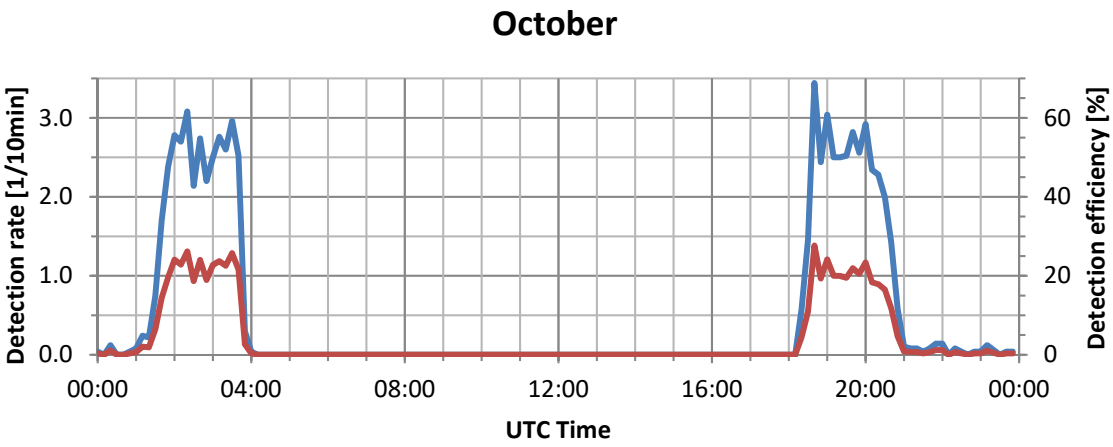

Figure 9.22: Detection rate (blue) and efficiency (red) over the time of the day (UTC) for four different months with zenith LOS. Simulations are performed in 10 min steps using the ANDOR ZYLA as camera and 135mm f2 as lens located at the DLR's UFO observatory. The results are averaged over the first ten days of the given month for each year, between the years 2011 and 2015.

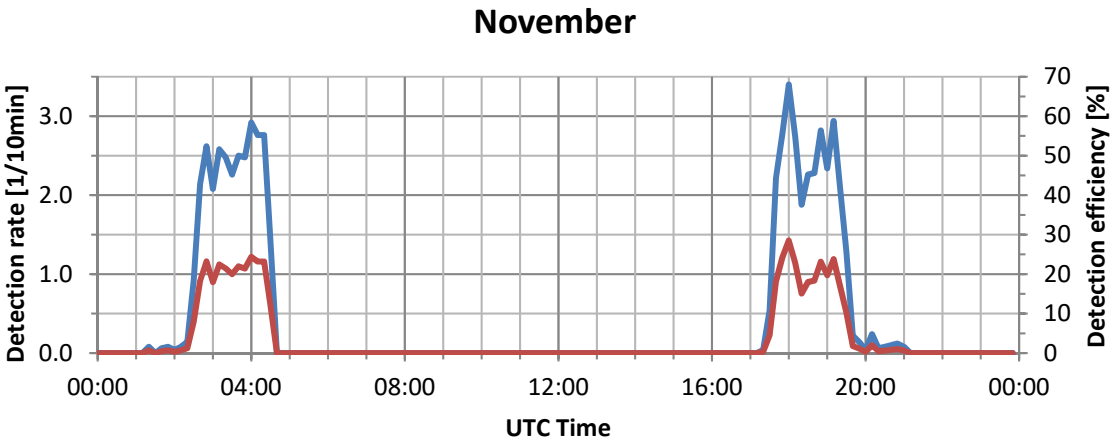

Figure 9.23: Detection rate (blue) and efficiency (red) over the time of the day (UTC) for four different months with zenith LOS. Simulations are performed in 10 min steps using the ANDOR ZYLA as camera and 135mm f2 as lens located at the DLR's UFO observatory. The results are averaged over the first ten days of the given month for each year, between the years 2011 and 2015.

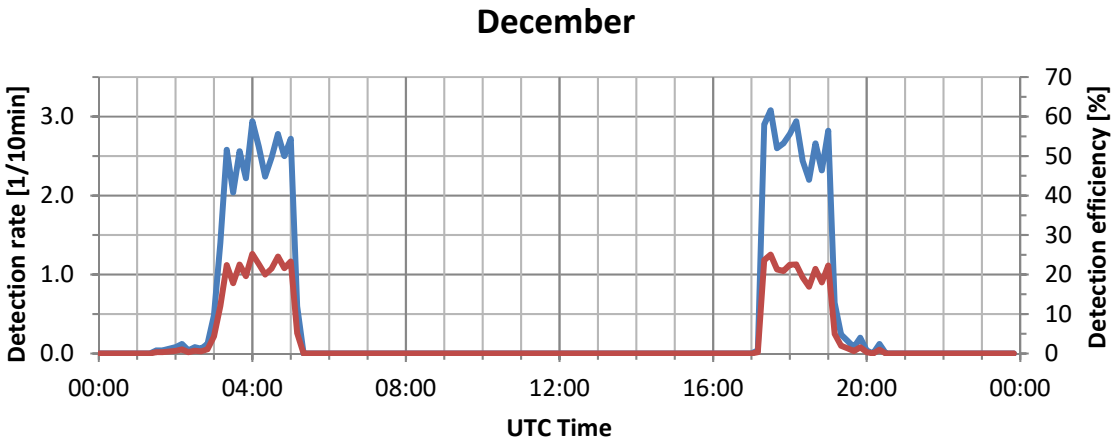

Figure 9.24: Detection rate (blue) and efficiency (red) over the time of the day (UTC) for four different months with zenith LOS. Simulations are performed in 10 min steps using the ANDOR ZYLA as camera and 135mm f2 as lens located at the DLR's UFO observatory. The results are averaged over the first ten days of the given month for each year, between the years 2011 and 2015.

9.2. APPARILLO2 OBSERVATION CAMPAIGNS

9.2.1. GENERAL META DATA OF APPARILLO2

Table 9.1 lists general meta data, which is saved in the FITS header of each image.

FITS Header entry	Value	Unit
FOCALLEN	0.2	[m]
APTDIA	0.1	[m]
APTAREA	0.007853981633974483	[m²]
BITPIX	16	
NAXIS	2	
NAXIS1, size of the image in px (after binning)	1528	
NAXIS2, size of the image in px (after binning)	1528	
XPIXSZ, size of the pixel in µm (after binning)	24.0	
YPIXSZ, size of the pixel in µm (after binning)	24.0	
EXPTIME	1.0	[s]
XBINNING	2	
YBINNING	2	
SITELAT	48.7489	[°]
SITELONG	9.102583333333333	[°]
SITEALT	492.0	[m]
BSCALE	1	
BZERO	32768	

Table 9.1: Meta data saved in the FITS image header.

9.2.2. IMAGE PROCESSING SETTINGS

Following tables lists the image processing settings used by the software made by KORMORAN TECHNOLOGIE to detect and measure LEO RSO, which is saved in TDM format (see Chapter 4.4.2). The settings are grouped after their corresponding category of the image processing.

HISTOGRAM	
lowerExtrapolationExponent	1.
upperExtrapolationExponent	1.5099999904632568e+00
lowerIntensityOffset	0
upperIntensityOffset	1003
flagCentralizeMedianIntensity	0

REMOVE_BACKGROUND	
numberIterations	5

SMOOTH_BACKGROUND	
boxFilterApplications	7
boxFilterRadius	5

SMOOTH_IMAGE	
medianFilterApplications	0
medianFilterRadius	1

FIND_STARS	
minimumNumberPixels	4
maximumNumberPixels	11013
boundaryDistance	5.4662292136760939e+00
minimumAspectRatio	0.
maximumAspectRatio	1.2861683422426564e+00
maximumMoments	3.0161857460980096e-01

FIND_SATELLITES	
minimumNumberPixels	12
maximumNumberPixels	11013
boundaryDistance	2.9819583101359484e+01
minimumLength	9.5268070111416083e+00
maximumLength	1.1013232874703393e+04
minimumWidth	0.
maximumWidth	1.0533992749074734e+01
minimumAspectRatio	3.4432067545013894e+00
maximumAspectRatio	1.1013232874703393e+04
maximumMoments	4.2702879582326538e+00

DILATE_SATELLITES	
marchingDistance	7.8008027576474364e+00

ADJUST_SATELLITES	
outlierIntensity	1.9187536661029673e+04
maximumCurvature	2.8624548113326727e+00
maximumConvergence	1.2203007839447599e-01

CONTINUE	
fastCalculation	1

ASTROMETRY, SOLVE_FIELD	
binaryPath	""
searchRadius	1.9004543625601841e+01
maximumDepth	20
maximumCpuTime	4.9902919868390700e+00
flagUseImageAsInput	0
flagGuessScale	1
flagNoPlots	1
flagOverwrite	1
flagUseInitialRaDec	1
flagSpecifyDepth	1
flagUseCpuLimit	1

OBJECT_PROCESSING, FIND_ORBITS	
maximumOrbitDeviation	1.0016590919044237e+00
maximumVelocityDeviation	1.0016590919044238e-01
maximumTimeDifference	1.0016590919044238e+02
minimumNumberImages	2
minimumNumberPoints	3

REMOVE_OUTLIERS	
numberOutlierIterations	5
longitudinalOutlierThreshold	9.9909769732634190e-01
transversalOutlierThreshold	9.9909769732634190e-01
longitudinalOutlierRmsFactor	3.
transversalOutlierRmsFactor	3.

TRACKING_DATA_MESSAGES	
originator	DLR-ST_ITP-AOS
station	ITP-APPARILLO2

Table 9.2: Image processing settings used by APPARILLO2 system during campaigns #1 - #5

9.2.3. DETECTION RESULTS

Zenith LOS

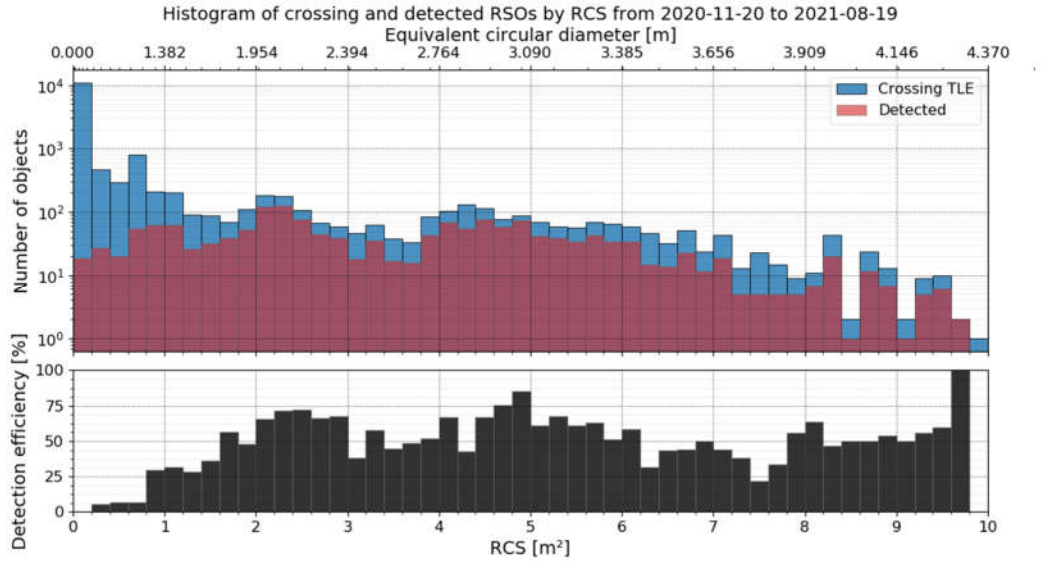

Figure 9.25: Top: Histogram of number of identified (red) and object passing the FOV (blue) according to the TLE catalog during observation to their RCS by APPARILLO measured in 2020 to 2021 under zenith LOS. Bottom: The detection efficiency (black) between detected (identified) and passing TLE objects to the RCS.

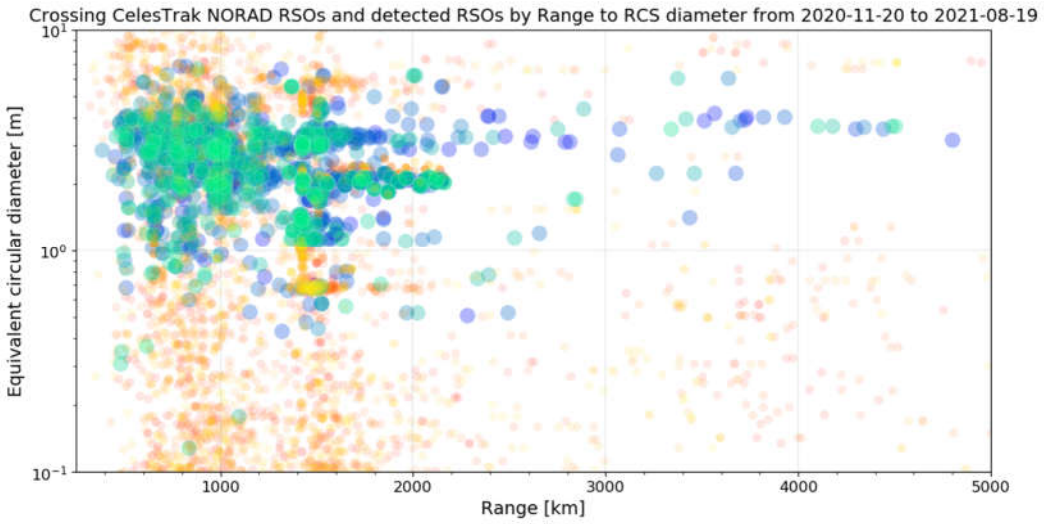

Figure 9.26: Detected (cyan and blue) and crossing (orange and red) RSO measured by APPARILLO2 during campaigns #1 December (blue/red) and #5 July (cyan/orange).

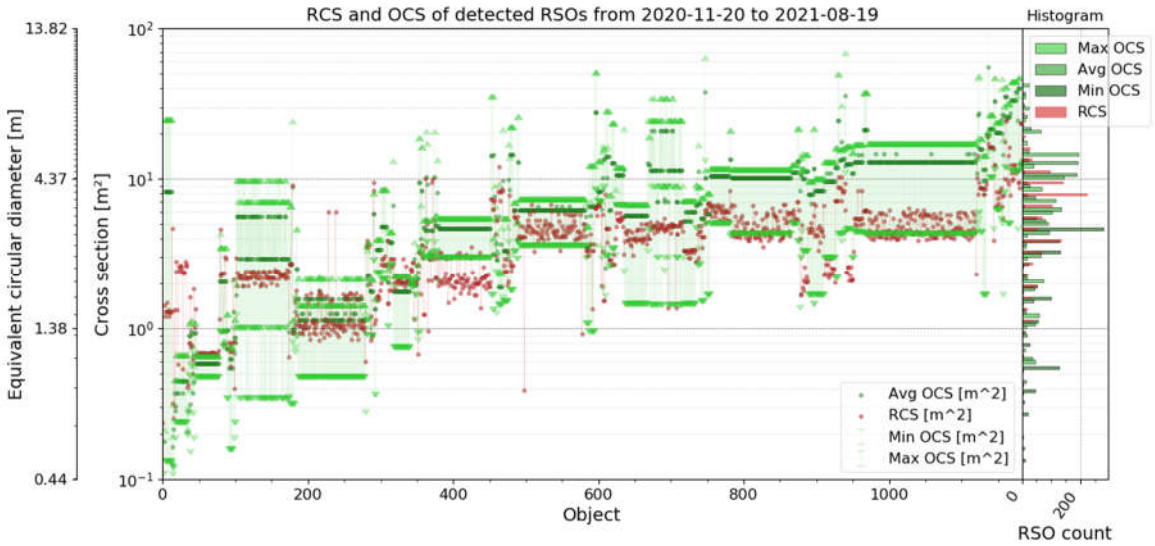

Figure 9.27: Comparison between RCS (red) obtained from the SATCAT and OCS (green) obtained from DISCOS catalog of RSO detected during campaigns #1 December and #5 July under zenith LOS. The minimum (dark green) and maximum OCS (light green) is shown as an error bar. On the right y-axis, the corresponding distribution of each dataset is shown using the same colors.

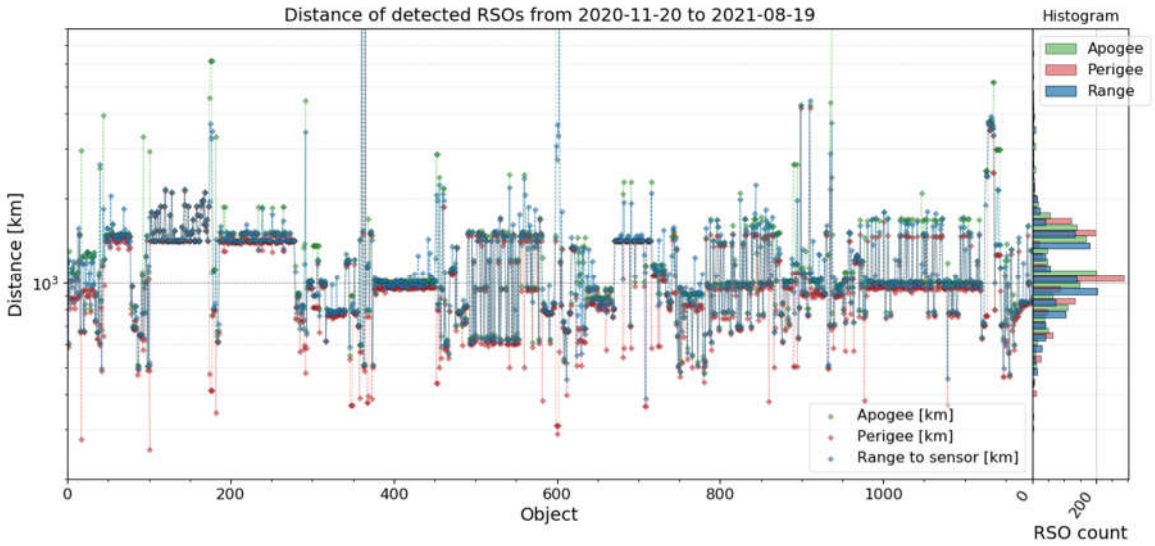

Figure 9.28: The apogee (green), perigee (red) and range (blue) of RSO detected during campaigns #1 December and #5 July under zenith LOS, sorted ascending to their volume. On the right y-axis is shown the corresponding distribution in the same colors.

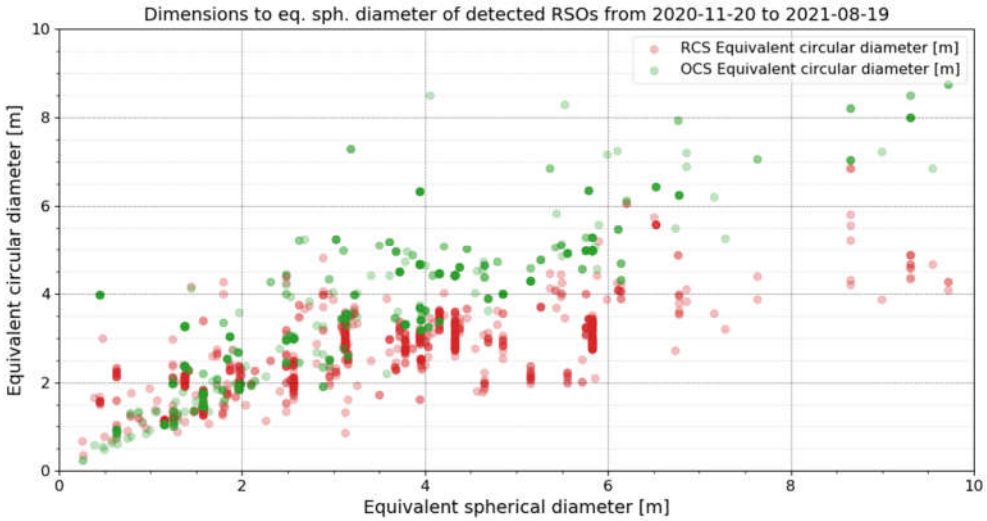

Figure 9.29: Comparison between the RCS's and OCS's equivalent circular diameter to the spherical diameter of RSO detected during campaigns #1 December and #5 July under zenith LOS.

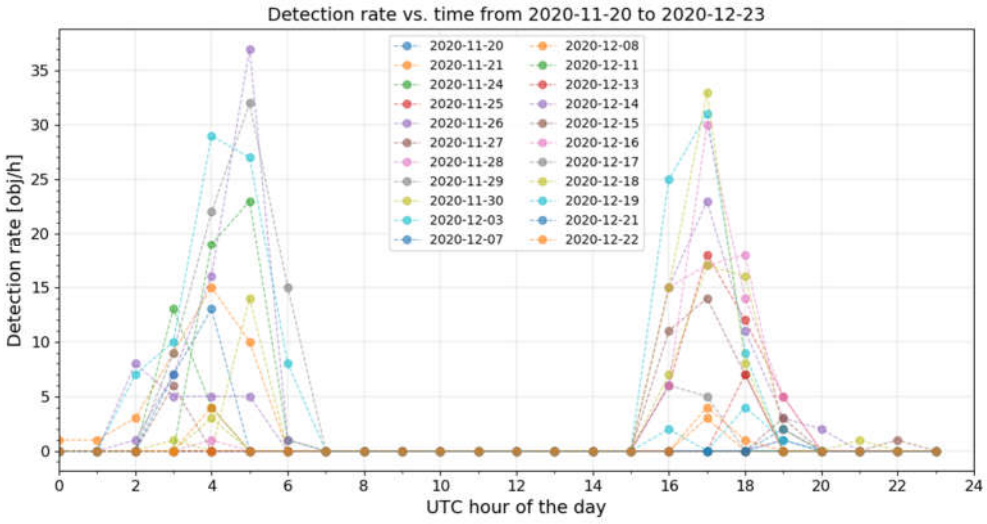

Figure 9.30: Detection rate of APPARILLO2 system during campaign #1 December. Days without any detections are excluded.

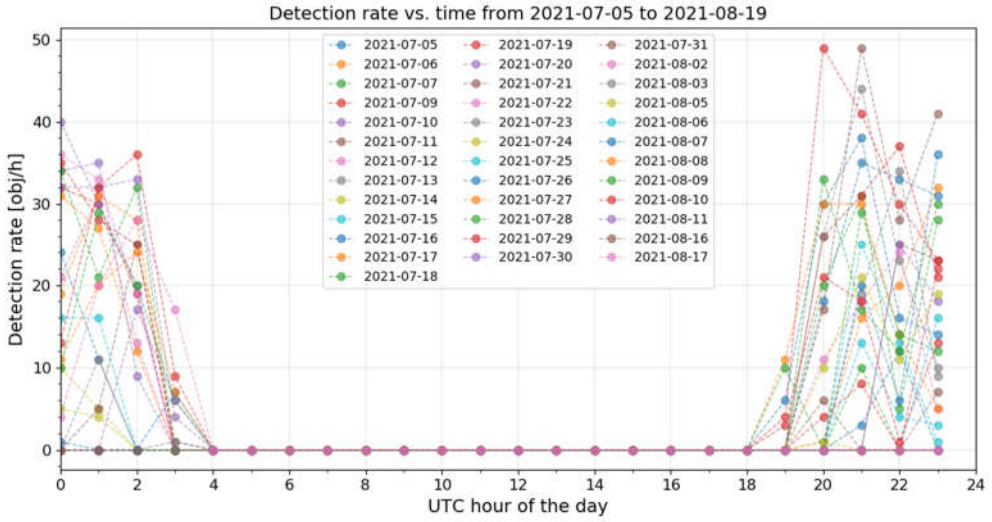

Figure 9.31: Detection rate of APPARILLO2 system during campaign #5 July. Days without any detections are excluded.

45° W LOS

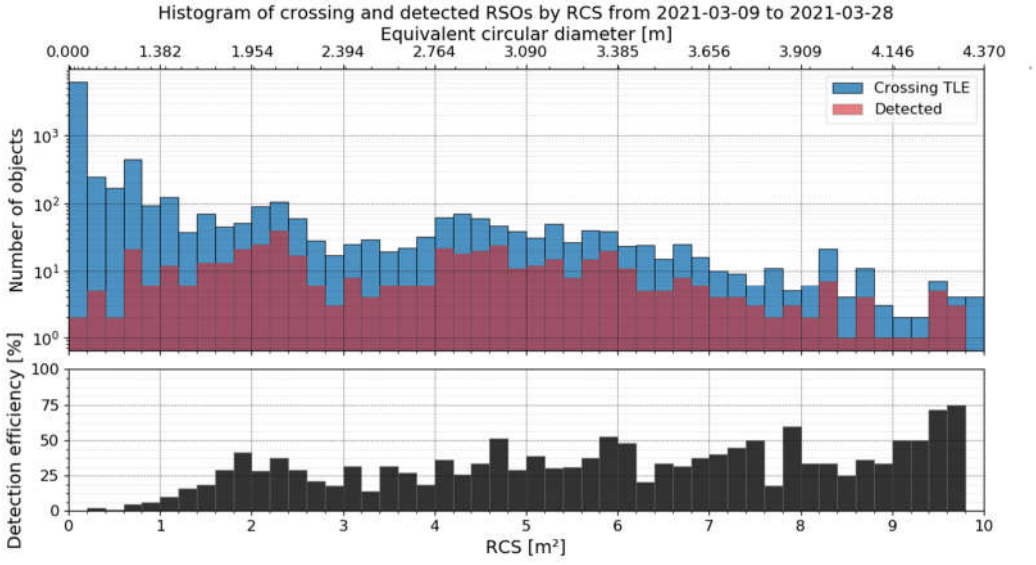

Figure 9.32: Top: Histogram of number of identified (red) and object passing the FOV (blue) according to the TLE catalog during observation to their RCS by APPARILLO measured in 2021 under 45° W LOS. Bottom: The detection efficiency (black) between detected (identified) and passing TLE objects to the RCS.

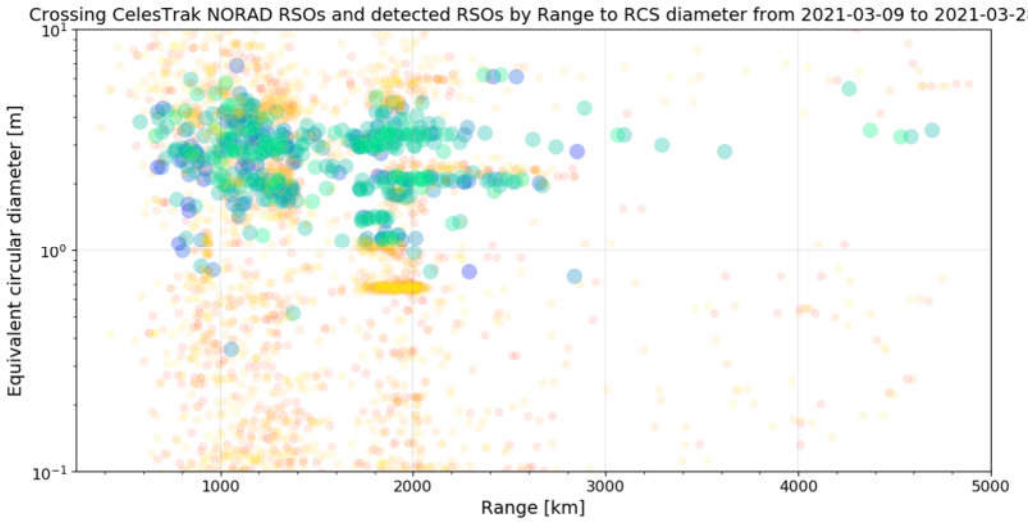

Figure 9.33: Detected (cyan and blue) and crossing (orange and red) RSO measured by APPARILLO2 during campaign #3 March.

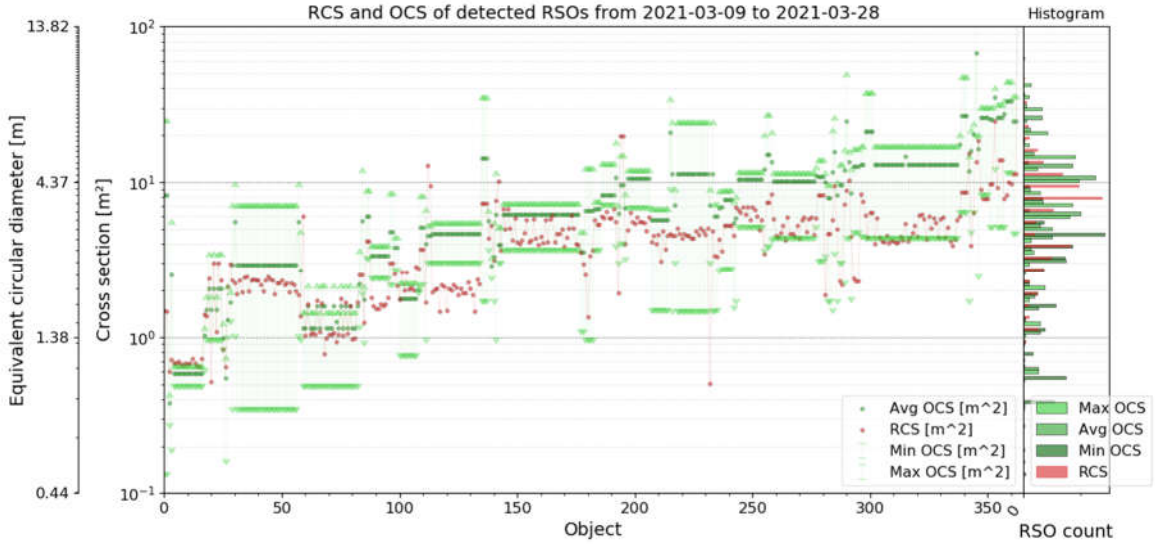

Figure 9.34: Comparison between RCS (red) obtained from the SATCAT and OCS (green) obtained from DISCOS catalog of RSO detected during campaign #3 March under 45° W LOS. The minimum (dark green) and maximum OCS (light green) is shown as an error bar. On the right y-axis, the corresponding distribution of each dataset is shown using the same colors.

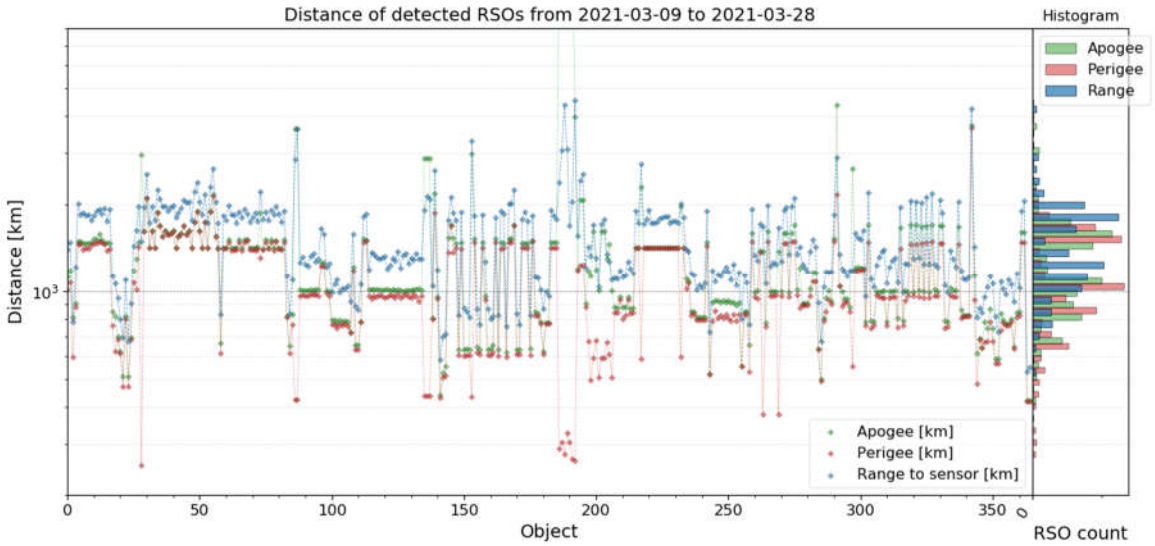

Figure 9.35: The apogee (green), perigee (red) and range (blue) of RSO detected during campaign #3 March under 45° W LOS, sorted ascending to their volume. On the right y-axis is shown the corresponding distribution in the same colors.

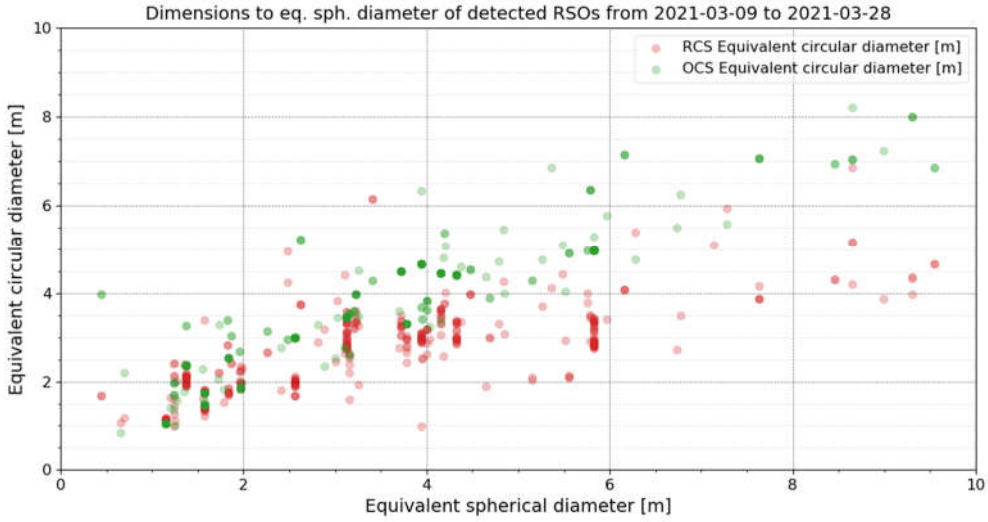

Figure 9.36: Comparison between the RCS's and OCS's equivalent circular diameter to the spherical diameter of RSO detected during campaign #3 March under 45° W LOS.

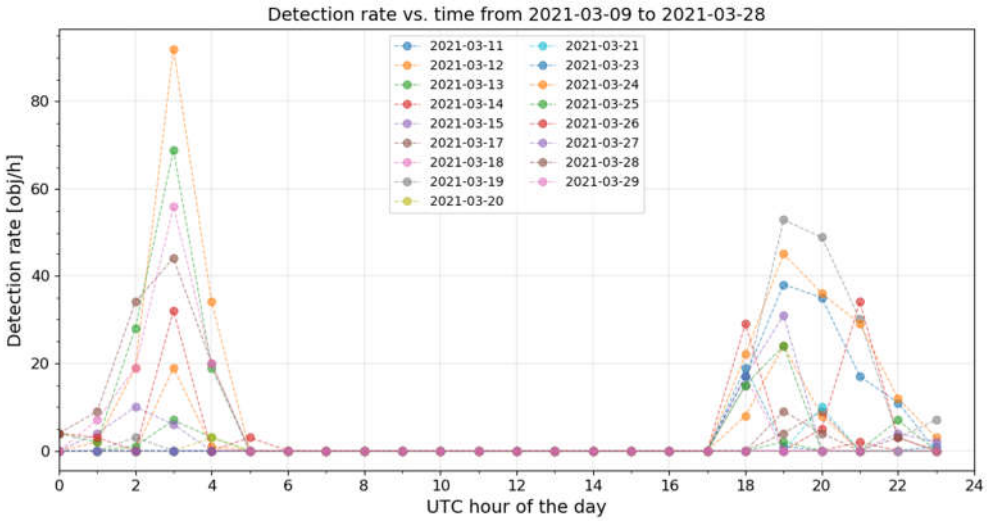

Figure 9.37: Detection rate of APPARILLO2 system during campaign #3 March. Days without any detections are excluded.

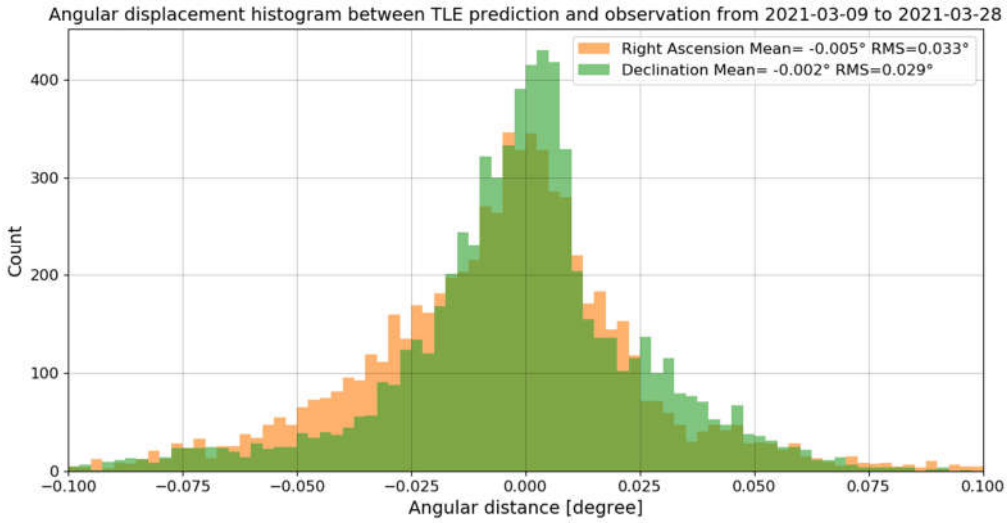

Figure 9.38: Angular displacement histogram of equatorial coordinates between measured object positions and their TLE predictions. Presented data is from all measured and correlated RSO under 45° W LOS during campaign #3 March.

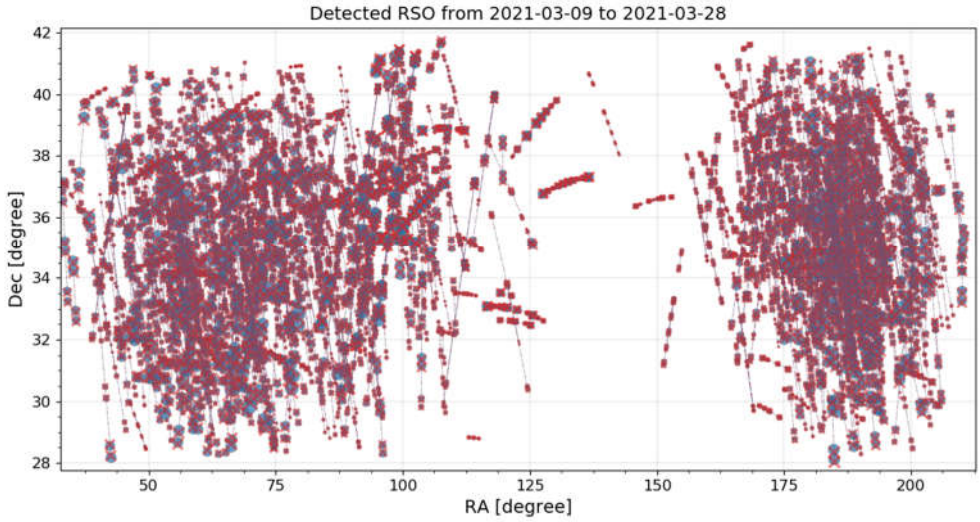

Figure 9.39: Equatorial positions of all detected RSO by APPARILLO2 (red cross) under 45° W LOS during campaign #3 March and the corresponding TLE objects (blue circle). The sizes of the markers show the relative angular displacement between measurements and predictions.

45° N LOS:

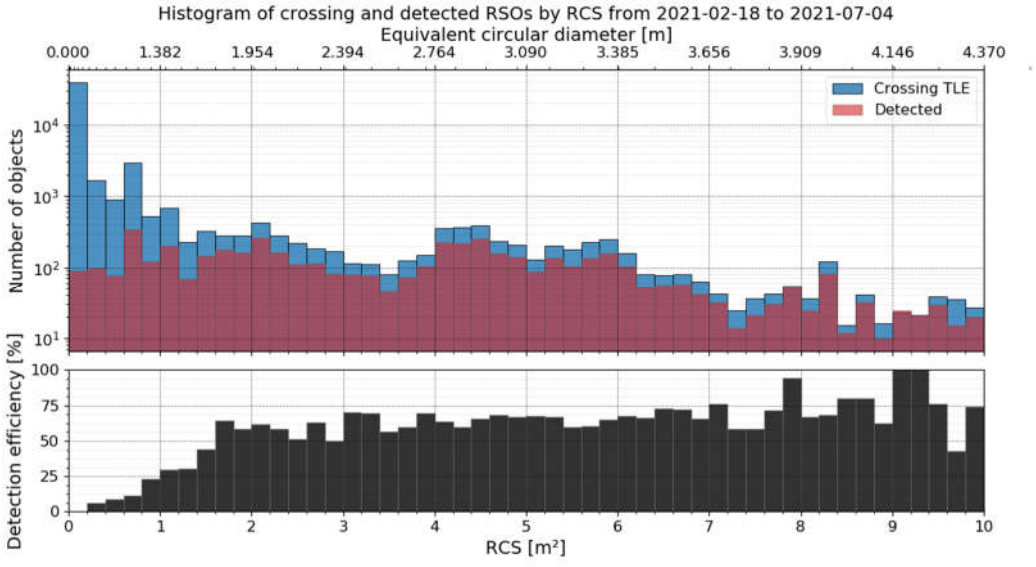

Figure 9.40: Top: Histogram of number of identified (red) and object passing the FOV (blue) according to the TLE catalog during observation to their RCS by APPARILLO measured in 2021 under 45° N LOS. Bottom: The detection efficiency (black) between detected (identified) and passing TLE objects to the RCS.

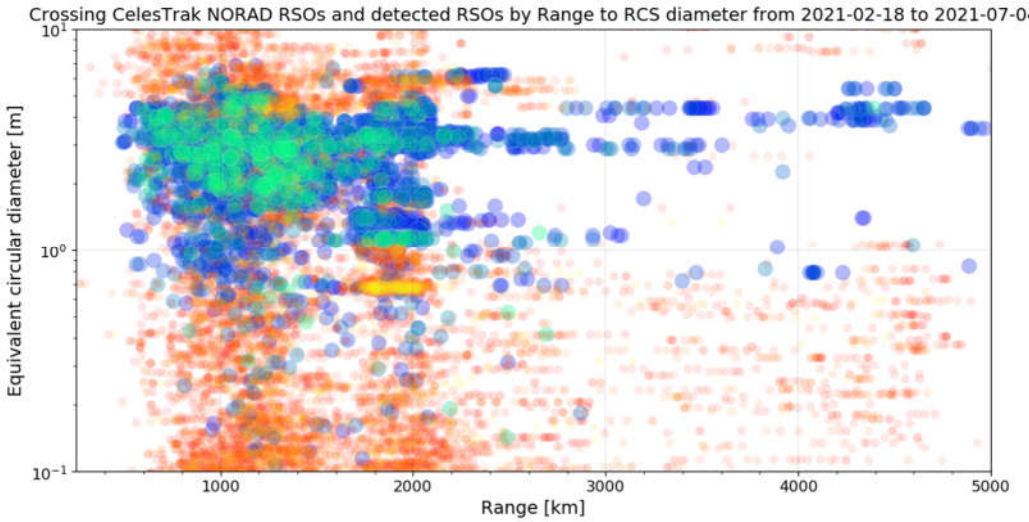

Figure 9.41: Detected (cyan and blue) and crossing (orange and red) RSO measured by APPARILLO2 during campaigns #2 February (blue/red) and #4 April-June (cyan/orange).

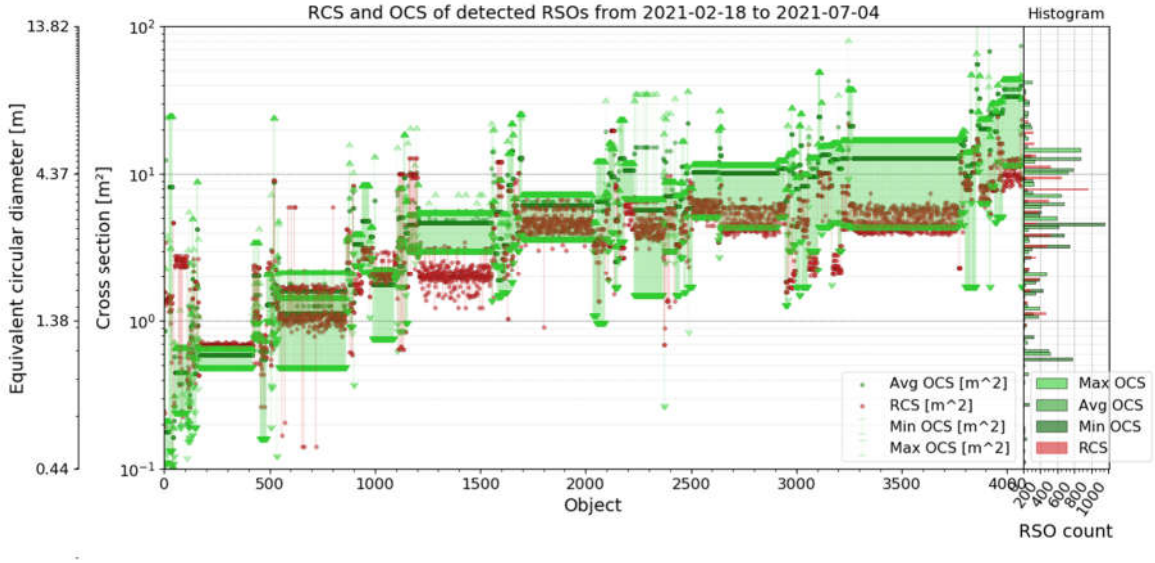

Figure 9.42: Comparison between RCS (red) obtained from the SATCAT and OCS (green) obtained from DISCOS catalog of RSO detected during campaigns #2 February and #4 April-June under 45° N LOS. The minimum (dark green) and maximum OCS (light green) is shown as an error bar. On the right y-axis, the corresponding distribution of each dataset is shown using the same colors.

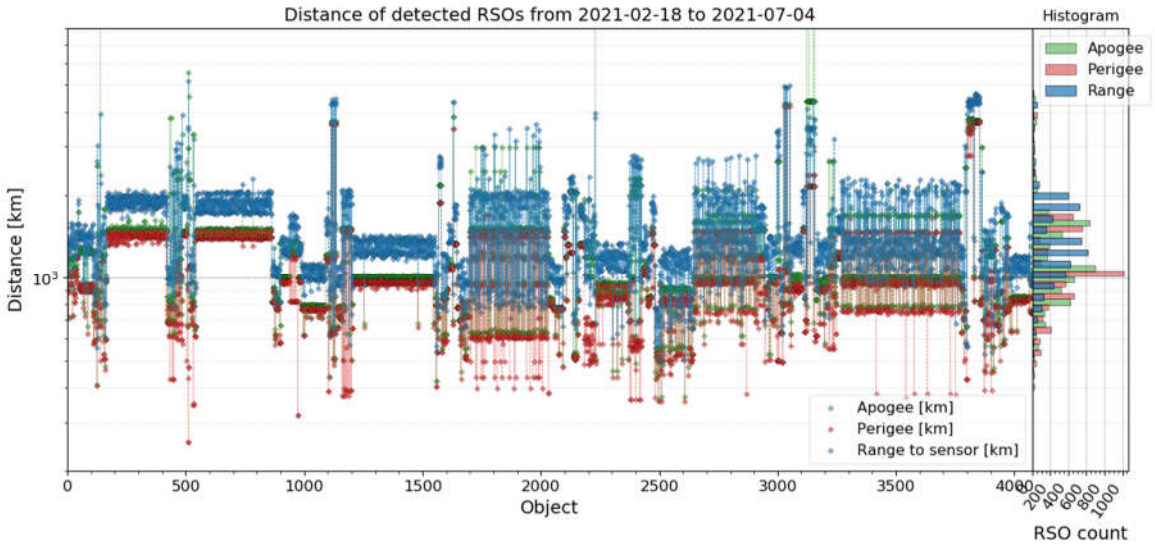

Figure 9.43: The apogee (green), perigee (red) and range (blue) of RSO detected during campaigns #2 February and #4 April-June under 45° N LOS, sorted ascending to their volume. On the right y-axis is shown the corresponding distribution in the same colors.

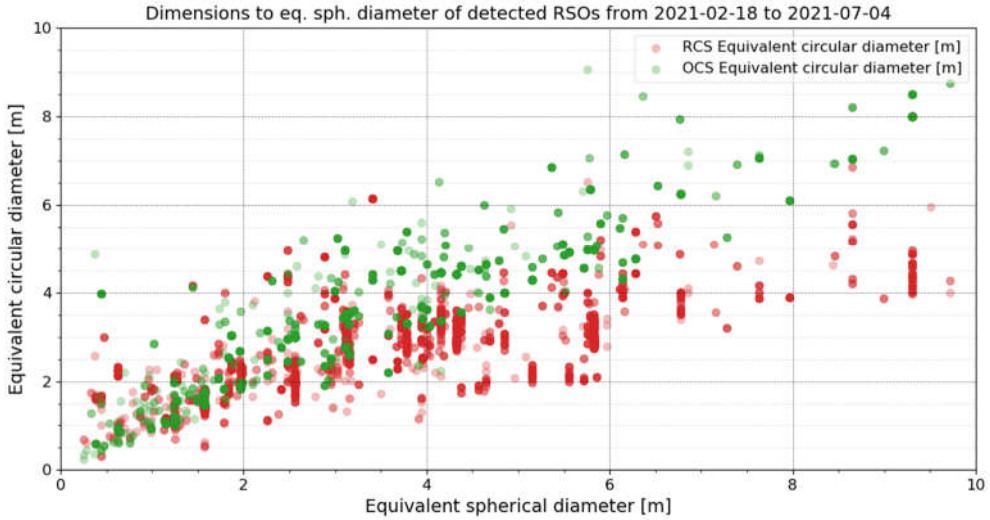

Figure 9.44: Comparison between the RCS's and OCS's equivalent circular diameter to the spherical diameter of RSO detected during campaigns #2 February and #4 April-June under 45° N LOS.

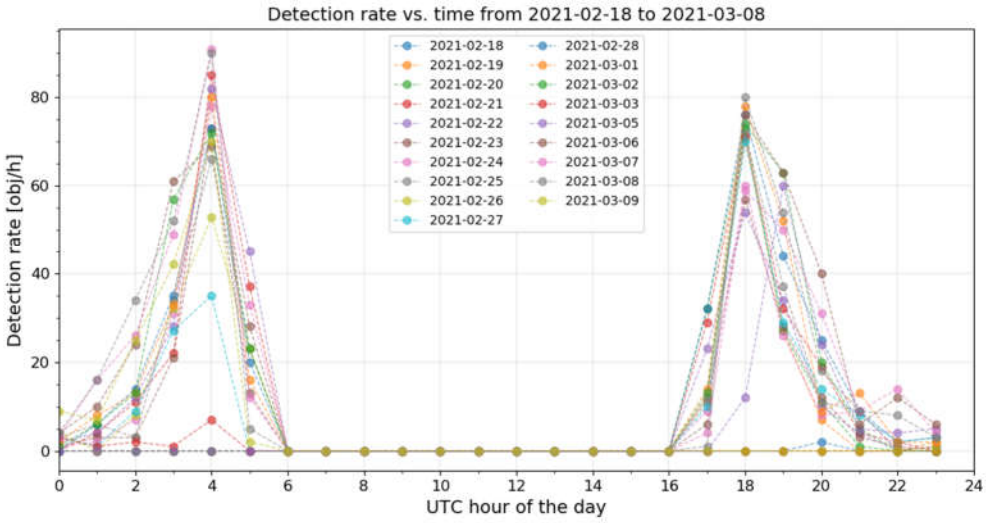

Figure 9.45: Detection rate of APPARILLO2 system during campaign #2 February. Days without any detections are excluded.

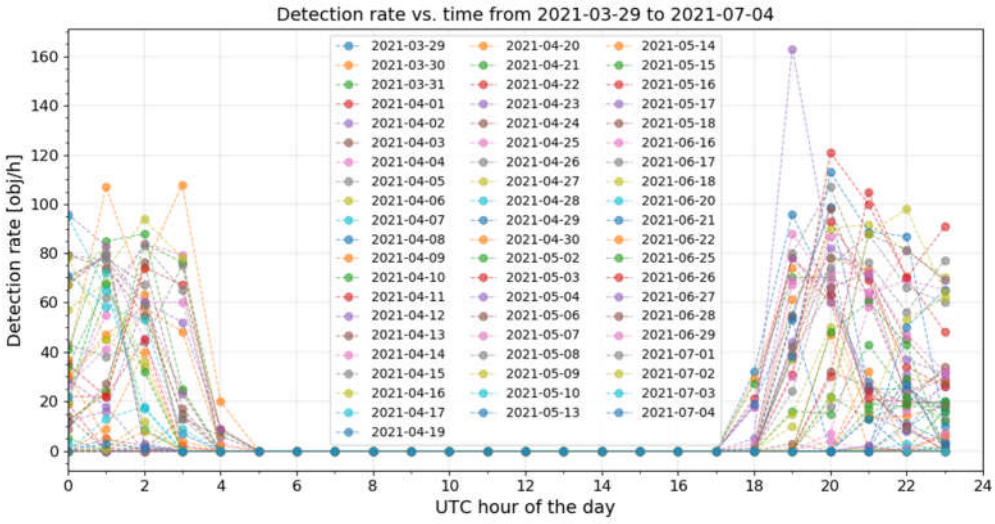

Figure 9.46: Detection rate of APPARILLO2 system during campaign #4 April-June. Days without any detections are excluded.

9.2.4. TIMING

The software records both times from system and GPS timer. Taking a closer look at the recorded timestamps shows that the GPS times shows some hick-ups every few minutes. Bottom half of Figure 9.47 below shows the measured exposure time from the GPS timer's start and stop time. A few blue dots appear below zero within a 50min time window. Those

obviously wrong GPS times have a much smaller difference to the system time as the correct values.

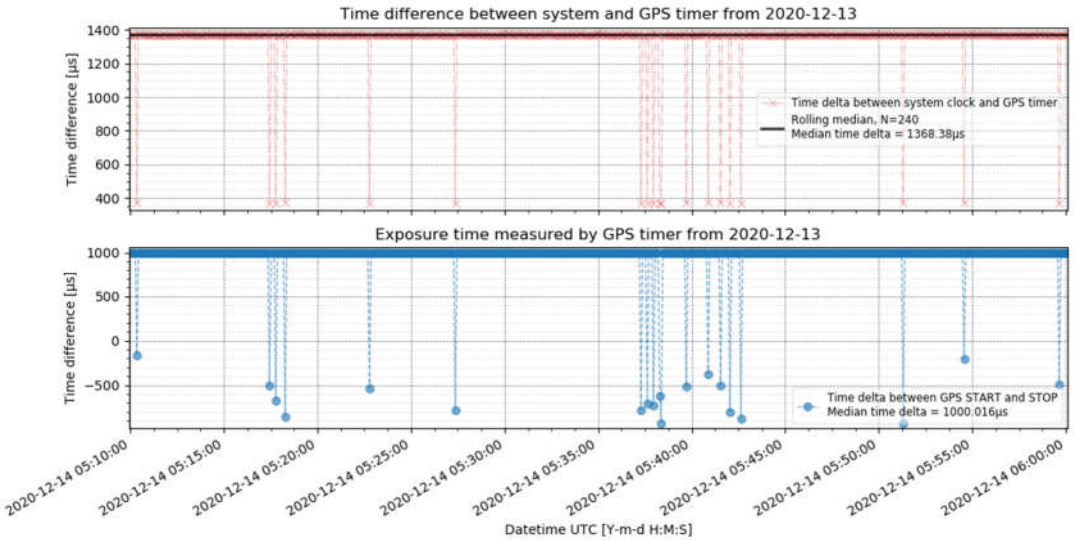

Figure 9.47: top graph shows the time delta between the system and GPS time in red. And the bottom graph shows the dime delta between the recorded GPS time of the end of image exposure and the GPS time of the start of the image exposure in blue.

When plotting the period of system time, GPS start and stop time from each recorded image it can be seen that GPS start and stop are off by 1 s from time to time, while the image recording period by the system is almost stable. In Figure 9.48 the image recording frequency set in the software was 5 s (or 0.2 Hz).

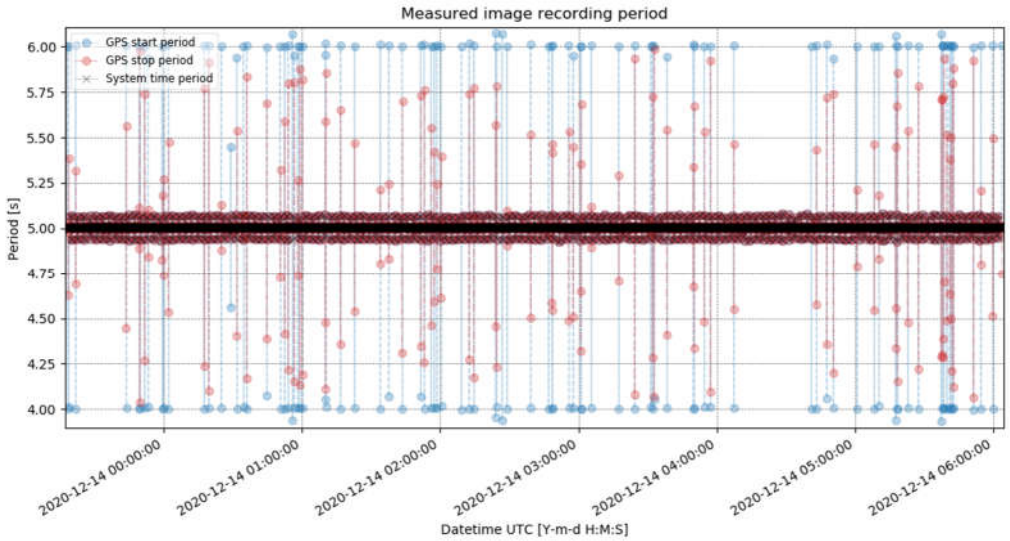

Figure 9.48: Image recording period measured using system and GPS time.

Despite those outliers the system time is drifting by a few µs over the night, see Figure 9.49 top. And the measured exposure time is very stable by less than µs, see Figure 9.49 bottom.

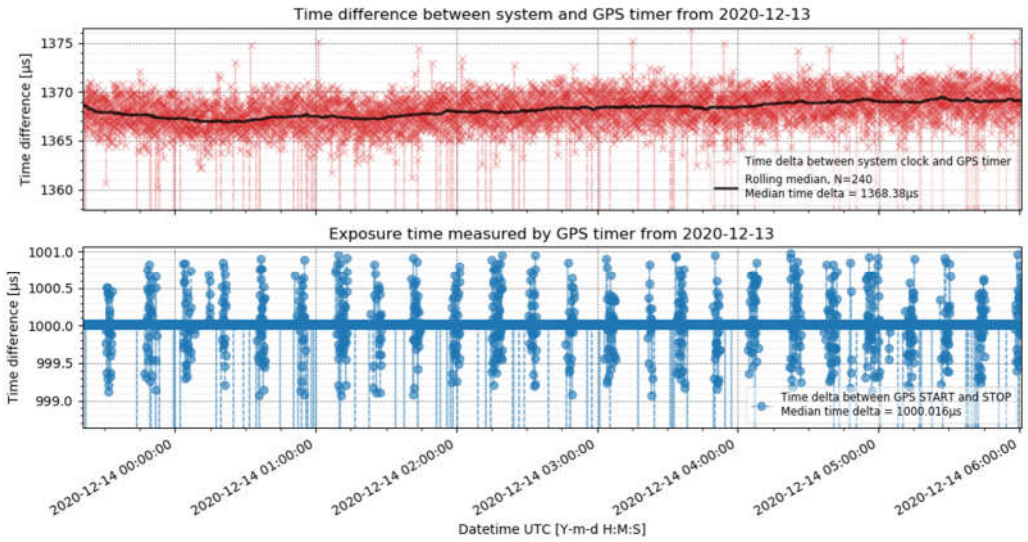

Figure 9.49: The same data as shown in Figure 9.47 zoomed closer into y-axis around the median values of the data. Top graph shows the time delta between the system and GPS time in red. And the bottom graph shows the dime delta between the recorded GPS time of the end of image exposure and the GPS time of the start of the image exposure in blue.

Reviewing the data from a different night the drift between system and GPS time and the measured exposure time were very similar but without those outliers, see Figure 9.50.

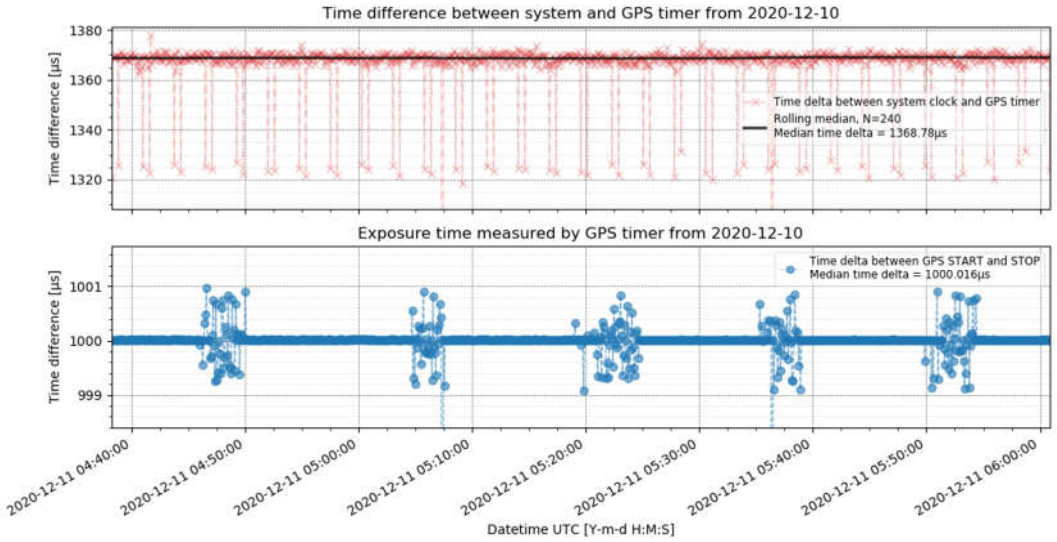

Figure 9.50: Top graph shows the time delta between the system and GPS time in red. And the bottom graph shows the dime delta between the recorded GPS time of the end of image exposure and the GPS time of the start of the image exposure in blue.

Without those hick ups the measured period varies of about 100µs every few minutes, see Figure 9.51. This could be caused by the image acquisition software.

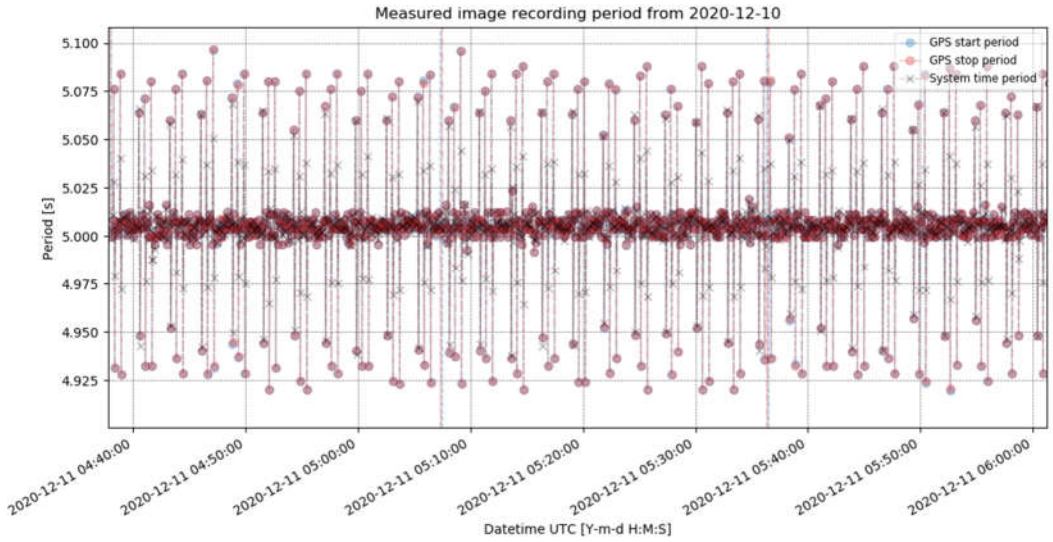

Figure 9.51: Image recording period measured using system and GPS time.

9.2.5. GPS

The mean geodetic coordinates derived by the ARDUINO GPS timer with the standard deviation is listed in Table 9.3 for two representative days.

Date	**2020-12-13**	**2020-12-10**
Latitude	$48.74885° \pm 5.0 \cdot 10^{-5}°$	$48.74885° \pm 5.1 \cdot 10^{-5}°$
Longitude	$9.10257° \pm 3.6 \cdot 10^{-5}°$	$9.10256° \pm 5.8 \cdot 10^{-5}°$
Altitude	486 m ± 6.2 m	483 m ± 6.5 m
Reference frame	MSL	MSL

Table 9.3: mean GPS position measured over one day of two representative days.

Figure 9.52 shows the recorded GPS position data over a duration of 24 h from two exemplary days.

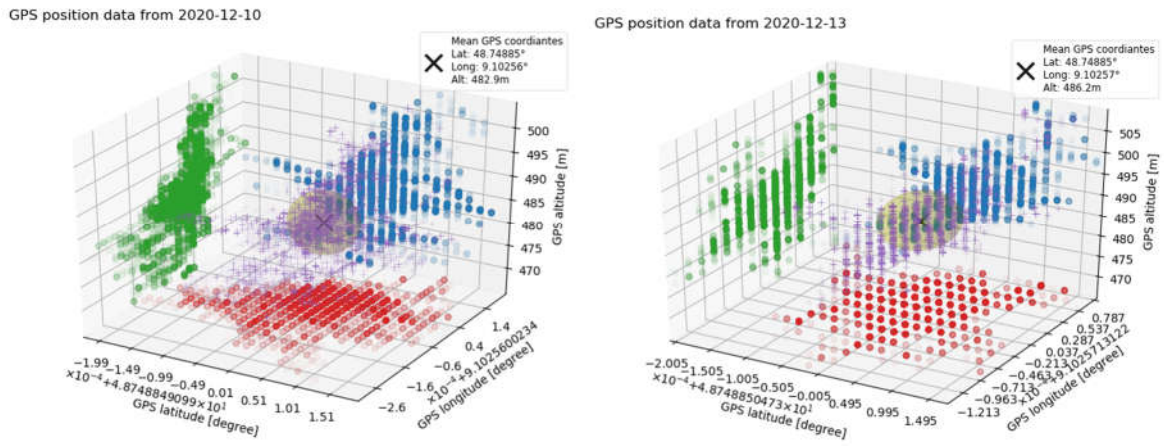

Figure 9.52: left and right are GPS position coordinates from 10th and 13th of December 2020 in latitude, longitude and altitude. The large black 'X' marks the mean position, while the purple '+' show each coordinate in 3D. The red, green and blue circles are the projection of latitude-longitude, longitude-altitude and latitude-altitude respectively. The transparent yellow surface shows the uncertainty ellipsoid of the mean GPS coordinate.

9.3. ELECTROMAGNETIC SPECTRUM

The divinations of the electromagnetic spectrum depending on wavelength is illustrated in Figure 9.53.

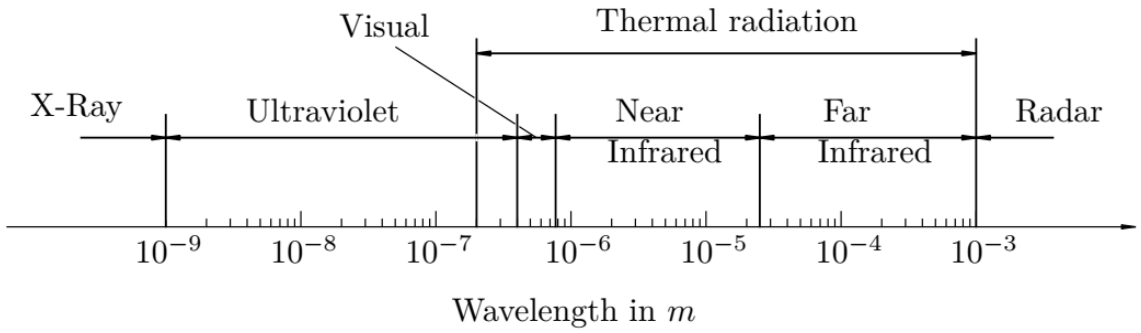

Figure 9.53: Divinations and corresponding spectral ranges of the electromagnetic spectrum. Source: [97].

9.3.1. RADAR SPECTRUM

Symbol	Denomination	Wavelength	Frequency
VLF	Very Low Frequency	$>$ 10 000 m	$<$ 30 KHz
LF	Low Frequency	1000-10 000 m	30-300 KHz
MF	Medium Frequency	100-1000 m	300-3000 KHz
HF	High Frequency	10-100 m	3-30 MHz
VHF	Very High Frequency	1-10 m	30-300 MHz
UHF	Ultra High Frequency	10 cm-1 m	300-3000 MHz
SHF	Super High Frequency	1 cm-10 cm	3 GHz-30 GHz
EHF	Extremely High Frequency	1 mm-1 cm	30-300 GHz

Table 9.4: Deviations of the RADAR frequency spectrum. Source: [98].

9.3.2. RADAR EQUATIONS

RADAR sensors measure the time difference between the emitted RADAR wave/pulse and received signal. The range to the RSO R_{RSO} is calculated by the speed of light c and the time of flight Δt [68].

$$R_{\mathrm{RSO}} = c\frac{\Delta t}{2} \tag{9.1}$$

The RADAR power budget, also called the link budget, allows assessing the sensitivity of a RADAR. The receiving power P_r can be calculated as follows [68].

$$P_{\mathrm{r}} = \frac{P_{\mathrm{t}} g_{\mathrm{t}} A_{\mathrm{r}}}{4\pi {R_{\mathrm{RSO}}}^2} \frac{\sigma_{\mathrm{RCS}}}{4\pi {R_{\mathrm{RSO}}}^2} \frac{1}{{L_{\mathrm{radome}}}^2} \frac{1}{{L_{\mathrm{atm}}}^2} \frac{1}{L_{\mathrm{r}}} \frac{1}{L_{\mathrm{t}}} \frac{1}{L_{\mathrm{pol}}} \tag{9.2}$$

Where P_t is the transmitting power, g_t the antenna gain, R_{RSO} the distance to the target, A_r the receiver antenna area, σ_{RCS} the RCS of the RSO, L_i the losses for transmitter (t), receiver (r), polarization (pol), atmosphere (atm), and RADAR dome (radome).

The range rate $\dot{r}$ can be derived from the transmitted frequency f_t, the speed of light c and the difference between the received frequency f_r and transmitted frequency, f_d.

$$f_{\mathrm{r}} - f_{\mathrm{t}} = f_{\mathrm{d}} = 2\dot{r}\frac{f_{\mathrm{t}}}{c - \dot{R}} \approx 2\dot{r}\frac{f_{\mathrm{t}}}{c} \tag{9.3}$$

9.4. ACTIVE-OPTICAL MEASUREMENTS

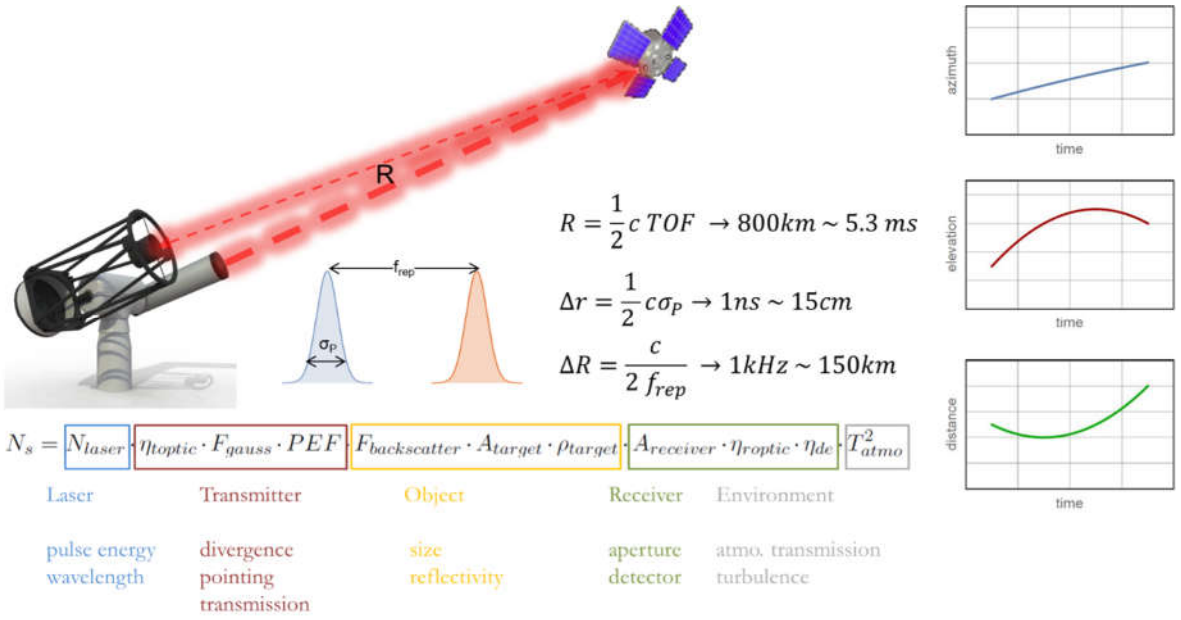

Figure 9.54: Laser ranging measurement of an RSO

9.4.1. PULSE RUNTIME MEASUREMENT

The range to the target results from roundtrip time Δt_{pulse} of a laser pulse and the speed of light c,

$$R_{\text{RSO}} = \frac{c_{\text{vac}}}{n_{\text{air}}(h, P_{air}, T)} \frac{\Delta t_{\text{pulse}}}{2} \tag{9.4}$$

The speed of light reduces by the refractive index of the medium the light n. the refractive index of air n_{air} depends on the height h, pressure P_{air} and temperature T.

In ranging, for each event, the time of flight is calculated. Hence, the events are scattered in two dimensions: First GPS synchronized time of measurement and second time of flight. Which allows temporal filtering of recorded data.

9.4.2. PHOTON DETECTION STATISTICS

During laser ranging the single photon detector (SPD) is usually temporally gated to prevent unwanted noise detection. This implies that the detector is only able to count photons N_S or noise N_N within the gate time T_{gate}. The gate is adjusted that the expected arrival time of the signal photons is within the gate. Because of the dead time t_{dead} only one event can be detected

per gate. A signal photon can only be detected if no noise event is detected till the signal photon arrives at the detector.

The detection probability of a single photon avalanche detector (SPAD) p_e follows Poisson statistics. So $p_{ph}(m)$ is the probability that m photo-electrons are generated during the time t [99].

$$p_{ph}(m) = \frac{{N_e}^m}{m!} e^{-N_e} \tag{9.5}$$

The mean number of photo-electrons generated during the time t is given by $N_e = f_e t$ with f_e being the generation rate of photo electrons. The probability p_e to detect at least one event is,

$$p_e(N_e) = 1 - e^{-N_e}. \tag{9.6}$$

Thus, the detection probability of a signal photon p_s is determined by the total noise rate f_{noise}, the number of signal photo electrons N_S and the time T_{gate} between the gate is opened and the signal photons arrive,

$$p_S = (1 - p_N)p_e(N_S) = e^{-N_{noise}}(1 - e^{-N_S}). \tag{9.7}$$

The first factor gives the probability that no noise event occurs till the signal arrives, whereas the second factor gives the probability that a signal event is detected. The gate is usually adjusted such, that the expected arrival time of the signal is centered within the gate. So $t_s \approx T_{gate}/2$. Thus, the detection probability of the signal decreases exponentially with increasing gate time T_{gate}. This is the return rate.

The probability of detecting a noise electron p_N within a gate is given by,

$$p_N = (1 - e^{-N_{noise}})(1 - p_S). \tag{9.8}$$

The first factor describes the probability of detecting a noise event within T_{gate}, whereas the second factor describes the probability that no signal event occurs. Since the signal strength is typically very weak, the probability to detect a noise event can be approximated to,

$$p_N = (1 - e^{-N_{noise}}). \tag{9.9}$$

For non-gated scenario the noise is Poisson distributed and the probability to detect a noise event $p_{N,free}$ is the noise rate f_{noise} by the dead time t_{dead} of the detector,

$$p_{N,free} = f_{noise} t_{dead} \tag{9.10}$$

If no noise event is detected the probability of detecting a signal event per pulse is the number of received signal photons N_S,

$$p_{S,free} = (1 - p_{N,free})N_S = (1 - f_{noise} t_{dead})N_S. \tag{9.11}$$

While the number of signal events $N_{S(NP)}$ within the time interval of a normal point T_{NP} is,

$$N_{S(NP)} = T_{NP} f_{Laser}(1 - n_{noise} t_{dead})N_S. \tag{9.12}$$

9.4.3. LASER LINK BUDGET EQUATION

The RADAR link budget equation is modified by Degnan [50] to represent the use of laser ranging. Following equation is the laser link equation, which gives the number of detected photon electrons N_S returning from the orbital target.

$$N_S = N_T g_T \sigma_{OCS} \left(\frac{1}{4\pi {R_{RSO}}^2}\right)^2 A_R \tau_R \tau_T Q E {\tau_{Atm}}^2 \quad (9.13)$$

Where N_T is the number of transmitted photons of the laser source, g_T the transmitter gain to represent beam divergence and pointing jitter loss, σ_{OCS} optical cross section of the RSO, A_R effective receiving aperture, τ_R and τ_T transmission loss from the laser transmitter and receiver respectively. QE is the quantum efficiency of the detector and τ_{Atm} transmission loss in atmosphere.

Number of emitted photons

The number of photons per pulse N_T emitted by the laser can be calculated using pulse energy of the laser source E_{Laser}, wavelength of the laser λ_{Laser}, Planck's constant h, and speed of light c;

$$N_T = E_{Laser} \frac{\lambda_{Laser}}{hc}. \quad (9.14)$$

Gain factor

The gain factor describes how much the signal is amplified by concentrating it in a narrow solid angle Ω in respect to 1 steradians [100].

$$g_T = \frac{1}{\Omega} \quad (9.15)$$

Note this is not the standard definition of the gain, which is in respect to 4π steradian. The solid angle of a cone with a half angle θ is [43],

$$\Omega = 4\pi \sin^2 \frac{\theta}{2} = 2\pi(1 - \cos\theta). \quad (9.16)$$

This allows calculating the transmitter gain g_T from the beam divergence θ_d which spreads the energy in the cone.

$$g_T = \frac{1}{4\pi \sin^2 \frac{\theta_d}{2}} \quad (9.17)$$

As the beam divergence is very small, $\sin(\theta)$ can be approximated to θ,

$$g_T \approx \frac{1}{4\pi \left(\frac{\theta_d}{2}\right)^2} = \frac{1}{\pi {\theta_d}^2}. \quad (9.18)$$

Pointing Error

This expression doesn't include losses by beam broadening and miss aliments. Thus, the pointing error factor (*PEF*) needs to be multiplied to the transmitter gain.

$$g_T = \frac{1}{\pi {\theta_d}^2} \cdot PEF \tag{9.19}$$

The angular deviation between the laser beam center and the RSO is called pointing error. Two different types of pointing errors are considered. The first is a constant pointing error φ_{con} where the laser beam is constantly displaced to the RSO every measurement (or its value changes only slowly compared to the inverse laser repetition rate). Thus, the pointing error factor of a constant displacement φ_{con} in respect to the beam divergence θ_d is given by,

$$PEF_{con} = e^{-2\left(\frac{\varphi_{con}}{\theta_d}\right)^2}. \tag{9.20}$$

The quantity *PEF*, which is between 0 and 1, describes the pointing error induced reduction of the expected photo-electrons per sent laser pulse N_S. Second a Gaussian distributed pointing error φ_{gauss}, which vary over short time scales. These are statistical pointing errors are:

- Turbulence induced beam wandering φ_{BW}
- Angular beam stability φ_{BS} of the laser beam
- Mechanical oscillations of the transmitter telescope and optics causing beam pointing errors φ_{MO}

The different statistical pointing errors are summed up geometrically to the total pointing error φ_{gauss}.

$$\varphi_{gauss} = \sqrt{\varphi_{BW}^2 + \varphi_{BS}^2 + \theta_{MO}^2} \tag{9.21}$$

If the constant pointing error φ_{con} is 0 and the statistical pointing error has a Gaussian distribution around the beam center with a standard deviation φ_{gauss}, the pointing error factor is given to,

$$PEF_{gauss} = \frac{1}{1 + \left(\frac{\varphi_{gauss}}{\theta_d}\right)^2}. \tag{9.22}$$

In this respect again, the value of *PEF* is between 0 and 1 and describes the reduction of the mean number of photo-electrons per pulse N_S. In case of a simultaneous constant and Gaussian distributed pointing error, the pointing error factor is calculated [50],

$$PEF = \frac{1}{1 + \left(\frac{\varphi_{gauss}}{\theta_d}\right)^2} e^{-2\left(\frac{\varphi_{con}}{\theta_d}\right)^2} e^{\frac{2\varphi_{con}^2}{\theta_d^4}\left(\frac{\varphi_{gauss}^2 \theta_d^2}{\varphi_{gauss}^2 + \theta_d^2}\right)}. \tag{9.23}$$

Optical cross section

The cross section ς_{OCS} is defined as the effective area A_{RSO} times the standard gain [100]. The standard gain is 4π times the gain defined in Eq (9.15), therefore the OCS can be described as,

$$\sigma_{\mathrm{OCS}} = 4\pi \cdot A_{\mathrm{RSO}} \cdot g_{\mathrm{RSO}}. \tag{9.24}$$

This can be applied to an RSO with an optical element which concentrates the reflected light into a solid angle Ω_{RSO}. A satellite equipped with a retro reflector, with the radius r_{Retro} has approximately a diffraction limited divergence θ_{Retro}. Thus, the gain of a cooperative RSO can be estimated to,

$$g_{\mathrm{RSO}} = \frac{1}{\pi(\theta_{\mathrm{Retro}})^2} = \frac{1}{\pi\left(\frac{\lambda}{r_{\mathrm{Retro}}\pi}\right)^2} = \frac{\pi {r_{\mathrm{Retro}}}^2}{\lambda^2}. \tag{9.25}$$

It is noted that this is a simplified approach, the actual retro reflector divergence pattern is more complex, see [100]. Thus, the OCS can be calculated by the effective area of the retro reflector A_{Retro} and its divergence θ_{Retro},

$$\sigma_{\mathrm{OCS}} = 4\pi \cdot A_{\mathrm{Retro}} \cdot \frac{1}{\pi(\theta_{\mathrm{Retro}})^2} = \frac{4\pi\, {r_{\mathrm{Retro}}}^2}{\left(\frac{\lambda}{r_{\mathrm{Retro}}\pi}\right)^2} = \frac{4\pi^3 {r_{\mathrm{Retro}}}^4}{\lambda^2} = 4\pi\left(\frac{\pi {r_{\mathrm{Retro}}}^2}{\lambda_{\mathrm{Laser}}}\right)^2. \tag{9.26}$$

The OCS of non-cooperative targets can be calculated from the BRDF (bidirectional reflectance distribution function) ϱ_{RSO} of the RSO body. The differential BRDF $\mathrm{d}\varrho_{RSO}$ gives the relation of incidence irradiance H_i and reflected radiance L_R per steradian. For a single point p on the RSO surface with the differential area $\mathrm{d}s$ it is gives as [101],

$$\mathrm{d}\rho_{\mathrm{RSO}}(\vec{p}, \theta_{\mathrm{i}}, \theta_{\mathrm{R}}, \varphi_{\mathrm{i}}, \varphi_{\mathrm{R}}) = 4\pi \frac{\mathrm{d}L_{\mathrm{R}}(\theta_{\mathrm{R}}, \varphi_{\mathrm{R}}) \cos\alpha_{\mathrm{i}} \cos\alpha_{\mathrm{R}}\, \mathrm{d}s}{\mathrm{d}H_{\mathrm{i}}(\theta_{\mathrm{i}}, \varphi_{\mathrm{i}})}. \tag{9.27}$$

Where p is the position vector on the differential surface $\mathrm{d}s$, θ_i and φ_i incidence angle of the light source, θ_R and φ_R the angle to observer. For the resulting BRDF ϱ_{RSO} of the RSO, the differential BRDF $\mathrm{d}\varrho_{RSO}$ needs to be integrated over all points p of the surface area $A_{surface}$.

$$\rho_{\mathrm{RSO}}(\theta_{\mathrm{i}}, \theta_{\mathrm{R}}, \varphi_{\mathrm{i}}, \varphi_{\mathrm{R}}) = 4\pi \iint_{A_{\mathrm{surface}}}^{\vec{p}} \frac{\mathrm{d}L_{\mathrm{R}}(\theta_{\mathrm{R}}, \varphi_{\mathrm{R}}) \cos\theta_{\mathrm{i}} \cos\theta_{\mathrm{R}}\, \mathrm{d}s}{\mathrm{d}H_{\mathrm{i}}(\theta_{\mathrm{i}}, \varphi_{\mathrm{i}})} \tag{9.28}$$

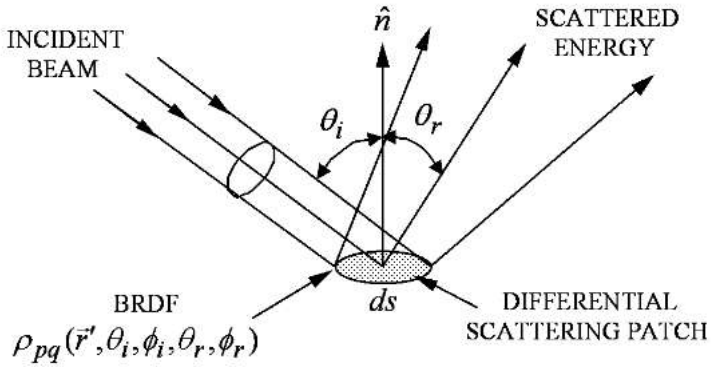

Figure 9.55: Illustration how the BRDF is defined. Source: [101]

The OCS from the BRDF can be calculated as follows [101],

$$\sigma_{\mathrm{OCS}} = 4\pi\, \rho_{\mathrm{RSO}}(\theta_{\mathrm{i}}, \theta_{\mathrm{R}}, \varphi_{\mathrm{i}}, \varphi_{\mathrm{R}}) \cos\theta_{\mathrm{i}} \cos\theta_{\mathrm{R}}. \tag{9.29}$$

The optical cross section of the optical cross section of finite components ς_i can simply be added,

$$\sigma_{\mathrm{OCS}} = \sum\nolimits_{Ai} \sigma_{\mathrm{i}} = \sigma_{\mathrm{diff}} + \sigma_{\mathrm{spec}}. \tag{9.30}$$

Like specular ς_{spec} and diffuse ς_{diff} reflected parts or all points of the surface A_i. Due to the various shapes and materials the calculation of the OCS is presented for two simple shapes as an example. For a flat diffuse scattering area A_{RSO} the BRDF is constant and the OCS is given by [101],

$$\sigma_{\mathrm{OCS}} = 4\,\pi\,\rho_{\mathrm{diff}}\,A_{\mathrm{RSO}}\,\cos^2(\theta_{\mathrm{R}}). \tag{9.31}$$

Where θ_R is the angle between surface and observer, and ϱ_{diff} the diffuse reflectivity of the RSO, whereas for a spherical RSO, the OCS can be calculated as follows [101],

$$\sigma_{\mathrm{OCS}} = 4\pi\,\rho_{\mathrm{RSO}}\,A_{\mathrm{RSO}}\,P(\psi)_{\mathrm{RSO}}. \tag{9.32}$$

Where $P(\psi)$ is the phase function and A_{RSO} the projected area of the sphere (πr_{RSO}^2). The specular phase function of a sphere is defined as [102],

$$P(\psi)_{\mathrm{Sphere,spec}} = \frac{1}{4\pi}. \tag{9.33}$$

And the diffuse phase function is [102],

$$P(\psi)_{\mathrm{Sphere,diff}} = \frac{2}{3\pi}[\sin(\psi) + (\pi - \psi)\cos(\psi)]. \tag{9.34}$$

Which leads to,

$$\sigma_{\mathrm{OCS}} = 4\pi\,A_{\mathrm{sphere}}\left[\rho_{\mathrm{diff}}P(\psi)_{\mathrm{diff}} + \rho_{\mathrm{spec}}P(\psi)_{\mathrm{spec}}\right]. \tag{9.35}$$

Transmission

The total transmission of both transmitter τ_T and receiver τ_R is the product of the transmissions of all elements in the system τ_i.

$$\tau_{\mathrm{T}} = \prod \tau_{\mathrm{i}} \tag{9.36}$$

Losses may also result from vignetting, detector or fiber coupling (encircled energy) in the receiving optical system. In the case that the *PSF* is larger than the detector surface or fiber area, not all of the power is coupled into the detector and losses occur. Furthermore, tracking error may be present resulting that the *PSF* center x_0, y_0 is offset to the detector center. The losses result from the overlapping area between the *PSF* (A_{PSF}) and detector (or fiber) area A_{Det} and the Intensity present in this area,

$$\tau_{\mathrm{T}} = \frac{\Phi(A_{\mathrm{Det}} \cap A_{\mathrm{PSF}})}{\Phi(A_{\mathrm{PSF}})} = \frac{\iint_{A_{\mathrm{Det}} \cap A_{\mathrm{PSF}}} PSF(x,y)\mathrm{d}x\mathrm{d}y}{\iint_{A_{\mathrm{PSF}}} PSF(x,y)\mathrm{d}x\mathrm{d}y}. \tag{9.37}$$

Atmospheric transmission τ_{atm} by the Mie scattering using the Kruse relation is described in Chapter 3.3 in more detail.

The Rayleigh scattering coefficient β_{m} is given as [103],

$$\beta_{\mathrm{m}} = 1.1 \times 10^{-3} \lambda^{-4}\ [\mathrm{km}^{-1}]. \tag{9.38}$$

Slant range

The slant range (or distance) R_{RSO} between a station and an object in space with orbit height h_{RSO} is given to [50],

$$R_{\mathrm{RSO}} = -(R_{\mathrm{E}} + h_{\mathrm{station}}) \cos\left(\frac{\pi}{2} - \alpha_{el}\right) + \sqrt{\left[(R_{\mathrm{E}} + h_{\mathrm{station}}) \cos\left(\frac{\pi}{2} - \alpha_{\mathrm{el}}\right)\right]^2 + 2R_{\mathrm{E}}(h_{\mathrm{RSO}} - h_{\mathrm{station}}) + h_{\mathrm{RSO}}^2 - h_{\mathrm{station}}^2}. \tag{9.39}$$

It is R_{E} the radius of the Earth, h_{station} the station height and α_{el} the elevation of the object as observed from the station (in respect to the horizon). For large elevations (>60°), this equation can be approximated to,

$$R_{\mathrm{RSO}} = \frac{h_{\mathrm{RSO}}}{\cos\left(\frac{\pi}{2} - \alpha_{\mathrm{el}}\right)}. \tag{9.40}$$

Receiver aperture

The effective receiver aperture results from the aperture area of the receiving optical system $A_{\mathrm{R,geometric}}$ and the amount of obscuration $\tau_{\mathrm{R,obscuration}}$ in respect to the receiving aperture,

$$A_{\mathrm{R}} = A_{\mathrm{R,geometric}}(1 - \tau_{\mathrm{R,obscuration}}). \tag{9.41}$$

For a circular aperture D_{R} with an obscuration diameter of D_{sec} the area is calculated as follows,

$$A_{\mathrm{R}} = \frac{\pi {D_{\mathrm{R}}}^2}{4} - \frac{\pi D_{\mathrm{sec}}^2}{4} = \frac{\pi}{4}({D_{\mathrm{R}}}^2 - {D_{\mathrm{sec}}}^2). \tag{9.42}$$

Noise modeling

There are three main noise sources which are shortly described in the section:

- Atmospheric background
- Target noise
- Detector noise

The noise rate $f_{\text{noise,atm}}$ by the atmospheric background radiation $H_{\text{atm}}(\lambda)$ is calculated by the Quantum efficiency of the detector $QE(\lambda)$, aperture area of the receiver A_{R}, the FOV of the SPD, and transmission of the receiver $\tau_{\text{R}}(\lambda)$ which should represent the bandpass filter transmission curve proposed for this systems. [99] [104]

$$f_{\text{noise,atm}} = \int_{\lambda_0}^{\lambda_1} QE(\lambda)\tau_{\text{R}}(\lambda)A_{\text{R}}FOV^2 H_{\text{Atm}}(\lambda)\text{d}\lambda \tag{9.43}$$

Where $H_{\text{Atm}}(\lambda)$ is the specific background radiation per wavelength and per sr. Wavelength range (λ_0 and λ_1) need to be chosen to cover the necessary spectrum.

Target noise rate $f_{\text{noise,RSO}}$ is Sun light which is reflected by the target. The target is effectively a point source which results in following calculation,

$$f_{\text{noise,RSO}} = \int_{\lambda_0}^{\lambda_1} QE(\lambda)\tau_{\text{R}}(\lambda)A_{\text{R}}A_{\text{RSO}}\rho_{\text{RSO}}H_{\text{Sun}}(\lambda)\text{d}\lambda. \tag{9.44}$$

Where ϱ_{RSO} is the albedo and A_{RSO} the area of the target. Note that ϱ_{RSO} is different to ς_{OCS}, while ϱ_{RSO} is the diffuse scatter of sunlight ς_{OCS} is the effective optical cross section of the incidence laser. $H_{\text{Sun}}(\lambda)$ is the specific radiation of the Sun. λ_0 and λ_1 is the relevant spectrum which is given by the detector's QE. This noise rate varies with RSO shape, orientation, materials and attitude. To block unwanted light bandpass filter are used and the integral can be linearly approximated.

$$\Delta\lambda = \lambda_1 - \lambda_0 \tag{9.45}$$

The dark count rate (DCR) is a sensor specific noise rate $f_{\text{noise,DCR}}$ and is given in the sensor specifications and can be measured,

$$f_{\text{noise,DCR}} = 2 \cdot 10^3[\text{s}^{-1}]. \tag{9.46}$$

The total noise count N_{noise} within the time interval T_{gate} is,

$$N_{\text{noise}} = \left(f_{\text{noise,atm}} + f_{\text{noise,RSO}} + f_{\text{noise,DCR}}\right)T_{\text{gate}}. \tag{9.47}$$

The combined noise rate can be measured by the system while tracking RSO and measuring the count rate of the detector. Combining the equations from the last three sections results in,

$$\mathrm{p_S} = e^{-(f_{\mathrm{noise,atm}}+f_{\mathrm{noise,RSO}}+f_{\mathrm{noise,DCR}})T_{\mathrm{gate}}} \cdot \left(1 - e^{-E_{\mathrm{Laser}}\frac{\lambda_{\mathrm{Laser}}}{hc}\frac{2}{\pi {R_{\mathrm{RSO}}}^2 {\Theta_{\mathrm{div}}}^2} e^{-2\left(\frac{\Theta_{\mathrm{PE}}}{\Theta_{\mathrm{div}}}\right)^2} \sigma_{\mathrm{OCS}} \left(\frac{1}{4\pi {R_{\mathrm{RSO}}}^2}\right)^2 A_{\mathrm{R}} \tau_{\mathrm{R}} \tau_{\mathrm{T}} Q E {\tau_{\mathrm{Atm}}}^2}\right). \quad (9.48)$$

Precision and signal to noise

The measurement precision of a single return photon is basically the laser pulse length t_{pulse}. The probability of a returning photon is negative exponential proportional to the intensity, for low return probabilities it results that the returning photons are distributed in the same distribution profile as the temporal laser pulse profile.

$$\Delta d_{\mathrm{r}} = 2 t_{\mathrm{pulse}} c \quad (9.49)$$

For higher probabilities that more than one photon returns, it is more likely that a photon in the beginning of the pulse. Furthermore, each measurement receives further jitter by the receiving electronics which include SPD $\measuredangle t_{\mathrm{SPD}}$ and event timer (ET) $\measuredangle t_{\mathrm{ET}}$. By approximating the distribution to Gaussian distribution, the uncertainty of a single return can be calculated,

$$\Delta d_{\mathrm{r}} = 2c\sqrt{{t_{\mathrm{pulse}}}^2 + {\Delta t_{\mathrm{ET}}}^2 + {\Delta t_{\mathrm{SPD}}}^2}. \quad (9.50)$$

By recording multiple returns the uncertainty drops under noise dominant environment by the square root of number of measurements [43] N_{NP} in the time frame of a normal point (NP) T_{NP} as follows,

$$\Delta d_{\mathrm{r}} = \frac{2c\sqrt{{t_{\mathrm{pulse}}}^2 + {\Delta t_{\mathrm{ET}}}^2 + {\Delta t_{\mathrm{SPD}}}^2}}{\sqrt{N_{\mathrm{NP}}}}. \quad (9.51)$$

To calculate the number of signal events N_{NP} within time interval T_{NP} previous equations can be used,

$$N_{\mathrm{S,free}} = T_{\mathrm{NP}} f_{\mathrm{Laser}} \left((1 - f_{\mathrm{noise}} t_{\mathrm{dead}}) N_{\mathrm{S}}\right). \quad (9.52)$$

For the gated scenario the number of signal events over the time period T_{NP} is,

$$N_{\mathrm{NP}} = T_{\mathrm{NP}} f_{\mathrm{laser}} p_{\mathrm{S}}. \quad (9.53)$$

To estimate the uncertainty of a ranging measurement the non-gated scenario is considered,

$$\Delta d_{\mathrm{r}} = \frac{2c\sqrt{{t_{\mathrm{pulse}}}^2 + {\Delta t_{\mathrm{ET}}}^2 + {\Delta t_{\mathrm{SPD}}}^2}}{\sqrt{T_{\mathrm{NP}} f_{\mathrm{Laser}} (1 - f_{\mathrm{noise}} t_{\mathrm{dead}}) N_{\mathrm{S}}}}. \quad (9.54)$$

By using equations from above $\measuredangle d_r$ results in,

$$\Delta d_{\mathrm{r}} = \frac{2c\sqrt{{t_{\mathrm{pulse}}}^2 + {\Delta t_{\mathrm{ET}}}^2 + {\Delta t_{\mathrm{SPD}}}^2}}{\sqrt{T_{\mathrm{NP}} f_{\mathrm{Laser}}(1 - f_{\mathrm{noise}} t_{\mathrm{dead}}) \cdot E_{\mathrm{Laser}} \frac{\lambda_{\mathrm{Laser}}}{hc} \cdot \frac{2}{\pi {R_{\mathrm{RSO}}}^2 {\Theta_{\mathrm{div}}}^2} e^{-2\left(\frac{\Theta_{\mathrm{PE}}}{\Theta_{\mathrm{div}}}\right)^2} \sigma_{\mathrm{OCS}} \left(\frac{1}{4\pi {R_{\mathrm{RSO}}}^2}\right)^2 A_{\mathrm{R}} \tau_{\mathrm{R}} \tau_{\mathrm{T}} Q E {\tau_{\mathrm{Atm}}}^2}}}, \tag{9.55}$$

This shows that the uncertainty is proportional to the system's hardware parameters as follows,

$$\Delta d_r \propto \frac{\sqrt{{t_{\mathrm{pulse}}}^2 + {\Delta t_{\mathrm{ET}}}^2 + {\Delta t_{\mathrm{SPD}}}^2}}{\sqrt{T_{\mathrm{NP}} f_{\mathrm{Laser}} \frac{\lambda_{\mathrm{Laser}} E_{\mathrm{Laser}}}{{\Theta_{\mathrm{div}}}^2}}} \propto \frac{t_{\mathrm{pulse}}}{\sqrt{\frac{\lambda_{\mathrm{Laser}} P_{\mathrm{Laser}}}{{\Theta_{\mathrm{div}}}^2}}}. \tag{9.56}$$

For the gated case the uncertainty, the previously presented return rate under 9.4.2 Photon detection statistics, is used to calculate the number of events to detect a photo electron $N_{\mathrm{S(NP)}}$ within the time interval of a normal point T_{NP},

$$N_{\mathrm{S(NP)}} = T_{\mathrm{NP}} f_{\mathrm{Laser}} e^{-N_{\mathrm{noise}}} (1 - e^{-N_{\mathrm{S}}}). \tag{9.57}$$

Which follows that for the gated scenario $\measuredangle d_r$ is,

$$\Delta d_{\mathrm{r}} = \frac{2c\sqrt{{t_{\mathrm{pulse}}}^2 + {\Delta t_{\mathrm{ET}}}^2 + {\Delta t_{\mathrm{SPD}}}^2}}{\sqrt{T_{\mathrm{NP}} f_{\mathrm{Laser}} e^{-N_{\mathrm{noise}}} (1 - e^{-N_{\mathrm{S}}})}}. \tag{9.58}$$

As many factors affect the link budget return rate, all parameters set fixed except the laser specific to give a simplified calculation how accurate the measurements can be in relation to laser power P_{Laser} ($P_{\mathrm{Laser}} = E_{\mathrm{Laser}} \cdot f_{\mathrm{Laser}}$), wavelength λ, beam divergence Θ_{div} and pulse length t_{pulse},

$$\Delta d_{\mathrm{r}} \propto \frac{t_{\mathrm{pulse}}}{\sqrt{f_{\mathrm{laser}} e^{-N_{\mathrm{noise}}} (1 - e^{-N_{\mathrm{S}}})}}. \tag{9.59}$$

Which is leading to,

$$\Delta d_r \propto \frac{t_{\mathrm{pulse}}}{\sqrt{f_{\mathrm{laser}} e^{-N_{\mathrm{noise}}} \left(1 - e^{-\frac{\lambda_{\mathrm{Laser}} E_{\mathrm{Laser}}}{{\Theta_{\mathrm{div}}}^2}}\right)}}. \tag{9.60}$$

If signal N_{S} is smaller 0.5; 1-exp*(-x)* can be linear approximated and if the noise is constant the range uncertainty Δd_{r} is proportional to,

$$\Delta d_{\mathrm{r}} \propto \frac{t_{\mathrm{pulse}}}{\sqrt{f_{\mathrm{laser}} e^{-N_{\mathrm{noise}}} \frac{\lambda_{\mathrm{Laser}} E_{\mathrm{Laser}}}{\Theta_{\mathrm{div}}{}^2}}} \propto \frac{t_{\mathrm{pulse}}}{\sqrt{\frac{\lambda_{\mathrm{Laser}} P_{\mathrm{Laser}}}{\Theta_{\mathrm{div}}{}^2}}}. \tag{9.61}$$

Note, that the noise has an exponential effect and therefore strongly affecting real world uncertainties.

The signal to noise ratio (*SNR*) is the variance of the noise. The variance of Poisson distributed events is the square root of the number noise events,

$$SNR = \frac{\sum_{\mathrm{i}} N_{\mathrm{S(i)}}}{\sqrt{\sum_{\mathrm{i}} \sigma_{\mathrm{N(i)}}{}^2}} = \frac{\sum_{\mathrm{i}} N_{\mathrm{S(i)}}}{\sqrt{\sum_{\mathrm{i}} N_{\mathrm{noise(i)}}}}. \tag{9.62}$$

The numbers of noise events are evenly distributed but the signal events arrive during the expected time of arrival, which is about 2 times the laser pulse length t_{pulse} (95% of the signal). Thus, noise events within this timespan interfere with the signal strength. The sum results from the laser pulse frequency f_{laser} and time interval of the normal point T_{NP},

$$N_{\mathrm{n}} = \left(2 t_{\mathrm{pulse}} f_{\mathrm{noise}}\right) T_{\mathrm{NP}} f_{\mathrm{Laser}}. \tag{9.63}$$

Where f_{noise} is the noise rate. Due to Poisson distribution of the noise the *SNR* is calculated as follows,

$$SNR = \frac{T_{\mathrm{NP}} f_{\mathrm{Laser}} \left((1 - n_{\mathrm{noise}} t_{\mathrm{dead}}) N_{\mathrm{S}}\right)}{\sqrt{\left(2 t_{\mathrm{pulse}} n_{\mathrm{noise}}\right) T_{\mathrm{NP}} f_{\mathrm{Laser}}}} = \frac{\sqrt{T_{\mathrm{NP}} f_{\mathrm{Laser}}} (1 - n_{\mathrm{noise}} t_{\mathrm{dead}}) N_{\mathrm{S}}}{\sqrt{2 t_{\mathrm{pulse}} n_{\mathrm{noise}}}}. \tag{9.64}$$

For the gated case the *SNR* can be calculated as follows,

$$SNR = \frac{T_{\mathrm{NP}} f_{\mathrm{Laser}} P_{\mathrm{S}}}{\sqrt{T_{\mathrm{NP}} f_{\mathrm{Laser}} P_{\mathrm{N}}}} = \frac{\sqrt{T_{\mathrm{NP}} f_{\mathrm{Laser}}} e^{-N_{\mathrm{noise}}} (1 - e^{-N_{\mathrm{S}}})}{\sqrt{(1 - e^{-N_{\mathrm{noise}}})}}. \tag{9.65}$$

When the number of return N_{S} is smaller 0.5 it can be linear approximated, while the noise term diverges to 1 for N_{noise} larger 2,

$$SNR \approx \frac{\sqrt{T_{\mathrm{NP}} f_{\mathrm{Laser}}} e^{-N_{\mathrm{noise}}} N_{\mathrm{S}}}{\sqrt{(1 - e^{-N_{\mathrm{noise}}})}} \approx \frac{\sqrt{T_{\mathrm{NP}} f_{\mathrm{Laser}}} \lambda_{\mathrm{Laser}} E_{\mathrm{Laser}}}{\Theta_{\mathrm{div}}{}^2} e^{-N_{\mathrm{noise}}}. \tag{9.66}$$

This makes the *SNR* proportional to,

$$SNR \propto \frac{\sqrt{f_{\mathrm{Laser}}} \lambda_{\mathrm{Laser}} E_{\mathrm{Laser}}}{\Theta_{\mathrm{div}}{}^2} = \frac{\lambda_{\mathrm{Laser}} P_{\mathrm{Laser}}}{\sqrt{f_{\mathrm{Laser}}} \Theta_{\mathrm{div}}{}^2}. \tag{9.67}$$

Figure 9.56 shows the calculated number of returning signal event using Eq. (9.52) (blue) and Eq. (9.53) (orange) in the upper graph and the corresponding calculated range uncertainty and signal to noise ratio in relation the measurement distance to the RSO. For the later two the number of photons is calculated using gated scenario.

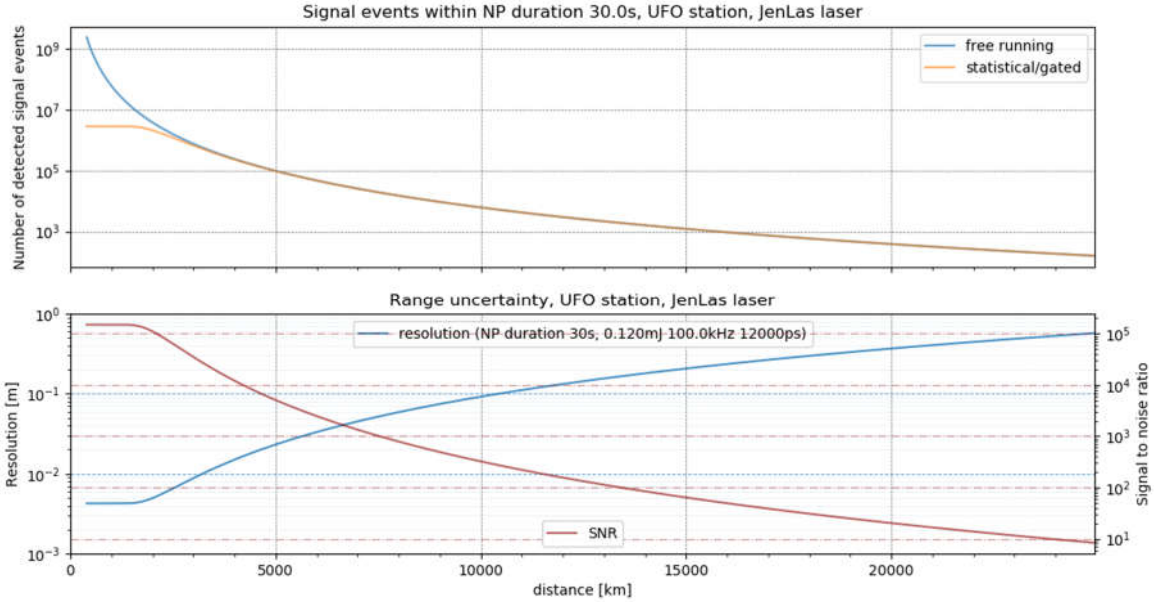

Figure 9.56: Number of detected signal events and corresponding modeled resolution and SNR depending on the distance to the RSO. The RSO reflects the transmitted laser pulses back to the observer by a retroreflector carried by LAGEOS satellite. Receiver and transmitter aperture are simulated with hardware parameters by the UFO observatory with a beam divergence of 120 µrad.

It can clearly be seen that in the situation of multi photon returns the number of events is limited. Thus, the SNR and uncertainty is constant. Below that the number of events and SNR are dropping while the uncertainty gets larger.

9.5. DEFINITION OF MANMADE SPACE OBJECTS

Definition of manmade space object defined by Ref. [12]:

- Payloads: space object designed to perform a specific function in space excluding launch functionality. This includes operational satellites as well as calibration objects.
- Payload mission related objects: space objects released as space debris which served a purpose for the functioning of a payload. Common examples include covers for optical instruments or astronaut tools.
- Payload fragmentation debris: space objects fragmented or unintentionally released from a payload as space debris for which their genesis can be traced back to a unique

event. This class includes objects created when a payload explodes or when it collides with another object.

- Payload debris: space objects fragmented or unintentionally released from a payload as space debris for which the genesis is unclear but orbital or physical properties enable a correlation with a source.
- Rocket body: space object designed to perform launch related functionality; This includes the various orbital stages of launch vehicles, but not payloads which release smaller payloads themselves.
- Rocket mission related objects: space objects intentionally released as space debris which served a purpose for the function of a rocket body. Common examples include shrouds and engines.
- Rocket fragmentation debris: space objects fragmented or unintentionally released from a rocket body as space debris for which their genesis can be traced back to a unique event. This class includes objects created when a launch vehicle explodes.
- Rocket debris: space objects fragmented or unintentionally released from a rocket body as space debris for which the genesis is unclear but orbital or physical properties enable a correlation with a source

9.6. DEFINITION OF ORBITAL REGIMES

Definitions of orbital regimes according to Ref. [12] by ESA can be found in Table 9.5.

Orbit	Description	Definition		
GEO	Geostationary Orbit	$i \in [0, 25]$	$h_p \in [35586, 35986]$	$h_a \in [35586, 35986]$
IGO	Inclined Geosynchronous Orbit	$a \in [37948, 46380]$	$e \in [0.00, 0.25]$	$i \in [25, 180]$
EGO	Extended Geostationary Orbit	$a \in [37948, 46380]$	$e \in [0.00, 0.25]$	$i \in [0, 25]$
NSO	Navigation Satellites Orbit	$i \in [50, 70]$	$h_p \in [18100, 24300]$	$h_a \in [18100, 24300]$
GTO	GEO Transfer Orbit	$i \in [0, 90]$	$h_p \in [0, 2000]$	$h_a \in [31570, 40002]$
MEO	Medium Earth Orbit	$h_p \in [2000, 31570]$	$h_a \in [2000, 31570]$	
GHO	GEO-superGEO Crossing Orbits	$h_p \in [31570, 40002]$	$h_a > 40002$	
LEO	Low Earth Orbit	$h_p \in [0, 2000]$	$h_a \in [0, 2000]$	
HAO	High Altitude Earth Orbit	$h_p > 40002$	$h_a > 40002$	
MGO	MEO-GEO Crossing Orbits	$h_p \in [2000, 31570]$	$h_a \in [31570, 40002]$	
HEO	Highly Eccentric Earth Orbit	$h_p \in [0, 31570]$	$h_a > 40002$	
LMO	LEO-MEO Crossing Orbits	$h_p \in [0, 2000]$	$h_a \in [2000, 31570]$	
UFO	Undefined Orbit			
ESO	Escape Orbits			

Table 9.5: Ranges defining each orbital class, with semi-major axis a, eccentricity e, inclination i, perigee height h_p and apogee height h_a. The units are km and degrees. Source: [12].

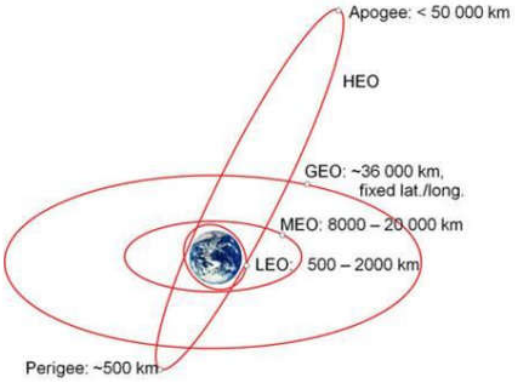

Figure 9.57: Overview of the heights and location of orbital regimes. Source: [105].

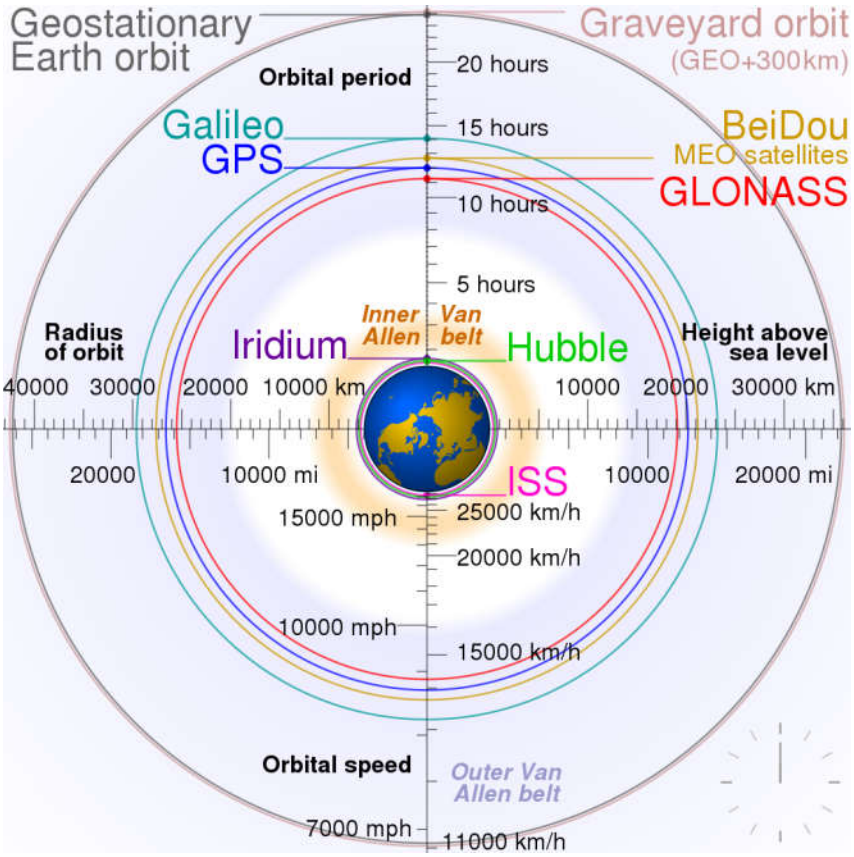

Figure 9.58: Comparison of GPS, GLONASS, Galileo and COMPASS (medium Earth orbit satellites) orbits with International Space Station, Hubble Space Telescope, geostationary and graveyard orbits, and the nominal size of the Earth. Source: [106] © CC-BY.

9.7. SPACEFLIGHT RELATED DEFINITIONS

Spaceflight related definitions by Ref. [107]:

Apogee: The point in the orbit that is the farthest from the center of the Earth. The apogee altitude is the distance of the apogee point above the surface of the Earth.

Ascending Node: The point in the orbit where a satellite crosses the Earth's equatorial plane in passing from the southern hemisphere to the northern hemisphere. Credible Failure Mode: A failure mode identified by failure mode and effects analyses or equivalent analyses, for which a quantitative failure probability is available and exceeds 0.000001 (1:1,000,000).

Decommissioning: The process of closing out the mission, including data archiving, hardware logistics, and management issues. Decommissioning follows passivation of the spacecraft.

Disposal: An end-of-mission process for moving a spacecraft (if necessary) to an orbit or trajectory considered acceptable for orbital debris limitation. Earth Orbital Velocity: Any velocity perpendicular to the Earth's radius vector at or above 130 km that is in excess of 7,826 m/sec.

Eccentricity: The apoapsis altitude minus periapsis altitude of an orbit divided by twice the semi-major axis. Eccentricity is zero for circular orbits and less than one for all elliptical orbits.

Launch Vehicle: Any space transportation mode, including expendable launch vehicles (ELVs), and reusable launch vehicles (RLVs).

Meteoroids: Naturally occurring particulates associated with solar system formation or evolution processes. Meteoroid material is often associated with asteroid breakup or material released from comets.

Mission Operations: Phase of a mission where the spacecraft is performing a useful function, including the design mission, primary mission, secondary mission, extended mission, and activities leading to disposal.

Orbital Debris: Artificial objects, including derelict spacecraft and spent launch vehicle orbital stages, left in orbit which no longer serve a useful purpose. In this document, only debris of diameter 1 mm and larger is considered. If liquids are to be released, they should explicitly be shown to be compliant with all mitigation requirements.

Orbital Lifetime: The length of time an object remains in orbit. Objects in LEO or passing through LEO lose energy as they pass through the Earth's upper atmosphere, eventually getting low enough in altitude that the atmosphere removes them from orbit.

Orbital Stage: A part of the launch vehicle left in a parking, transfer, or final orbit (excluding solar/interplanetary orbits with no potential intercept with Earth) during or after payload

insertion; includes liquid propellant systems, solid rocket motors, and any propulsive unit jettisoned from a spacecraft.

Passivation: The process of removing stored energy from a space structure which could credibly result in eventual generation of new orbital debris after End of Mission. This includes removing energy in the form of electrical, pressure, mechanical, or chemical.

Perigee: The point in the orbit that is nearest to the center of the Earth. The perigee altitude is the distance of the perigee point above the surface of the Earth.

Postmission Disposal: The process of intentionally changing the orbit of a spacecraft after the end of the operational mission.

Prompt Injury: A medical condition received as a result of the falling debris which requires (or should have required) professional medical attention within 48 hours of the impact.

Right Ascension of Ascending Node: The angle between the line extending from the center of the Earth to the ascending node of an orbit and the line extending from the center of the Earth to the vernal equinox, measured from the vernal equinox eastward in the Earth's equatorial plane.

Semi-major Axis: Half the sum of the distances of apogee and perigee from the center of the Earth (or other body) equal to half the length of the major axis of the elliptical orbit.

Spacecraft: This includes all components contained within or attached to a space borne payload such as instruments and fuel.

Space Debris: General class of debris, including both meteoroids and orbital debris. Space Structures: Spacecraft and launch vehicle orbital stages. This includes all components contained within the object such as instruments and fuel.

Stabilized: When the spacecraft maintains its orientation along one or more axes. Sun Synchronous Orbit (SSO): An orbit in which the angle between the Sun-Earth vector and the intersection of the plane of a satellite's orbit and the Earth's equator is a constant and does not change with the season.

9.8. DEBRIS MITIGATION MEASURES

According to Ref. [12] most internationally accepted space debris mitigation measures can be traced back to the following objectives:

- The limitation of space debris released during normal operations; i.e. in all operational orbit regimes, payloads and rocket bodies should be designed not to release space

debris during normal operations. Where this is not feasible, any release of debris should be minimised in number, area and orbital lifetime.

- The minimisation of the potential for on-orbit break-ups; i.e. in all operational regimes one should minimise the potential for break-ups during operational phases, e.g. by thorough analysis of the failure trees, increase (sub)system reliability, etc., minimise the potential for post-mission break-ups resulting from stored energy, e.g. stored in tanks, batteries, flywheels, etc., and the avoidance of intentional destruction and other harmful activities, e.g. intentional break-ups should avoided at all cost but if need be they should be conducted at sufficiently low altitudes so that orbital fragments are short lived.
- Post mission disposal; i.e. two protected regimes, LEO and Geostationary Orbit (GEO), have been identified and should be cleared from permanent or (quasi-) periodic presence of non-functional man-made objects. Payloads or rocket bodies that are terminating their operational phases in other orbital regions should be manoeuvred to reduce their orbital lifetime, commensurate with LEO lifetime limitations, or relocated if they cause interference with highly utilised orbit regions.
- Prevention of on-orbit collisions; i.e. in developing the design and mission profile of a space object, a project should estimate and limit the probability of accidental collision with known objects during the payload or rocket body's orbital lifetime. If reliable orbital data is available, avoidance manoeuvres and co-ordination of launch windows may be considered if the collision risk is not considered negligible.

9.9. TECHNICAL SPECIFICATIONS

Raymetrics enclosure

Enclosure		
External Dimensions	400 x 1000 x 450 mm (W x H x D) (approximately)	
IP Rating	67	
Material	Aluminum inner and outer covers, steel frame	
Connectors	IP68 Power plug, RJ45 and USB connectors	
Mobility – deployment	Casters and leveling feet	
Accessibility	Front door, slides and canopy for hatch maintenance	
Optical Window		
Window available sizes	**Diameter**	**Thickness**
	200mm	20mm
	300mm	25mm
Surface quality	λ/10	
Antireflection coating	From 355nm to 1064nm	
Mount	Aluminum mount with clear top for easy cleaning	
Anti-dew	Internal fan external blower	
Cleaning	External blower	
Automation		
Motorized Hatch	Yes	
Hatch speed	Up to	
Finger safe	Yes, configurable force (up to 100N)	
Input – control	• From external signal (cloud, rain, sun detector), • Power loss, • enclosure rocker switch, • Computer controlled via USB	
Sensors	• 2 x Relative humidity & Temperature. Used for anti-dew system • Rain & sun sensor used for the hatch	
Air conditioning		
Cooling heating Type	2 x Thermoelectric coolers	
Cooling capacity	L35, L35 – 166 Watts per cooler	
Heating capacity	146 Watts per cooler	
Dehumidifier type	Thermoelectric	
Extraction capacity	1lt per 24hr	
Extra		
Surge protection	Type 1&2 and type 3, Cat5 RJ45	
UPS	1kVA	

Table 9.6: Specifications of the weatherproofed housing by RAYMETRICS. Source: [108]

9.9.1. CAMERAS

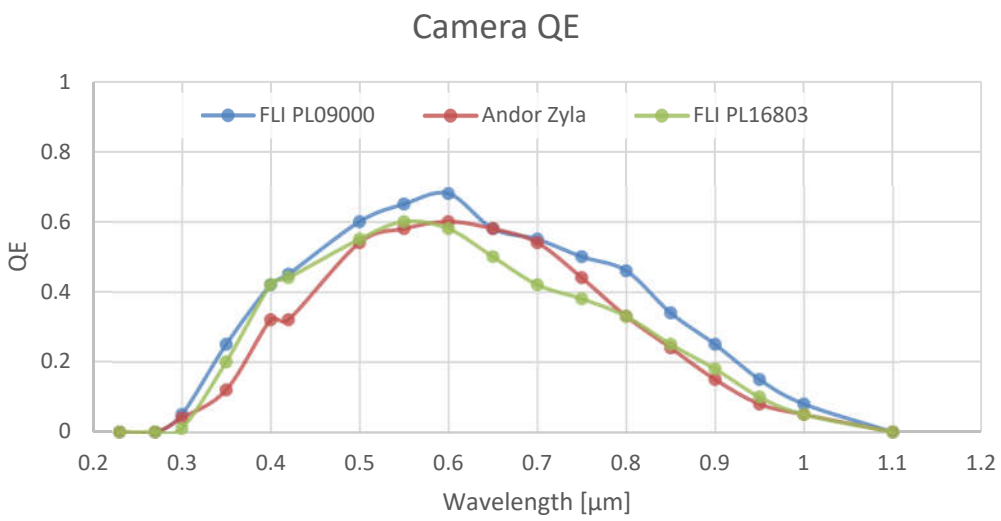

Figure 9.59: QE of the FLI PL16803 (green), FLI PL09000 (blue), and ANDOR ZYLA (red) cameras.

FLI PL16803

Sensor Specifications (from manufacturer)					
Sensor	On Semi KAF-16803				
Pixels	4096 x 4096	**Sensor Size**	36.8 X 36.8 mm	**Megapixels**	16.8
Pixel Size	9 µm	**Sensor Diagonal**	52 mm	**Video Size (inch)**	3.3
Full Well Capacity	100000 electrons	**CCD Variants**			
Color Options	Monochrome	**CCD Grades**	Standard		
CCD Type	Front Illuminated	**Anti-Blooming**	> 100X saturation		

Camera Performance					
Typical Maximum Cooling	55°C below ambient	**Dark Current (typical)**	<0.005 electrons/pixel/sec at -35°C		
Temperature Stability	0.1°C	**Cooling Method**	Air (Optional liquid)		
Digitization Speed	1 MHz, 8 MHz				
Typical System Noise	10e- @ 1 MHz; 14-e @ 8 MHz			**Non-Linearity**	<1%
Housing Dimensions	6.2 X 6.2 X 3.8 inches (15.7 X 15.7 X 9.6 cm)			**Weight**	5.85 lbs (2.6 kg)
Focal Plane to Face Plate	21 mm				
Lens Mounts	Optional Nikon F-mount or Canon EOS mount				
Interface	USB 2.0	**Camera Channels**	1		
Available Shutters	63.5 mm				
External Triggering	Standard				
Environment	-30°C to 45°C | 10% - 90% Relative Humidity				
Power	12V (100-240V AC to 12V DC power supply included). With TEC off: <1A. TEC at 100%: 4.6A. Shutter open: 4A pulse for 100msec. Shutter held open, add 0.22A.				

Table 9.7: Specifications of the FLI PL16803 camera. Source: [71]

FLI PL09000

Sensor Specifications (from manufacturer)

Sensor	On Semi KAF-09000				
Pixels	3056 x 3056	**Sensor Size**	36.6 X 36.6 mm	**Megapixels**	9.3
Pixel Size	12 µm	**Sensor Diagonal**	51.7 mm	**Video Size (inch)**	3.2
Full Well Capacity	110000 electrons	**CCD Variants**			
Color Options	Monochrome	**CCD Grades**	Standard		
CCD Type	Front Illuminated	**Anti-Blooming**	> 100X saturation		

Camera Performance

Typical Maximum Cooling	55°C below ambient	**Dark Current (typical)**	0.02 electrons/pixel/sec at -35°C
Temperature Stability	0.1°C	**Cooling Method**	Air (Optional liquid)
Digitization Speed	1 MHz, 8 MHz		
Typical System Noise	10e- @ 1 MHz; 15e- @ 8 MHz	**Non-Linearity**	<1%
Housing Dimensions	6.2 X 6.2 X 3.8 inches (15.7 X 15.7 X 9.6 cm)	**Weight**	5.6 lbs (2.5 kg)
Focal Plane to Face Plate	21 mm		
Lens Mounts	Optional Nikon F-mount or Canon EOS mount		
Interface	USB 2.0	**Camera Channels**	1
Available Shutters	65 mm	**Shutter MTBF**	1000000
External Triggering	Standard		
Environment	-30°C to 45°C | 10% - 90% Relative Humidity		
Power	12V (100-240V AC to 12V DC power supply included). With TEC off: <1A. TEC at 100%: 4.6A. Shutter open: 4A pulse for 100msec. Shutter held open, add 0.22A.		

Table 9.8: Specifications of the FLI PL09000 camera. Source: [70]

Andor Zyla

General Specifications[•1]

Pixel size (W x H)	6.5 µm
Pixel well depth (e-)	30,000
Linearity (%, maximum)[•5] Full light range Low light range (< 1000 electrons signal)	 Better than 99.8% Better than 99.9%
MTF (Nyquist @ 555 nm)	45%
Pixel binning	Hardware binning: 2 x 2, 3 x 3, 4 x 4, 8 x 8
Anti-blooming factor	x 10,000
I/O	External Trigger, Fire, Fire n, Fire All, Fire Any, Arm
Trigger Modes	Internal, External, External Start, External Exposure, Software Trigger
Software Exposure Events[•6]	Start exposure - End exposure (row 1), Start exposure - End exposure (row n)
Hardware timestamp accuracy	25 ns
Internal memory	1 GB

Table 9.9: Specifications of the ANDOR ZYLA camera. Source: [69]

Model	Zyla 5.5			Zyla 4.2 PLUS	
Sensor type	Front Illuminated Scientific CMOS			Front Illuminated Scientific CMOS	
Active pixels (W x H)	2560 x 2160 (5.5 Megapixel)			2048 x 2048 (4.2 Megapixel)	
Sensor size	16.6 x 14.0 mm 21.8 mm diagonal			13.3 x 13.3 mm 18.8 mm diagonal	
Pixel readout rate (MHz)	200 (100 MHz x 2 sensor halves) 560 (280 MHz x 2 sensor halves)			Slow Read 216 (108 MHz x 2 sensor halves) Fast Read 540 (270 MHz x 2 sensor halves)	
Read noise (e^-) Median [rms] •2		Rolling Shutter	Global Shutter		Rolling Shutter
	@ 200 MHz	0.9 [1.2]	2.3 [2.5]	@ 216 MHz	0.90 [1.1]
	@ 560 MHz	1.2 [1.6]	2.4 [2.6]	@ 540 MHz	1.10 [1.3]
Maximum Quantum Efficiency •3	64%			82%	
Sensor Operating Temperature Air cooled Water cooled	0°C (up to 30°C ambient) -10°C*			0°C (up to 27°C ambient) -10°C*	
Dark current, e^-/pixel/sec @ min temp •4 Air cooled Water cooled	0.10 0.019			0.10 0.019	
Readout modes	Rolling Shutter and True Global Shutter (Snapshot)			Rolling Shutter and Global Clear •5	
Maximum dynamic range	33,000:1			33,000:1	
Photon Response Non-Uniformity (PRNU) Half-light range Low light range	< 0.01% < 0.1%				
Pre-defined Region of Interest (ROI)	2048 x 2048, 1920 x 1080, 1392 x 1040, 512 x 512, 128 x 128			1920 x 1080, 1392 x 1040, 512 x 512, 128 x 128	
User defined ROI (granularity)	Yes (1 pixel) **				
Data range	12-bit (fastest USB 3.0 speeds) and 16-bit (maximum dynamic range)				
Interface options	USB 3.0•9 Camera Link 10-tap				

* Cooling temperature must be above the dew point
** Minimum ROI size: 4 x 8 (W x H) possible for 12- or 16-bit modes and for both Camera Link 10-tap and USB 3.0 models

Table 9.10: Specifications of the ANDOR ZYLA camera. Source: [69]

UNIBLITZ CS-65 Shutter

Delay time on opening after current applied	9.0
Transfer time on opening	45.0
Total opening time	54.0
Min. dwell time with min. input pulse	22.0
Min. equivalent exp. time	70.0
Transfer time on closing	52.0
Total window time	119.0
Min. exposure time	75.0
Typical exposure pulse	>65.0

Table 9.11: Specifications of the UNIBLITZ CS-65 shutter which is used in the FLI PL16803 and PL09000 cameras. Source: [78]

9.9.2. LENSES

200mm f2

Manufacturer and product name	**Canon EF 200mm f/2L IS USM**
Focal length	200 mm
F-number	2
Aperture diameter	100 mm
Specified image circle	42.5 mm
Specified FOV	12°
Manufacturer Spec Size (DxL)	128 mm x 208 mm
Measured Size (DxL)	162 mm x 216.7 mm
Manufacturer Specification Weight	2520 g
Measured Weight	2585 g
Lenses / Groups	17/12
Lens mount	(Canon) EF
Year Introduced	2008
List Price	6 309 € [https://store.canon.de/canon-ef-200mm-f-2l-is-usm-objektiv/2297B005/]

Table 9.12: Specifications of Canon 200mm f2 lens. Source: [75]

135mm f2

Manufacturer and product name	**Canon EF 135mm f/2L USM**
Focal length	135 mm
F-number	2
Aperture diameter	67.5 mm
Specified image circle	42.5 mm
Specified FOV	18°
Manufacturer Spec Size (DxL)	83 mm x 112 mm
Measured Size (DxL)	82 mm x 119.5 mm
Manufacturer Specification Weight	750 g
Measured Weight	725 g
Lenses / Groups	10/8
Lens mount	(Canon) EF
Year Introduced	1996
List Price	1 055 € [https://store.canon.de/canon-ef-135mm-f-2l-usm-objektiv/2520A015/]

Table 9.13: Specifications of Canon 135mm f2 lens. Source: [74]

85mm f1.2

Manufacturer and product name	**Canon EF 85mm f/1.2L II USM**
Focal length	85 mm
F-number	1.2
Aperture diameter	70.8 mm
Specified image circle	42.5 mm
Specified FOV	28.5°
Manufacturer Spec Size (DxL)	91.5 mm x 84 mm
Measured Size (DxL)	91 mm x 95.3 mm
Manufacturer Specification Weight	1025 g
Measured Weight	970 g
Lenses / Groups	8/7
Lens mount	(Canon) EF
Year Introduced	2006
List Price	2 129 € [https://store.canon.de/canon-ef-85mm-f-1-2l-ii-usm-objektiv/1056B005/]

Table 9.14: Specifications of Canon 85mm f1.2 lens. Source: [73]

400mm f2.8

Manufacturer and product name	**Canon EF 400mm f/2.8L II IS USM**
Focal length	400 mm
F-number	2.8
Aperture diameter	142 mm
Specified image circle	42.5 mm
Specified FOV	3.5°
Manufacturer Spec Size (DxL)	163 mm x 343 mm
Measured Size (DxL)	163 mm x 350 mm
Manufacturer Specification Weight	3850 g
Measured Weight	3825 g
Lenses / Groups	16/12
Lens mount	(Canon) EF
Year Introduced	2011
List Price	12 999 € [https://ac-foto.com/product/ef-40028l-is-usm-iii]

Table 9.15: Specifications of Canon 400mm f2.8 lens. Source: [76]

9.9.3. UFO OBSERVATORY

ASTELCO NTM-500

Model	**NTM-500**
Manufacturer	ASTELCO
Slewing speed	20°/s
Acceleration/deacceleration	20°/s²
Pointing precision	<1 arcsec
Weight	85 kg
Load capacity	90 kg
Drive	Direct drive

Table 9.16: Specifications of the ASTELCO NTM-500 mount used at the UFO observatory. Source: [109]

PLANEWAVE CDK 17

Model	**CDK17**
Manufacturer	PLANEWAVE Instruments
Optic design	Ritchey-Chretien
Image circle	52 mm
Aperture	430 mm
Focal length	2939 mm
Focal ratio	f/6.8
Back focus	127 mm
Primary mirror	Al-coated, prolate ellipsoid, 431.8 mm, f/2.6
Secondary mirror	Al-coated, spherical, 152.4 mm
Lens group	2x 90 mm single lenses, AR coated

Table 9.17: Specifications of the PLANEWAVE CDK17 telescope, which is used as the tracking telescope at the UFO observatory. Source: [110]

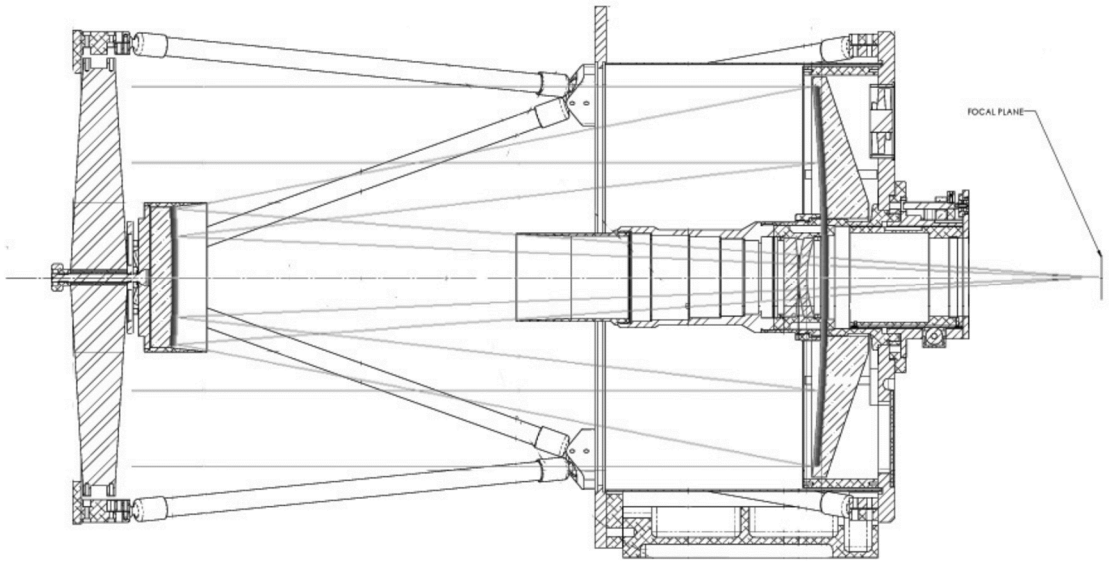

Figure 9.60: Mechanical drawing of the PLANEWAVE CDK17 telescope. Source: [110]

9.9.4. COMPUTER HARDWARE

Staring system notebook

Fujitsu Lifebook E754

Windows 7

Intel Core i7 4702MQ

8GB RAM

1TB HDD SATA

APPARILLO1-PC

Fujitsu Celsius W530 power

Linux Ubuntu 18.4

Intel Xeon E3-1276 v3

32GB RAM

1TB NVMe SSD M.2

APPARILLO2-PC

Fujitsu Celsius W550

Linux Ubuntu 18.4

Intel Xeon E3-1275

32GB RAM

Nvidia Quadro K2200

1 TB NVMe SSD M.2

CURRICULUM VITAE

Date of Birth:	16.02.1989 in Wernigerode, Germany
Nationality:	German

Educational history

May 2017 - April 2022	Promotion, **University of Stuttgart**, Stuttgart, Germany
March 2012 - February 2014	**University of Applied Science Darmstadt**, Darmstadt, Germany Optical technology and image processing, Master of Science
September 2008 - February 2012	**University of Applied Science Darmstadt**, Darmstadt, Germany Optical technology and image processing, Bachelor of Science
2000 - 2008	**Gerhart-Hauptmann-Gymnasium**, Wernigerode, Germany

Diploma:

April 2022	**Doctor of Engineering Sciences**, Dr.-Ing.
February 2014	**Optical Technology and Image Processing**, M.Sc.
February 2012	**Optical Technology and Image Processing**, B.Sc.
2008	High-School diploma

Practical experience:

Since August 2022	Research Scientist, Institute of Communications and Navigation, **German Aerospace Center** (DLR), Oberpfaffenhofen, Germany
February 2014 - July 2022	Research Scientist, Institute of Technical Physics, **German Aerospace Center** (DLR), Stuttgart, Germany
August 2013 - January 2014	Master thesis "Laser-induced contamination on high-reflective optics", Institute of Technical Physics, **German Aerospace Center** (DLR), Stuttgart, Germany
September 2011 - February 2012	Bachelor thesis "Development and characterization of optical strain sensors", **Hochschule Darmstadt** und **Industrial Research Ltd.**, Darmstadt, Germany
August 2010 - February 2011	Research Internship, Photonics Department, **Industrial Research Ltd**., Lower Hutt, Wellington, New Zealand